UNIVERSITY OF KENT

DOCTORAL THESIS

Spectrometer-based Optical Coherence Tomography Systems with Extended Functionality

Author:
Manuel Jorge
MONTEIRO MARQUES

Supervisor:
Prof Adrian
Gh. PODOLEANU

A thesis submitted in fulfilment of the requirements
for the degree of Doctor of Philosophy

in the

Applied Optics Group
School of Physical Sciences

September 2016
Internal examiner: Dr Stuart Gibson
External examiner: Prof Christoph K Hitzenberger.
Viva-voce examination 2nd August 2016.

Declaration of Authorship

I, Manuel Jorge MONTEIRO MARQUES, declare that this thesis titled, "Spectrometer-based Optical Coherence Tomography Systems with Extended Functionality" and the work presented in it are my own. I confirm that:

- This work was done wholly or mainly while in candidature for a research degree at this University.
- Where any part of this thesis has previously been submitted for a degree or any other qualification at this University or any other institution, this has been clearly stated.
- Where I have consulted the published work of others, this is always clearly attributed.
- Where I have quoted from the work of others, the source is always given. With the exception of such quotations, this thesis is entirely my own work.
- I have acknowledged all main sources of help.
- Where the thesis is based on work done by myself jointly with others, I have made clear exactly what was done by others and what I have contributed myself.

Signed:

Date:

Last compiled: Monday 19th September, 2016 at 9:19am.

"I am among those who think that science has great beauty. A scientist in his laboratory is not only a technician: he is also a child placed before natural phenomena which impress him like a fairy tale. We should not allow it to be believed that all scientific progress can be reduced to mechanisms, machines, gearings, even though such machinery also has its beauty. Neither do I believe that the spirit of adventure runs any risk of disappearing in our world. If I see anything vital around me, it is precisely that spirit of adventure, which seems indestructible and is akin to curiosity."

Maria Skłodowska-Curie, French-Polish physicist and chemist

UNIVERSITY OF KENT

Abstract

Faculty of Sciences
School of Physical Sciences

Doctor of Philosophy

Spectrometer-based Optical Coherence Tomography Systems with Extended Functionality

by Manuel Jorge MONTEIRO MARQUES

OPTICAL coherence tomography (OCT) has evolved over the last two decades to become a major optical imaging modality in the biomedical optics field. By performing high-resolution, multi-dimensional imaging of translucent structures, it enables real-time tissue imaging *in-vivo* and *in-situ* with resolutions in the micrometre range.

This Thesis focuses on extending the functionality of spectral-domain OCT (SD-OCT) systems operating at 800 nm. On a secondary level, it also aims to address some of the performance issues involving SD-OCT, such as the ambiguity on the sign of the optical path difference and the finite axial range of the OCT system due to the sampling resolution limit of the spectrometer. Addressing these issues has been achieved through the modification of the spectrometer, exploring an effect first reported by William Fox Talbot in the mid-19th century, Talbot Bands, which effectively allows a degree of control over the SD-OCT visibility profile shape and position.

This extended functionality manifests itself by the addition of a confocal channel (applied to retinal imaging, hence creating a scanning laser ophthalmoscope, SLO), also by controlling the shape and position of the visibility profile with a novel spectrometer design employing Talbot Bands, which improves the power efficiency by coupling the two arms of the interferometer within the spectrometer itself.

Further functionality has been added to OCT technology by carrying out research on the interferometer at the core of the OCT system. A new single-detector, polarisation-sensitive OCT (PS-OCT) configuration, immune to disturbances caused by the collecting fibre was devised. This ultimately leads to a design of a plug-in PS-OCT module capable of enabling polarimetric measurements in any existing OCT system.

Acknowledgements

THIS Thesis (and the work described in it) would have not been possible if it wasn't for the presence of some truly amazing people with whom I've contacted over these past 3-4 years. Some more directly, others perhaps somewhat indirectly, but all have influenced it.

First and foremost (because I have to start somewhere) I would like to acknowledge my main supervisor, Prof Adrian PODOLEANU. From his continuous guidance to his impeccable work ethic, always having some time to discuss a problem even after a very busy day which regularly starts before 8 AM. My gratitude also goes to Dr Sylvain RIVET and Dr Adrian BRADU: from steering my research towards a completely new direction (thanks Sylvain!) to always being there and able to help, even if that ''help" often meant spending a considerable amount time proof-reading my *turbulent* writing!

The amazing people I've worked with in the Applied Optics Group (in addition to the three I have already mentioned above) also deserve considerable recognition. Starting with my fellow students, some of whom have since moved on, I would like to thank (now Dr) Chris COSTA, (and also now Dr) Radu STANCU, Michaël MARIA, Yong HU, Felix FLEISCHAUER, Michael EVERSON, Catherine CHIN, Philip BROADBRIDGE, Florin TOADERE and Dr Mantas ŽURAUSKAS for our useful Optics discussions but also for our sometimes *extended* lunch breaks where we discussed about many other interesting things ☺. I would also like to acknowledge the remaining researchers at the AOG, Dr Ramona CERNAT, Dr Brian STEER (also for showing me some nice scenery in our occasional Kentish bike rides), Dr John ROGERS (from whom we benefited from a lot of equipment) and Dr Jingyu WANG, as well as Prof David JACKSON (who supervised my very first fibre splice!). Also many exchange students, external researchers and collaborators came and went in almost 4 years (hopefully I will not be forgetting anyone!). Namely I would like to acknowledge Adam EFFENBERGER, Dr Julio POSADA, Konstantin KAPINCHEV, Dr Virgil DUMA, Dr Niels ISRAELSEN, Cecile VALET, Steven MOSER and Dr Christian NISTOR. Lastly, but not least, I also want to acknowledge my second supervisor, Dr George DOBRE, with whom I've also collaborated in running one of the undergraduate lab modules as a condition of my funding.

Speaking of funding, I am grateful to the University of Kent for providing me with a studentship and also the opportunity to be engaged in some teaching. I am also very grateful to the European Research Council (through the "COGATIMABIO" project, grant number 249889) for funding a 6-month researcher position which greatly enriched the content described in this Thesis. The two main Optics societies, Optical Society of America (OSA) and the Society for Photo-Optical Instrumentation Engineers (now just SPIE) also deserve considerable recognition for providing me with much-needed funding for me to attend two major Optics conferences in the US, Frontiers in Optics 2014 and Photonics West 2016.

Some technicalities of the work described were also considerably eased with the assistance of the School's Technical Services, which I acknowledge. Peter VERALL needs to be thanked in particular since he carried out many "quick" repairs when I didn't think these would be possible at all.

Moving to a more personal level (with less of a direct impact in the Thesis, but impacting it anyway!) I would like to thank my wonderful girlfriend Sally MAKIN, for putting up with so much at times and making this last year (which would seemingly be the most stressful one) actually quite enjoyable. I am also very grateful for the very through proof-reading she carried out in some of the chapters!

Throughout 2013 and 2014 I have also been involved (by sitting in the committee) with the Portuguese Association for Researchers and Students in the UK (PARSUK). Not only has this experience taught me a lot in terms of time and resource management (juggling a full-time PhD, plus teaching hours with meetings, reviews, reports, answering e-mails, managing the finances? We did all that!) but I also had the chance of knowing and working alongside some truly stellar individuals: Dr Joana FLORES, Ivo TIMÓTEO, Dr Nuno BIMBO, Dr Ana REBOCHO, José REIS, Joel ALVES, Mário PEREIRA, and Roberto MOREIRA. I'm also grateful to some wonderful people from the Portuguese community I've met while living in Canterbury, namely Anabela SOARES, Ana LEITE, André MAGALHÃES, Melissa GAMA, Diogo VERÍSSIMO, Joana AMARAL, Vítor MALTA, Elsa GRAVE, and Rita SILVA.

For providing a very friendly and welcoming home, I also acknowledge some of the great people I've had the chance of flat-sharing with while living at 3 Link Road: Harrison DEVANY, James HARDING and Adam EFFENBERGER (who got to be acknowledged twice!...). I would also like to thank Victoria FIELD for taking me in as a lodger in her house during the very first months of my stay at Kent.

Keeping myself sane throughout these 4 years had obviously to involve rowing. On a very broad manner, I would like to acknowledge all of my three "surrogate" rowing clubs, Herne Bay Amateur Rowing Club (HBARC), Spitfire Boat Club and also the University of Kent Rowing Club, for making me feel welcome and providing me with much-needed respite from my work. Being part of HBARC in particular over my final year has made the whole "thesis writing" stage a lot more enjoyable, since it allowed alternating it with some good intense evening sessions at the boathouse! Through rowing, I have met some really top-notch individuals throughout these last years, too many to list. Still, a few stand out: Richard D'ARIFAT, Aut ANGPANITCHAROEN, Rory SEMPLE and Michael KENNEDY.

Last, but not least, I would like to acknowledge my family, in particular my parents Manuel Joaquim MARQUES and Marisa MONTEIRO, my grandparents Mário and Marília MONTEIRO, and my siblings Rui and Maria João MARQUES, for always being there (on Skype) and giving me the chance to still speak some Portuguese once in a while.

Finally (because I said I would do it ☺), I would like to acknowledge the coffee machines in the lab - the KRUPS Nespresso XN100 and the Braun Type 3085 - for providing me with much-needed caffeine and allowing the always-important coffee breaks to occur.

Contents

List of Abbreviations

FWHM	**F**ull **W**idth at **H**alf **M**aximum
OCT	**O**ptical **C**oherence **T**omography
WLI	**W**hite **L**ight **I**nterferometry
OPD	**O**ptical **P**ath **D**ifference
M-Z	**M**ach–**Z**ehnder (interferometer)
SMF	**S**ingle-**M**ode Fibre
MMF	**M**ulti-**M**ode Fibre
TB	**T**albot **B**ands
FD-OCT	**F**requency-**D**omain **O**ptical **C**oherence **T**omography *(also **F**ourier-**D**omain **O**ptical **C**oherence **T**omography, equivalent)*
TD-OCT	**T**ime-**D**omain **O**ptical **C**oherence **T**omography
PS-OCT	**P**olarisation-**S**ensitive **O**ptical **C**oherence **T**omography
SD-OCT	**S**pectral-**D**omain **O**ptical **C**oherence **T**omography *(equivalent to **Sp-OCT** , **Sp**ectrometer-based **OCT**)*
SS-OCT	**S**wept **S**ource **O**ptical **C**oherence **T**omography
FT	**F**ourier **T**ransform
MSI	**M**aster **S**lave **I**nterferometry

Chapter 1

Introduction to the Thesis

The experimental chapters presented in this Thesis cover the work carried out at the Applied Optics Group, School of Physical Sciences, from October 2012 to December 2015. All the projects described involved extending functionality and attending to the drawbacks of spectrometer-based, spectral-domain optical coherence tomography (OCT) systems.

Contents

OPTICAL coherence tomography (OCT) has evolved over the last two decades to become a major optical imaging modality in the biomedical optics field [1]. By performing high-resolution, multi-dimensional imaging of translucent structures, it enables real-time tissue imaging *in-vivo* and *in-situ* with resolutions in the order of a few micrometres, one or two orders of magnitude finer than conventional ultra-sound [1].

To do so, OCT measures the magnitude and echo time delay of back-scattered light from the sample being analysed [2], in a way similar to ultra-sound imaging. Each echo time delay mapping generates an axial scan (or A-scan[1]), which corresponds to an uni-dimensional depth profile of the sample. Multi-dimensional imaging is possible by transversally scanning the incident optical beam and acquiring sequential A-scans.

The set of features present in OCT imaging makes it particularly attractive to medical imaging, although in recent years several other applications have been reported, including non-destructive testing (NDT), material characterisation and conservation [3–7]. Nevertheless, medical imaging is still the largest field of application for OCT, since it performs "optical biopsy", which is defined [1] as being the real time, *in situ* visualisation of tissue microstructure and pathology, without

[1]The complete terminology comprising the different imaging modes is described in Section 3.4.

the need to remove and process specimens [8, 9]. Histopathology (H&E) is still the gold standard for detailed, high-resolution imaging of tissue specimens, however it involves a lengthy destructive procedure [1].

Whilst not attaining the resolution or the selectivity of H&E, OCT is useful in several specific clinical situations:

- Where standard excisional biopsy is hazardous or impossible to perform – this includes imaging of retinal structures (the transparency of the eye provides easy and contactless optical access to the retina [10]), arteries or neural tissue (using catheters and endoscopic probes);
- Where standard excisional biopsy has sampling error, such as when locating and characterising cancerous tissue. The standard diagnosis procedure for it involves a biopsy and further H&E characterisation, however if the excised tissue misses the cancerous region this may lead to a false negative;
- For guidance of surgical procedures (surgical OCT): the ability to probe beneath the surface of the tissue in question or in regions surgically not accessible (such as the back of the eye) make OCT a valuable asset to obtain information prior to or during surgery. Moreover, since OCT is also endoscope-compatible, this enabled its use in imaging the gastro-intestinal tract and the inside of arteries (allowing it to assist with stent placement, for instance);
- Finally, research worldwide has extended OCT imaging beyond structural information. Functional imaging is possible with several novel techniques: Doppler OCT (and OCT angiography) that enable quantification of blood flow and display of blood vessels in tissue. An important marker of cellular organisation is given by polarisation-sensitive OCT (PS-OCT), which enables measurement of tissue birefringence [11, 12]. Spectroscopic OCT allows differentiation of parts of tissue due to their spectral absorption properties [13]. Important recent work has been dedicated to optical coherence elastography (OCE) [14], that allows the characterisation of the tissue's mechanical properties.

1.1 OCT in a nutshell

An intuitive way of explaining the inner workings of OCT in broad terms (and to a non-specialist audience) is to employ an analogy to ultra-sound, due to both

methods measuring distances, although such analogy possesses some shortcomings, since OCT does not employ any echoes. Another difference is the nature of the waves being used: while ultra-sound uses sound waves, OCT uses light, which is mostly near infra-red/visible due to the nature of the applications and the availability of optoelectronic devices operating at this wavelength range.

Using light instead of sound means that the propagating velocities are considerably higher. In ultra-sound imaging, assuming a velocity of $\sim 1500\,\mathrm{m/s}$ (typical value for ultra-sound imaging at $10\,\mathrm{MHz}$ in water [15]) and a feature size of $\sim 100\,\mu\mathrm{m}$, a time resolution of $\sim 100\,\mathrm{ns}$ is required, which is well within the limits of conventional detectors and processing electronics [1]. On the other hand, in order to resolve a feature size of $\sim 10\,\mu\mathrm{m}$ (typical OCT axial resolution figure) with light (the speed of light in vacuum being $3 \times 10^8\,\mathrm{m/s}$) one would need a resolution of $\sim 30\,\mathrm{fs}$, which is impossible to attain with direct electronic methods, if one was to complete the analogy with ultra-sound. Therefore, in order to resolve such time events, indirect measurement techniques need to be used, one of them being low-coherence interferometry, or white light interferometry (WLI) which forms the base of the OCT technique and is described in detail in Chapter 2.

Beyond the analogy presented above, OCT as an imaging technique has features which put it alongside established techniques such as confocal microscopy and high-frequency ultra-sound. In Figure 1.1, a comparison in terms of depth penetration and resolution between these three imaging techniques is represented.

Typical clinical ultra-sound imaging have resolution figures of $0.1 - 1\,\mathrm{mm}$, depending on the wavelength of the sound wave employed. At these wavelengths, absorption by the tissues is minimal, hence depth penetrations of a few centimetres are possible. High-frequency ultra-sound (HFUS) allows a significant improvement in the resolution [15] (by one or two orders of magnitude, with figures of $15 - 20\,\mu\mathrm{m}$ having been reported [1]), with however a significant decrease in penetration depth (down to $4{-}5\,\mathrm{mm}$). Additionally, ultra-sound imaging requires contact between the ultra-sonic transducer and the tissue being imaged, which is not ideal in terms of patient comfort (for instance, when imaging corneal tissue *in-vivo*).

Confocal microscopy possesses high transverse resolution, these being determined by optical diffraction from the interface optics. Due to the nature of the optical system and the inevitable scattered light from the sample, though, the depth penetration is limited to a few hundreds of microns, which limits its applications, especially in *in-vivo* cases.

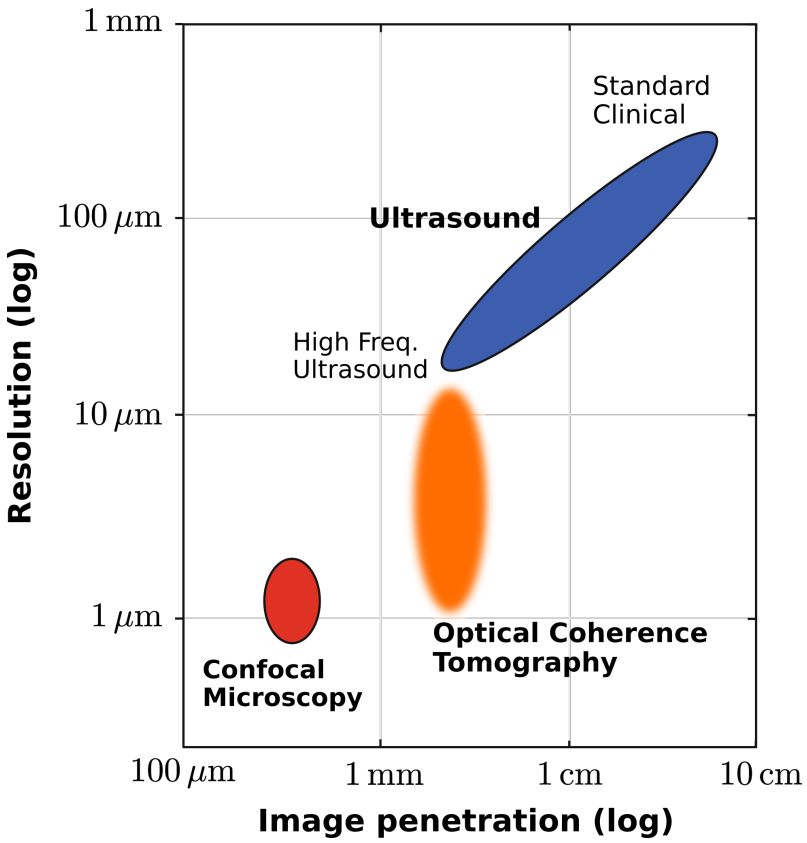

FIGURE 1.1: Comparison of ultra-sound, OCT and confocal microscopy in terms of imaging depth and resolution, considering scattering tissue. (adapted from Fujimoto *et al.* [1]).

As represented in Figure 1.1, OCT fills a gap between ultrasound and confocal microscopy [1] in terms of resolution and penetration depth. One of the most fundamental properties in OCT is the fact that the axial and transversal resolutions are de-coupled, with the former being dictated by the optical source parameters and the latter by the interface optics. In fact, the transversal resolution should be that of the confocal microscope equivalent configuration at the core of the OCT system, since any OCT system is assembled by adding a reference beam to a confocal microscope. The transversal resolution in OCT is however affected by speckle, which reduces the transversal resolution in relation to what would be achievable by solely the confocal microscope at the core of the OCT system

Typical optical sources for OCT in the near-infrared region yield axial resolutions ranging from 1 to a few tens of μm, corresponding to an improvement of respectively 100 to 10 times over the axial resolution figures achievable by conventional ultra-sound systems. However, the penetration depth in most tissues is limited to $\sim 2\,\mathrm{mm}$ due to the high scattering of light in these. Still, since OCT can be implemented in fibre optics it means that the measurements can be integrated

with a wide range of medical instruments such as endoscopes, catheters, laparoscopes and needles [1], allowing *in-situ* imaging of the tissues with improved resolution over ultra-sound methods.

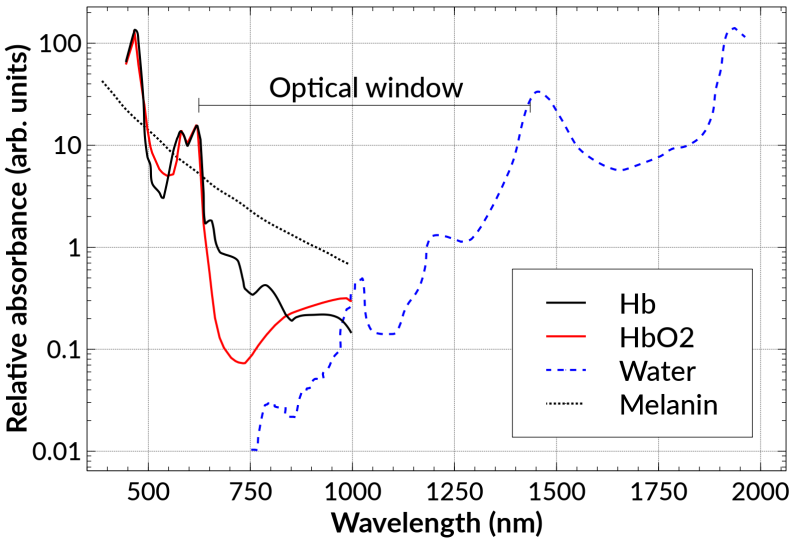

FIGURE 1.2: Optical window in biological tissues, adapted from Huang *et al.* [16]. Hb refers to haemoglobin, whereas HbO2 refers to its oxygenated variant, oxyhaemoglobin.

In theory, an OCT system can be implemented at any optical wavelength, provided that the optical source has the coherence properties which are described in Chapter 2. However, there is a spectral range (from about the longer end of the visible spectrum until about $1.5\,\mu\mathrm{m}$) where the absorption of light by tissue is minimal, often labelled as an "optical window" in the literature [16] (Figure 1.2) or therapeutic window. Due to the development of optical fibre communications at near-infrared wavelengths over the last four decades, optical sources, detectors and fibre devices for OCT became available [17] at a relatively low cost. The two factors mentioned above probably explain why most OCT systems operate in the region of 800 to 1500 nanometres, although some systems operating at longer wavelengths have been reported [7, 18], which are however geared to non-biomedical applications.

1.2 Organisation of the Thesis

The anatomy of a generic OCT system is described in Figure 1.3. The operation of any OCT system can be taken as a flow diagram with the purpose of taking an object (the sample) and characterising it (in terms of both its structure and other morphological properties, such as birefringence and dichroism); that is achieved

by the *white light interferometer*, which is illuminated by an *optical source*. The probing beam must be *scanned* over the object by means of specific hardware placed in the sample arm of the interferometer. *Detecting* the interferometric signal is also a fundamental part of any OCT system, which can happen in either time- and frequency-domain. The detected signal requires additional *processing* (the nature of which depends on the detection domain considered and the functional extensions in place) in order to retrieve the object's depth profile, or information from a fixed depth for all lateral pixels. All these steps combined produce a meaningful representation of the object in the form of an *image* of its structure.

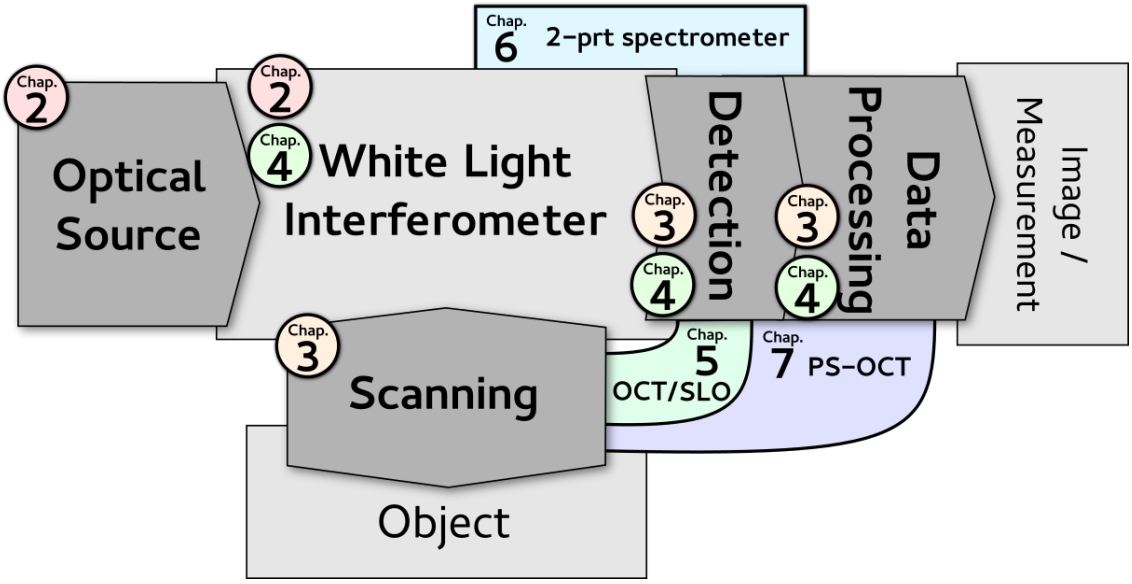

FIGURE 1.3: Schematic diagram of an OCT system, highlighting its fundamental blocks: optical source, scanning system, detection and signal processing, with a white light interferometer at its core. The circles depict the chapters in the Thesis where the theoretical fundamentals of each of the blocks are presented; the remaining references (to Chapters 5–7) relate to the experimental work carried out which focused on specific blocks of the OCT system.

This Thesis is organised around the fundamental blocks necessary for the successful implementation of an OCT system:

Part I: Theory

- As stated earlier, a white light interferometer is the core element of any OCT system, allowing one to temporally resolve the back-scattered light from the sample. Chapter 2 focuses on the fundamentals of white light interferometry, utilising a Michelson interferometer illuminated by an optical source with a varying degree of temporal coherence. In the same chapter the different detection schemes (in time- and frequency-domain) are discussed in general terms.

- Since all work presented in this Thesis involves spectral-domain OCT systems, Chapter 3 covers the methodologies and technology directly associated with such a method:
  - A detailed presentation of the theory concerning spectrometers as detection systems for OCT set-ups. This includes the theoretical formalism of Talbot Bands which is an integral part of two of the experimental set-ups presented in this Thesis, covered in detail in Chapters 5 and 6.
  - Additional data processing required by frequency-domain OCT;
  - Given that any imaging system requires some form of scanning, considerations on scanning are also presented in this chapter.
- Chapter 4 is a detailed introduction to Polarisation-Sensitive OCT (PS-OCT) that establishes the perspectives and the motivation to the experimental work presented in Chapter 7. In order to extend the functionality of an OCT system to accommodate polarisation-sensitive measurements, one needs to modify the detection scheme, data processing, and the interferometer itself.

Part II: Experimental Work

Three chapters follow the theoretical part, covering the experimental work carried out throughout the duration of the various PhD projects. These projects involve different blocks of the OCT system:

- Chapter 5 describes a spectral-domain OCT system with Talbot bands (hence with control over the shape and position of the visibility profile in depth) to which an additional confocal channel has been added. Since this SD-OCT system is designed for retinal imaging, the confocal channel behaves as a scanning laser ophthalmoscope (SLO), which can run in parallel or sequentially with the OCT channel. Designing and developing such a system involved modifying the detection block and also the scanning, since several scanning strategies had to be implemented.
- Chapter 6 describes another spectral-domain OCT system featuring a novel spectrometer configuration in the detection arm, delivering Talbot bands. This configuration has the particularity that the two arms of the interferometer are coupled in the spectrometer itself, a property that confers an increase in power-efficiency, while totally removing the mirror terms.
- Chapter 7 describes three fibre-based, polarisation-sensitive OCT designs which have the particularity of being insensitive to polarimetric disturbances

caused by the collecting fibre and coupler. Implementing PS-OCT systems typically involve modifying the detection arm, introducing additional data processing steps, and, as a requirement for the designs presented, altering the sample (scanning) arm.

- Lastly, in Chapter 8 the final remarks regarding the work carried out throughout the three main projects described in this Thesis are presented, and future, follow-up work is discussed.

Publications in peer-reviewed journals directly stemming from work reported in this Thesis

Full-text prints of these publications are available in Appendix C.

- Sylvain Rivet, **Manuel J. Marques**, Adrian Bradu, and Adrian Podoleanu. "Optical module to extend any Fourier-domain optical coherence tomography system into a polarisation-sensitive system", *Journal of Optics* 16.065607 (May 2016).[2]
- **Manuel J. Marques**, Sylvain Rivet, Adrian Bradu, and Adrian Podoleanu. "Polarization-sensitive optical coherence tomography system tolerant to fiber disturbances using a line camera", *Optics letters* 40.16 (Sept 2015), pp. 3858–3861, DOI: 10.1364/OL.40.003858.
- **Manuel J. Marques**, Adrian Bradu, and Adrian Podoleanu. "Two-grating Talbot bands spectral-domain interferometer", *Optics letters* 40.17 (Aug 2015), pp. 4014–4017, DOI: 10.1364/OL.40.004014
- **Manuel J. Marques**, Adrian Bradu, and Adrian Gh. Podoleanu. "Towards simultaneous Talbot bands based optical coherence tomography and scanning laser ophthalmoscopy imaging", *Biomedical Optics Express* 5.5 (Apr. 2014), p 1428, ISSN: 2156-7085, DOI: 10.1364/BOE.5.001428.

Conference proceedings directly stemming from work reported in this Thesis

- **Manuel J. Marques**, Sylvain Rivet, Adrian Bradu, and Adrian Podoleanu, "Spectral-domain, polarization-sensitive optical coherence tomography system insensitive to fiber disturbances", *SPIE BiOS*, 2016, p. 96971K.

[2]Regarding this publication where I am listed as second author, I've contributed with part of the writing and the creation of the supporting diagrams. Dr Sylvain Rivet has carried out the numerical simulations present in the publication.

- **Manuel J. Marques**, Adrian Bradu, and Adrian Podoleanu, "Optical Coherence Tomography and Scanning Laser Ophthalmoscopy: approaches to dual-channel retinal tissue imaging", *Frontiers in Optics 2014*, 2014, p. FTu2F.3.

Content published beyond the scope of this Thesis

- Michaël Maria, **Manuel J. Marques**, Christopher Costa, Adrian Bradu, Thomas Feuchter, Lasse Leick, and Adrian Podoleanu, "Broadband master-slave interferometry using a super-continuum source", *SPIE BiOS*, 2016, p. 96972R.
- Mohammad R. N. Avanaki, **Manuel J. Marques**, Adrian Bradu, Ali Hojjatoleslami, and Adrian Podoleanu, "A new algorithm for speckle reduction of optical coherence tomography images", *SPIE BiOS*, 2014, p. 893437.
- Adrian Bradu, **Manuel J. Marques**, Petr Bouchal, and Adrian Podoleanu, "Combining Gabor and Talbot bands techniques to enhance the sensitivity with depth in Fourier domain optical coherence tomography", *Optical Coherence Tomography and Coherence Domain Optical Methods in Biomedicine XVII*, 2013, vol. 8571, pp. 857136–857136–6.
- **Manuel J. Marques**, Adrian Bradu, and Adrian Podoleanu, "Tuning a fast linear camera used within a Talbot bands spectrometer-based optical coherence tomography set-up", *8th Iberoamerican Optics Meeting and 11th Latin American Meeting on Optics, Lasers, and Applications*, Proc. of SPIE Vol. 8785, 8785E1, 2013, vol. 8785, no. 1, p. 8785E1.

References

[1] J. G. Fujimoto and W. Drexler, "Introduction to oct", in *Optical Coherence Tomography: Technology and Applications*, W. Drexler and J. G. Fujimoto, Eds., 2nd ed., Springer, 2015, ch. 1.

[2] D. Huang, E. A. Swanson, C. P. Lin, J. S. Schuman, W. G. Stinson, W. Chang, M. R. Hee, T. Flotte, K. Gregory, C. A. Puliafito, *et al.*, "Optical coherence tomography", *Science*, vol. 254, no. 5035, pp. 1178–1181, 1991. [Online]. Available: http://science.sciencemag.org/content/254/5035/1178.short;%20http://www.ncbi.nlm.nih.gov/pmc/articles/PMC4638169/.

[3] E. N. Morel, N. A. Russo, J. R. Torga, and R. Duchowicz, "Interferometric system based on swept source-optical coherence tomography scheme applied to the measurement of distances of industrial interest", *Opt. Eng*, vol. 55, no. 1, p. 014 105, Jan. 2016, ISSN: 0091-3286. DOI: 10.1117/1.oe.55.1.014105. [Online]. Available: http://dx.doi.org/10.1117/1.OE.55.1.014105.

[4] Z. Chen, Y. Shen, W. Bao, P. Li, X. Wang, and Z. Ding, "Identification of surface defects on glass by parallel spectral domain optical coherence tomography", *Optics Express*, vol. 23, no. 18, p. 23 634, Aug. 2015, ISSN: 1094-4087. DOI: 10.1364/oe.23.023634. [Online]. Available: http://dx.doi.org/10.1364/OE.23.023634.

[5] M. Iwanicka, G. Lanterna, C. G. Lalli, F. Innocenti, M. Sylwestrzak, and P. Targowski, "On the application of optical coherence tomography as a complimentary tool in an analysis of the 13th century byzantine bessarion reliquary", *Microchemical Journal*, vol. 125, pp. 75–84, Mar. 2016, ISSN: 0026-265X. DOI: 10.1016/j.microc.2015.11.014. [Online]. Available: http://dx.doi.org/10.1016/j.microc.2015.11.014.

[6] R. Su, M. Kirillin, E. W. Chang, E. Sergeeva, S. H. Yun, and L. Mattsson, "Perspectives of mid-infrared optical coherence tomography for inspection and micrometrology of industrial ceramics", *Optics Express*, vol. 22, no. 13, p. 15 804, Jun. 2014, ISSN: 1094-4087. DOI: 10.1364/oe.22.015804. [Online]. Available: http://dx.doi.org/10.1364/OE.22.015804.

[7] C. S. Cheung, M. Tokurakawa, J. M. O. Daniel, W. A. Clarkson, and H. Liang, "Long wavelength optical coherence tomography for painted objects", *Optics for Arts, Architecture, and Archaeology IV*, L. Pezzati and P. Targowski, Eds., May 2013. DOI: 10.1117/12.2021700. [Online]. Available: http://dx.doi.org/10.1117/12.2021700.

[8] J. G. Fujimoto, M. E. Brezinski, G. J. Tearney, S. A. Boppart, B. Bouma, M. R. Hee, J. F. Southern, and E. A. Swanson, "Optical biopsy and imaging using optical coherence tomography", *Nature medicine*, vol. 1, no. 9, pp. 970–972, 1995. [Online]. Available: http://biophotonics.illinois.edu/pubs/biophotonics_current/opticalbiopsyandimagingusingoct.pdf.

[9] M. E. Brezinski, G. J. Tearney, B. E. Bouma, J. A. Izatt, M. R. Hee, E. A. Swanson, J. F. Southern, and J. G. Fujimoto, "Optical coherence tomography for optical biopsy properties and demonstration of vascular pathology", *Circulation*, vol. 93, no. 6, pp. 1206–1213, 1996. [Online]. Available: http://

circ.ahajournals.org/content/93/6/1206.short;%20http://circ.ahajournals.org/content/93/6/1206.full.

[10] J. S. Schuman, C. A. Puliafito, J. G. Fujimoto, and J. S. D. (eds.), *Optical Coherence Tomography of Ocular Diseases*, 3rd ed., ser. Slack Incorporated, 2012, ISBN: 1556428642,9781556428647.

[11] M. R. Hee, E. A. Swanson, J. G. Fujimoto, and D. Huang, "Polarization-sensitive low-coherence reflectometer for birefringence characterization and ranging", *JOSA B*, vol. 9, no. 6, pp. 903–908, 1992.

[12] J. F. De Boer, T. E. Milner, M. J. van Gemert, and J. S. Nelson, "Two-dimensional birefringence imaging in biological tissue by polarization-sensitive optical coherence tomography", *Optics letters*, vol. 22, no. 12, pp. 934–936, 1997. [Online]. Available: https://www.osapublishing.org/abstract.cfm?uri=ol-22-12-934;%20http://dare.uva.nl/document/2/2960.

[13] M. D. Kulkarni and J. A. Izatt, "Spectroscopic optical coherence tomography", in *Conference on Lasers and Electro-Optics*, ser. 1996 OSA Technical Digest Series, Optical Society of America, vol. 9, Washington, DC, 1996, pp. 59–60. [Online]. Available: http://ieeexplore.ieee.org/xpls/abs_all.jsp?arnumber=864357.

[14] J. M. Schmitt, "Oct elastography: imaging microscopic deformation and strain of tissue", *Optics express*, vol. 3, no. 6, pp. 199–211, 1998. [Online]. Available: https://www.osapublishing.org/abstract.cfm?uri=oe-3-6-199.

[15] D. Thomas and G. Duguid, "Optical coherence tomography—a review of the principles and contemporary uses in retinal investigation", *Eye*, vol. 18, no. 6, pp. 561–570, Feb. 2004, ISSN: 1476-5454. DOI: 10.1038/sj.eye.6700729. [Online]. Available: http://dx.doi.org/10.1038/sj.eye.6700729.

[16] Y.-Y. Huang, A. Chen, and M. Hamblin, "Low-level laser therapy: an emerging clinical paradigm", *SPIE Newsroom*, 2009, ISSN: 1818-2259. DOI: 10.1117/2.1200906.1669. [Online]. Available: http://dx.doi.org/10.1117/2.1200906.1669.

[17] J. M. Schmitt, "Optical coherence tomography (oct): a review", *Selected Topics in Quantum Electronics, IEEE Journal of*, vol. 5, no. 4, pp. 1205–1215, 1999. [Online]. Available: http://ieeexplore.ieee.org/xpls/abs_all.jsp?arnumber=796348;%20http://www.uhnresearch.ca/labs/

biophotonics/staff_papers/vitkin/OCT_schmitt_overview.pdf.

[18] U. Sharma, E. W. Chang, and S. H. Yun, "Long-wavelength optical coherence tomography at 1.7 μm for enhanced imaging depth", *Optics Express*, vol. 16, no. 24, p. 19 712, Nov. 2008, ISSN: 1094-4087. DOI: 10.1364/oe.16.019712. [Online]. Available: http://dx.doi.org/10.1364/OE.16.019712.

Part I

Theory

Chapter 2

White Light Interferometry

Author's note: portions of this chapter are based upon the introductory section of the author's MSc thesis written in 2012 [1], which was submitted for evaluation at the University of Porto.

Contents

ALL experimental work described in the chapters of this Thesis refer to white light interferometry (WLI). Without the property of low coherence time of light it would be impossible to measure the path imbalance between the two arms of an interferometer illuminated with such light. Thus, locating the scatterers in a sample in depth would not be possible, which is the basis of the operation of optical coherence tomography (OCT) imaging.

A widely used interferometric device is the Michelson interferometer (Figure 2.1), which was devised by Albert Abraham Michelson in 1881. It is perhaps more widely known due to its role in disproving the existence of the luminiferous aether in outer space, through an experiment carried out by Michelson and Morley in 1887 [2]. Years later, this result eventually paved the way towards the special theory of relativity by Albert Einstein.

Before analysing the theory of WLI in detail it is important to define the concepts of *temporal* and *spatial* coherence.

Spatial coherence can be defined as the degree to which two separate points in a given electromagnetic (EM) wavefront have the same phase, and hence are correlated at all times. Laser and similar sources, such as super-luminiscent diodes (SLD), have a high degree of spatial coherence. A coherence region where all points of the wavefront are correlated can always be defined [3]. The higher the spatial coherence, the better the phase stability and the better the interferometric fringe contrast, since phase instability leads to fringe wash-out [4]. On the other hand, a highly spatially coherent beam induces a considerable amount of speckle [5, 6] that degrades any imaging performed by an interferometric system.

Temporal coherence, on the other hand, can be defined as the degree to which the phase at a specific point in time of the EM wave does not undergo any sudden phase "jumps". We can define the coherence time t_c as the time between two of such phase jumps. This time interval can be estimated from the full width at half maximum (FWHM) of the autocorrelation $\Gamma(\tau)$ of the electric field $E(t)$:

$$\Gamma(\tau) = \int_{-\infty}^{+\infty} E(t)\, E^*(t+\tau)\, dt, \tag{2.1}$$

where $E^*(t)$ denotes the complex conjugate of $E(t)$. From the Wiener-Kintchin theorem, one can relate the autocorrelation function $\Gamma(\tau)$ to the power spectrum of the EM wave, $S(k)$:

$$\int_{-\infty}^{+\infty} \Gamma(\tau)\, e^{jk\tau}\, d\tau = S(k)\,. \tag{2.2}$$

In the case of a perfectly monochromatic source, the spectrum can be represented by $S(k) = \delta(k - k_0)$, where $\delta()$ denotes the Dirac delta function. Inserting $S(k)$ into Equation (2.2) leads to an infinitely large coherence time. For quasi-monochromatic sources whose spectrum shape is Gaussian (or near-Gaussian), $\Gamma(\tau)$ will also have a Gaussian shape with a finite width. In the literature concerning WLI and OCT it is more common to refer to the coherence *length*, l_c, instead of the coherence *time*, t_c. These two quantities are linked by the group velocity v_g as $l_c = v_g \cdot t_c$; in free space v_g is numerically equal to c, the speed of light in vacuum.

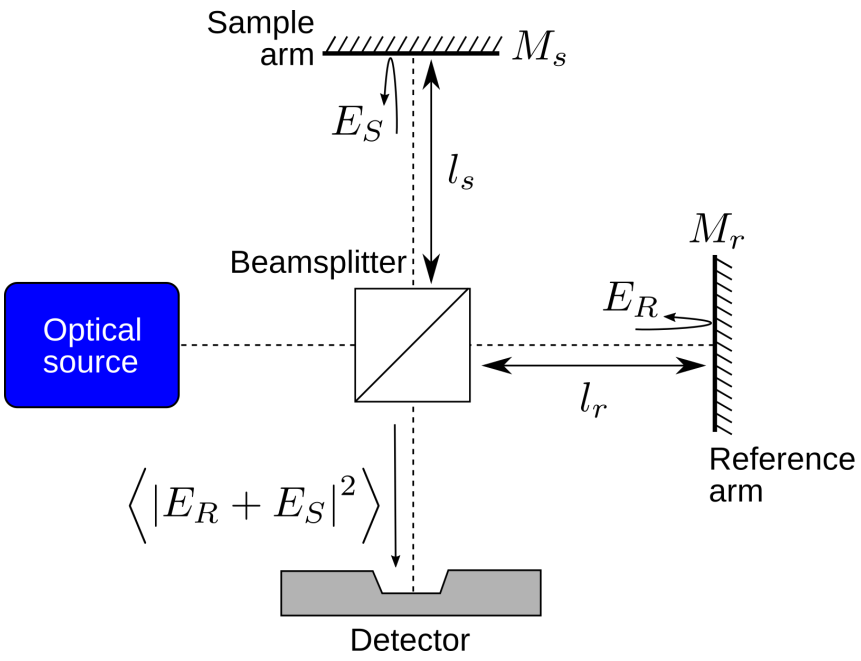

FIGURE 2.1: Schematic representation of a Michelson interferometer.

2.1 Michelson interferometer with varying temporal coherence

In the simplest possible Michelson configuration, as depicted in Figure 2.1, the amplitude of the light beam emitted by the optical source is divided between the two arms of the interferometer (in the diagram labelled as sample and reference arms). The two beams suffer reflection on the mirrors at the end of each arm and are recombined at the beam-splitter, with the output being directed towards a screen or a detector.

We start with the illumination being carried out by a highly coherent source, such as a monochromatic laser, arriving at the expected result of a series of alternating bright and dim spots being observed at the detector arm as the path length is increased in one of the arms. Afterwards, the temporal coherence of the source is diminished by increasing its spectral bandwidth. This limits the extension of the series of bright/dim spots being observed to a narrower region of path length differences around the alignment point of the interferometer (where $l_r = l_s$). Finally, the approximation for a Gaussian-shaped spectrum is presented, which yields the widely used expression for the axial resolution of a WLI/OCT system.

2.1.1 Highly coherent source (monochromatic light)

If the optical path length of the two arms is matched , constructive interference occurs at the detector with a strong signal being recorded, which will happen regardless of how temporally coherent the source is. If the path lengths differ by half a wavelength, destructive interference will occur and a considerably weaker signal will be detected[1]. If the optical path difference (OPD continues to be increased, the interference signal varies in strength. Very strong interference is observed with OPDs equal to even numbers of half wavelengths of the source, whilst weak interference corresponds to OPDs equal to odd numbers of half wavelengths. This behaviour ceases only when the OPD is greater than the coherence length of the source, l_c.

To quantify this effect, let us denote by E_S and E_R the (complex) electrical fields of the sample and reference beams respectively, which are taken as monochromatic, linearly polarised EM waves, with amplitudes equal to A_S and A_R. Immediately before they interfere at the beam-splitter after one round-trip in each of the arms, the two fields are described by

$$E_R = A_R \exp\left[-j\left(2\beta_R l_R - \omega t\right)\right] \tag{2.3a}$$

$$E_S = A_S \exp\left[-j\left(2\beta_S l_S - \omega t\right)\right], \tag{2.3b}$$

where ω is the optical frequency, and $\beta_{S,R}$ are, respectively, the propagation constant for the sample and reference arms. For the purpose of this study $\beta_{S,R}$ are taken as real quantities since we are considering lossless media; however in general the propagation constant is a complex quantity, in which case the imaginary component dictates the attenuation of the medium. The irradiance, I_D, of the incident beam at the detector is proportional to the time average of the modulus of the electric field [7]. This is converted into a detectable photo-current:

$$I_D\left(\omega, l_S, l_R\right) \propto \left\langle \left| E_R\left(\omega, t, l_R\right) + E_S\left(\omega, t, l_S\right)\right|^2 \right\rangle. \tag{2.4}$$

[1] If the polarisation state of the two beams is exactly matched and the beam-splitter divides the power equally between the two arms, no signal will be detected - the weak, but still visible signal is a consequence of the mismatch between polarisation states or non-equal power splitting at the beam-splitter.

$|E_R(\omega,t,l_R)+E_S(\omega,t,l_S)|^2$ represents the intensity of the output electric field $E_{out}=E_R+E_S$. By expanding Equation (2.4), we obtain

$$\begin{aligned} I_D &\propto \langle |E_R E_R^*|+|E_S E_S^*|+A_R A_S\left\{\exp\left[2j\left(\beta_R l_R-\beta_S l_S\right)\right]+\exp\left[-2j\left(\beta_R l_R-\beta_S l_S\right)\right]\right\}\rangle \\ &\propto \left[|A_R|^2+|A_S|^2+2A_S A_R\cos\left[2\left(\beta_R l_R-\beta_S l_S\right)\right]\right] \\ &\propto \left[I_R+I_S+2\sqrt{I_S I_R}\cos\left[2\left(\beta_R l_R-\beta_S l_S\right)\right]\right], \end{aligned} \tag{2.5}$$

where $I_{R,S}=|A_{R,S}|^2$ are, respectively, the intensity of the reference arm and the sample arm fields. If the medium in both arms is free space, then Equation (2.5) reduces to

$$I_D \propto \left[I_R+I_S+2\sqrt{I_R I_S}\Pi\cos\left(\frac{4\pi}{\lambda}\Delta l\right)\right], \tag{2.6}$$

where $\Delta l=l_R-l_S$ is the optical path length difference between the two arms (in free space), and Π is a factor introduced to represent the polarisation of the sample and reference arm beams, ranging between 0 and 1, where $\Pi=1$ represents a complete polarisation state match. The first two terms correspond to the DC intensities of the two arms of the interferometer, while the third one, termed interferometric term, arises due to the interference between the two arms of the interferometer, scaling with the cosine of the optical path length Δl, hence exhibiting the alternating behaviour described at the beginning of this section.

If we now analyse Equation (2.6) and assume $I_R=I_S=I$ and $\Pi=1$ for simplification purposes, for $\Delta l=0$ the two arms are matched in length and I_D is maximised (to $4I$), since the third term (the interferometric term) is maximum. If $\Delta l=\lambda/2$ the interferometric term is at its minimum value ($-2I$), hence $I_D=0$.

2.1.2 Wide optical bandwidth, low coherence time

Let us analyse the same interferometric set-up, now illuminated by a light source having a finite optical bandwidth, rather than just a single frequency. As stated before, this increase in optical bandwidth impacts the temporal coherence, which is no longer infinite. Equations (2.3a) and (2.3b) need have to be readjusted, since the propagation constant, β, now changes with ω:

$$E_R(\omega)=A_R(\omega)\exp\left[-j\left(2\beta_R(\omega)l_R-\omega t\right)\right] \tag{2.7a}$$

$$E_S(\omega)=A_S(\omega)\exp\left[-j\left(2\beta_S(\omega)l_S-\omega t\right)\right]. \tag{2.7b}$$

If I_D is expanded as before, its value will be proportional to the sum of interferences caused by each monochromatic plane wave component (among other incoherent terms):

$$I_D \propto \Re\left\{\int_{-\infty}^{+\infty} E_S(\omega)\, E_R^*(\omega)\, \frac{d\omega}{2\pi}\right\}, \tag{2.8}$$

with $\Re\{\}$ denoting the real part. The expression above can be rearranged as

$$I_D \propto \Re\left\{\int_{-\infty}^{+\infty} S(\omega) \exp\left(-j\Delta\phi(\omega)\right) \frac{d\omega}{2\pi}\right\}, \tag{2.9}$$

considering $S(\omega) = A_S(\omega)\, A_R^*(\omega)$ as the optical spectrum of the source (provided that there are no band-dependent absorptions in either arm) and $\Delta\phi(\omega) = 2\left[\beta_S(\omega)\, l_S - \beta_R(\omega)\, l_R\right]$ as the phase mismatch between the two arms. If we also assume that both arms sit in the same optical medium, with equivalent dispersion characteristics, we can assume $\beta_S(\omega) = \beta_R(\omega)$. By expanding the propagation constant $\beta(\omega) = \beta_S(\omega) = \beta_R(\omega)$ around the central frequency ω_0, we obtain

$$\beta(\omega) = \beta(\omega_0) + \left.\frac{d\beta(\omega)}{d\omega}\right|_{\omega=\omega_0} (\omega - \omega_0) + \ldots \tag{2.10}$$

Since it is assumed that the two arms are exactly the same in terms of material propagation, the phase mismatch $\Delta\phi(\omega) = 2\left[\beta_S(\omega)\, l_S - \beta_R(\omega)\, l_R\right]$ is only going to depend on the path length difference $\Delta l = l_S - l_R$. Substituting Equation (2.10) into the expression for $\Delta\phi(\omega)$, we obtain

$$\Delta\phi(\omega) = \beta(\omega_0)(2\Delta l) + \left.\frac{d\beta(\omega)}{d\omega}\right|_{\omega=\omega_0} (\omega - \omega_0)(2\Delta l), \tag{2.11}$$

where we disregarded terms higher than the first order expansion, since we are assuming propagation through a uniform, linear, and non-dispersive medium in both arms. Substituting Equation (2.11) into Equation (2.9) gives

$$I_D \propto \Re\left\{\exp\left[-j2\Delta l\beta(\omega_0)\right] \int_{-\infty}^{+\infty} S(\omega - \omega_0) \exp\left[-j(\omega - \omega_0)\right] \left.\frac{d\beta(\omega)}{d\omega}\right|_{\omega=\omega_0} \frac{d(\omega - \omega_0)}{2\pi}\right\}. \tag{2.12}$$

By defining the phase and group delays, respectively $\Delta\tau_p$ and $\Delta\tau_g$ as

$$\Delta\tau_p = \frac{2\Delta l}{v_p}, \quad \Delta\tau_g = \frac{2\Delta l}{v_g}, \tag{2.13}$$

and recalling that the phase velocity v_p is related to the propagation constant by $v_p = {}^{\omega}/_{\beta(\omega)}$ and the group velocity by $v_g = \frac{d\omega}{d\beta}$, these two identities become

$$\Delta\tau_p = \frac{\beta(\omega_0)}{\omega_0} 2\Delta l \tag{2.14}$$

$$\Delta\tau_g = \left.\frac{d\beta(\omega)}{d\omega}\right|_{\omega=\omega_0} 2\Delta l. \tag{2.15}$$

Equation (2.12) can finally be expressed as

$$I_D \propto \Re\left\{\exp\left[-j\omega_0\Delta\tau_p\right]\int_{-\infty}^{+\infty} S(\omega-\omega_0)\exp\left[-j(\omega-\omega_0)\Delta\tau_g\right]\frac{d(\omega-\omega_0)}{2\pi}\right\}. \tag{2.16}$$

This expression can be interpreted as the multiplication of a carrier wave $\exp\left[-j\omega_0\Delta\tau_p\right]$ which is oscillating at frequency ω_0 by a temporal envelope given by the integral, this being simply the inverse Fourier transform of the power spectrum of the source. Therefore, Equation (2.16) presents the statement of the Wiener-Kintchin theorem, since I_D can be related to $\Gamma(\tau)$, but according to this derivation it is also $\mathfrak{F}^{-1}\{S(\omega)\}$.

2.1.3 Approximation to a Gaussian spectrum

It is a common and reasonable assumption to take the spectral shape of a broadband source employed in WLI as a Gaussian. If so, $S(\omega-\omega_0)$ can be expressed as

$$S(\omega-\omega_0) = \sqrt{\frac{2\pi}{\sigma_\omega^2}}\exp\left[-\frac{(\omega-\omega_0)^2}{2\sigma_\omega}\right], \tag{2.17}$$

where σ_ω is the standard deviation of the spectrum around its central frequency ω_0. If we substitute this into Equation (2.16) for the interferometric part of the detected signal, we get

$$I_D \propto \sqrt{\frac{2\pi}{\sigma_\omega^2}}\Re\left\{e^{i\omega_0\Delta\tau_p}\int_{-\infty}^{+\infty} e^{-\frac{(\omega-\omega_0)^2}{2\sigma}} e^{-j(\omega-\omega_0)\Delta\tau_g}\frac{d(\omega-\omega_0)}{2\pi}\right\}. \tag{2.18}$$

By normalising the source's power spectral density to unit power, $\int_{-\infty}^{+\infty} S(\omega)\frac{d\omega}{2\pi} = 1$, the integral can be simplified to the definition of an inverse Fourier transform

of a Gaussian function, $\int_{-\infty}^{+\infty} e^{-(\omega-\omega_0)\Delta\tau_g} d\,(\omega-\omega_0)$, which is also a Gaussian function. Hence, I_D can be expressed as

$$I_D \propto \Re\left\{\exp\left[-j\omega_0\Delta\tau_p\right]\exp\left[-\frac{\sigma_\omega^2\Delta\tau_g^2}{2}\right]\right\}. \tag{2.19}$$

The above expression represents the autocorrelation term for a Gaussian source, and contains two terms: $\exp\left[-j\omega_0\Delta\tau_p\right]$ represents a rapid oscillation containing the phase information, which can be useful in Doppler and dispersion assessments [7]; and $I_{AC} = \exp\left[-\frac{\sigma_\omega^2\Delta\tau_g^2}{2}\right]$ represents the envelope of the autocorrelation function. It is to be expected that this second component is also Gaussian, since it is known from the Wiener-Kintchin theorem that the autocorrelation function is equal to the inverse Fourier transform of the source power spectrum.

With this in mind, we can revisit the analysis for the monochromatic Michelson interferometer and introduce the Gaussian-shaped, slowly varying factor of the autocorrelation function on the interferometric term into Equation (2.6),

$$I_D \propto \left[I_R + I_S + 2\sqrt{I_S I_R}\Gamma(\tau_g)\Pi\cos\left(\frac{4\pi}{\lambda}\Delta l\right)\right]. \tag{2.20}$$

It is now clear that the interference signal will only arise when the lengths of the interferometer arms are matched within the width of the slowly varying function $\exp\left[-\frac{\sigma_\omega^2\Delta\tau_g^2}{2}\right]$ (since $\Delta\tau_g \propto \Delta l$) , with σ_ω depending on the optical source parameters. This width determines the resolution of the WLI, as will be shown over the following section.

In order to check whether this expression is consistent with the previous analysis for the monochromatic source in the interferometer, we can consider $\sigma_\omega \ll 1$; in this way the corresponding autocorrelation function envelope will increase its width, since the argument of the exponential function is scaling with σ_ω^2. In the limit where $\sigma_\omega \to 0$, $\Gamma(\tau_g) \to 1$, Equation (2.20) tends towards Equation (2.6), as expected.

2.1.4 Resolution of a White Light Interferometer

The Gaussian envelope considered in the previous section ultimately dictates the coherence-limited axial resolution of the white light interferometer Δl,

$$\Delta l = \frac{2\ln 2\lambda_0^2}{\pi\Delta\lambda}, \tag{2.21}$$

where λ_0 denotes the central wavelength of the source and $\Delta\lambda$ the wavelength span of the source spectrum. The expression above is obtained from Equation (2.18) by imposing the condition that the amplitude attains half of the maximum value. If Equation (2.16) is re-written in terms of optical frequency, one obtains

$$I \propto \Re\left\{\exp\left[-j2\pi f_0\Delta\tau_p\right]\int_{-\infty}^{+\infty} S(f-f_0)\exp\left[-j2\pi\left(f-f_0\right)\Delta\tau_g\right]d\left(f-f_0\right)\right\}. \tag{2.22}$$

Since a Gaussian-shaped spectrum is being considered, then using Equation (2.17), the slowly varying term I_{AC} of the solution to the above equation is isolated, and given by

$$I_{AC} = \exp\left(-2\pi^2\sigma_f^2\Delta\tau_g^2\right), \tag{2.23}$$

where $\sigma_f = 2\pi\sigma_\omega$. We can calculate the FWHM of this slowly varying envelope by solving the following equation to the group delay, $\Delta\tau_g$:

$$\exp\left(-2\pi^2\sigma_f^2\Delta\tau_g^2\right) = \frac{1}{2}, \tag{2.24}$$

obtaining $\Delta\tau_g = \frac{\sqrt{\ln 2}}{\sqrt{2}\pi\sigma_f}$. The standard deviation of the optical frequency, σ_f, can be expressed as a function of the standard deviation of the source spectrum σ_λ:

$$\sigma_f = \frac{c\sigma_\lambda}{\lambda_0^2}. \tag{2.25}$$

Since the standard deviation σ_λ of the source spectrum can be related to the FWHM of its bandwidth $\Delta\lambda$ by the expression $\Delta\lambda = 2\sqrt{2\ln 2}\sigma_\lambda$, we can rewrite the expression above as

$$\sigma_f = \frac{c\Delta\lambda}{2\lambda_0^2\sqrt{2\ln 2}}. \tag{2.26}$$

Using this identity in the expression for $\Delta\tau_g$ yields

$$\Delta\tau_g = \frac{4\ln 2\lambda_0^2}{\pi c\Delta\lambda}. \tag{2.27}$$

Since the group delay here is given by the path imbalance Δl between the two arms of the interferometer, $\Delta\tau_g = \frac{\Delta l}{c}$. We can replace $\Delta\tau_g$ in the equation above and solve for Δl, obtaining

$$\Delta l = \frac{4 \ln 2 \lambda_0^2}{\pi \Delta\lambda}. \tag{2.28}$$

This is the standard equation for defining the axial resolution for any white light interferometer or OCT system. This resolution increases with the square of the central wavelength λ_0 and is inversely proportional to the FWHM of the source's optical bandwidth $\Delta\lambda$. If the case of the very coherent source, e.g. a laser, is revisited (which was covered in Section 2.1.1), $\Delta\lambda \sim 0$, which brings Δl to infinity. As a consequence, there is no coherence gate applicable in this case, and the interferometer output will alternate between constructive and destructive interference as the optical path difference between the two arms is varied.

If the depth coordinate z is considered instead of the optical path imbalance Δl, (still assuming that both arms of the interferometer are operating in reflection) an additional factor of 2 should be used in the expression, since one needs to account for the double-pass nature of the interferometer. Δl is then halved, and the equation below is the one often found in the literature [8] when referring to the axial resolution of an OCT system (assuming a Gaussian-shaped spectrum for the optical source):

$$\Delta z = \frac{\Delta l}{2} = \frac{2 \ln 2}{\pi} \frac{\lambda_0^2}{\Delta\lambda}. \tag{2.29}$$

2.2 Acquisition domains

Detecting the interferometric signal detailed in the previous section can be done in either time or frequency domain. Time-domain was the variant with which low-coherence interferometry and consequently OCT began in the early 1990s [9]; with the advent of faster detectors, sources and signal processing systems, frequency- (or Fourier-) domain processing became the technique of choice after 2000, due to the dramatic increases in imaging speed it introduced [8].

The main difference between these two different detection methods, apart from the domain they operate in, is the fact that time domain operates around OPD $= 0$ while frequency (Fourier) domain works normally away from OPD $= 0$.

If we recall Equation (2.20) and assume that there are N scattering centres (assumed reflectors) in the sample arm, then I_D is given by

$$I_D \propto \left[I_R + \sum_{i=1}^{N} I_{S,i} + \sum_{i=1}^{N} 2\sqrt{I_R I_{S,i}} \Gamma\left(\tau_{g,i}\right) \Pi \cos\left(2k \cdot z_i\right) \right]. \tag{2.30}$$

In Equation (2.20) it had been assumed that the propagation took place exclusively in free space, hence the argument in the cosine had $k = 2\pi/\lambda$.

Using a time-domain acquisition method the path length in the reference arm is varied during the signal acquisition, using for example a precision positioning system scanning the reference arm at a constant speed. Even if there are multiple scattering centres present in the sample arm at multiple depths, due to the limited coherence length of the source only the one situated at the same path length as the reference arm yields an interferometric signal. By synchronising the adjustment of the OPD with the time-stamp of the complete acquired signal it is possible to map the location of the different scatterers in terms of their depth.

The obvious drawback with this approach is that, in order to obtain a single depth profile along the sample arm one must mechanically scan the reference arm. The simplest approach is to employ a retro-reflector mounted on a linear translation stage [10]. Throughout the late 1990s and early 2000s technical improvements have been made in order to increase the reference arm scanning speeds, namely by employing more complex scanning reference arm designs to achieve faster sweeps in linear/angular scans [10], or by employing phase-modulation techniques such as Fourier-domain rapid scanning delay lines [11, 12].

Frequency-domain methods, on the other hand, rely on acquiring the optical spectrum at the detector port of the interferometer. This produces a modulation whose frequency is proportional to the OPD between the two arms of the interferometer. Considering Equation (2.30), by considering a single scatterer (therefore $N = 1$) at depth $z = z_n$, the argument of the cosine term becomes $2z_n \cdot k$. Let us express the equation as a function of the optical frequency $\nu = c/\lambda$ instead of the wavenumber $k = 2\pi/\lambda$. In order to retrieve the the period of oscillation of the interferometric component the following equation is used (similarly to the treatment in Leitner [13]):

$$\cos\left(2z_n \cdot 2\pi\frac{\nu}{c}\right) = 1, \tag{2.31}$$

whose solution is:

$$2z_n \cdot 2\pi\frac{\nu}{c} = 2\pi m, \tag{2.32}$$

where m is an integer. Therefore, the spectrum resulting from the interference with a scatterer at a depth z_n exhibits a modulation period δ_ν given by:

$$\delta_\nu = \frac{c}{2z_n} = \frac{c}{\mathrm{OPD}}. \tag{2.33}$$

This expression corroborates the observation that larger depths (and thus larger OPDs) yield smaller modulation periods, or higher modulation frequencies.

The total number of fringes observed can be estimated by assuming that the fringe pattern extends throughout the whole detected bandwidth $\Delta\lambda$ and that the spectrum shape is Gaussian. We can consider Equation (2.33) as the fringe periodicity; hence, the total number of fringes $N_{fringes}$ is given by $\Delta\nu/\delta\nu$, where $\Delta\nu$ corresponds to the whole spectral span but in the ν-domain.

It is possible to relate Δ_ν and $\Delta\lambda$ by expanding $\nu = c/\lambda$:

$$\Delta\nu \simeq -\frac{c}{\lambda^2}\Delta\lambda. \tag{2.34}$$

Solving for $\Delta\lambda$ and replacing that expression in Equation (2.29) yields

$$\Delta z = l_c = -\frac{2\ln 2}{\pi}\frac{\lambda^2}{\frac{\lambda^2}{c}\Delta\nu} = -\frac{2\ln 2}{\pi}\frac{c}{\Delta\nu}, \tag{2.35}$$

with l_c being the coherence length of the optical source. Therefore, $\Delta\nu \propto 1/l_c$. As mentioned earlier, the total number of fringes is given by $N_{fringes} \sim \Delta\nu/\delta_\nu$, hence by replacing the terms with those obtained above it can be approximated by $N_{fringes} = \mathrm{OPD}/l_c$. For an OPD of $500\,\mu\mathrm{m}$ and a coherence length of $\sim 15\,\mu\mathrm{m}$ (corresponding to an optical source at $830\,\mathrm{nm}$ with a Gaussian-shaped spectrum with a $20\,\mathrm{nm}$ FWHM), one obtains ~ 33 fringes.

The biggest advantage to using frequency-domain methods is the fact that a spectral read yields the entire depth profile (making it a single-shot measurement). The existence of more scattering centres in the sample arm simply introduce more modulation frequencies in the spectrum. By Fourier-transforming the detected spectrum the locations of all scattering centres along the axial coordinate can be mapped, thus decoding the spectral encoding of OPD values on the modulation frequency.

Let us consider reflectivity parameters r_R and r_S (for the reference and sample arms, respectively) in either arm of the interferometer, and multiple reflectors at different depths in the sample arm. Following an analysis similar to that in [7,

14], Equations (2.7a) and (2.7b) can be re-written as

$$E_R(\omega) = E_0(\omega) r_R \exp\left[-j\left(2\beta_R(\omega) l_R - \omega t\right)\right] \tag{2.36}$$

$$E_S(\omega) = E_0(\omega) \int_{-\infty}^{+\infty} r_S\left(l_S\right) \exp\left[-j\left(2\beta_S\left(\omega\right) l_S - \omega t\right)\right] dl_S, \tag{2.37}$$

where $E_0(\omega) r_R$ replaces $A_R(\omega)$ (with $E_0(\omega)$ being the electric field incident on either the reference mirror or the multiple scatterers in the sample arm) and $A_S(\omega)$ contains the reflectance information for multiple scatterers, which are represented in the function $r_S\left(l_S\right)$. For a discrete reflector, $r_S\left(l_S\right)$ is defined as

$$r_S\left(l_S\right) = r_S\left(l_{S0}\right) \delta\left(l_S - l_{S0}\right), \tag{2.38}$$

with δ denoting the delta function, and l_{S0} the location of said reflector.

If, as before, we assume that no dispersion has been left uncompensated for, then $\beta_R(\omega)$ and $\beta_S(\omega)$ can be simplified to $\frac{\beta_R}{n_R}$ and $\frac{\beta_S}{n_S}$, where n_R is taken as 1 (free space propagation) and n_S is the average refractive index of the sample. Furthermore, the identity $\frac{\beta_R}{n_R} = \frac{\beta_S}{n_S} = k = \frac{\omega}{c}$ is valid. With this in mind, it is possible to calculate the spectral interferogram $I(k)$, defined by

$$I(k) = \left|E_R\left(\omega = kc\right) + E_S\left(\omega = kc\right)\right|^2. \tag{2.39}$$

Expanding this expression using Equations (2.36) and (2.37) gives

$$I(k) = S(k) r_R^2 \tag{2.40a}$$

$$+ S(k) \left(\int_{-\infty}^{+\infty} \int_{-\infty}^{+\infty} r_S\left(l_S\right) r_S\left(l'_S\right) \exp\left[-j2kn_S\left(l_S - l'_S\right)\right] dl_S dl'_S \right) \tag{2.40b}$$

$$+ 2S(k) r_R \int_{-\infty}^{+\infty} r_S\left(l_S\right) \cos\left[2k\left(n_S l_S - l_R\right)\right] dl_S, \tag{2.40c}$$

with the source power spectral density defined as $S(k)$, as before.

The first term (2.40a) in the above equation is a DC term, corresponding solely to the power returning from the reference arm, which can be measured when blocking the power contribution from the sample arm, which effectively sets $r'_S\left(l_S\right)$ to zero.

The second term (2.40b) is designated the "self-interference" (or "auto – correlation") term, and only contains contributions from the sample arm, in the form of interference between the partial waves originating from the different sample depths, whose axial locations are encoded in $r_S(l_S)$.

The final term (2.40c) denotes the cross-interference term which arises from the interference between the different sample reflectors (again, distributed axially according to $r_S(l_S)$) and the reference arm. This term encodes the axial distribution $r_S(l_S)$ with the cosine inside the integral. Since we are detecting the spectrum, $k = \frac{2\pi}{\lambda}$ is the free parameter, and $2(n_S l_S - l_R)$ is the modulation frequency. The deeper the origin of the backscattered partial wave, the higher this modulation frequency.

It is then possible to decode this last term to retrieve the axial distribution of $r_S(l_S)$. This is achieved by taking a Fourier transformation of $I(k)$, under the assumption that r_S is a symmetric function with respect to l_S, which is possible since $r_S(l_S) = 0$ for all l_S shorter than the location of the first sample interface (one only has free space propagation above the sample). Following [14], it is possible to replace $r_S(l_S)$ with the symmetric expansion $\hat{r_S}(l_S) = r_S(l_S) + r_S(-l_S)$, Equation (2.40) can be written as

$$\begin{aligned} I(k) =& S(k)\left(r_R^2 + \frac{1}{4}\int_{-\infty}^{+\infty}\int_{-\infty}^{+\infty}\hat{r_S}(l_S)\,\hat{r_S}(l'_S)\,e^{-j2kn_S\left(l_S-l'_S\right)}dl_S dl'_S\right. \\ &\left. + \int_{-\infty}^{+\infty}\hat{r_S}(l_S)\,e^{-j2kn_S l_S}dl_S\right). \end{aligned} \tag{2.41}$$

In the expression above, the cosine term (Equation (2.40c)) has been replaced with a complex exponential, this effectively means that only the real part of the integrand is being considered at this stage. Moreover, the integral in l'_S in the second to last term represents the auto-correlation function $\mathcal{AC}[\hat{r_S}(l_S)]$ of $\hat{r_S}(l_S)$; hence, the expression can be simplified to

$$I(k) = S(k)\left(r_R^2 + \frac{1}{4}\int_{-\infty}^{\infty}\mathcal{AC}\left[\hat{r_S}(l_S)\right]e^{-j2kn_S l_S}dl_S + \int_{-\infty}^{+\infty}\hat{r_S}(l_S)\,e^{-j2kn_S l_S}dl_S\right). \tag{2.42}$$

These integrals are nothing more than the Fourier transforms of either $\hat{r_S}(l_S)$ or $\mathcal{AC}[\hat{r_S}(l_S)]$, hence

$$I(k) = S(k)\left(1 + \frac{1}{8}\mathfrak{F}\left\{\mathcal{AC}\left[\hat{r_S}(l_S)\right]\right\} + \frac{1}{2}\mathfrak{F}\left\{\hat{r_S}(l_S)\right\}\right), \tag{2.43}$$

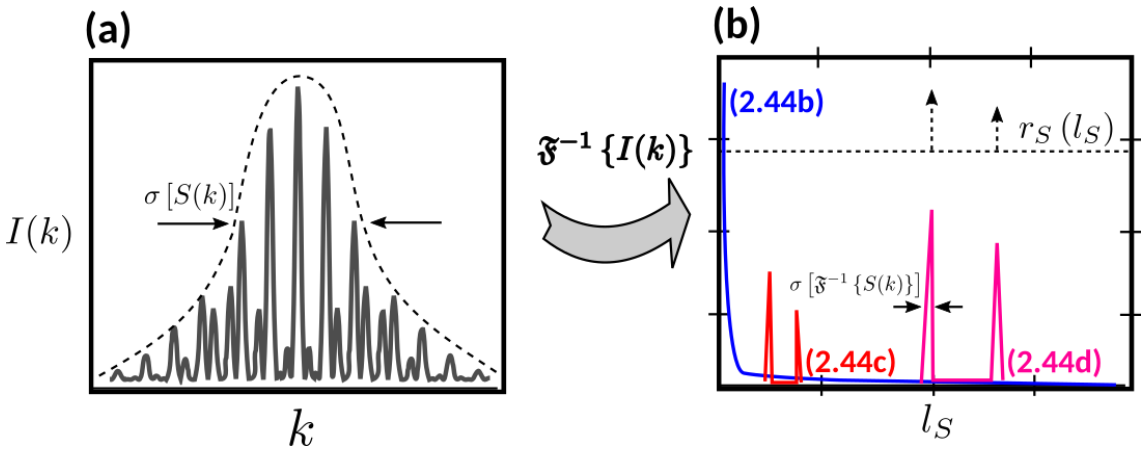

FIGURE 2.2: A Fourier analysis $\mathfrak{F}^{-1}\{I(k)\}$ of the interferogram $I(k)$ (which is represented in **(a)**), yields three different terms which are presented and defined in Equation (2.44). Dashed line on graph **(b)** represents the location of the different scatterers in the sample arm (i.e., the graphical representation of $r_S\,(l_S)$). $\sigma\,[\,]$ represents the FWHM of the envelopes of the functions $S(k)$ and of its Fourier-transformed variant $\mathfrak{F}^{-1}\{S(k)\}$.

where $\mathfrak{F}\{\}$ denotes the Fourier transform on the l_S domain. By performing an inverse Fourier transform $\mathfrak{F}^{-1}\{\}$ on the above expression, we are then able to recover $r_S\,(l_S)$ from the detected signal $I(k)$. By applying the convolution property of the Fourier transform, Equation (2.43) can be written as

$$\begin{aligned}
\mathfrak{F}^{-1}\{I(k)\} =& \mathfrak{F}^{-1}\{S(k)\} && \text{(2.44a)}\\
&\otimes \Big[\delta\,(l_S) && \text{(2.44b)}\\
&+ \frac{1}{8}\mathcal{AC}\,[\hat{r_S}\,(l_S)] && \text{(2.44c)}\\
&+ \frac{1}{2}\hat{r_S}\,(l_S)\Big], && \text{(2.44d)}
\end{aligned}$$

where $\otimes$ denotes convolution. If we now plot this signal as a function of l_S, as was done in Figure 2.2, the three components presented in Equation (2.40) are also present in the spectrum.

The blue component (Equation 2.44b), which concerns the DC component from the reference arm, corresponds to the $l_S = 0$ region in the frequency spectrum. This component can easily be removed by high-pass filtering, not affecting the information to be retrieved from the interference spectra.

The (red) auto-correlation term (Equation 2.44c) arises due to the interference between the waves back-reflected by different scatterers within the sample. Since

these components scale with the back-reflected power from the sample only, they are comparably smaller than the interferometric terms, which are proportional to $r_R \cdot r_S\left(l_S\right)$. Moreover, the auto-correlation components tend to be located around $l_S = 0$ [7, 14], hence they can also be avoided by adjusting the location of the sample within the interferometer.

Finally, the information about the actual locations of different scatterers is found in the cross-correlation term (Equation 2.44d), represented in magenta. If a change in the OPD is created, this will be the only term which will be shifted in l_S. Furthermore, given that this term is being convolved with the inverse Fourier transform of $S(k)$, one ultimately arrives at the same result as that of the time-domain detection - the wider the spectral width, the narrower is $\mathfrak{F}^{-1}\left\{S(k)\right\}$, and therefore the better is the axial resolution (which is coherence-limited). The resolution in the channelled spectra acquisition is not important for the axial resolution, but impacts the axial range of the system, as will be shown in the next chapter, specifically in Section 3.2.

2.3 Conclusions

In this chapter we have established the fundamentals of WLI, which is the core of any OCT system. It has been demonstrated that one can achieve depth selection by employing a low-coherence optical source to illuminate an interferometer, with one of its arms containing the sample we are interested in characterising.

Detection of the interferometric signal can be performed in either time or frequency (Fourier) domain. The time-domain method was referred to in this chapter for historical context, since it was the first to be implemented. However, this detection method requires the path length of the reference arm to be varied during acquisition. Such variation was initially performed by mechanically scanning a mirror in the reference arm [9]; more sophisticated methods were reported afterwards, such as spectral-delay lines and phase modulators [10]. With Fourier-domain detection methods , however, the sensitivity is typically boosted between 50-100 times compared to time-domain methods. This has the corresponding effect of increasing imaging speeds [8].

Frequency-domain methods have evolved significantly over the last two decades, mainly due to the availability of faster and lower-cost detectors (in the form of line cameras) but also due to the increase in computing power which allowed real-time processing of the detected spectra. Removing the requirement for reference arm scanning brought a significant improvement in the axial scanning

rate [15], since a single spectral read can yield the entire depth profile. However, frequency-domain methods also present some drawbacks, which will be discussed further in the next chapter.

Until this point the frequency-domain detection theory which was presented in the previous section has been developed assuming an optical source with a Gaussian spectrum and a spectrometer, a technique which is often referred to in the OCT field as spectral-domain OCT (SD-OCT). There is, however, an alternative modality employing a tunable (swept) source and photo-detectors, usually labelled as swept-source OCT (SS-OCT), which brings some additional advantages, that will be briefly mentioned in the next chapter. The underlying theory, however, is similar to that of its spectrometer-based counterpart.

References

[1] M. J. Marques, "Experiments in spectrometer-based , fourier-domain optical coherence tomography", MSc thesis, Faculdade de Ciencias da Universidade do Porto, 2012.

[2] A. A. Michelson and E. W. Morley, "On the relative motion of the earth and the luminiferous ether", *Am. J. Sci.*, vol. 34, no. 203, pp. 333–345, 1887.

[3] M. Born and E. Wolf, *Principles of Optics: Electromagnetic Theory of Propagation, Interference and Diffraction of Light (7th Edition)*, 7th. Cambridge University Press, 1999, ISBN: 0521642221.

[4] M. Hughes, "Optical coherence tomography for art conservation and archaeology: methods and applications", PhD thesis, University of Kent, 2010.

[5] L. Allen and D. Jones, "An analysis of the granularity of scattered optical maser light", *Physics Letters*, vol. 7, no. 5, pp. 321–323, 1963. [Online]. Available: http://www.sciencedirect.com/science/article/pii/0031916363900544.

[6] J. C. Dainty, *Laser speckle and related phenomena*. Springer Science & Business Media, 2013, vol. 9.

[7] M. E. Brezinski, *Optical Coherence Tomography: Principles and Applications*. Academic Press, 2006, ISBN: 9780080464947.

[8] J. G. Fujimoto and W. Drexler, "Introduction to oct", in *Optical Coherence Tomography: Technology and Applications*, W. Drexler and J. G. Fujimoto, Eds., 2nd ed., Springer, 2015, ch. 1.

[9] D. Huang, E. A. Swanson, C. P. Lin, J. S. Schuman, W. G. Stinson, W. Chang, M. R. Hee, T. Flotte, K. Gregory, C. A. Puliafito, *et al.*, "Optical coherence tomography", *Science*, vol. 254, no. 5035, pp. 1178–1181, 1991. [Online]. Available: http://science.sciencemag.org/content/254/5035/1178.short;%20http://www.ncbi.nlm.nih.gov/pmc/articles/PMC4638169/.

[10] A. M. Rollins and J. A. Izatt, "Reference optical delay scanning", in *Handbook of Optical Coherence Tomography*, B. E. Bouma and G. J. Tearney, Eds., Marcel Dekker, 2002, ch. 4.

[11] G. Tearney, B. Bouma, and J. Fujimoto, "High-speed phase-and group-delay scanning with a grating-based phase control delay line", *Optics Letters*, vol. 22, no. 23, pp. 1811–1813, 1997. [Online]. Available: https://www.osapublishing.org/abstract.cfm?uri=ol-22-23-1811.

[12] A. Rollins, S. Yazdanfar, M. Kulkarni, R. Ung-Arunyawee, and J. Izatt, "In vivo video rate optical coherence tomography", *Optics Express*, vol. 3, no. 6, pp. 219–229, 1998. [Online]. Available: https://www.osapublishing.org/abstract.cfm?uri=OE-3-6-219.

[13] M. Leitner, "White light interferometry: applications in high resolution sensing and biomedical imaging", PhD thesis, Faculdade de Ciencias da Universidade do Porto, 2010.

[14] M. W. Lindner, P. Andretzky, F. Kiesewetter, and G. Hausler, "Spectral radar: optical coherence tomography in the fourier domain", in *Handbook of Optical Coherence Tomography*, B. E. Bouma and G. J. Tearney, Eds., Marcel Dekker, 2002, ch. 12.

[15] A. G. Podoleanu, "Optical coherence tomography", *Journal of microscopy*, vol. 247, no. 3, pp. 209–219, 2012. [Online]. Available: http://onlinelibrary.wiley.com/doi/10.1111/j.1365-2818.2012.03619.x/full.

Chapter 3

Spectral-domain Optical Coherence Tomography: Technologies and Methodologies

BUILDING up from the WLI theory presented in the previous chapter, the technology of Optical Coherence Tomography is presented here. Given the wide scope of the field, the author has chosen to limit himself to the technologies and methodologies which have been used in the experimental set-ups described throughout Part II of this Thesis, which all pertain to spectral-domain OCT.

Contents

EVER since the first demonstration of spectral interferometry by Fercher *et al.* [1] and Häusler *et al.* [2] in the mid-1990s, high resolution near-IR spectrometers have played a part in OCT imaging.

As mentioned in the previous section, detecting the interferometric signal in frequency-domain allows for instant acquisition of the full depth profile without

having to manually scan the reference arm, which was the case with TD-OCT. With the availability of faster and less expensive detector arrays and computer systems, spectral-domain OCT (SD-OCT) has gained preference over TD-OCT systems, especially since it brought a reduction in the level of the noise detected, as demonstrated simultaneously in 2003 by three research groups [3–5]. The first retinal image using SD-OCT was obtained by Wojtkowski *et al.* in 2002 [6], and from that point onwards SD-OCT became the *de facto* detection modality in OCT systems, which is still the case in the $800\,\mathrm{nm}$ wavelength region.

Swept-source OCT (SS-OCT) has gained significant importance over the last decade, especially since it can operate over the $1 - 1.3\,\mu\mathrm{m}$ range where the sensitivity for silicon-based line cameras drops and more expensive InGaAs cameras are required [7]. Moreover, tunable sources can exhibit coherence lengths far superior to the equivalent coherence lengths of wavetrains after diffraction on gratings, therefore SS-OCT gives access to larger axial ranges than SD-OCT. The link between high spectral sampling resolution and large OCT axial range is presented in Section 3.2.

Another issue specific to both SD-OCT and SS-OCT is the existence of mirror (conjugate) terms, which is detailed in Section 3.1.

Material dispersion mismatch in OCT systems is a significant issue, which degrades the axial resolution. The wider the bandwidth available in the system, the larger the dispersion effect. Therefore, addressing the issue of dispersion is paramount in broadband systems aiming to achieve ultra-high resolution OCT imaging (UHR-OCT). In Section 3.3 the analysis of the detected photo-current at the output of a WLI system, presented in Sections 2.1.2 and 2.1.3 is extended to account for the presence of material dispersion.

The "T" in the OCT acronym (which stands for tomography) is covered in Section 3.4, where considerations related to raster-scanning imaging systems are presented, namely the modifications needed to perform retinal imaging with a flying-spot OCT system.

3.1 Ambiguity on the sign of the path difference: mirror terms

The existence of mirror (conjugate) terms arise as a consequence of the fact that the interference terms recorded in the frequency domain are real functions. Since the Fourier Transform (FT) of a real function is always Hermitian [8], the Fourier transform contains terms for both positive and negative values of the optical path

difference axis. The consequence of this is the ambiguity in the sign of the path difference. Let us consider, without loss of generality, a simple co-sine function $\cos(2k \pm \Delta l)$ as the interference term (Equation (2.40c)). Its FT can be written as [9]:

$$\mathfrak{F}\{\cos(2k \pm \Delta l)\} = \frac{1}{2}[\delta(k - 2\Delta l) + \delta(k + 2\Delta l)]. \tag{3.1}$$

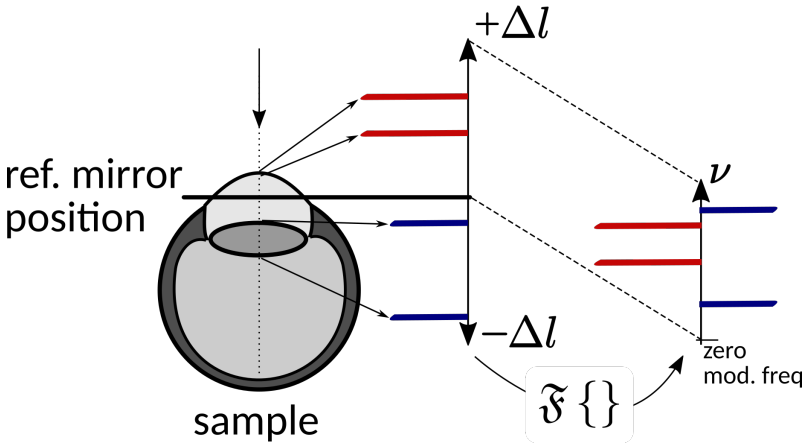

FIGURE 3.1: Schematic representation of the problem of mirror terms in SD- and SS-OCT. The "zero" point of the WLI ($\Delta l = 0$), labelled "ref. mirror position", is placed in the middle of the sample (left), hence there is a range of positive and negative OPDs whose FT pairs are overlapped in the Fourier domain (right). In other words, the original positions of the interfaces with respect to their OPD values are not distinguishable in terms of their sign (adapted from Leitgeb *et al.* [9]).

It is clear from the expression above that symmetrical values in terms of the OPD within the argument of the co-sine will yield exactly the same Fourier transform peaks. In other words, the sample features located in either the positive or the negative side of the "zero" point of the WLI are not distinguishable from each other in the signal produced by the Fourier transform, as shown in Figure 3.1. Since only the absolute value of the OPD is preserved, features of the sample being analysed lying on either side of the "zero" point overlap on the depth profile.

Many different methods have been reported in the literature to address this issue. The key point is that the signal being detected is real; if it could be turned into a complex-domain signal, one would be able to separate the two terms corresponding to a single reflector (which are complex conjugates of each other [10]) and resolve the ambiguity, thus allowing the features placed at positive OPD values to become distinguishable from those placed at negative OPD values. This

behaviour enables access to the whole axial range (up to the sampling limit). Several methods have been proposed to attenuate or remove the mirror terms. Methods based on phase modulation have been developed, where the phase variation is controlled in a variety of ways: by stepping the reference mirror [9, 11–13]; by employing optoelectronic phase modulators [14, 15]; by using a 3×3 coupler to create a phase shift between the detection ports [16–18]; by creating a phase shift between adjacent A-scans, either by syncing the reference mirror movement with the scanning mirror [19], using the scanning mirror slightly off-axis [20] or placing the sample at an angle [21]. Other methods use frequency shifting [22–24], either by using a frequency modulator or by using the object beam off-axis of the pivot of the galvo-scanner. To enhance the efficiency of the operation, polarisation diversity [25] or frequency encoding [26] methods have been reported. Another method, which has been implemented with a SS-OCT system, is the one reported by Fechtig *et al.* [27], where a line-field OCT system [1] is used and a linear phase shift is introduced by adopting an off-axis configuration on the reference arm.

The methods described above are effectively *cancellation* methods, allowing the recovery of the full depth range. However, they require additional hardware and signal processing in order to retrieve the complex spectra and resolve the ambiguity. It may prove beneficial to still use the real spectra without any additional processing.

Talbot Bands, an exquisite effect observed by William Fox Talbot in 1837 [28], is one way of doing so. Using a purely hardware-based approach, which does not require any additional hardware, resorting to modifications in the spectrometer and how the two arms of the interferometer are coupled. This method is covered in detail[2] in Subsection 3.2.1.

Recently, a method applicable only to SS-OCT has been reported [30], which shifts the visibility profile towards longer OPDs resorting to coherence revival. This refers to producing interference using waves that come from different laser cavity ends, and thus requires for the two interferometer arms to be mismatched by an integer multiple of the laser cavity length. An exquisite property of coherence revival peaks is that the phase is automatically modulated due to the modulation of the tuning element's cavity length in the swept source.

[1] A line-field OCT system employs a tunable source as the optical source but, unlike a conventional 2-D raster-scan SS-OCT system, it uses a 1-D line camera to paralelise the data acquisition, effectively requiring only one scanner to acquire a full volume.

[2] Portions of this section were adapted from content previously written in the author's MSc thesis [29], submitted for evaluation at the University of Porto in 2012.

3.2 Spectrometers for SD-OCT systems

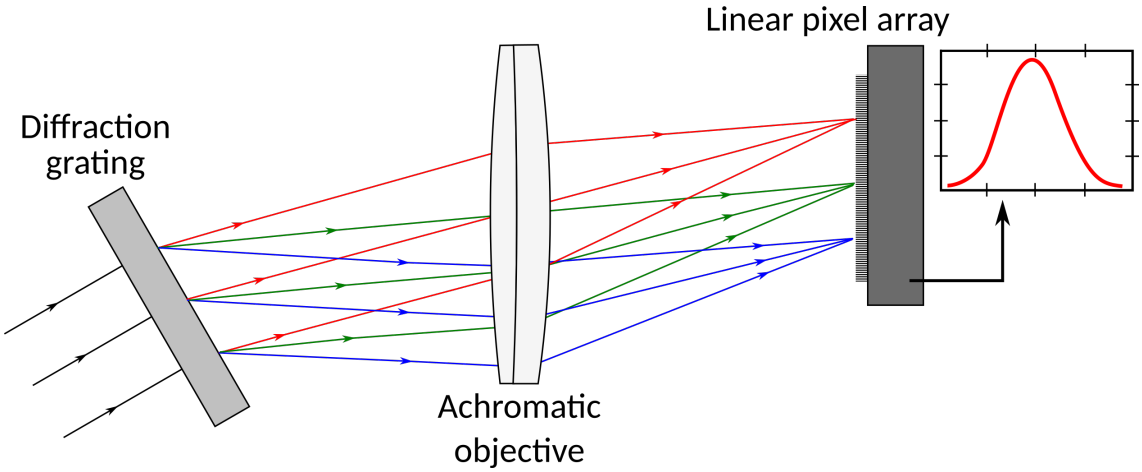

FIGURE 3.2: Schematic representation of a spectrometer with a diffraction grating operating in transmission, and assuming a collimated beam delivery.

The typical components of a spectrometer comprise a dispersive element (a prism or a diffraction grating, or a combination thereof), one or more objective lenses, and a linear detector, as shown in Figure 3.2. Additionally, if the device is to be fibre coupled, a collimating lens will also be needed to collimate the optical fibre output towards the dispersive element.

The spectrometer samples the spectra $I(k)$ which result from the superposition of the two signals from the arms of the interferometer (as given by Equation (2.43)). All components mentioned above determine the sampling resolution of the spectrometer. This can be inferred by applying the sampling (Nyquist) theorem. This also dictates the maximum axial range that the system is capable of attaining.

Several reports have been published [4, 31, 32] in the past on how to analytically describe the impact of each of the spectrometer parameters on two measurement parameters: axial resolution and decay with path difference. Hu *et al.* [32] have focused their analysis on the detector array and its finite pixel size, which in turn yields a finite-width sampling function. They have determined that the signal amplitude decay with depth $A(z)$ can be given by

$$A(z) \propto \Delta x R \exp\left[-\frac{a^2 R^2 z^2}{4 \ln 2}\right] \frac{\sin(\Delta x R z)}{\Delta x R z}, \tag{3.2}$$

where Δx is the pixel width, $R = \Delta k/\Delta x$ is the linear dispersion of the wavenumbers k on the detector array, z is the measurement depth and a is the FWHM of the spot profile when a single wavelength at the centre of the spectrum is considered.

This analysis is limited to the case where the waves from the two arms of the interferometer are perfectly superposed on the diffraction grating, as is the case when they have been previously recombined in a fibre-based directional coupler (corresponding to the conventional SD-OCT configuration). Another limitation is the fact that the first factor in Equation (3.2) is applicable only to the case where the power distribution within the footprint of the beams on the grating is described by a Gaussian power distribution.

With regards to the first term in Equation (3.2), a more complete theory is presented by Podoleanu [33, 34] and Woods [35, 36]. This covers both the case of the two beams falling on different areas of the grating, as well as the general case of power distribution within each beam. This theory explains the sensitivity decay versus measurement depth due to the degree of overlap between the finite length of the two diffracted wavetrains, a wavetrain for each arm of the interferometer. This formalism follows from an earlier study on Talbot Bands carried out by Podoleanu *et al.* [37, 38] in the late 1990s where the wavetrain model was employed. This is in fact equivalent to the wavetrain analysis applied at the spectrometer in SD-OCT, since the spectrometer resolution and the wavetrain length describe the FWHMs of two entities that form a Fourier pair [39].

In the following sub-sections an abbreviated version of the Talbot Bands formalism using the wavetrain model is presented, which is then extended to the analysis of the spectrometer in a SD-OCT system, ultimately finishing with the unified model described by Michael Hughes in his PhD thesis [39]. This combines the effect of the spectrometer's optical elements (using the wavetrain model) with the limited sampling caused by the finite pixel size as presented by Hu *et al.* [32] in the second term in Equation (3.2).

Both models mentioned above assume that the projected spectrum is linear in k, which makes it easy to convert back to depth dimensions since k and z are Fourier pairs. However, the grating equation [40] for the diffraction order $m = 1$ gives us $a\left(\sin\theta_d - \sin\theta_i\right)$, where a is the grating pitch, θ_d is the diffracted angle and θ_i the angle of incidence. Since $k = 2\pi/\lambda$, we have

$$k = \frac{2\pi}{a\left(\sin\theta_d - \sin\theta_i\right)}, \tag{3.3}$$

which is clearly a non-linear relation between k and θ_d. If the spectral information is not sampled in k before the inverse Fourier transform is performed, this

leads to a depth-dependent decrease in the axial resolution, in a similar way to what would happen if the interferometer had uncompensated material dispersion (which is covered in Section 3.3). Several procedures have been devised to perform the re-sampling operation to turn the spectra linear in k; this is covered in some depth in Section 3.2.3.

3.2.1 Talbot Bands

The first observation of Talbot bands was reported in 1837 by William Fox Talbot in a note to the Royal Society of London [28]. When a glass plate was inserted half-way into the spectrum from a white light source which had been dispersed by a prism, dark bands were observed, as shown in Figure 3.3. Talbot explained the observed phenomena under the "undulating theory of light", based upon the propagation of waves through ether (Michelson and Morley's experiment [41] only disproved the existence of ether decades later, in 1887). The scientific community at the time was deeply divided between supporters of the "undulating" theory and those supporting the "emission" theory, the latter group considering that light was in fact propagating as parallel beams and not waves [36].

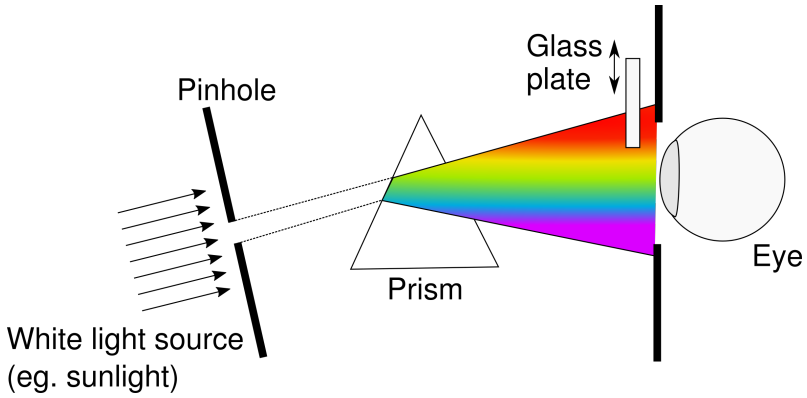

FIGURE 3.3: The original experiment producing Talbot bands with a white light source (e.g., sunlight). A thin glass plate is introduced half-way into the dispersed spectrum, generating dark bands in the observed image. (adapted from Woods [36])

Talbot's explanation proposed that the wavefronts of the light traversing the glass plate suffered an additional delay, and any wavefronts delayed by an odd multiple of half-wavelengths would interfere destructively with the light from the other half of the beam.

However, later that same year, Sir David Brewster (a close friend to Talbot and a supporter of the opposing "emission" theory) announced at the annual meeting of the British Association for the Advancement of Science [42] that Talbot's

theory on the bands was incorrect. He had repeated the experiment with additional precision by introducing an achromatic telescope configuration between the dispersive medium and the glass plate, allowing him to control with greater precision where in the transversal section of the beam the glass plate was being inserted. With that, Brewster was able to observe that the appearance of the dark bands in the spectrum was effectively dependent on which side in the transversal section of the beam the glass plate was introduced into: the dark bands appeared when the plate was introduced on the red side of the spectrum (top part of Figure 3.3), but not when it was inserted onto the violet side of the spectrum (bottom part of the same figure). Brewster attributed this observed behaviour to a "new polarity" of light [43], but three years later Airy showed that it was no more than a curious manifestation of diffraction [44].

3.2.1.1 Theoretical background: wavetrain model

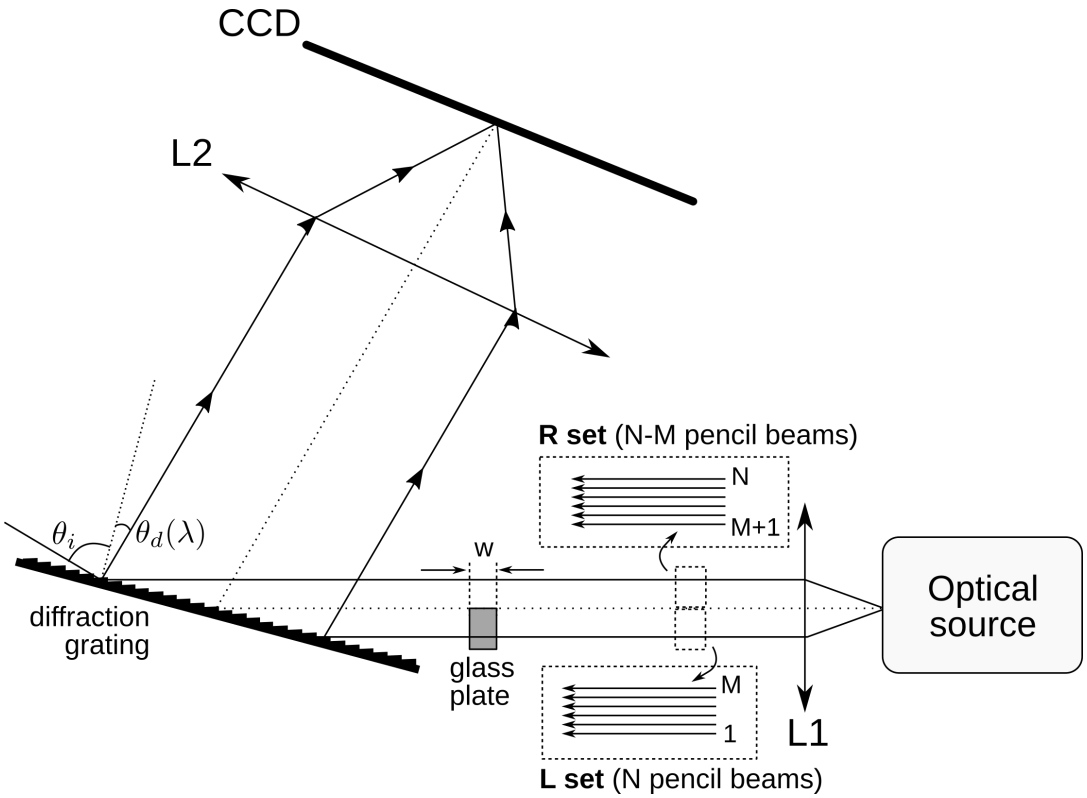

FIGURE 3.4: Experimental set-up devised for the observation of Talbot bands (adapted from Marques [29], based on Podoleanu *et al.* [37]).

Talbot's original explanation of the observed phenomena, based on interference of the delayed versus un-delayed parts of the beam, is correct. However, this explanation does not take into consideration the dispersion due to the prism and how that influences the phase delay for each pencil beam making up the full

beam profile. Only diffraction fully explains the behaviour observed by Brewster when the glass plate is introduced halfway into different sides of the oncoming beam, where bands may or may not be observed.

Consider the experimental set-up depicted in Figure 3.4, where a diffraction grating is used (instead of a prism as in Talbot's original experiment). The optical source employed has a very broad spectrum and therefore a short coherence time, such as those considered in the previous chapter throughout Section 2.1.2. We can think of the collimated beam output as a set of N pencil beams which have travelled up to this point the same path length. A sub-set of those pencil beams (**L set**, comprising M beams, as shown in Figure 3.4) traverses a glass plate with thickness w; the remaining $N - M$ pencil beams which make up **R set** then travel along an optical path shorter by $(n_g - 1)\, w$ in relation to that of the **L set,** n_g being the index of refraction of the glass plate.

The glass plate can be introduced in various positions with respect to the propagation direction of the oncoming beam. In Figure 3.5 four cases are considered, with the plate being inserted on the left (L), right (R), bottom (B) and top (A) side of the beam. Figure 3.4 shows the L case where the glass plate is introduced on the left-hand side of the beam as it propagates from the right to the left side of the page.

If there is no glass plate inserted, each pair of adjacent pencil beams exiting the diffraction grating (as shown in Figure 3.6) will have a delay between them given by

$$D = \left[a\left(\sin\theta_i - \sin\theta_d\right)\right], \tag{3.4}$$

where θ_i is the angle of incidence, $\theta_d\left(\lambda\right)$ is the diffraction angle, and a is the grating pitch. According to Bragg's law, $D = n\lambda$, assuming λ to be the central wavelength λ_0 of the broad spectrum considered and $n = 1$ (first order), therefore $D = \lambda_0$ and the delay between *each* pencil beam and the next becomes $\Delta r_s = \lambda_0$.

We can now generalise this result to all N pencil beams comprising the main beam, obtaining

$$r_s = (s-1)\left[a\left(\sin\theta_i - \sin\theta_d\right)\right] = (s-1)\, D, \quad s = 1, \ldots, N. \tag{3.5}$$

For each wavelength in the spectrum, all pencil beams are diffracted at the same angle, with the focusing lens L2 directing all of them towards a single point on the CCD plane. If we now extend this analysis to all the wavelengths within the spectrum, the full source spectrum extends over the whole CCD.

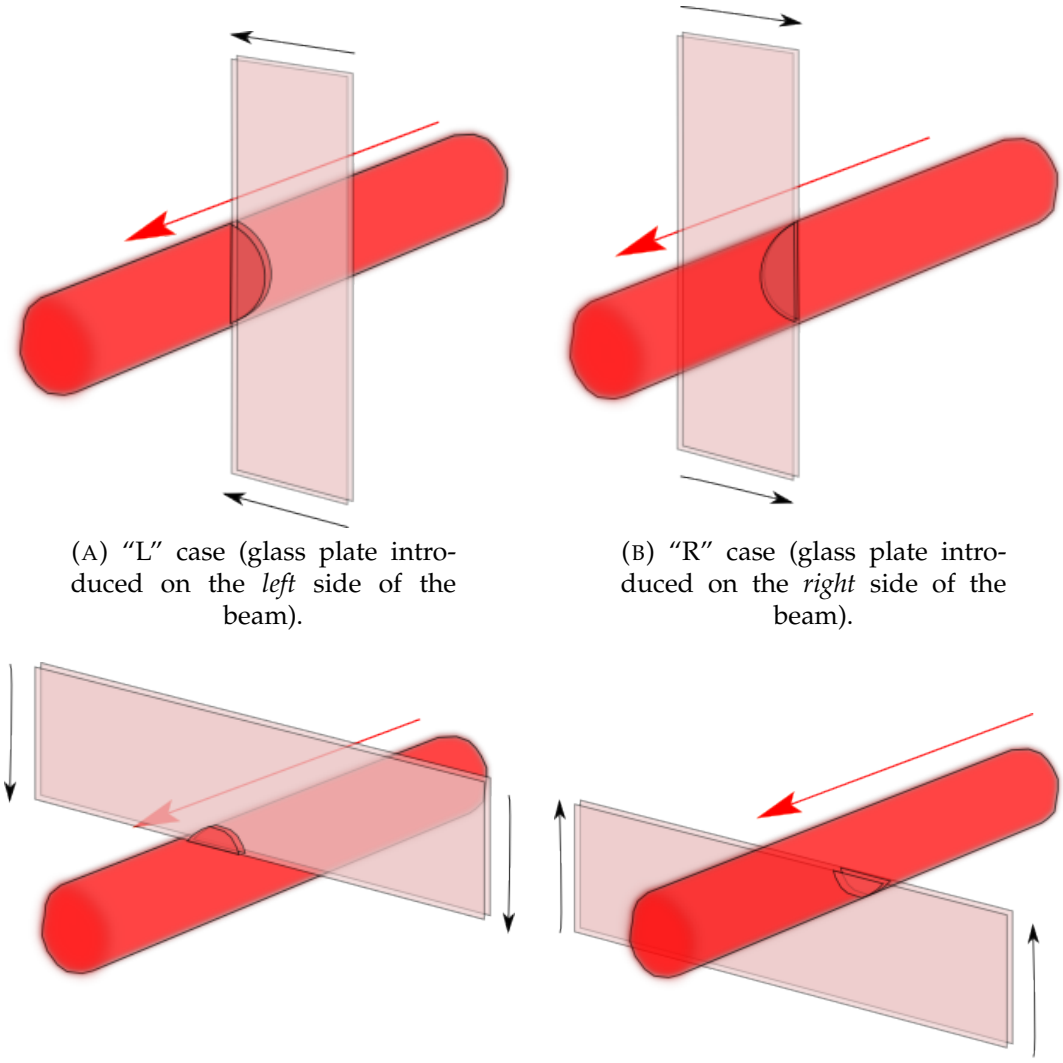

(A) "L" case (glass plate introduced on the *left* side of the beam).

(B) "R" case (glass plate introduced on the *right* side of the beam).

(C) "A" case (glass plate introduced on the *top* side of the beam).

(D) "B" case (glass plate introduced on the *bottom* side of the beam).

FIGURE 3.5: The four possible glass plate insertion configurations (retrieved from Marques [29]).

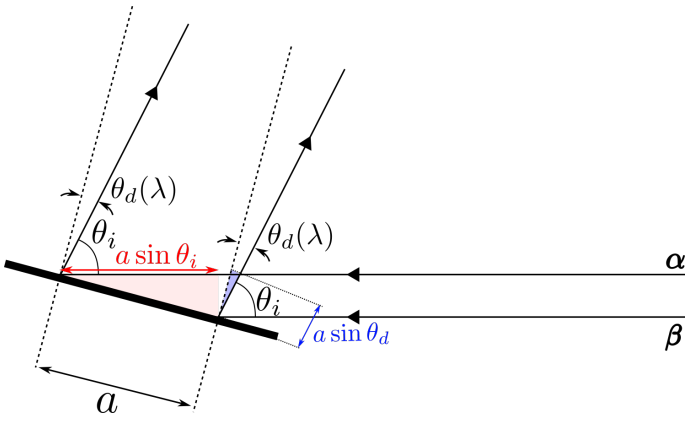

FIGURE 3.6: Delay between two adjacent pencil beams, α and β, which amounts to $a \sin \theta_i - a \sin \theta_d$, effectively equal to λ_0 (adapted from Marques [29]).

If, however, we now introduce the glass plate according to the L case (as depicted in Figure 3.4), we need to not only take into account the delay between the two sets of pencil beams imprinted by the diffraction grating, but also that caused by the additional optical path travelled by the pencil beams within the region where the glass plate was introduced. Let us consider the path length encountered by the L set (which traverses the glass plate). This yields:

$$r_s = n_g w + (s-1)D, \quad s = 1, \ldots, M \tag{3.6}$$

The R set of pencil beams does not traverse the glass plate, but given that the count for the pencil beams starts at $M+1$ we need to add an offset of $M \times \lambda_0$, or MD:

$$r_p = w + (p-1)\,D + MD. \quad p = (M+1), \ldots, N \tag{3.7}$$

Effectively, since the two sets of beams are mutually delayed by a net path difference of $(n_g - 1)\,w$, then depending on the value chosen for w one should be able to observe (or not) an interference pattern at the CCD plane. This pattern is composed of alternating bright and dark bands superposed on the spectral shape previously obtained, and it is effectively what both Talbot and Bragg noticed experimentally. These bands appear due to constructive and destructive interference happening between the two sets of pencil beams. Since θ_d exhibits a dependence on λ while θ_i remains constant throughout, at certain wavelengths one will observe constructive interference and at others the interference will be destructive, depending on the phase difference accumulated.

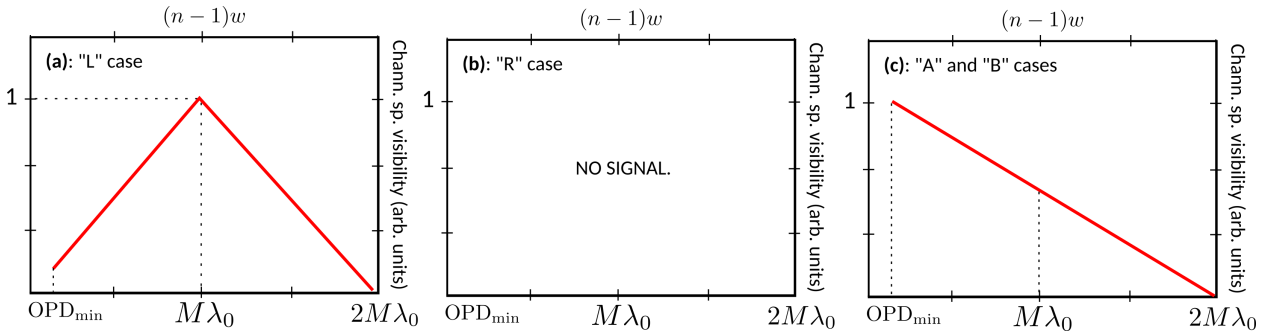

FIGURE 3.7: Visibility of the channelled spectrum for the four different cases considered in Figure 3.5, versus the thickness w of the glass plate. (adapted from Podoleanu *et al.* [37])

As shown in Figure 3.7 (a), the occurrence of the interference pattern depends on the thickness w of the glass introduced; it is maximum when $(n-1)w = M\lambda_0$, and drops to zero when $(n-1)w = 2M\lambda_0$.

This behaviour can be explained by employing the wavetrain formalism as described in [34]. Each pencil beam, prior to its interaction with the diffraction grating, has a coherence length l_c which depends on the properties of the optical source used. After the diffraction grating, each of these wavetrains is going to suffer a shift equal to $D = \lambda_0$ in relation to the previous one, following from Equations (3.4) – (3.7). This is visible in Figure 3.8 (a), where the glass thickness is equal to zero (corresponding to no glass being introduced). Since there is no spatial (or temporal) overlap between the two sets of beams, no interference is observed.

By changing the glass thickness, the L set of pencil beams is delayed in relation to the R set; consequently, a portion of the wavetrains belonging to it is now overlapping a portion of those belonging to the R set, thus some modulation intensity is observed. This is the case illustrated in Figure 3.8 (b), which corresponds to the region with the positive slope between $\mathrm{OPD}_{\min}$ and $M\lambda_0$ in Figure 3.7 (a).

As mentioned above, the interference pattern is maximised when the condition $w(n-1) = M\lambda_0$ is met; it is evident from Figure 3.8 (c) why, since the two wavetrains corresponding to the two different sets of beams are completely overlapped.

If the glass thickness continues to be increased, the width of the overlapped region will decrease (Figure 3.8 (d)). Ultimately, if $w(n-1) = 2M\lambda_0$ (it has been assumed here that the glass window covers exactly half of the transversal beam profile), the L set is delayed by $M\lambda_0$ in relation to the R set ($-M\lambda_0$ due to the

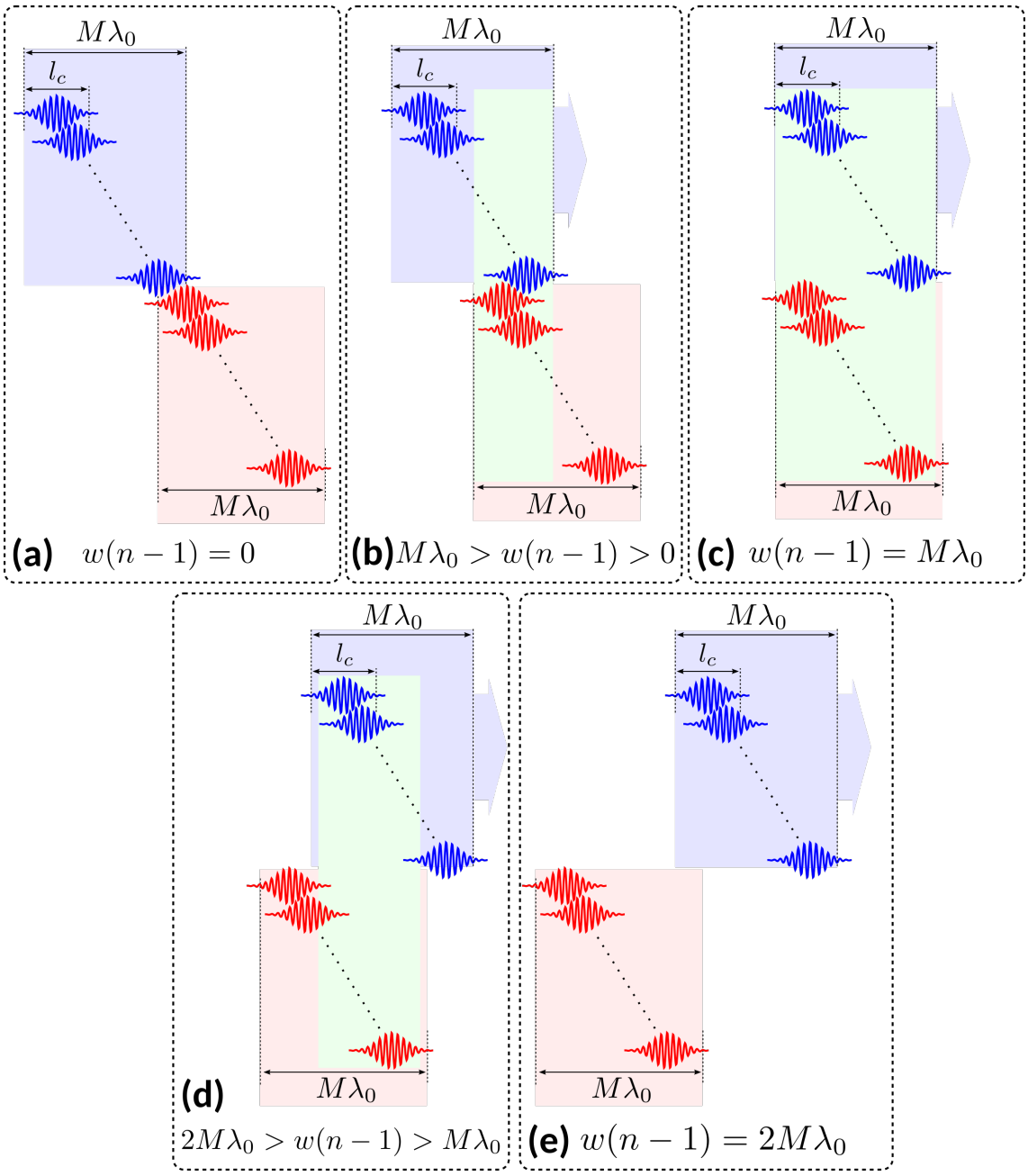

FIGURE 3.8: Schematic representation of the wavetrain overlap after diffraction for the "L" case, assuming the glass window covers half of the beam profile. In all sub-figures, the wavetrains propagate from the right to the left of the page. **(a)** glass thickness is equal to zero (i.e., no glass is inserted - system behaves as a spectrometer); **(b)** glass thickness ensures the condition $M\lambda_0 > w(n-1) > 0$, corresponding to a point in the positive slope in the graph in Figure 3.7 (a); **(c)** glass thickness ensures $w(n-1) = M\lambda_0$, the diffracted wavetrains corresponding to the two portions of the un-diffracted beam overlap completely and the interference pattern has its maximum amplitude value, as shown in Figure 3.7 (a); **(d)** when $w(n-1) > M\lambda_0$ a decrease in the intensity of the interference pattern is observed, with it disappearing altogether in **(e)**, where $w(n-1) = 2M\lambda_0$ and the two wavetrains do not overlap. The blue wavetrains correspond to the L set of pencil beams and the red wavetrains to the R set of pencil beams; the green shaded region delimits the region where the two wavetrains are matched in path length (and thus interference is observed).

grating, plus $2M\lambda_0$ due to the additional glass introduced), resulting in no overlap between the two wavetrains and consequently no interference, as shown in Figure 3.8 (e).

This observed behaviour, however, changes depending on the side of the beam in which the glass plate is introduced, which is what Brewster himself observed.

Let us consider now the "R" case (Figure 3.5). The analysis is similar to that of the "L" case, with Equations (3.6) and (3.7) becoming

$$r_s = (s-1)D + w, \quad s = 1, \ldots, M \qquad \textbf{(L set)} \tag{3.8}$$

$$r_p = (p-1)D + MD + nw, \quad p = (M+1), \ldots, N. \qquad \textbf{(R set)} \tag{3.9}$$

It is evident from the equations above that, regardless of the value w of the glass plate thickness, the two sets of pencil beams will never have delays between them which will allow the two wavetrains to overlap. In other words, if one again considers the diagrams represented in Figure 3.8, increasing the glass length moves the R set along the same direction as the L set in the previous case, hence no overlap will ever be achieved. Therefore, if the glass plate is introduced on the right side of the beam, no modulation will be observed.

The last two cases, "A" and "B", are quite similar since the system is assumed to be symmetric in the z direction (which, in this case, is perpendicular to the paper surface), which means that the insertion of the glass plate on the top side of the beam yields the same result as if the plate had been inserted on the bottom side of it.

These two cases mimic a two arms interferometer in free space, since the portion of the beam traversing the glass plate travels a different optical path than the other portion which misses the plate. Such a configuration has been used for measuring the thickness of glass plates [45].

3.2.1.2 Application to a White Light Interferometer

In order to apply the wavetrain model considered in the previous subsection to a white light interferometer (WLI), let us consider a Mach-Zehnder interferometer whose configuration is similar to that reported in [33], and which is schematically represented in Figure 3.9.

For simplicity, and without loss of generality, the sample arm is implemented in the exact same way as the reference arm, in a transmissive configuration. A slight difference in optical path length in air, z_0, is considered. All the supplying (stemming from the fibre directional coupler DC) and collecting fibres are exactly

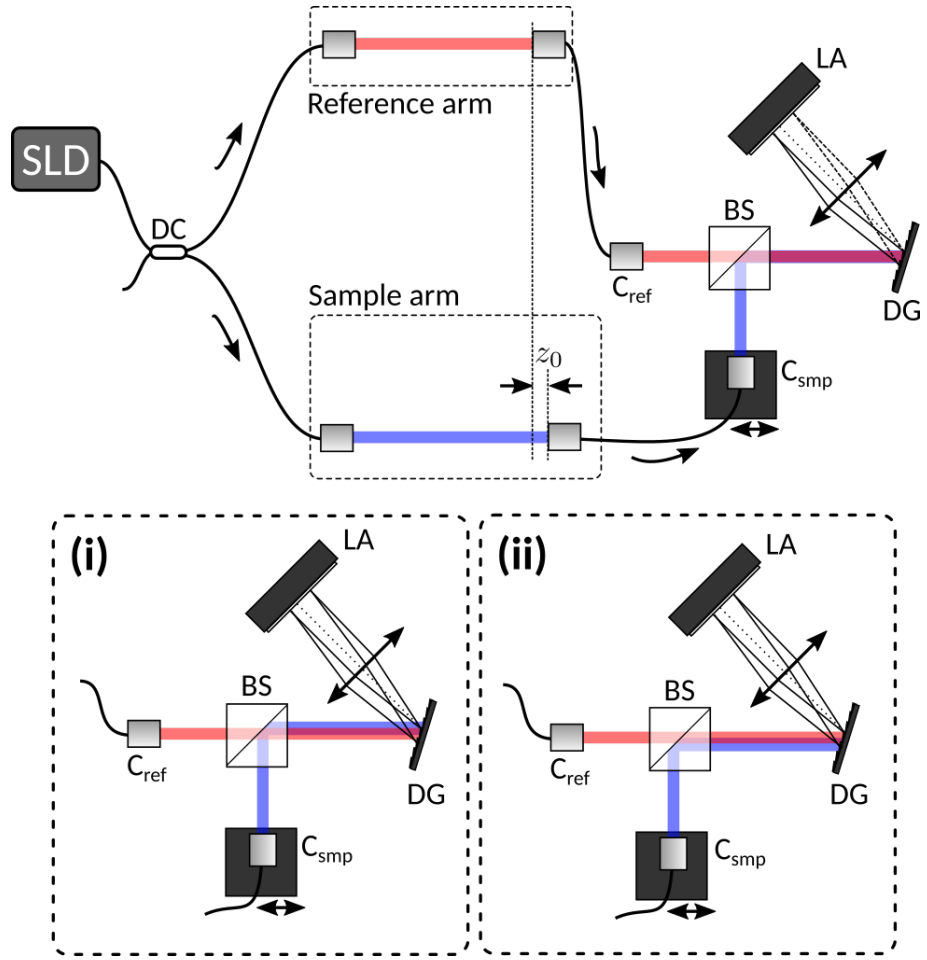

FIGURE 3.9: Mach-Zehnder WLI for the study of Talbot Bands. DC, fibre-based 2x2 directional coupler; C_{ref} and C_{smp}, collimators; BS, bulk beam-splitter; DG, diffraction grating operating in reflection; LA, linear detector array. The two beams are recombined by a beam-splitter BS. In the top figure, the two beams are superposed onto each other on their way towards the grating. Inset: **(i)** C_{smp} is moved to the right of its initial position; **(ii)** C_{smp} is moved to the left of its initial position.

matched in length, hence the overall OPD between the two arms of the interferometer is effectively z_0. This path difference introduces a delay between the two arms, which will termed *extrinsic*.

In the coupling point of the two arms of the interferometer (the beam-splitter BS), one is able to shift one of the beam profiles in relation to the other by adjusting the lateral position of collimator C_{smp}.

If we now focus our analysis on the BS and diffraction grating DG, the two beams will overlap perfectly on the DG and the dispersed spectra will be focused on the linear detector array (LA). Following the theory in the previous chapter, since there is a slight optical path difference between the two interferometer arms,

a modulation whose frequency is proportional to z_0 is observed in the spectrum. This is the case one can observe in conventional SD-OCT.

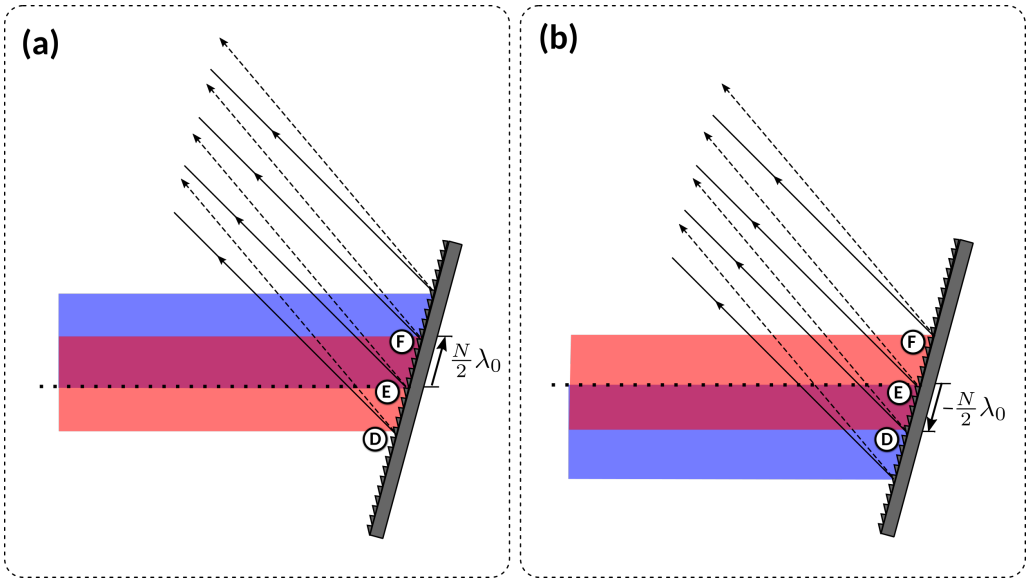

FIGURE 3.10: Detail of the incidence of the two beams (blue: sample arm; red: reference arm; purple: overlapping region) on the diffraction grating for the two positions of C_{smp} specified in the insets (i) and (ii) of Figure 3.9, with **(a)** representing the case where C_{smp} is moved to the right of its initial position and **(b)** the case where C_{smp} is moved to the left of its initial position.

We will now change the relative position of the projection of the sample arm beam on the DG by changing the lateral position of C_{smp} to the left and the right of its original position. This has been schematically represented in insets (i) and (ii) within Figure 3.9, respectively.

If we recall Figure 3.6, between two successive pencil beams diffracted by two neighbouring grating lines, a delay λ_0 is created (where λ_0 is the central wavelength of the source). It is possible to relate the number of illuminated grating lines with the width of the beams, S, since $N = S \times a$ (with a being the grating pitch, normally given in lines per mm). Therefore, the wave diffracted by the N^{th} illuminated line accumulates a delay equal to $N\lambda_0$. This is termed the *intrinsic* delay of the system (caused by the diffraction grating and the relative position of the two beams), as described in [33–35].

Let us now consider the two positions of the sample collimator, C_{smp}, and focus our analysis on the diffraction grating, as shown in Figure 3.10. If we assume that the observer is positioned to the left of the DG, as shown in Figure 3.10 (a), then the sample arm beam (in blue) is moved to the left of the reference arm beam (in red, starting at point D). The sample arm beam starts at point E, which in this case was chosen to be at the centre of the reference arm beam. According to the theory presented before (in section 3.2.1.1), this means that the sample arm beam

exhibits an additional phase delay offset of $^{N}/_{2}\lambda_0$. Conversely, if the sample arm beam is moved in the opposite direction by the same amount (as is the case in Figure 3.10 (b)) this means that the *reference* arm beam is that which is delayed by $^{N}/_{2}\lambda_0$; alternatively, it accumulates a phase delay of $-^{N}/_{2}\lambda_0$ in relation to the sample arm beam.

Recalling the "extrinsic" delay z_0 introduced by the WLI itself (since the two arms may not be matched in length), the sample wave after diffraction can travel a different optical path length than the reference wave after diffraction.

Figure 3.11 schematically shows the effect of the wavetrain shift due to both the "extrinsic" delay of the WLI and the intrinsic delay [34] caused by the diffraction. The intrinsic delay is that which is imprinted between the two diffracted wavetrains after diffraction, when the glass plate thickness is zero. This intrinsic delay, as explained in [34] determines the degree of overlap between the two wavetrain lengths after diffraction. For the interference to take place, the diffracted wavetrains must have the combined intrinsic and extrinsic delay within the coherence length of the wavetrains after diffraction. The overlap is represented by the shaded region between the two coloured bars, which represent the set of wavetrains for each of the beams: the larger the extent of this region, the stronger the amplitude of modulation observed on the detector plane.

In Figure 3.11, three "extrinsic" delays of the WLI are represented for three different relative positions of the two interferometer beams. Starting with the case where there is no "extrinsic" delay (Case 1), in all three settings we are able to observe some modulation. However, it is worth noticing that the maximum overlap between the two sets of wavetrains happens for the case with no separation between the beams (c1). Also, a symmetric behaviour is observed: the amount of modulation observed when the two beams are laterally shifted in either direction by the same amount is similar.

In the second case, a positive "extrinsic" delay is introduced in the interferometer. Now, the symmetry no longer holds - in (a2) the intrinsic delay in conjunction with the extrinsic delay lead to no overlap between the two sets of diffracted wavetrains, which means that no modulation is observed. On the other hand, more intense interference is noticed in the case (b2), but not (c2). In other words, the positive extrinsic delays seem to be *favoured* in relation to the negative ones in terms of the strength of the modulation observed.

Lastly, in Case 3 a negative "extrinsic" delay is introduced in the interferometer, and now the *negative extrinsic delays are favoured* - (a3) now has the maximum modulation since it has the largest overlap, and no modulation whatsoever is

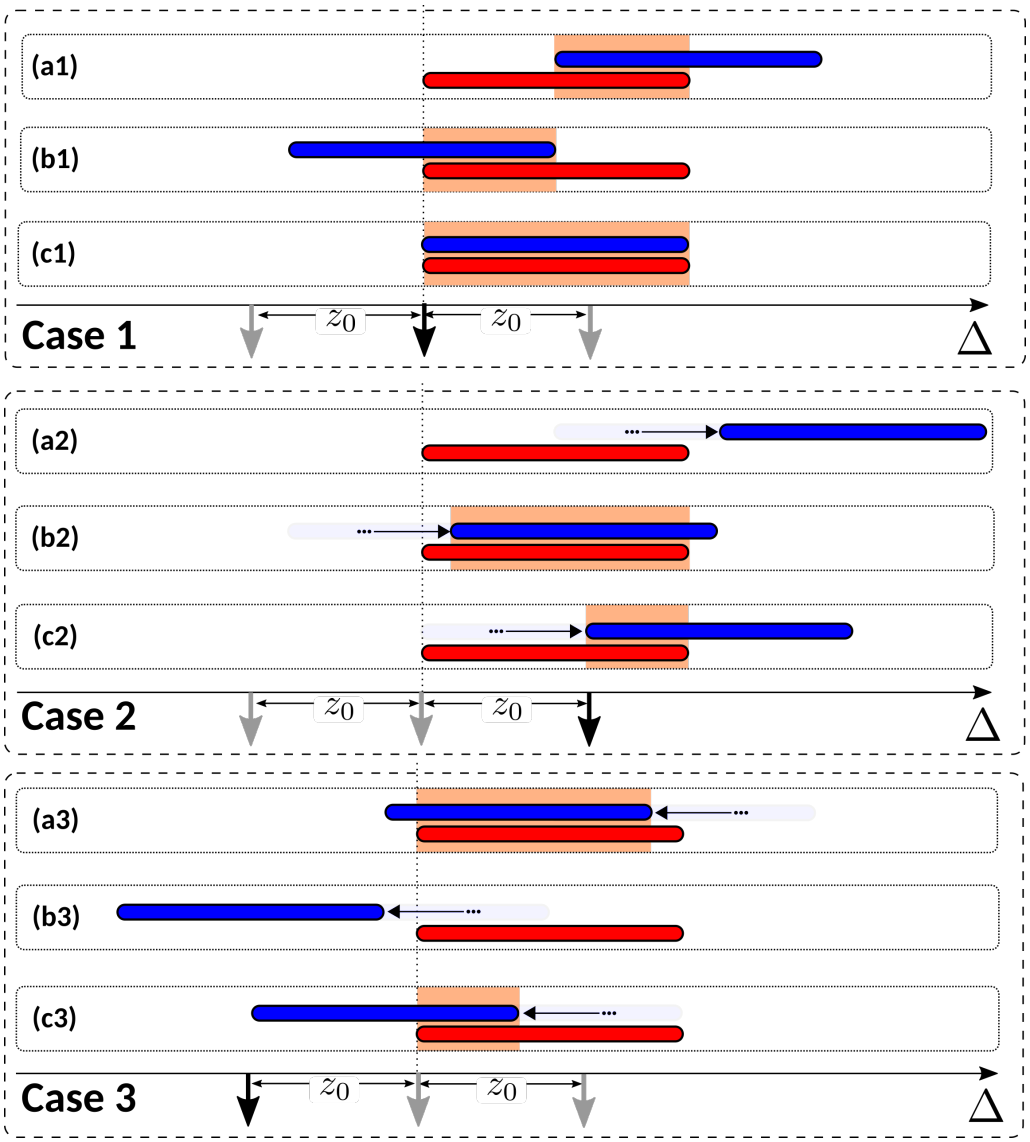

FIGURE 3.11: Analysis of Talbot Bands in a WLI using the wavetrain model, for the case described in Figures 3.9 and 3.10.

Case 1: interferometer has no "extrinsic" delay ($\Delta = 0$). **(a1)**, sample arm beam is shifted to the right of its original position; **(b1)**, sample arm beam is shifted to the left of its original position; **(c1)** sample arm launcher in the original position, making the sample and reference arm beams completely superposed.

Case 2: a positive "extrinsic" delay is introduced in the interferometer ($\Delta = z_0, z_0 > 0$). **(a2)**, sample arm beam is shifted to the right of its original position; **(b2)**, sample arm beam is shifted to the left of its original position; **(c2)**, sample arm beam and reference arm beam are completely superposed.

Case 3: a negative "extrinsic" delay is introduced in the interferometer ($\Delta = z_0, z_0 < 0$). **(a3)**, sample arm beam is shifted to the right of its original position; **(b3)**, sample arm beam is shifted to the left of its original position; **(c3)**, sample arm beam and reference arm beam are completely superposed.

The orange-shaded regions define the extent of the diffracted wavetrains which exhibit interference.

observed in (b3). It is also worth noticing that (c2) and (c3) exhibit similar modulation strengths, because the shift between the two diffracted wavetrains is the same.

3.2.1.3 Signal theory analysis

An equivalent manner of analysing the effect of beam overlap at the diffraction grating is to employ signal theory, which is the approach taken in [35, 39]. Let us assume that the beam profiles at the diffraction grating are given by the functions $C_s(l)$ and $C_r(l)$ which respectively represent the power from the sample and reference arms on each line l of the diffraction grating. References [35, 39] have shown that the visibility of the signal is determined by the cross-correlation of $C_s(l)$ and $C_r(l)$, written as:

$$\gamma(z) = \lambda_0 \sum_{l=1}^{\infty} C_s(l) C_r(l+z). \tag{3.10}$$

For simplicity, a normalisation constant has been ignored in the expression above. We can express $C_s(l)$ and $C_r(l)$ as a function of the actual (physical) lateral profile of the two beams, $S_s(l)$ and $S_r(l)$ respectively, and the grating pitch a:

$$C_s = \frac{S_s(l)}{a} \quad \text{and} \quad C_r = \frac{S_r(l)}{a}. \tag{3.11}$$

Since a is typically quite small ($1/a \sim 600 - 1,800$ lines/mm), we can approximate the summation in Equation (3.10) as an integral, yielding

$$\gamma(z) = \lambda_0 \left(C_s \star C_r\right), \tag{3.12}$$

where $\star$ denotes cross-correlation.

The relation between the equation above and the behaviour shown in the diagram present in Figure 3.11 should now be clear. If the two diffracted wavetrains completely overlap and present exactly the same FWHM, their convolution yields a perfectly symmetrical profile for the visibility around OPD = 0.

On the other hand, if one of the profiles is shifted laterally, that will equate to it being convolved with a Dirac delta at a nonzero position, i.e. $C'(l) = C(l) \otimes \delta\left(l - l_0\right)$, with l_0 being the amount of lateral shift introduced. By replacing one of the two C profiles by C', one will have $\gamma(z) \otimes \delta\left(l - l_0\right)$, hence the visibility profile is also shifted and is no longer symmetric in relation to OPD = 0. This is the case for sub-figures (b1-3) and (c1-3) in Figure 3.11.

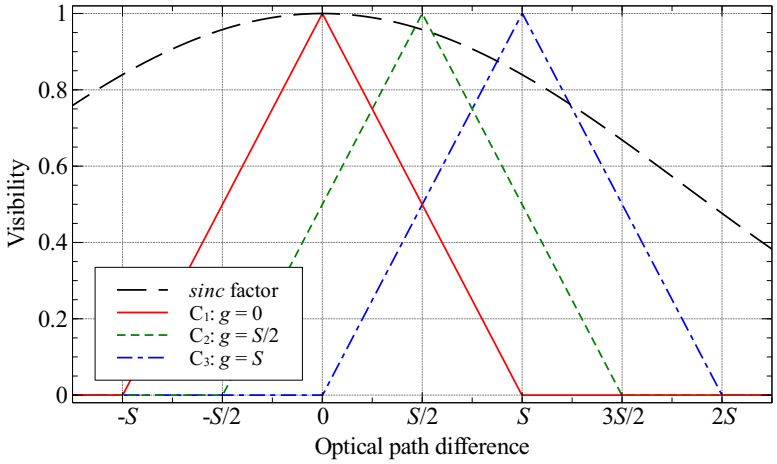

FIGURE 3.12: Numerical simulation for the visibilities observed in a conventional spectral-domain white light interferometer and in one employing Talbot bands effect (graph taken from Marques *et al.* [46]). In this simulation, the beams were assumed as top-hats with diameter $S = 4\,\mathrm{mm}$, with a varying gap size g between them, expressed as a function of the beam diameter. The black dashed curve represents the contribution from the resolution limit of the detector array, as modelled in Equation (3.2).

In Figure 3.12 visibility profiles are simulated for several values of the gap g between the two footprints on the grating. The beam profiles were assumed to be flat-tops of width S, and after being correlated they generate a triangular profile whose location depends on the amount of shifting (gap g introduced) between the beam profiles. This effect is a more rigorous explanation of the first factor in the model presented by Hu *et al.* [32] in Equation (3.2). The shift of the visibility profile is multiplied with the second factor in Equation (3.2), as shown by the dashed black curve in Figure 3.12.

3.2.2 Sampling resolution of the line array

The model presented above only takes into consideration the effects of the diffraction grating and the relative position of the projection of the two beams upon it. As mentioned before, the sampling resolution of the line array also plays an important part in the overall axial range. The models presented by Hu *et al.* [32] and by Häusler *et al.* [2], do not take into consideration partially overlapping beams at the diffraction grating plane; moreover, they assume Gaussian profiles for the beams illuminating the diffracion grating. Hughes [39] has described a generalised expression for the sensitivity decay which combines all effects previously described; the main conclusions will now be presented here.

We now consider the interferometric component of the signal as given by Equation (2.40) in the previous chapter, and assume that there is only one scatterer in the sample arm. By doing some additional simplifications ($r_R = 1,\ r_S = \delta(l_S - z_0),\ n_S = 1,\ l_S - l_R = z_0$), and concentrating on the cross-interference term (represented in magenta in Equation (2.40)), we have the spectrum over the linear array described by:

$$I_{cc}(k) = S(k)\cos\left(2kz_0\right). \tag{3.13}$$

This assumes a linear spectrometer, where the display along the linear array is proportional to the wavenumber k. If we now consider pixel i in the line detector array, which is centred at position x_i, and consider that the projection of the different wavenumbers onto the detector array is already linear (as shown in Section 3.2.3, linearisation is a requirement for FD-OCT). Each wavenumber k_i is mapped to a position x_i by

$$k_i = Rx_i + k_0, \tag{3.14}$$

where R is the reciprocal linear dispersion (in wavenumbers), and k_0 is the wavenumber incident at one end of the detector array (the starting wavelength). By substituting this into Equation (3.13), we can now represent I_{cc} as a function of each pixel i in the detector array,

$$I_{cc}(i) = S(k_i)\cos\left(2k_iz_0\right). \tag{3.15}$$

Effectively, each pixel in the detector array receives the contribution of more than one grating line. This is linked to the extent of the beam projections over the diffraction grating; one can introduce a function $B(k)$, termed the point cross spectral density function, which we assume to be the same for each of the pixels. Equation (3.15) can then be re-written as:

$$I_{cc}(i) = \cos\left(2k_iz_0\right)\int_0^\infty S(k)B\left(k - k_i\right)dk, \tag{3.16}$$

or, since the integral effectively defines a convolution in k-space:

$$I_{cc}(i) = \cos\left(2k_iz_0\right)\left[S \otimes B\right]. \tag{3.17}$$

So far we have assumed that the pixels are infinitesimally narrow, but if we take them as having a width Δx, then the intensity that a pixel effectively "sees" is given by the integral of the equation above over the wavenumber range in

question, which is given by $R\Delta x$. If we model the shape of the pixel as a rectangular function $P(k)$, we can sample $I_{cc}(i)$ with $P(k)$ (taken as the response of the system), and the equation is then

$$I_{cc}(i) = \cos\left(2k_i z_0\right)\left[S \otimes B \otimes P\right]. \tag{3.18}$$

As before, by Fourier transforming the intensity one is able to retrieve the depth profile $A(z)$. Hence,

$$A(z) = \mathfrak{F}\left\{\cos\left(2k_i z_0\right)\left[S \otimes B \otimes P\right]\right\}, \tag{3.19}$$

and by taking the convolution property of the Fourier transform we finally obtain

$$A(z) \propto \delta(z \pm 2z_0) \otimes \left(\mathfrak{F}(S)\mathfrak{F}(B)\mathfrak{F}(P)\right). \tag{3.20}$$

This is the general expression for the OCT signal amplitude when a reflector is present at depth z_0. In Figure 3.13 a schematic representation of these terms is presented. Let us recall from the previous chapter that the axial resolution is given by the Fourier transform of the spectral density function, $\mathfrak{F}(S)$ (right-hand side graph in Figure 3.13 (a1)). By convolving $\mathfrak{F}(S)$ with the location of the reflector, which is given by the Dirac delta function $\delta\left(z \pm 2z_0\right)$ (as shown in the left-hand side graph in Figure 3.13 (a1)), one will introduce the effect of the coherence gate as presented before, which is schematically represented in Figure 3.13 (d).

$\mathfrak{F}(B)$ and $\mathfrak{F}(P)$ describe the fall-off with depth introduced by the spectrometer. Let us recall Equation (3.12) and apply the Wiener-Kintchin theorem. One can then express $B(k)$ as [39]:

$$B(k) = \mathfrak{F}^{-1}\left\{\gamma(z)\right\} = \left\{\lambda_0\left(C_s \star C_r\right)\right\}. \tag{3.21}$$

In Figure 3.13 (b1) the two beam profiles are depicted. As an approximation, they have been considered as rectangular functions, which after being correlated lead to a triangular profile (Figure 3.13 (b2)), which describes $\mathfrak{F}(B) = \mathfrak{F}\left\{\mathfrak{F}^{-1}\left\{\lambda_0\left(C_s \star C_r\right)\right\}\right\}$. If, as in Figure 3.11 (b1-3) and (c1-3), the two beams had been shifted in relation to each other, that would have horizontally moved the triangular profile and created the asymmetry already described, which has been illustrated in the simulations represented in Figure 3.12.

On the other hand, in Figure 3.13 (c1) the sampling function of the line detector array is depicted, which has been assumed to be a rectangular function whose

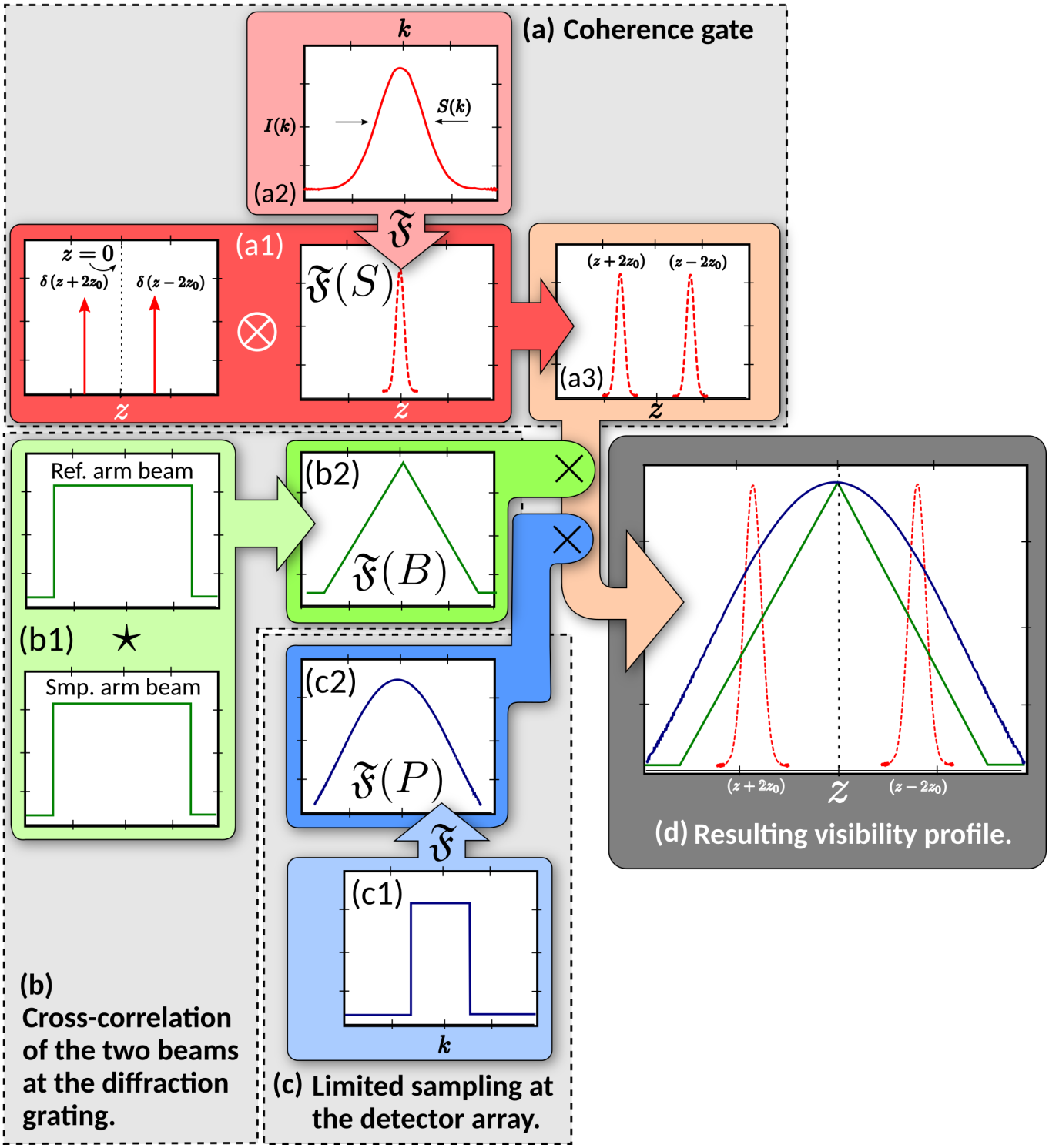

FIGURE 3.13: Schematic representation of the four terms of Equation (3.20). See text for details.

width represents the CCD wavelength pitch $\Delta\lambda/M$, corresponding to a projected optical bandwidth $\Delta\lambda$ over M pixels, as described in Bradu *et al.* [47]. If a top hat function is considered, then the Fourier transform of it leads to $\mathfrak{F}(P)$, which is effectively a *sinc* function ($\operatorname{sinc} x = \sin x/x$).

Finally, the plot of Equation (3.20) is represented in Figure 3.13 (e). Both the triangular and the *sinc* profiles influence the axial range of the system, whilst the optical bandwidth from the source dictates the axial resolution (the width of the peaks at $z = \pm 2z_0$).

Equation (3.20) can be further developed by taking into consideration the analytical definitions for both $B(k)$ and $P(k)$, finally arriving at

$$A(z) \propto \delta(z \pm 2z_0) \otimes \left[\lambda_0 \left(C_s \star C_r\right) \cdot \mathfrak{F}(S) \cdot \frac{\sin\left(\Delta x R z\right)}{\Delta x R z}\right]. \tag{3.22}$$

Expressing the equation above while considering the irradiance rather than the amplitude:

$$I_{\text{dropoff}}(z) \propto \left[\lambda_0 \left(C_s \star C_r\right)\right]^2 \left(\frac{\sin\left(\Delta x R z\right)}{\Delta x R z}\right)^2. \tag{3.23}$$

3.2.3 Linearisation in $\vec{k}$

The spectral signal delivered by both spectrometer-based OCT systems and tunable-source-based OCT systems does not vary linearly with the optical frequency. With some errors, the temporal axis of the signal read by spectrometers is proportional to the wavelength. Wojtkowski *et al.* [6] was the first to report on the importance of proper wavelength assignment in FD-OCT. As stressed earlier in Subsection 3.2.1.3 it is imperative to have a signal uniformly sampled in the wavenumber $\vec{k}$ since this is Fourier pair of the depth coordinate z.

In the case of a spectrometer using a diffraction grating in transmission, with the incident beam normal to the grating (such as the configuration schematically represented in Figure 3.2), the position x as a function of the wavenumber k can be given by [39]

$$x(k) = L \tan\left[\sin^{-1}\left(\frac{2\pi}{ka}\right)\right], \tag{3.24}$$

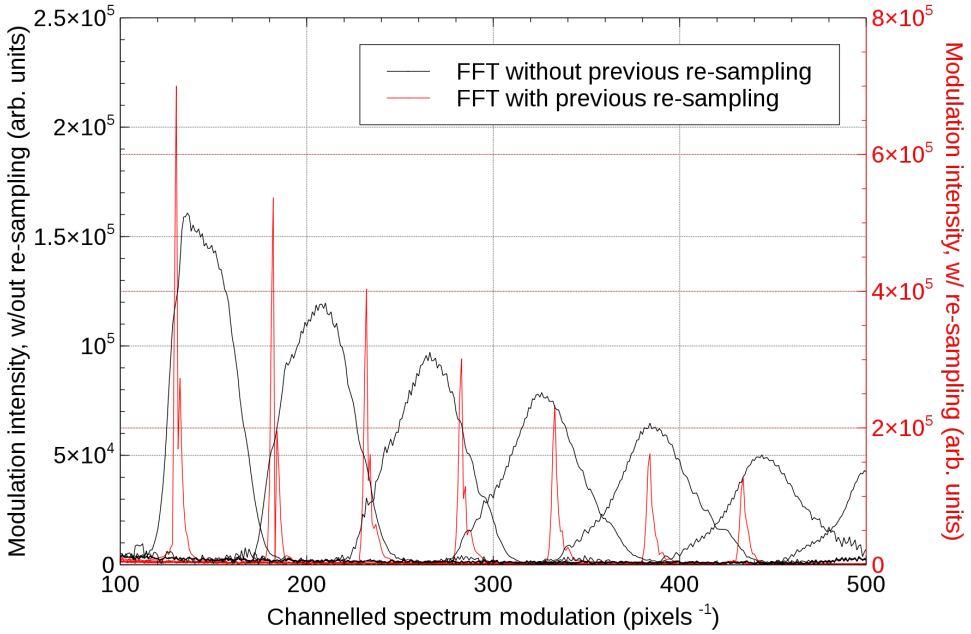

FIGURE 3.14: Representation of the PSF corresponding to a metallic mirror (assumed to be a perfect reflector) in the sample arm for various OPD settings, for the case with (red trace, right y-axis) and without (black trace, left y-axis) previous re-sampling of the incoming spectra. This data was produced with a SD-OCT system based upon a Michelson interferometer, illuminated by a super-continuum source (NKT Photonics) at $\lambda_0 = 830\,\mathrm{nm}$ with an optical bandwidth of $120\,\mathrm{nm}$ [48]. The calibration algorithm employed is based on that reported by Makita [49] and used to process the experimental data throughout Chapters 5–7.

where L is the distance between the diffraction grating and the linear detection array, and a is the grating pitch. From this expression it is evident that the pixels in the detector will not be mapped to a linear distribution in k.

If the incoming spectra after digitisation are Fourier transformed whilst not being linearly sampled in k, a progressive broadening of the PSF function with the OPD is to be expected [6], in a way that is not too dissimilar to that observed when dispersion is present in the system [50], even when a perfect reflector is employed as the sample. This effect can be observed in Figure 3.14. This shows a comparison of the PSFs between the cases with (red trace) and without (black trace) correct previous resampling of the incoming spectra for different OPDs, with a mirror being employed as a sample. In this case, a wide bandwidth source ($120\,\mathrm{nm}$ optical bandwidth centred at $\lambda_0 = 830\,\mathrm{nm}$) was used in a SD-OCT system based on a Michelson interferometer. It can be seen that the peak widths in the black trace increase with the OPD, i.e. the larger the OPD, the worse the axial resolution. Due to the peak widening, its height is comparably lower than that of the data set where previous re-sampling has been carried out, thus diminishing

the SNR as well. The effect is still fairly visible at lower OPD values as well due to the fact that there is some uncompensated dispersion in this system, which leads to a broadening of the PSF, as will be shown in Section 3.3.

To perform the re-sampling operation, several strategies have been proposed in the literature. Some of them involve hardware-based methods: in 1990, Traub [51] reported the use of a grism, which is a combination of a diffraction grating and a prism with opposite dispersion slopes, therefore linearising the dispersed spectra in hardware. Another method reported by Payne *et al.* in 2012 [52] employs a spectrometer equipped with an analogue camera. The camera is clocked with a data transfer signal suitably chirped to compensate for the non-linearity in the optical signal distribution along the camera. In this way, the camera outputs a signal whose time delivery is proportional to $\vec{k}$.

Spectrometers for OCT based on tilted fibre Bragg gratings have been reported [53]; by modifying the fibre geometry it might be possible (although it has not been reported yet) to produce an already chirped spectral output which is then projected onto a linearly sampled detector, removing the need for post-acquisition re-sampling.

However, hardware-based methods for spectrometer-based OCT configurations have not been widely adopted; most solutions consist of dedicated signal processing procedures employing previously stored information, normally involving phase extraction along the data array for one or more given OPD values, when the object is a mirror.

The method employed in the later experimental chapters of this Thesis is based upon the one reported by Makita *et al.* [49, 54]. This method employs one high-visibility channelled spectrum with a single modulation frequency, extracting the phase and using that as a basis to create a set of evenly-spaced phases, which can then be used to interpolate the incoming data.

As before, the interferometric term can be expressed as in Equation (2.20), with a dependency on a co-sine function. One can then obtain the phase of this signal by using either the Hilbert transform or the Fourier transform method [55]. After re-transforming it back to the detection domain, we have a complex interference signal $\tilde{I}\left[k\left(x_i\right)\right]$ given by

$$\tilde{I}\left[k\left(x_i\right)\right] = S\left[k\left(x_i\right)\right]\sqrt{R_r R_s}\exp\left[j\phi\left(x_i\right)\right], \tag{3.25}$$

where $k\left(x_i\right)$ is the function mapping the wavenumbers into each pixel x_i in the detector, R_r and R_s are the reflection coefficients of the reference and sample arms

respectively, and $S\left[k\left(x_i\right)\right]$ is the source spectrum as a function of the wavenumber. The phase $\phi\left(x_i\right)$ can be expressed as

$$\phi\left(x_i\right) = 2k\left(x_i\right) z_0 = 2 \times 2\pi \frac{\nu\left(x_i\right)}{c} z_0, \tag{3.26}$$

where z_0 is the OPD (assuming free space in both arms of the interferometer). The phase is linearly proportional to the optical frequency ν ($1/\lambda = n\nu/c$, with $n = 1$ in this case), which is in turn a function of the pixel index x_i. Given this dependence, the newly generated set of evenly-spaced points, x_l', has to sample ϕ as a linear function. Inverting the function $\phi\left(x_i\right)$ and fitting it with a polynomial leads to a series representation of the pixel as a function of the local phase ϕ_i:

$$x\left(\phi_i\right) = a_0 + a_1\phi_i + a_2\phi_i^2 + a_3\phi_i^3 + \ldots \tag{3.27}$$

Re-sampling requires inference of the set of parameters $\{a_0, a_1, a_2, a_3, \ldots\}$. These parameters can be obtained by fitting. Once known, then they can be used to generate a regularly-spaced set of re-sampled locations, x_l',

$$x_l' = a_0 + a_1\left(\phi_0 + l\Delta\phi\right) + a_2\left(\phi_0 + l\Delta\phi\right)^2 + a_3\left(\phi_0 + l\Delta\phi\right)^3 + \ldots, \tag{3.28}$$

where $\Delta\phi$ is the phase step between each array element, and l is the array indexing variable. The saved set of evenly-spaced points for the pixel locations x_l' is then used for each acquired spectrum to perform an interpolation prior to the FFT operation. The interpolation operation allows the re-sampling of data from the original domain x_i to a corrected set in the domain x_l', stepped equally in wavenumber.

This interpolation can be carried out with many different algorithms, with the spline one being used on the data in the experiments described in this Thesis. The algorithm choice was a purely empirical one, selecting the algorithm which provided a more consistent axial resolution throughout the whole axial range.

One must stress the fact that this method may fail (or under-perform) for a large dispersion mismatch left uncompensated-for in the system. This mismatch introduces depth-dependent non-linearities in the interferometric phase, thus the assumptions taken before (in Equation (3.26)) are no longer valid. This is the case observed in the re-sampled data presented in Figure 3.14, where the peak widths are still increasing with depth, even after the re-sampling procedure has been applied. It is possible to compensate that mismatch either partially or fully, as shown in the next section.

A totally different signal processing technique for the spectra at the interferometer output, Master-Slave Interferometry, has been reported by Bradu *et al.* [56] and enhanced by Rivet *et al.* [57]. This method involves no hardware compensation techniques, instead relying on a comparison operation of the currently acquired spectra against a database of pre-recorded spectra. The comparison operation is based on correlation [58] or on a modified, faster, simplified correlation algorithm [56]. Since both entities to be compared (correlated) have been recorded with the same dispersion properties and by the same detector array (with the same non-linearity in $\vec{k}$) it is possible to directly achieve the theoretically expected axial resolution without the need for any compensation.

3.3 Dispersion effects in interferometer systems

The analysis carried out in Sections 2.1.2 and 2.1.3 of Chapter 2 does not take into account any material dispersion mismatch between the two interferometer arms. This introduces a group velocity dispersion (GVD) mismatch which leads to the broadening in the width of the interferometric autocorrelation function [59].

In Chapter 2 the propagation constants β_R and β_S were Taylor expanded versus wavenumber k around $\omega = \omega_0$, with only the terms up to the first order being retained. By including the second-order term into the series development, this takes into account the GVD:

$$\beta(\omega) = \beta(\omega_0) + \dot{\beta}(\omega_0)(\omega - \omega_0) + \frac{1}{2}\ddot{\beta}(\omega_0)(\omega - \omega_0)^2 + \mathcal{O}(\omega - \omega_0)^3, \qquad (3.29)$$

where the dot denotes a derivative operation in relation to ω and $\mathcal{O}(\omega - \omega_0)^3$ denotes higher-order terms. Let us now assume that a GVD mismatch is due to an accumulated length L of the OPD in addition to a first-order group delay given by a path length difference $2\Delta l$. The phase mismatch can be written in a similar form to that of Equation (2.11):

$$\Delta\phi(\omega) = \beta(\omega_0)(2\Delta l) + \dot{\beta}(\omega_0)(\omega - \omega_0)(2\Delta l) + \frac{1}{2}\ddot{\Delta\beta}(\omega_0)(\omega - \omega_0)^2(2L), \qquad (3.30)$$

where the higher-order terms have been omitted for clarity, and $\ddot{\Delta\beta}(\omega_0) = \ddot{\beta}_S(\omega_0) - \ddot{\beta}_R(\omega_0)$ is the GVD mismatch between the two paths of the interferometer. If the material dispersion is perfectly compensated-for in the interferometer, then this

term disappears (since $L = 0$) and the series development reduces to that presented in Chapter 2.

Inserting Equation (3.30) into the expression for the detected photo-current I_D (Equation (2.9)) and using the identities given in Equations (2.14) and (2.15), we obtain:

$$I_D \propto \Re\left\{\exp\left[-j\omega_0\Delta\tau_p\right]\int S\left(\omega-\omega_0\right)\exp\left[-j\frac{1}{2}\ddot{\Delta\beta}\left(\omega_0\right)\left(\omega-\omega_0\right)^2\left(2L\right)\right]\right.$$
$$\left.\exp\left[-j\left(\omega-\omega_0\right)\Delta\tau_g\right]\frac{d\left(\omega-\omega_0\right)}{2\pi}\right\}. \tag{3.31}$$

A similar approximation to that carried out in Section 2.1.3 can also be taken. Assuming a Gaussian-shaped spectrum (Equation (2.17)) and remembering the uncertainty relation between the standard deviations in the two domains (σ_τ time and σ_ω angular frequency), $\sigma_\tau\sigma_\omega = 1$, I_D simplifies to [59]

$$I_D \propto \frac{\sigma_\tau}{\Gamma(2L)}\exp\left[-\frac{\Delta\tau_g^2}{2\Gamma(2L)^2}\right]\exp\left[-j\omega_0\Delta\tau_p\right]. \tag{3.32}$$

Let us compare the equation above with Equation (2.19). The width of the Gaussian envelope is now given by the complex-valued parameter $\Gamma(2L)$, which is defined as

$$\Gamma(2L)^2 = \sigma_\tau^2 + j\ddot{\Delta\beta}\left(\omega_0\right)2L. \tag{3.33}$$

Following Hee's notation [59], a dispersion parameter τ_c can be defined as

$$\tau_c = \sqrt{\ddot{\Delta\beta}\left(\omega_0\right)2L}, \tag{3.34}$$

and by rearranging the terms in Equation (3.33):

$$\frac{1}{\Gamma(2L)^2} = \frac{\sigma_\tau^2}{\sigma_\tau^4+\tau_c^4} - j\frac{\tau_c^2}{\sigma_\tau^4+\tau_c^4}. \tag{3.35}$$

By using this expression for $\Gamma(2L)$ in Equation (3.32) it is now evident that a broadening of the Gaussian envelope is taking place:

$$I_D \propto \exp\left[-\frac{\Delta\tau_g^2}{2\Re\left\{\Gamma(2L)^2\right\}}\right] = \exp\left[-\Delta\tau_g^2\cdot\frac{1}{2}\left(\frac{1}{\sigma_\tau^2\left(1+\left(\frac{\tau_c}{\sigma_\tau}\right)^4\right)}\right)\right]. \tag{3.36}$$

The broadened standard deviation $\tilde{\sigma_\tau}$ can then be expressed as

$$\tilde{\sigma_\tau} = \sigma_\tau \sqrt{1 + \left(\frac{\tau_c}{\sigma_\tau}\right)^4}. \tag{3.37}$$

Assuming a GVD of $\ddot{\Delta}\beta = 350\,\mathrm{fs}^2/\mathrm{cm}$ for a fused silica fibre at $800\,\mathrm{nm}$ [59, 60] and a typical resolution of $\Delta l = 10\,\mu\mathrm{m}$, achieved by an OCT system operating at the said wavelength, $\sigma_\tau = 28\,\mathrm{fs}$. Therefore, a mismatch of more than $2L = 1\,\mathrm{mm}$ is enough to double the width of the coherence-limited Gaussian envelope.

A GVD mismatch also has an impact on the phase of the signal, since the parameter $\Gamma(2L)$ is complex-valued. The phase of the expression in Equation (3.32) is given by

$$\phi = \arg\left\{\exp\left[-j\left(\omega_0 \Delta\tau_p + \frac{\Delta\tau_g^2}{2}\frac{\tau_c^2}{\sigma_\tau^4 + \tau_c^4}\right)\right]\right\} \tag{3.38}$$

Considering again the identities in Equations (2.14) and (2.15), and by differentiating the phase with respect to Δl, one can quantify the amount of chirping introduced in the interferometric signal:

$$k = \frac{d\phi}{d(\Delta l)} = 2\beta\left(\omega_0\right) - \frac{\tau_c^2}{\sigma_\tau^4 + \tau_c^4} 4\dot{\Delta\beta}\left(\omega_0\right)^2 \Delta l \tag{3.39}$$

With no material dispersion, the spatial frequency of the fringes varies linearly with Δl (the value of the derivative is constant and equal to $2\beta\left(\omega_0\right)$). On the other hand, $\tau_c \neq 0$ will turn this expression into a non-linear relation which depends on Δl, introducing a chirp in the fringe distribution. Having a chirped channelled spectra means that some of the methods presented in the previous section to linearise the spectra in $\vec{k}$ will fail; hence it is paramount that the material dispersion is perfectly compensated for in OCT systems, especially those illuminated by sources with larger optical bandwidths.

Enlarging the width of the Gaussian envelope impacts the peak height, ultimately diminishing the SNR of the output signal. The decrease in the photocurrent amplitude can be described by [59]

$$\frac{\sigma_\tau}{|\Gamma(2L)|} = \frac{1}{\sqrt[4]{1+(\tau_c/\sigma_\tau)^4}}. \tag{3.40}$$

From Equation (3.40), the reduction in amplitude scales with the square root of the broadening factor, defined as the ratio τ_c/σ_τ between the dispersion parameter τ_c and the (unbroadened) standard deviation in the temporal width σ_τ. If the dynamic range is quantified in terms of optical power, then an additional power of two applies in the equation above, and the dynamic range scales linearly with the broadening factor [59].

3.3.1 Dispersion compensation mechanisms

The simplest way to compensate for the material dispersion mismatch in the system is to employ the exact same optical components in both arms [61]. A spectral scanning delay line employing a diffraction grating can also be used to provide dispersion compensation concurrently with group and phase delay scanning [62]. As a different procedure, mentioned in the previous section, the Master-Slave Interferometry (MSI) method [56–58] can be used, since it is tolerant to dispersion in the interferometer and avoids the need for compensation altogether.

However, these techniques are only applicable if the dispersion mismatch is stable - in case of any dispersion variability, then the system needs to be readjusted. When using MSI, new sets of masks need to be acquired. The problem is even more complex if the sample is dispersive, in which case dispersion varies with the depth interrogated in the sample. Dynamic, depth-dependent numerical dispersion compensation [63] is possible however, since one is able to access the fringes of the interferometric signal [61].

When performing retinal imaging, it is commonplace to insert a cuvette of $25\,\mathrm{mm}$ of water in the reference arm to compensate for the dispersion introduced by the ocular medium (namely, the vitreous humour filling up the ocular globe), since it has been shown [64] that the dispersive properties of water mimic those of the vitreous humour. Compensating for the dispersion due to the vitreous humour is more critical for obtaining high axial resolution than balancing the dispersion of the system itself [60].

3.4 Imaging in OCT systems

In order to perform imaging, the OCT beam probing the sample is scanned over it; alternatively, in a variant of OCT called full-field OCT [65], a collimated beam illuminates the sample and the resulting interferometric signal is detected by a two-dimensional camera, thus removing the need for scanning the beam. The full-field concept is also applicable to spectrometer-based OCT systems by using line illumination [66], in which case a 2-D camera can be used to deliver a B-scan image. Another method reported by Hüttmann's group [67] employs a swept-source in conjunction with a high-speed ($> 60,000$ fps) 2-D camera to obtain volumetric information without any scanning.

Scanning the probing beam over the sample is normally achieved with galvanometric scanners (galvo-scanners) or resonant scanning mirrors (these allow higher scanning speeds [68] but are less versatile due to the fixed resonance frequency). Moving the sample with a 2-D translation stage whilst keeping the probing beam stationary is another option, especially when increased transversal resolution is required, since the aberrations present are the same for all lateral pixels in the image.

In this section, different imaging modes are presented, along with the specifics of optical design of the interface optics in the sample arm, depending on the particular application of the OCT system in question.

3.4.1 Imaging modes

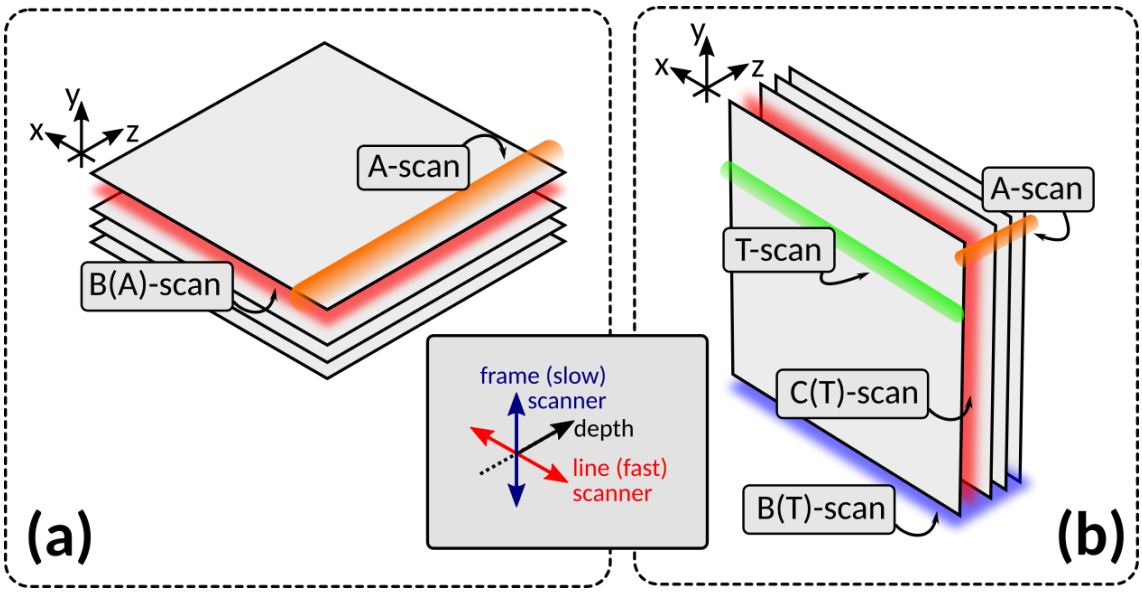

FIGURE 3.15: Imaging regimes used in OCT. **(a)**, depth priority; **(b)**, transversal scanning priority. Inset: representation of the different scanning axes.

Possible different scanning strategies to be employed in OCT imaging are represented in Figure 3.15. Sub-figures (a) and (b) represent the two priority modes: (a) depth priority mode (the depth profile is acquired prior to the transversal scan), and (b) transversal scanning priority mode (depth is fixed at a specific value and the transversal profile is being either 1- or 2-D acquired).

Let us assume that a dual scanning head is employed. One of the two scanners (the line scanner) is driven faster than the other, drawing a line over the surface of the sample. The other scanner only shifts the beam in a direction perpendicular to the line once the movement over the line has been completed. This is represented in the inset within Figure 3.15; for this case, x (horizontal) is the fast scanning axis and y (vertical) is the slow one.

With the advent of fast spectrometers and tunable sources, the transversal scanning priority mode lost ground, as the depth profile is acquired in a single spectral read (or source sweep), hence the depth is always prioritised.

A single depth scan is called an *A-scan* ("A" for amplitude, which corresponds to a reflectivity profile in depth). This is a one-dimensional structure, corresponding to a specific position of both the line and the frame scanner (for a selected lateral pixel). Another one-dimensional structure is the *T-scan* ("T" for transversal, which corresponds to a transversal reflectivity profile). A T-scan is obtained at a constant depth, with one of the two transversal scanners providing the movement and the other one remaining stationary. There is also the possibility of a constant-depth T-scan using both lateral scanners, where the beam is scanned circularly or elliptically over the target, for instance by applying signals with similar frequencies but with a phase difference of $\pi/2$.

A *B-scan* ("B" for brightness) is a bi-dimensional slice of the object, where one of its axis is *always* the depth coordinate. One can build a B-scan out of a series of adjacent A-scans (along the fast scanner's direction of movement), creating in that way a B(A)-scan. It is also possible to build a B-scan out of a series of adjacent T-scans acquired at different depths, creating a B(T)-scan. Fundamentally, these two structures represent the same information, albeit constructed differently.

It is also possible to obtain constant depth frames which represent a cross-section of the sample being imaged. These structures are called *C-scans*, and are normally composed of multiple T-scans stacked together, forming a C(T)-scan.

Three-dimensional volumes of data can also be produced by stacking together series of B(A)- or C(T)-scans. As soon as a full volume is acquired, this may be cut along any desired direction to provide any of the structures listed above, or any other customised slicing desired.

3.4.2 Lateral resolution considerations

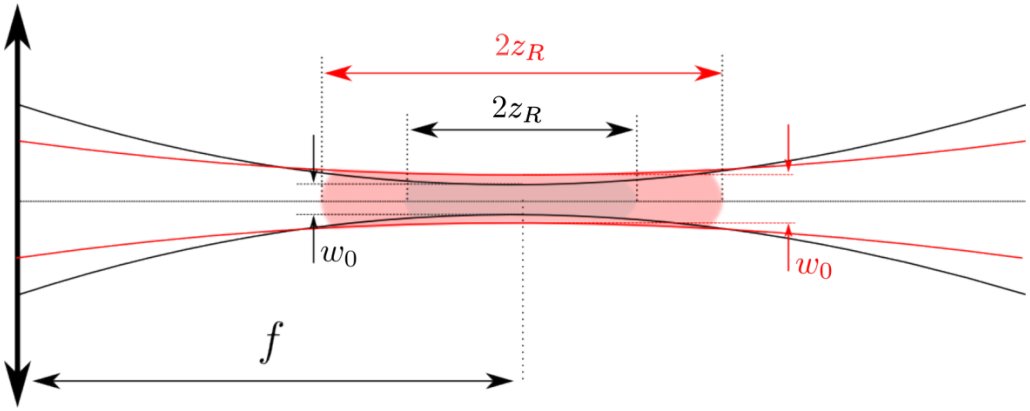

FIGURE 3.16: Effect of the numeric aperture (NA) of a lens on the confocal (Rayleigh) range and on the spot size w_0 (adapted from Marques [29]). Considering the same value of f, the black and red traces have different aperture values depending on different beam diameters which in turn influence z_R and w_0.

Both high lateral resolution and large depth of focus are important parameters to consider when designing an OCT imaging system. Unfortunately, these two parameters are inversely related - increasing the lateral resolution will involve employing larger NA interface optics, which will in turn diminish the depth of focus. This can be appreciated in the diagram within Figure 3.16, where two beams traversing optics with different NA are represented.

If we assume that the beam illuminating the sample is Gaussian, we can define the depth of focus z_0 as being twice the Rayleigh range, $z_R = \frac{\pi w_0^2}{\lambda}$,

$$z_0 = 2z_R = \frac{2\pi w_0^2}{\lambda}, \tag{3.41}$$

where w_0 is the beam waist at the focus (located at distance f from the lens) and λ is the wavelength.

The Rayleigh range is defined as the distance between the focal point (where the beam waist is equal to w_0) and the point where the waist becomes $\sqrt{2}w_0$. Again, for a Gaussian beam the dependence of the waist size $w(z)$ on z (the axial coordinate) is given by [69]

$$w(z) = w_0\sqrt{1 + \left(\frac{\lambda}{\pi w_0}z\right)^2},$$

or

$$w(z) = w_0\sqrt{1+\left(\frac{z}{z_R}\right)^2}. \tag{3.42}$$

At a large distance ($z/z_R \gg 1$), w increases linearly with z, hence it is possible to quantify the beam divergence as $\theta_d = w/z$ [69], obtaining

$$\theta_d = \frac{\lambda}{\pi w_0}. \tag{3.43}$$

We can relate θ_d with the NA of the interface optics, since $\mathrm{NA} = \sin\theta_d$ [70]. For low NA, the beam will diverge less (θ_d will be smaller), hence for the same f we shall have a larger w_0, hence a larger diffraction-limited spot size (which will decrease the lateral resolution). On the other hand, since $z_R \propto w_0^2$, the depth of focus increases. Conversely, if a better lateral resolution is desired, higher NA optics are necessary, which narrows w_0 but necessarily decreases z_0.

In TD-OCT a technique known as dynamic focus [71] can be used to preserve the same lateral resolution irrespective of depth. However, dynamic focusing is not possible to implement in FD-OCT systems, since the whole depth profile is acquired in a single spectral read. To compensate for this problem, three possible solutions have been proposed. (i) division of the object beam into several axially shifted optical apertures, each with a different focus position [72]; (ii) Gabor fusion [73], where the acquisition is repeated for a number of foci adjustments; and (iii) numerical refocusing with lensless imaging [67].

3.4.3 Optical design for the sample arm

In Figure 3.17 three different sample arm designs are represented. In (a) the whole optical assembly is translated, allowing the beam to be scanned over the region being studied. Alternatively, the sample can also be translated in relation to the optical system, achieving the same effect.

On the other hand, both (b) and (c) involve the use of one (or two) scanning mirrors, which can be attached to a galvanometric or resonant scanner. The main difference between them is the kind of sample they are designed to image. Configuration (b) is the standard scanning microscope configuration, in which the beam is scanned over the surface of the objective lens, creating a raster pattern over the surface. However, such a configuration would not work when performing retinal imaging, since the human eye has a fairly limited aperture ($< 7\,\mathrm{mm}$)

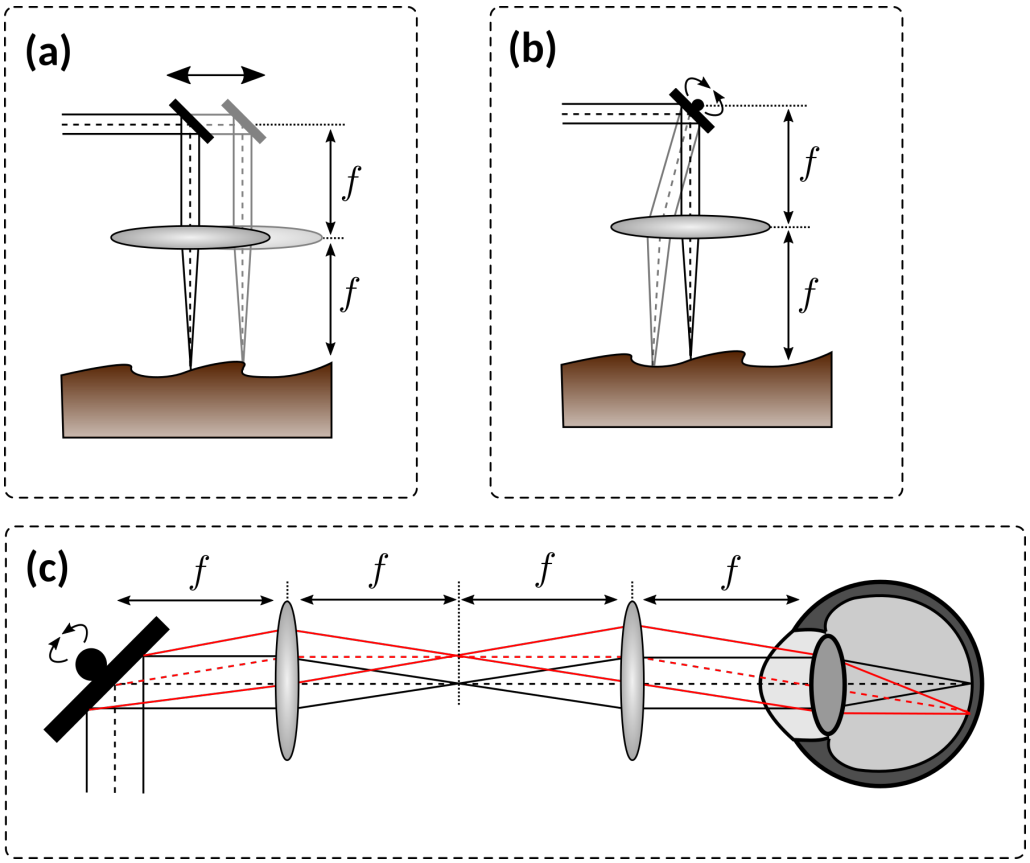

FIGURE 3.17: Different sample arm designs for OCT systems. **(a)**: the optical system or the sample are physically translated in relation to each other; **(b)**: the sample arm beam is scanned across the objective lens, which in turn scans the spot over the sample surface; **(c)**: modified sample arm configuration for retinal scanning, where the beam pivots through the eye's entrance pupil.

and the span of the region of interest in the retina exceeds $1\,\mathrm{cm}$.Hence, a telecentric configuration is employed, which ensures that the beam pivots through the entrance pupil instead of scanning over it. This is the configuration employed by the system described in Chapter 5 (and reported in [74]). To reduce the beam diameter at the pupil, the two lenses can have different focal lengths.

References

[1] A. F. Fercher, C. K. Hitzenberger, G. Kamp, and S. Y. El-Zaiat, "Measurement of intraocular distances by backscattering spectral interferometry", *Optics Communications*, vol. 117, no. 1, pp. 43–48, 1995.

[2] G. Häusler, M. W. Lindner, *et al.*, "'coherence radar" and "spectral radar"—new tools for dermatological diagnosis", *Journal of biomedical optics*, vol. 3, no. 1, pp. 21–31, 1998. [Online]. Available: http://biomedicaloptics.spiedigitallibrary.org/article.aspx?articleid=1101159.

[3] J. F. De Boer, B. Cense, B. H. Park, M. C. Pierce, G. J. Tearney, and B. E. Bouma, "Improved signal-to-noise ratio in spectral-domain compared with time-domain optical coherence tomography", *Optics letters*, vol. 28, no. 21, pp. 2067–2069, 2003. [Online]. Available: http://www.osapublishing.org/abstract.cfm?uri=OL-28-21-2067;%20http://www.osapublishing.org/viewmedia.cfm?uri=ol-28-21-2067&seq=0.

[4] R. Leitgeb, C. K. Hitzenberger, A. F. Fercher, *et al.*, "Performance of fourier domain vs. time domain optical coherence tomography", *Opt. Express*, vol. 11, no. 8, pp. 889–894, 2003.

[5] M. Choma, M. Sarunic, C. Yang, and J. Izatt, "Sensitivity advantage of swept source and fourier domain optical coherence tomography", *Optics express*, vol. 11, no. 18, pp. 2183–2189, 2003. [Online]. Available: http://www.osapublishing.org/abstract.cfm?uri=oe-11-18-2183;%20http://www.osapublishing.org/viewmedia.cfm?uri=oe-11-18-2183&seq=0.

[6] M. Wojtkowski, R. Leitgeb, A. Kowalczyk, T. Bajraszewski, and A. F. Fercher, "In vivo human retinal imaging by fourier domain optical coherence tomography", *Journal of biomedical optics*, vol. 7, no. 3, pp. 457–463, 2002. [Online]. Available: http://biomedicaloptics.spiedigitallibrary.org/article.aspx?articleid=1101514.

[7] J. G. Fujimoto and W. Drexler, "Introduction to oct", in *Optical Coherence Tomography: Technology and Applications*, W. Drexler and J. G. Fujimoto, Eds., 2nd ed., Springer, 2015, ch. 1.

[8] R. Bracewell, *The Fourier Transform and its Applications*, Second. Tokyo: McGraw-Hill Kogakusha, Ltd., 1978.

[9] R. A. Leitgeb, C. K. Hitzenberger, A. F. Fercher, and T. Bajraszewski, "Phase-shifting algorithm to achieve high-speed long-depth-range probing by frequency-domain optical coherence tomography", *Optics letters*, vol. 28, no. 22, pp. 2201–2203, 2003. [Online]. Available: https://www.osapublishing.org/abstract.cfm?uri=OL-28-22-2201.

[10] J. A. Izatt, M. A. Choma, and A.-H. Dhalla, "Theory of optical coherence tomography", in *Optical Coherence Tomography: Technology and Applications*, W. Drexler and J. G. Fujimoto, Eds., 2nd ed., Springer, 2015, ch. 2.

[11] M. Wojtkowski, A. Kowalczyk, R. Leitgeb, and A. F. Fercher, "Full range complex spectral optical coherence tomography technique in eye imaging.", *Opt. Lett.*, vol. 27, no. 16, pp. 1415–1417, 2002, ISSN: 0146-9592. DOI: 10.1364/OL.27.001415.

[12] P. Targowski, I. Gorczyńska, M. Szkulmowski, M. Wojtkowski, and A. Kowalczyk, "Improved complex spectral domain oct for in vivo eye imaging", *Opt. Commun.*, vol. 249, no. 1-3, pp. 357–362, 2005, ISSN: 00304018. DOI: 10.1016/j.optcom.2005.01.016.

[13] P. Targowski, M. Wojtkowski, A. Kowalczyk, T. Bajraszewski, M. Szkulmowski, and I. Gorczyńska, "Complex spectral oct in human eye imaging in vivo", *Opt. Commun.*, vol. 229, no. 1-6, pp. 79–84, 2004, ISSN: 00304018. DOI: 10.1016/j.optcom.2003.10.041.

[14] E. Gotzinger, M. Pircher, R. Leitgeb, and C. Hitzenberger, "High speed full range complex spectral domain optical coherence tomography", *Opt. Express*, vol. 13, no. 2, pp. 583–594, 2005.

[15] J. Zhang, J. S. Nelson, and Z. Chen, "Removal of a mirror image and enhancement of the signal-to-noise ratio in fourier-domain optical coherence tomography using an electro-optic phase modulator", *Opt. Lett.*, vol. 30, no. 2, pp. 147–149, 2005.

[16] M. A. Choma, C. Yang, and J. A. Izatt, "Instantaneous quadrature low-coherence interferometry with 3 x 3 fiber-optic couplers.", *Opt. Lett.*, vol. 28, no. 22, pp. 2162–2164, 2003, ISSN: 0146-9592. DOI: 10.1364/OL.28.002162.

[17] M. Sarunic, M. A. Choma, C. Yang, and J. A. Izatt, "Instantaneous complex conjugate resolved spectral domain and swept-source oct using 3x3 fiber couplers.", *Opt. Express*, vol. 13, no. 3, pp. 957–967, 2005, ISSN: 1094-4087. DOI: 10.1364/OPEX.13.000957.

[18] M. V. Sarunic, B. E. Applegate, and J. A. Izatt, "Real-time quadrature projection complex conjugate resolved fourier domain optical coherence tomography", *Opt. Lett.*, vol. 31, no. 16, pp. 2426–2428, 2006, ISSN: 0146-9592. DOI: 10.1364/OL.31.002426.

[19] Y. Yasuno, S. Makita, T. Endo, G. Aoki, M. Itoh, and T. Yatagai, "Simultaneous b-m-mode scanning method for real-time full-range fourier domain optical coherence tomography.", *Appl. Opt.*, vol. 45, no. 8, pp. 1861–1865, 2006, ISSN: 0003-6935. DOI: 10.1364/AO.45.001861.

[20] R. A. Leitgeb, R. Michaely, T. Lasser, and S. C. Sekhar, "Complex ambiguity-free fourier domain optical coherence tomography through transverse scanning.", *Opt. Lett.*, vol. 32, no. 23, pp. 3453–3455, 2007, ISSN: 0146-9592. DOI: 10.1364/OL.32.003453.

[21] H. Bian and W. Gao, "Stage-based frequency-modulated full-range complex fourier-domain optical coherence tomography", *Opt. Rev.*, 2015, ISSN: 1340-6000. DOI: 10.1007/s10043-015-0126-1. [Online]. Available: http://link.springer.com/10.1007/s10043-015-0126-1.

[22] S. Yun, G. Tearney, J. de Boer, and B. Bouma, "Removing the depth-degeneracy in optical frequency domain imaging with frequency shifting.", *Opt. Express*, vol. 12, no. 20, pp. 4822–4828, 2004, ISSN: 1094-4087. DOI: 10.1364/OPEX.12.004822.

[23] A. M. Davis, M. a. Choma, and J. a. Izatt, "Heterodyne swept-source optical coherence tomography for complete complex conjugate ambiguity removal", *J. Biomed. Opt.*, vol. 10, no. 6, p. 064 005, 2005, ISSN: 10833668. DOI: 10.1117/1.2136147.

[24] A. Bachmann, R. Leitgeb, and T. Lasser, "Heterodyne fourier domain optical coherence tomography for full range probing with high axial resolution.", *Opt. Express*, vol. 14, no. 4, pp. 1487–1496, 2006, ISSN: 1094-4087. DOI: 10.1364/OE.14.001487.

[25] B. J. Vakoc, S. H. Yun, G. J. Tearney, and B. E. Bouma, "Elimination of depth degeneracy in optical frequency-domain imaging through polarization-based optical demodulation", *Opt. Lett.*, vol. 31, no. 3, pp. 362–364, 2006, ISSN: 0146-9592. DOI: 10.1364/OL.31.000362.

[26] S. M. R. Motaghian Nezam, B. J. Vakoc, A. E. Desjardins, G. J. Tearney, and B. E. Bouma, "Increased ranging depth in optical frequency domain imaging by frequency encoding.", *Opt. Lett.*, vol. 32, no. 19, pp. 2768–70, 2007, ISSN: 0146-9592. DOI: 10.1364/OL.32.002768. [Online]. Available: http://www.pubmedcentral.nih.gov/articlerender.fcgi?artid=2703590%7B%5C&%7Dtool=pmcentrez%7B%5C&%7Drendertype=abstract.

[27] D. J. Fechtig, T. Schmoll, B. Grajciar, W. Drexler, and R. A. Leitgeb, "Line-field parallel swept source interferometric imaging at up to 1 mhz", *Opt. Lett.*, vol. 39, no. 18, p. 5333, 2014, ISSN: 0146-9592. DOI: 10.1364/OL.39.005333. [Online]. Available: http://www.opticsinfobase.org/abstract.cfm?URI=ol-39-18-5333.

[28] H. F. Talbot, "An experiment on the interference of light", *Philos. Mag*, vol. 10, p. 364, 1837.

[29] M. J. Marques, "Experiments in spectrometer-based , fourier-domain optical coherence tomography", MSc thesis, Faculdade de Ciencias da Universidade do Porto, 2012.

[30] A.-H. Dhalla, D. Nankivil, and J. a. Izatt, "Complex conjugate resolved heterodyne swept source optical coherence tomography using coherence revival", *Biomed. Opt. Express*, vol. 3, no. 3, p. 633, 2012, ISSN: 2156-7085. DOI: 10.1364/BOE.3.000633.

[31] S. Yun, G. Tearney, B. Bouma, B. Park, and J. de Boer, "High-speed spectral-domain optical coherence tomography at 1.3 μm wavelength", *Optics Express*, vol. 11, no. 26, p. 3598, Dec. 2003, ISSN: 1094-4087. DOI: 10.1364/oe.11.003598. [Online]. Available: http://dx.doi.org/10.1364/OE.11.003598.

[32] Z. Hu, Y. Pan, and A. M. Rollins, "Analytical model of spectrometer-based two-beam spectral interferometry", *Applied optics*, vol. 46, no. 35, pp. 8499–8505, 2007. [Online]. Available: http://www.osapublishing.org/ao/fulltext.cfm?uri=ao-46-35-8499&id=148372.

[33] A. G. Podoleanu and D. Woods, "Power-efficient fourier domain optical coherence tomography setup for selection in the optical path difference sign using talbot bands", *Opt. Lett.*, vol. 32, no. 16, pp. 2300–2302, 2007.

[34] A. G. Podoleanu, "Unique interpretation of talbot bands and fourier domain white light interferometry", *Opt. Express*, vol. 15, no. 15, pp. 9867–9876, 2007.

[35] D. Woods and A. G. Podoleanu, "Controlling the shape of talbot bands' visibility", *Opt. Express*, vol. 16, no. 13, pp. 9654–9670, 2008.

[36] D. Woods, "Selection in depth in fourier domain optical coherence tomography", PhD thesis, University of Kent, Mar. 2008.

[37] A. G. Podoleanu, S. R. Taplin, D. J. Webb, and D. A. Jackson, "Talbot-like bands for a laser diode below threshold", *Pure Appl. Opt. J. Eur. Opt. Soc. Part A*, vol. 6, p. 413, 1997.

[38] A. G. Podoleanu, S. R. Taplin, D. J. Webb, and D. A. Jackson, "Theoretical study of talbot-like bands observed using a laser diode below threshold", *Pure Appl. Opt. J. Eur. Opt. Soc. Part A*, vol. 7, p. 517, 1998.

[39] M. Hughes, "Optical coherence tomography for art conservation and archaeology: methods and applications", PhD thesis, University of Kent, 2010.

[40] E. Hecht, *Optics*, 4th ed. Addison Wesley, 2002, ch. 10.

[41] A. A. Michelson and E. W. Morley, "On the relative motion of the earth and the luminiferous ether", *Am. J. Sci.*, vol. 34, no. 203, pp. 333–345, 1887.

[42] D. Brewster, "On a new property of light", British Asssociation for the Advancement of Science, vol. 7, Liverpool, Sep. 1837, pp. 12–13.

[43] D. Brewster, "On a new kind of polarity in homogeneous light", British Asssociation for the Advancement of Science, vol. 8, Newcastle, Aug. 1838, pp. 13–14.

[44] G. B. Airy, "Supplement to a paper" on the theoretical explanation of an apparent new polarity in light"", *Philosophical Transactions of the Royal Society of London*, vol. 131, pp. 1–10, 1841. [Online]. Available: http://rstl.royalsocietypublishing.org/content/131/1.full.pdf;%20http://www.jstor.org/stable/108237.

[45] S. C. Zilio, "Simultaneous thickness and group index measurement with a single arm low-coherence interferometer", *Opt. Express*, vol. 22, no. 22, p. 27 392, 2014, ISSN: 1094-4087. DOI: 10.1364/OE.22.027392. [Online]. Available: https://www.osapublishing.org/oe/abstract.cfm?uri=oe-22-22-27392.

[46] M. J. Marques, A. Bradu, and A. Podoleanu, "Two-grating talbot bands spectral-domain interferometer", *Optics letters*, vol. 40, no. 17, pp. 4014–4017, 2015.

[47] A. Bradu and A. G. Podoleanu, "Attenuation of mirror image and enhancement of the signal-to-noise ratio in a talbot bands optical coherence tomography system", *J. Biomed. Opt.*, vol. 16, p. 76 010, 2011.

[48] M. Maria, M. J. M. Marques, C. Costa, A. Bradu, T. Feuchter, L. Leick, and A. G. H. Podoleanu, "Broadband master-slave interferometry using a super-continuum source", *Optical Coherence Tomography and Coherence Domain Optical Methods in Biomedicine XX*, J. A. Izatt, J. G. Fujimoto, and V. V. Tuchin, Eds., Mar. 2016. DOI: 10.1117/12.2214753. [Online]. Available: http://dx.doi.org/10.1117/12.2214753.

[49] S. Makita, "High-speed spectral-domain optical coherence tomography and *In Vivo* human eye imaging", PhD thesis, University of Tsukuba, 2007.

[50] J. F. de Boer, "Spectral/fourier domain optical coherence tomography", in *Optical Coherence Tomography: Technology and Applications*, W. Drexler and J. Fujimoto, Eds., 2nd ed., Springer, 2015, ch. 5.

[51] W. A. Traub, "Constant-dispersion grism spectrometer for channeled spectra", *JOSA A*, vol. 7, no. 9, pp. 1779–1791, 1990. [Online]. Available: https://www.osapublishing.org/abstract.cfm?uri=josaa-7-9-1779.

[52] A. Payne and A. G. Podoleanu, "Direct electronic linearization for camera-based spectral domain optical coherence tomography", *Optics letters*, vol. 37, no. 12, pp. 2424–2426, 2012. [Online]. Available: http://www.osapublishing.org/ol/fulltext.cfm?uri=ol-37-12-2424&id=238355.

[53] S. Remund, A. Bossen, X. Chen, L. Wang, A. Adebayo, L. Zhang, B. Považay, and C. Meier, "Cost-effective optical coherence tomography spectrometer based on a tilted fiber bragg grating", *Optical Fibers and Sensors for Medical Diagnostics and Treatment Applications XIV*, I. Gannot, Ed., Feb. 2014. DOI: 10.1117/12.2039409. [Online]. Available: http://dx.doi.org/10.1117/12.2039409.

[54] S. Makita, T. Fabritius, and Y. Yasuno, "Full-range, high-speed, high-resolution 1-μm spectral-domain optical coherence tomography using bm-scan for volumetric imaging of the human posterior eye", *Optics express*, vol. 16, no. 12, pp. 8406–8420, 2008. [Online]. Available: https://www.osapublishing.org/abstract.cfm?uri=oe-16-12-8406.

[55] M. Takeda, H. Ina, and S. Kobayashi, "Fourier-transform method of fringe-pattern analysis for computer-based topography and interferometry", *J. Opt. Soc. Am.*, vol. 72, no. 1, p. 156, Jan. 1982, ISSN: 0030-3941. DOI: 10.1364/josa.72.000156. [Online]. Available: http://dx.doi.org/10.1364/JOSA.72.000156.

[56] A. Bradu, K. Kapinchev, F. Barnes, and A. Podoleanu, "Master slave en-face oct/slo", *Biomed. Opt. Express*, vol. 6, no. 9, p. 3655, Aug. 2015, ISSN: 2156-7085. DOI: 10.1364/boe.6.003655. [Online]. Available: http://dx.doi.org/10.1364/BOE.6.003655.

[57] S. Rivet, M. Maria, A. Bradu, T. Feuchter, L. Leick, and A. Podoleanu, "Complex master slave interferometry", *Optics Express*, vol. 24, no. 3, p. 2885, Feb. 2016, ISSN: 1094-4087. DOI: 10.1364/oe.24.002885. [Online]. Available: http://dx.doi.org/10.1364/OE.24.002885.

[58] A. G. Podoleanu and A. Bradu, "Master–slave interferometry for parallel spectral domain interferometry sensing and versatile 3d optical coherence tomography", *Optics Express*, vol. 21, no. 16, p. 19 324, Aug. 2013, ISSN: 1094-4087. DOI: 10.1364/oe.21.019324. [Online]. Available: http://dx.doi.org/10.1364/OE.21.019324.

[59] M. R. Hee, "Optical coherence tomography: theory", in *Handbook of Optical Coherence Tomography*, B. E. Bouma and G. J. Tearney, Eds., Marcel Dekker, 2002, ch. 2.

[60] W. Drexler, Y. Chen, A. D. Aguirre, B. Považay, A. Unterhuber, and J. G. Fujimoto, "Ultrahigh resolution optical coherence tomography", in *Optical Coherence Tomography: Technology and Applications*, W. Drexler and J. G. Fujimoto, Eds., 2nd ed., Springer, 2015, ch. 9.

[61] M. Wojtkowski, S. Vivek, T. Ko, J. Fujimoto, A. Kowalczyk, and J. Duker, "Ultrahigh-resolution, high-speed, fourier domain optical coherence tomography and methods for dispersion compensation.", *Opt Express*, vol. 12, no. 11, pp. 2404–22, May 2004.

[62] B. Golubovic, B. E. Bouma, G. J. Tearney, and J. G. Fujimoto, "Optical frequency-domain reflectometry using rapid wavelength tuning of a cr4+:forsterite laser", *Opt. Lett.*, vol. 22, no. 22, p. 1704, Nov. 1997, ISSN: 1539-4794. DOI: 10.1364/ol.22.001704. [Online]. Available: http://dx.doi.org/10.1364/OL.22.001704.

[63] A. Fercher, C. Hitzenberger, M. Sticker, R. Zawadzki, B. Karamata, and T. Lasser, "Numerical dispersion compensation for partial coherence interferometry and optical coherence tomography", *Optics Express*, vol. 9, no. 12, p. 610, Dec. 2001, ISSN: 1094-4087. DOI: 10.1364/oe.9.000610. [Online]. Available: http://dx.doi.org/10.1364/OE.9.000610.

[64] W. Drexler, C. Hitzenberger, A. Baumgartner, O. Findl, H. Sattmann, and A. F. Fercher, "Investigation of dispersion effects in ocular media by multiple wavelength partial coherence interferometry", *Experimental Eye Research*, vol. 66, no. 1, pp. 25–33, Jan. 1998.

[65] A. Dubois, K. Grieve, G. Moneron, R. Lecaque, L. Vabre, and C. Boccara, "Ultrahigh-resolution full-field optical coherence tomography", *Applied Optics*, vol. 43, no. 14, p. 2874, May 2004, ISSN: 1539-4522. DOI: 10.1364/ao.43.002874. [Online]. Available: http://dx.doi.org/10.1364/AO.43.002874.

[66] B. Grajciar, M. Pircher, A. F. Fercher, and R. A. Leitgeb, "Parallel fourier domain optical coherence tomography for in vivo measurement of the human eye", *Optics Express*, vol. 13, no. 4, p. 1131, 2005, ISSN: 1094-4087. DOI: 10.1364/opex.13.001131. [Online]. Available: http://dx.doi.org/10.1364/OPEX.13.001131.

[67] D. Hillmann, G. Franke, C. Lührs, P. Koch, and G. Hüttmann, "Efficient holoscopy image reconstruction", *Optics Express*, vol. 20, no. 19, p. 21 247, Sep. 2012, ISSN: 1094-4087. DOI: 10.1364/oe.20.021247. [Online]. Available: http://dx.doi.org/10.1364/OE.20.021247.

[68] C. Hitzenberger, P. Trost, P.-W. Lo, and Q. Zhou, "Three-dimensional imaging of the human retina by high-speed optical coherence tomography", *Optics Express*, vol. 11, no. 21, pp. 2753–2761, 2003. [Online]. Available: https://www.osapublishing.org/abstract.cfm?uri=OE-11-21-2753;%20https://www.osapublishing.org/abstract.cfm?uri=oe-11-21-2753.

[69] O. Svelto, *Principles of lasers*, 4th, ser. Springer, 2009, ISBN: 0-306-45748-2.

[70] M. Born and E. Wolf, *Principles of Optics: Electromagnetic Theory of Propagation, Interference and Diffraction of Light (7th Edition)*, 7th. Cambridge University Press, 1999, ISBN: 0521642221.

[71] J. Schmitt, S. Lee, and K. Yung, "An optical coherence microscope with enhanced resolving power in thick tissue", *Optics Communications*, vol. 142, no. 4, pp. 203–207, 1997. [Online]. Available: http://www.sciencedirect.com/science/article/pii/S0030401897002800.

[72] J. G. Fujimoto, J. A. Izatt, and V. V. Tuchin, Eds., *Image blending and speckle noise reduction in multi-beam OCT*, SPIE-Intl Soc Optical Eng, Feb. 2009. DOI: 10.1117/12.808575. [Online]. Available: http://dx.doi.org/10.1117/12.808575.

[73] P. Meemon, J. Widjaja, and J. P. Rolland, "Spectral fusing gabor domain optical coherence microscopy", *Opt. Lett.*, vol. 41, no. 3, p. 508, Jan. 2016, ISSN: 1539-4794. DOI: 10.1364/ol.41.000508. [Online]. Available: http://dx.doi.org/10.1364/OL.41.000508.

[74] M. J. Marques, A. Bradu, and A. G. Podoleanu, "Towards simultaneous talbot bands based optical coherence tomography and scanning laser ophthalmoscopy imaging", *Biomed. Opt. Express*, vol. 5, no. 5, p. 1428, Apr. 2014, ISSN: 2156-7085. DOI: 10.1364/BOE.5.001428.

Chapter 4

Polarisation-sensitive OCT systems

Contents

OCT can be regarded as a mature technology, having been already deployed commercially in some key areas, namely in the ophthalmic field. One of the fundamental aims of this Thesis is the development of additional OCT functionality. This chapter refers to polarisation-sensitive OCT (PS-OCT), which allows the measurement of the polarimetric properties of samples, namely their retardation and neutral optical axis orientation.

PS-OCT is often described as a contrast-enhancing technique [1] in OCT biomedical imaging, allowing one to distinguish between different types of tissue in ways that intensity-based OCT methods cannot [2]. More recently, there is a trend towards quantification of the polarimetric information; PS-OCT has gone beyond providing simply additional contrast to supplying more information on the morphology and composition of the tissue being imaged.

The polarisation state of the light can be affected by several light-tissue interaction mechanisms: birefringence, diattenuation and depolarisation. As presented below, not all of these mechanisms can be identified with PS-OCT.

Several kinds of tissues within the human eye (such as the corneal stroma, the sclera and the retinal nerve fibre layer) as well as muscle fibres, tendons, nerves, bones, cartilages and teeth are known for exhibiting birefringence [3]. As such, PS-OCT has been employed in many different applications, including anterior [2, 4–7] and posterior eye imaging [2, 8–11], skin imaging [12–15], burn depth and thermal damage assessment [16–20], dental imaging [21, 22], and atherosclerotic plaque characterisation within blood vessels [23–25].

A material is said to be birefringent if the real part of its refractive index is polarisation state-dependent [26], which causes an anisotropy in the propagation velocities of the waves corresponding to the different polarisation states. If we consider a linear, uniaxial, birefringent medium with a refractive index difference Δn between the two transversal directions (one parallel and another perpendicular to the optical axis of the material [1]), a phase retardation δ is created between the two polarisation states, given by [26]

$$\delta = \frac{2\pi \Delta n z}{\lambda}, \tag{4.1}$$

where z is the distance travelled through the medium, and λ is the optical wavelength. This phase retardation ultimately introduces a change in the polarisation state of the beam, which can be ultimately quantified by the PS-OCT system. Knowing the propagation length and having the phase retardation measurement enables quantification of the material birefringence.

As mentioned, a number of human tissues, such as tendon, muscle, nerve, bone, cartilage, teeth, and the retinal nerve fibre layer (RNFL) [28], are known to exhibit form birefringence [29], since these are laid out as organised linear structures [26].

If, however, Δn exhibits an imaginary component (as mentioned in the beginning of Chapter 2), a differentiated attenuation arises between the two orthogonal states. This property is termed diattenuation, quantified by a parameter denominated similarly as diattenuation d, that can be expressed by the ratio [30]

$$d = \frac{P_{\perp}^2 - P_{\parallel}^2}{P_{\perp}^2 + P_{\parallel}^2}, \tag{4.2}$$

where $P_{\perp}$ and $P_{\parallel}$ are the amplitude attenuation ratios of the electric fields perpendicular and parallel to the optic axis of the material, respectively. One can easily obtain these ratios P_i from the imaginary part κ_i of the (complex) index of refraction $\tilde{n_i} = n_i + j\kappa_i$ [26],

$$P_i = e^{-2\pi \kappa_i z/\lambda}, \tag{4.3}$$

[1] The optical axis of a uniaxial material is defined [27] as the direction of propagation along which a beam of light suffers no birefringence effects.

where z is the distance travelled through the diattenuating medium. Unlike birefringence, the amount of diattenuation does not scale linearly with the distance travelled, the above equation describes an exponential relation.

Lastly, a material can also alter the state of polarisation of light by changing its degree of polarisation (DoP). This parameter, which can vary between 0 and 1, determines how polarised the beam of light is - in the extreme case where the degree of polarisation is zero the polarisation state is completely random, which is the case after many accumulated scattering events [31]. Conversely, a fully polarised beam has a DoP equal to one.

To mathematically describe the states of polarised light and the mechanisms influencing them, one can use either the Jones [32] or the Müller-Stokes formalism. The former relies on amplitude measurements of the EM field, whilst the latter employs irradiance (intensity) measurements, providing a complete representation of the polarisation properties of light. It is possible to shift from the Jones to the Müller-Stokes formalism but the reverse is not possible, since the Jones formalism is unable to quantify the depolarisation of the light, and thus part of the information provided under the Müller-Stokes formalism would be lost. The Jones formalism applies to totally polarised light only.

PS-OCT can measure some of the properties listed above, albeit with some limitations, due to the fact that:

- OCT is a *coherent* method, therefore it cannot quantify the irradiance of the (incoherent) returned signal. This renders OCT unable to measure the depolarisation introduced by the medium.

- OCT is based on the selection of ballistic (single scattered) photons. With this in mind, any circular retardance or diattenuation introduced by the tissue will not be detected, since any sample arm design is necessarily a round-trip configuration.

- Also due to the round-trip configuration, any possible measurement of the retardance or orientation of the optical axis of the sample will be of its overall contribution; that is, if one wants to isolate in depth individual contributions of the different materials in the sample, complex computational methods are required [8, 33–37].

With these limitations in place, any sample analysed by a PS-OCT system must be considered as a linear retarder/diattenuator. Given the coherent nature of OCT imaging (relying on low-coherence interferometry), an amplitude-based representation of the polarisation states is obtained that can only account for fully

polarised states, hence the need to employ the Jones formalism. It is possible to extend the theoretical model to the Müller-Stokes formalism (usually referred to as Jones-Müller in the literature), but no information on the DoP can be inferred - thus, the degree of polarisation measured is always going to be equal to one, even if the medium is effectively depolarising. Incoherent methods, on the other hand, yield the Stokes vectors directly and are therefore able to give a measure of the DoP; however, these do not allow depth sectioning as possible in OCT imaging through coherence gating.

It is possible to quantify how uniform the medium is in terms of its polarimetric properties by employing a metric defined as the degree of polarisation uniformity (DoPU) [38] which relies on performing a spatial averaging of the Stokes vectors within a region. It has been hinted by Götzinger *et al.* [38] that this property has relations to the degree of polarisation which can be measured with incoherent methods, although some care has to be taken into resolving any ambiguities that may arise from its computation from a single polarisation state [39]. This will be briefly mentioned in Section 4.1.2.

In the following section, a brief introduction to Jones formalism is presented, using as an example the first PS-OCT system reported [40] (by Hee *et al.* in 1992), with the theory behind its operation being extensively covered in a book chapter by Hitzenberger and Pircher [28]. This will be followed by a short introduction to the Müller-Stokes formalism, namely on how one is able to apply such formalism to a coherent method such as OCT, and what kind of additional sample polarimetric information it provides.

4.1 Mathematical formalism: Jones vectors and matrices

As previously mentioned, the Jones formalism can be applied to the calculation of polarisation states of fully polarised beams (it cannot accommodate partially or completely unpolarised light).

Let us consider a beam linearly polarised along $\hat{y}$ (the hat in $\hat{y}$ denotes a unitary vector along the y-direction), . Its electric field is given by $\tilde{\mathbf{E}} = \tilde{E}\hat{y} = E_0 \exp(j\omega t)\hat{y}$[2], where E_0 is the field amplitude[3], and ω is the angular frequency. In Jones formalism, one employs a complex-valued column matrix to describe the

[2]In this chapter, bold font represents vector notation, and the tilde ($\sim$) a complex number.

[3]For simplification purposes, we shall ignore the oscillating term and set $E_0 = 1$ in the analysis that follows.

two orthogonal polarisation states (which in this case are defined along $\hat{x}$ and $\hat{y}$). $\tilde{\mathbf{E}}$ is then defined as

$$\tilde{\mathbf{E}} = \tilde{E} \begin{bmatrix} 0 \\ 1 \end{bmatrix}. \tag{4.4}$$

The above column matrix is a Jones vector, and it fully describes the polarisation state of the light (minus the limitations already mentioned). Any modification in the polarisation state of the light can be formally expressed by a product of a 2×2 (also complex-valued) matrix by the column matrix. The square matrix (defined as a *Jones matrix*) describes the polarisation response of the optical element being considered. In the case where many optical elements are considered, one can simply calculate the product of the various Jones matrices, ordered in the direction of the propagation of the light beam.

A few examples of Jones matrices for polarisation elements can be found in Appendix B. As an example (taken from [41]), the Jones matrix of a general linear retarder of retardation δ and fast axis orientation θ is given by

$$\mathbf{J}_{\text{ret}}(\delta, \theta) = \begin{bmatrix} \cos^2\theta + \sin^2\theta \cdot \exp(-j\delta) & \cos\theta \cdot \sin\theta \cdot (1 - \exp(-j\delta)) \\ \cos\theta \cdot \sin\theta \cdot (1 - \exp(-j\delta)) & \cos^2\theta \cdot \exp(-j\delta) + \sin^2\theta \end{bmatrix}. \tag{4.5}$$

For a quarter-wave retarder oriented at $\theta = 45$ degrees, $\delta = \pi/2$, hence

$$\mathbf{J}_{\text{ret}}(\pi/2, \pi/4) = \frac{1}{2} \begin{bmatrix} 1-j & 1+j \\ 1+j & 1-j \end{bmatrix} \tag{4.6}$$

When applied to the Jones vector in Equation (4.4), we have

$$\frac{1}{2} \begin{bmatrix} 1-j & 1+j \\ 1+j & 1-j \end{bmatrix} \cdot \begin{bmatrix} 0 \\ 1 \end{bmatrix} = \frac{1}{2} \begin{bmatrix} 1+j \\ 1-j \end{bmatrix}. \tag{4.7}$$

Calculating the difference between the two phasors corresponding to the orthogonal components, leads to j, or a phasor angle of $\pi/2$. This means that one of the components is $\pi/2$ ahead of the other, which describes a specific elliptical polarisation state where the axes of the ellipse correspond to the axes of the basis considered. Moreover, since the moduli of both orthogonal components are equal, this Jones vector describes a circular polarisation state.

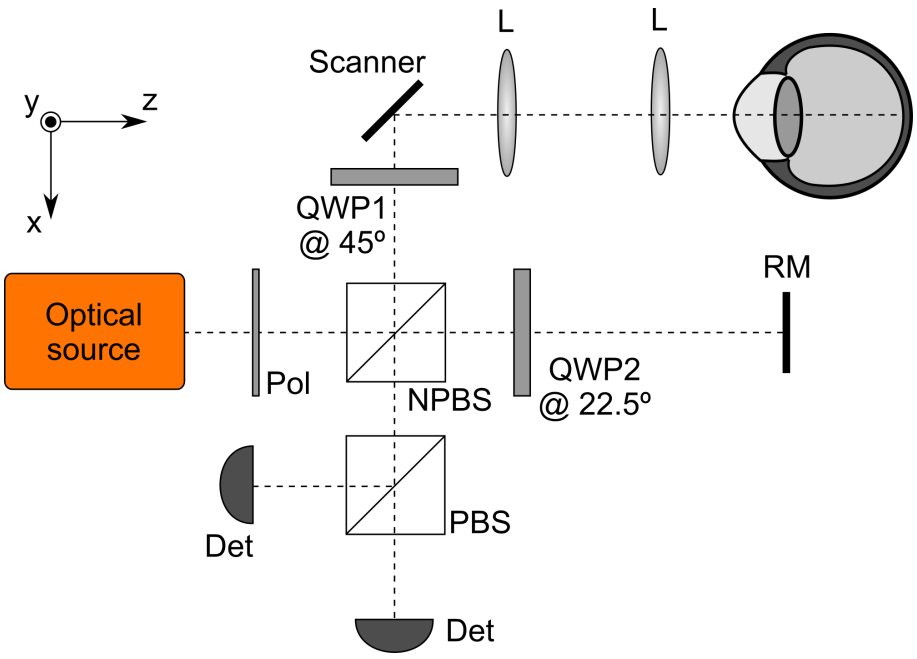

FIGURE 4.1: Schematic representation of the first PS-OCT set-up reported, adapted from Hee *et al.* [40]. NPBS, non-polarising beam-splitter; PBS, polarisation-sensitive beam-splitter; Pol, linear polariser oriented along $\hat{y}$; QWP1-2, quarter-wave plates (QWP1 oriented at 45º in relation to $\hat{y}$, QWP2 oriented at 22.5º in relation to $\hat{y}$); RM, reference mirror; L, lenses forming the telecentric retinal scanning configuration.

4.1.1 First PS-OCT system (1992)

Figure 4.1 shows a schematic representation of the first PS-OCT system, as reported by Hee *et al.* [40]. This uses a Michelson interferometer in a time-domain configuration; however, many of the systems that followed (including those presented in Chapter 7) share similar traits with this configuration.

The system is illuminated by a low-coherence source, a SLD in the case of the paper described. It is important to ensure a single, linear input polarisation state, hence a linear polariser Pol (oriented along $\hat{y}$) is placed immediately after the optical source output.

Light is then split between the two arms of the Michelson interferometer using a non-polarising beam-splitter (NPBS). It is important to illuminate the sample with circularly polarised light, since it ensures that the measurement of the sample retardation is independent of its optical axis orientation [28]. A circular polarisation state can be attained by using a quarter-wave plate (QWP1) oriented at 45 degrees in relation to $\hat{y}$, as mentioned in Section 4.1 in Equation (4.7). The rest of the sample arm design is similar to that employed for retinal imaging, which has been presented in Section 3.4.3.

When the sample interacts with the circularly polarised light, typically the polarisation state will shift from circular to elliptical, since an additional phase shift is introduced between the two orthogonal components. If the sample is assumed to be a linear, homogeneous retarder, with a retardation $\delta_s(z)$ and an axis orientation θ_s (which is considered constant with depth), the reflected electric field is given by the following [42, 43]:

$$\tilde{\mathbf{E}}_s(z) = \frac{1}{2}\mathbf{J}_{\text{ret}}^{\text{QWP}} \cdot \mathbf{J}_{\text{ret}}\left(\delta_s(z), \theta_s\right) \cdot \sqrt{R(z)} \cdot \mathbf{J}_{\text{ret}}\left(\delta_s(z), \theta_s\right) \cdot \mathbf{J}_{\text{ret}}^{\text{QWP}} \cdot \begin{bmatrix} 0 \\ 1 \end{bmatrix} \quad (4.8)$$

$$= \frac{\sqrt{R(z)}}{2} \begin{bmatrix} \exp\left(-j\delta_s(z)\right) \cos\delta_s(z) \\ -\exp\left(-j\left(\delta_s(z)+\theta_s\right)\right) \sin\delta_s(z) \end{bmatrix} \cdot \exp\left(-j2k_0 z\bar{n}\right) \quad (4.9)$$

where z describes the distance from the top of the sample to a scattering centre within the sample, and $\bar{n}$ is the mean index of refraction (comprising the ordinary and extraordinary beams). $\delta_s(z)$ is described as in Equation (4.1). For simplicity and without loss of generality, the distance from NPBS to the top of the sample is considered in air, matched by a similar length in the reference path.

In the reference arm another quarter-wave plate is used, oriented at an angle of 22.5 degrees with the vertical direction $\hat{y}$. The combined effect of traversing this wave plate twice in opposite directions will rotate the linear polarisation state by 45 degrees, since

$$\tilde{\mathbf{E}}_{\mathbf{r}}(l_r) = \frac{1}{2}\mathbf{J}_{\text{ret}}(\pi/2, 3\pi/8) \cdot \mathbf{J}_{\text{ret}}(\pi/2, 3\pi/8) \cdot \begin{bmatrix} 0 \\ 1 \end{bmatrix} = \frac{1}{2\sqrt{2}} \begin{bmatrix} 1 \\ 1 \end{bmatrix}, \quad (4.10)$$

where the factor $1/2$ appears due to the reduction in power caused by traversing the non-polarising beam-splitter twice. It is assumed that the reference arm path matches that between NPBS and the sample surface, hence no exponential term is considered.

After recombination at the beam-splitter NPBS, the beams from the two arms of the interferometer interfere. They travel to the polarisation-sensitive beam-splitter PBS where the two orthogonal components of the interference signal are separated and sent to two detectors, corresponding to the vertical and horizontal polarisation channels, A_V and A_H, respectively. Given that the polarisation state

of the reference beam is oriented at 45 degrees with the vertical axis $\hat{y}$, this ensures an equal reference power for the two channels. The interference terms in each channel are given by [28]

$$A_{H,V}(z, \Delta z) = A_{H,V;0}(z, \Delta z) \cdot \cos\left[\phi_{H,V}(\Delta z)\right], \tag{4.11}$$

where $A_{H;0}$ and $A_{V;0}$, the envelopes of the interference signals caused by a single reflective site in the sample at depth z, are respectively given by

$$A_{H;0} = \frac{\sqrt{R(z)}}{2\sqrt{2}} \cdot \cos\left[\delta_s(z)\right] \cdot |\gamma(\Delta z)| \tag{4.12}$$

$$A_{V;0} = \frac{\sqrt{R(z)}}{2\sqrt{2}} \cdot \sin\left[\delta_s(z)\right] \cdot |\gamma(\Delta z)| \tag{4.13}$$

and the phases for each of the components (again, depending on z) are respectively given by

$$\phi_H(\Delta z) = 2k_0 \Delta z \tag{4.14}$$

$$\phi_V(\Delta z) = 2k_0 \Delta z + \pi - 2\theta_s, \tag{4.15}$$

with $\Delta z = z\bar{n}$ being the OPD between the two arms, and $|\gamma(\Delta z)|$ describes the coherence gate profile, as presented in Section 2.1.3. In the pair of equations above the common phase term $j\delta_s(z)$ has been omitted.

In order to obtain the sample reflectivity distribution with depth $R(z)$ and the *net* retardance distribution $\delta_s(z)$, it is only necessary to work with the envelopes of the two functions $A_{H,V}$, $A_{H;0}$ and $A_{V;0}$. Supposing that a coherence function of infinitesimal width is considered (i.e. $|\gamma(\Delta z)|$ is nonzero for $\Delta z = 0$ only), as done in [28], it is then allowed to omit the dependence on Δz in the equations for $R(z)$ and $\delta_s(z)$:

$$R(z) \propto A_{H;0}(z)^2 + A_{V;0}(z)^2 \tag{4.16}$$

$$\delta_s(z) = \arctan\left(\frac{A_{V;0}(z)}{A_{H;0}(z)}\right). \tag{4.17}$$

Additionally, the orientation of the optical axis θ_s can be extracted by analysing the phase difference between the two signals, $\phi_H - \phi_V$:

$$\theta_s = (\pi - \phi_H + \phi_V)/2. \tag{4.18}$$

In the original paper on PS-OCT [40] no measurement of the orientation of the optical axis has been reported. TD-OCT makes it more challenging to obtain it since one does not have direct access to the phase of the interferometric signal. There have been techniques reported in the past which allow for the phase recovery in TD-OCT (and thus allow the measurement of the orientation of the optical axis), namely by employing lock-in demodulation [5] or by using the analytic continuation enabled by the Hilbert transform [43]. Frequency-domain methods, however, allow for a direct retrieval of the phase information, since the inverse Fourier transform of the real-valued interferogram is already a complex-valued signal:

$$\mathfrak{F}^{-1}\left\{I_{H,V}(k)\right\} \propto A_{H,V;0}(z)\exp\left[j\phi_{H,V}(z)\right], \tag{4.19}$$

with $I_{H,V}(k)$ being the intensity distribution of the interferogram in the k-domain in the two (horizontal and vertical) detection channels. For simplicity, not all terms which were presented in Equation (2.44) are represented in the equation above, but just the cross-interference term, which depends on the contributions of both arms of the interferometer.

4.1.2 Additional information: Stokes parameters and Muller matrices

The Jones formalism, as mentioned before, only models completely polarised light (ie, with a degree of polarisation equal to 1). Hence, the Jones formalism is not applicable to partially polarised or completely depolarised light; for the same reason, processes leading to depolarisation cannot be modelled (and measured) using the Jones formalism.

It is possible to address these shortcomings with the Müller-Stokes formalism, which involves quantities based on transmitted irradiance [27], not on coherent interference; in this way it is possible to access the individual beam irradiances without the influence of the interference [26]. This formalism is usually referred

to as *incoherent* precisely for this reason, and given that it is not reliant on interference it is able to quantify depolarisation effects.

According to the treatment in Bohren and Huffman [44] and summarised by Park and de Boer [26], one can describe the polarisation state of the light using a set of four elements resulting from specific irradiance measurements, which when combined can completely and unequivocally describe the polarisation state of the light. Assuming that a set of perfect polarisers is used to isolate the two orthogonal states and that the detector is not biased to any of them, we have

$$S = \begin{bmatrix} I \\ Q \\ U \\ V \end{bmatrix} = \begin{bmatrix} \left\langle E_{\parallel} E_{\parallel}^{*} + E_{\perp} E_{\perp}^{*} \right\rangle \\ \left\langle E_{\parallel} E_{\parallel}^{*} - E_{\perp} E_{\perp}^{*} \right\rangle \\ \left\langle E_{\parallel} E_{\perp}^{*} - E_{\perp} E_{\parallel}^{*} \right\rangle \\ \left\langle j \left(E_{\parallel} E_{\perp}^{*} - E_{\perp} E_{\parallel}^{*} \right) \right\rangle \end{bmatrix}, \tag{4.20}$$

where $\langle \dots \rangle$ denotes a time average, and $E_{\perp,\parallel}$ denote the detected electric fields corresponding to the two orthogonal positions of the linear polariser performing the analysis in each of the cases.

The first parameter, I, describes the overall irradiance of the beam. This is the time-averaged value that one would obtain if no analysers were placed in the path of the beam.

Parameter Q defines whether the polarisation state is oriented vertically or horizontally, since it takes the difference between the irradiances obtained for the case where the polariser was oriented vertically or horizontally.

The above parameter may quantify the amplitude of the electric field on each orthogonal polarisation state, but does not specify anything about the phase difference between these states. This is achieved by parameters U and V, where U enables the complete characterisation of a linearly polarised beam (together with Q) by performing a similar measurement to that in Q but with the analysers rotated by 45 degrees. Parameter V can be measured by using a pair of circular polarisers with opposite handednesses. Therefore, Q and U describe linear polarisation states in planes rotated by 45 degrees between them, whereas the V parameter describes circular polarisation states.

This set of parameters can be visualised in a 3-D representation by means of the Poincaré sphere [46], which is shown in Figure 4.2. Points on the sphere surface describe linear, circular, or elliptical polarisation states; these are, however, fully polarised (as long as their corresponding Stokes vectors lie on the surface

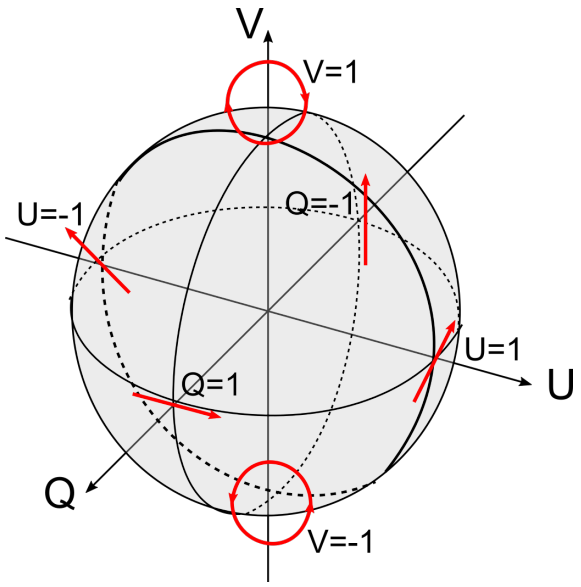

FIGURE 4.2: Representation of the polarisation states on the Poincaré sphere, adapted from [45]. The extreme cases of each parameter (Q,U,V) are represented on the sphere. $Q = \pm 1$ describe linearly polarised light oriented along the principal axis. $U = \pm 1$ is a similar description to the previous one, but with the principal axes rotated by 45 degrees. $V = \pm 1$ describe circularly polarised light with left- or right-handedness.

of the sphere). Partially polarised light descriptions lie *within* the sphere; effectively, the degree of polarisation *DoP* mentioned at the beginning of this chapter can now be described as

$$DoP = \sqrt{\frac{Q^2 + U^2 + V^2}{I^2}}. \tag{4.21}$$

From the equation above, it can be seen that both the polarised and unpolarised parts of the light contribute to the overall irradiance I; however, only the polarised parts are present in the remaining parameters of the Stokes vector. For partially polarised light, then $|I| > \sqrt{Q^2 + U^2 + V^2}$, and the *DoP* is less than 1. Complete unpolarised light has $Q = U = V = 0$, or a zero *DoP*, which corresponds to the centre of the Poincaré sphere.

Measuring Stokes parameters using PS-OCT

In order to measure the Stokes vector elements with a PS-OCT system, at first glance one needs to carry out a series of measurements according to the definition of each of the parameters (I, Q, U, V). It is, however, possible to determine the Stokes vector from a two-channel measurement such as that presented in [40],

provided that the phase information is also present, as mentioned in the previous section. From Equation (4.20), one can write [28]

$$S = \begin{bmatrix} I \\ Q \\ U \\ V \end{bmatrix} = \begin{bmatrix} A_{H;0}^2 + A_{V;0}^2 \\ A_{H;0}^2 - A_{V;0}^2 \\ 2A_{H;0}A_{V;0}\cos\Delta\phi \\ 2A_{H;0}A_{V;0}\sin\Delta\phi \end{bmatrix}. \tag{4.22}$$

Using Stokes formalism, it should be possible to calculate the degree of polarisation, according to Equation (4.21). However, one must remember that OCT, being a coherent method, only measures the light reflected from the sample arm that interferes with that from the reference arm - hence, by application of Equation (4.22) unity is obtained for all the degrees of polarisation calculated.

Therefore, a more useful quantity can be derived, the degree of polarisation uniformity (DoPU) [28, 38]. This metric is obtained by averaging the adjacent Stokes vectors on a moving window - if the Stokes vectors corresponding to the pixels within that region differ considerably between them (even if they are all on the surface of the Poincaré sphere, as shown in by the blue dots in Figure 4.3), the end result after averaging them is a vector which sits *inside* the Poincaré sphere, having length that determines a DoPU < 1. Götzinger *et al.* [38] have conjectured that there is a link between the depolarisation properties of the sample and the DoPU metric; however, a DoPU < 1 can be achieved even with a non-depolarising sample. In 2000 Jiao *et al.* [47] reported on a Jones-Müller PS-OCT system which yielded a metric of DoPU by adjacent averaging; they have obtained values of DoPU under 1 when imaging a liquid sample (intrallipid solution at different concentrations), with an increase in the concentration producing a faster apparent depolarisation. A conjecture was then presented explaining this result as being caused by the Brownian motion of the scattering particles and the signal averaging during data acquisition. Moreover, Lippok *et al.* [39] have noted the fact that the DoPU metric, when carried out with a singular polarisation state, is heavily dependent on the sample retardation, diattenuation and orientation of its depolarisation axes, which means that a contribution from the depolarisation alone cannot be decoupled from the rest, unless some prior assumptions are considered for the sample in question.

It is possible to describe the Stokes vector of a partially polarised wave $\mathbf{S}_{PP}$ as the sum of a vector $\mathbf{S}_{FP}$ representing a fully polarised wave (with $I = \sqrt{Q^2 + U^2 + V^2}$) with another vector $\mathbf{S}_{\text{depol}}$ representing the amount of depolarisation present:

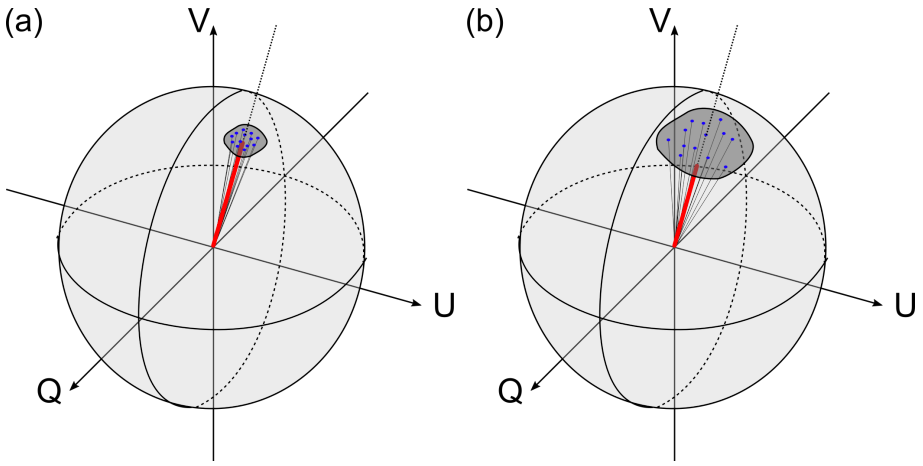

FIGURE 4.3: Schematic representation of the calculation of the DoPU using several Stokes vectors on the Poincaré sphere, corresponding to adjacent points in the OCT image. From **(a)** to **(b)** the uniformity of the Stokes vectors decreases, with a resulting decrease in the degree of polarisation uniformity (length of the averaged Stokes vector, represented in red).

$$\mathbf{S}_{PP} = \mathbf{S}_{FP} + \mathbf{S}_{\text{depol}} = \begin{bmatrix} \sqrt{Q^2+U^2+V^2} \\ Q \\ U \\ V \end{bmatrix} + \begin{bmatrix} I - \sqrt{Q^2+U^2+V^2} \\ 0 \\ 0 \\ 0 \end{bmatrix}. \quad (4.23)$$

It is worth noticing that the vector corresponding to the depolarisation $\mathbf{S}_{\text{depol}}$ is represented on the Poincaré sphere as the origin (with coordinates $(0,0,0)$), depicting complete depolarised light with an intensity equal to $I - \sqrt{Q^2+U^2+V^2}$.

This treatment is useful since it is often interesting to characterise the *average* retardance and optical axis orientation, which can be derived from the *average* Stokes vector (that determines the DoPU). Normally one obtains the Stokes vectors corresponding to the different spatial positions from the amplitude and phase of the detected signal in the two channels (from Equation (4.22)). To obtain the average retardance and optical axis orientation, one has to carry out the steps in reverse: from the Stokes vector, using Equation (4.22) and the identities in Equations (4.17) and (4.18), it is then possible to obtain $\bar{\delta}_s$ and $\bar{\theta}_s$, the spatial average values for the retardance and for the optical axis orientation.

	Time-domain OCT		Frequency-domain OCT	
	Bulk	**Fibre-based**	**Bulk**	**Fibre-based**
Using circ. polarised light (H, V)	Hee *et al.* (1992) [40]; de Boer *et al.* (1997) [48]; Hitzenberger *et al* (2001) [43];	Al-Qaisi *et al.* (2008) [50]	Götzinger *et al.* (2005) [51]	Trasischker *et al.* (2014) [52]; Lippok *et al.* [53] (2015); Marques *et al.* (2015) [54]
Stokes vector measurement	de Boer *et al.* (1999) [55]	Saxer *et al.* (2000) [56]; Roth *et al.* (2001) [57];		Zhang *et al.* (2004) [58]; Cense *et al.* (2005) [59]; Wang *et al.* (2014) [3];
Jones-Müller matrix measurement	Yao *et al.* (1999) [60]	Park *et al.* [61] (2004)	Yasuno *et al.* (2002) [12]	

TABLE 4.1: Brief summary of key PS-OCT systems referred in this section, grouped by implementation type and detection domain. This has been adapted from a larger table by Yamanari *et al.* [62]

4.2 PS-OCT systems in the literature

The system reported by Hee *et al.* [40] produced depth profiles only; in 1997, de Boer *et al.* [48] presented B-scans of PS-OCT imaging. *En-face* PS-OCT imaging was reported in 2003 by Cucu *et al.* [49]. Since then, a significant amount of novel PS-OCT configurations have been reported, differing on the number of measurements required per sample location, the number of polarisation states interrogating the sample, the number of evaluated polarisation parameters (i.e. if it is only possible to retrieve the phase retardance or if the full Stokes parameters can be retrieved, and consequently the full Jones and Müller matrices), and also on the OCT detection technique employed [2].

Table 4.1 summarises some of the key breakthroughs in PS-OCT methodology (although it is by no means an exhaustive listing). Three horizontal categories were chosen, following the treatment in [62]: systems which probe the sample with circularly polarised light (also labelled in Yasuno *et al.* [63] as the "Hee-Hitzenberger" method, which results in a simplified analysis of the two orthogonal polarisation channels), systems which retrieve the full Stokes vector (but employ methodologies other than probing the sample with circularly polarised light), and systems which measure the full Jones-Müller matrix of the sample by

taking irradiance measurements within the OCT system (normally requiring 16 measurements, since the Müller matrix size is 4×4).

Time-domain PS-OCT systems were still developed until the early 2000s. The major limitation of TD systems for PS-OCT is that they do not yield the phase information directly; instead, one needs to resort to additional methods [5, 43, 55, 57] (which typically use more measurements per sample location and/or additional probing polarisation states) in order to extract the phase and with that obtain the full characterisation of the sample.

The very first PS-OCT system operating in frequency-domain was reported in 2002 by Yasuno *et al.* [12]. This system allowed the calculation of the full Müller matrix of the sample by manually adjusting the polarisation state of the probing beam, yielding a total of 16 OCT images. Given the number of measurements required, only *in vitro* samples were imaged. In 2005, Götzinger *et al.* reported [51] the first high-speed spectral-domain PS-OCT system for retinal imaging, which was capable of an A-line rate of $20\,\mathrm{kHz}$.

Implementing a spectral-domain PS-OCT system has its challenges, though: if one desires a simultaneous measurement of the two orthogonal channels (as in [40] and represented in Figure 4.1), it is necessary to replace the two photodetectors employed with two spectrometers. These spectrometers need near-perfect pixel matching between them [28], otherwise depth-dependent artefacts arise [51]. A single-camera design [64, 65] may be employed, but an additional processing step correcting for the sample mismatch becomes necessary [28]. Furthermore, a single-camera design simultaneously sampling the two orthogonal polarisation channels means that one has to either divide the detector into two [65] or multiplex the orthogonal states in the channelled spectrum frequency [66], both normally with some impact on both the OCT axial range and axial resolution, depending on the implementation. Single-detector, sequential systems including some of the designs [54] presented in Chapter 7 may allow access to the full axial range, but due to their sequential nature additional steps need to be taken into consideration in order to provide all polarimetric information (including the optical axis orientation, which is given by the phase of the interference signal).

Using tunable (swept) sources in a PS-OCT systems [3, 52, 53] may address some of these issues, due to reduction in the complexity of the detector side; moreover, given the longer axial range enabled by the large coherence length of recent sources, it is possible to passively encode the two orthogonal polarisation states in depth [3] without sacrificing too much of the system axial range. SS-OCT

also allows for balanced detection configurations, which necessarily improves the SNR.

Most PS-OCT systems reported in the 1990s and in the early 2000s were implemented in free space (bulk-based), due to the difficulty of maintaining predictable polarisation states in conventional fibres [57], and also since that, once aligned, they can be used without recalibration over extended periods of time [28]; moreover, using optical fibres may alter the polarisation state of the collected signal, with a combined effect of the sample polarimetric properties and the fibre contribution being measured [2, 67]. Still, implementing a PS-OCT system in fibre (especially single-mode fibre) has its advantages in terms of ease of alignment and handling [28, 56], in addition to simplification of the sample arm that can admit flexible fixtures [57]. This secures compatibility of PS-OCT operation with endoscopic or hand-held probe, for instance. Part of the work presented in this Thesis involves three different fibre-based, PS-OCT configurations which are immune to fibre-based disturbances [54, 68]. A detailed description, along with a more complete comparison of these designs with other fibre-based PS-OCT systems is presented in Chapter 7.

Continuing the trend towards quantification of the information provided by PS-OCT systems, more recently several groups have started working on obtaining *true* retardance maps. Most systems mentioned in this Section (including the ones presented in this Thesis later in Chapter 7) provide only the *net* (cumulative) retardation, which for a deeper layer in the sample being imaged corresponds to the contributions of all the birefringent layers present above it. One can separate individual contributions by making some assumptions on the sample properties and using computational post-processing methods, therefore unveiling the actual local (*true*) retardance map of the sample. Cense *et al.* [8, 33] employed a linear regression over the retardance data to retrieve the local retardation information; more sophisticated methods using Stokes parameter analysis [34] or Jones matrix analysis have since been reported [35–37].

Finally, as a side note, polarisation properties can also be employed in OCT systems to achieve functionality other than polarimetric measurements; Rogers *et al.* [69] employed PM fibres and couplers in order to implement recirculating loops to achieve multiple depth *en-face* imaging with a TD-OCT system, and Dhalla *et al.* [70] have implemented a polarisation-encoded sample arm to simultaneously image the anterior and posterior segments of the eye.

References

[1] M. E. Brezinski, "Polarization and polarization sensitive oct", in *Optical Coherence Tomography: Principles and Applications*. Academic Press, 2006, ch. 8, ISBN: 9780080464947.

[2] M. Pircher, C. K. Hitzenberger, and U. Schmidt-Erfurth, "Polarization sensitive optical coherence tomography in the human eye", *Progress in retinal and eye research*, vol. 30, no. 6, pp. 431–451, 2011.

[3] Z. Wang, H.-C. Lee, O. O. Ahsen, B. Lee, W. Choi, B. Potsaid, J. Liu, V. Jayaraman, A. Cable, M. F. Kraus, *et al.*, "Depth-encoded all-fiber swept source polarization sensitive oct", *Biomedical optics express*, vol. 5, no. 9, pp. 2931–2949, 2014. [Online]. Available: http://www.osapublishing.org/boe/fulltext.cfm?uri=boe-5-9-2931&id=297388.

[4] E. Götzinger, M. Pircher, M. Sticker, A. F. Fercher, C. K. Hitzenberger, *et al.*, "Measurement and imaging of birefringent properties of the human cornea with phase-resolved, polarization-sensitive optical coherence tomography", *Journal of Biomedical Optics*, vol. 9, no. 1, pp. 94–102, 2004. [Online]. Available: http://biomedicaloptics.spiedigitallibrary.org/article.aspx?articleid=1101662.

[5] M. Pircher, E. Goetzinger, R. Leitgeb, and C. K. Hitzenberger, "Transversal phase resolved polarization sensitive optical coherence tomography", *Physics in medicine and biology*, vol. 49, no. 7, p. 1257, 2004.

[6] R. G. Cucu, J. Pedro, R. B. Rosen, and A. G. Podoleanu, "Polarization-sensitive oct system using single-mode fiber", in *Photonics North*, International Society for Optics and Photonics, 2004, pp. 170–177. [Online]. Available: http://proceedings.spiedigitallibrary.org/proceeding.aspx?articleid=851531.

[7] Y. Lim, M. Yamanari, S. Fukuda, Y. Kaji, T. Kiuchi, M. Miura, T. Oshika, and Y. Yasuno, "Birefringence measurement of cornea and anterior segment by office-based polarization-sensitive optical coherence tomography", *Biomedical optics express*, vol. 2, no. 8, pp. 2392–2402, 2011. [Online]. Available: https://www.osapublishing.org/abstract.cfm?uri=boe-2-8-2392.

[8] B. Cense, T. C. Chen, B. H. Park, M. C. Pierce, and J. F. de Boer, "In vivo depth-resolved birefringence measurements of the human retinal nerve fiber layer by polarization-sensitive optical coherence tomography", *Optics letters*, vol. 27, no. 18, pp. 1610–1612, 2002. [Online]. Available: https://

www.osapublishing.org/abstract.cfm?uri=OL-27-18-1610; %20https://www.researchgate.net/profile/Barry_Cense/publication/5819837_Invivo_depth-resolved_birefringence_measurements_of_the_human_retinal_nerve_fiber_layer_by_polarization-sensitive_optical_coherence_tomography/links/00b49522051c0c2c27000000.pdf.

[9] M. Pircher, E. Götzinger, R. Leitgeb, H. Sattmann, O. Findl, and C. K. Hitzenberger, "Imaging of polarization properties of human retina in vivo with phase resolved transversal ps-oct", *Optics Express*, vol. 12, no. 24, pp. 5940–5951, 2004. [Online]. Available: https://www.osapublishing.org/abstract.cfm?uri=oe-12-24-5940.

[10] A. G. Podoleanu, R. G. Cucu, and R. B. Rosen, "In vivo t-scan-based polarization-sensitive oct of the optic nerve", in *Biomedical Optics 2004*, International Society for Optics and Photonics, 2004, pp. 300–305. [Online]. Available: http://proceedings.spiedigitallibrary.org/proceeding.aspx?articleid=838744.

[11] M. Pircher, E. Götzinger, O. Findl, S. Michels, W. Geitzenauer, C. Leydolt, U. Schmidt-Erfurth, and C. K. Hitzenberger, "Human macula investigated in vivo with polarization-sensitive optical coherence tomography", *Investigative ophthalmology & visual science*, vol. 47, no. 12, pp. 5487–5494, 2006. [Online]. Available: http://iovs.arvojournals.org/article.aspx?articleid=2163676.

[12] Y. Yasuno, S. Makita, Y. Sutoh, M. Itoh, and T. Yatagai, "Birefringence imaging of human skin by polarization-sensitive spectral interferometric optical coherence tomography", *Optics letters*, vol. 27, no. 20, pp. 1803–1805, 2002.

[13] M. C. Pierce, J. Strasswimmer, B. H. Park, B. Cense, and J. F. de Boer, "Birefringence measurements in human skin using polarization-sensitive optical coherence tomography", *Journal of biomedical optics*, vol. 9, no. 2, pp. 287–291, 2004. [Online]. Available: http://biomedicaloptics.spiedigitallibrary.org/article.aspx?articleid=1101701;%20http://www.engr.ucr.edu/~hylepark/publications/13/Pierce%20HumanBiref%20JBO2004.pdf.

[14] M. Pircher, E. Goetzinger, R. Leitgeb, and C. Hitzenberger, "Three dimensional polarization sensitive oct of human skin in vivo", *Optics express*, vol. 12, no. 14, pp. 3236–3244, 2004. [Online]. Available: https://www.osapublishing.org/abstract.cfm?uri=oe-12-14-3236;%20https://www.osapublishing.org/oe/fulltext.cfm?uri=oe-12-14-3236.

[15] J. Strasswimmer, M. C. Pierce, B. H. Park, V. Neel, and J. F. de Boer, "Polarization-sensitive optical coherence tomography of invasive basal cell carcinoma", *Journal of biomedical optics*, vol. 9, no. 2, pp. 292–298, 2004. [Online]. Available: http://biomedicaloptics.spiedigitallibrary.org/article.aspx?articleid=1101703;%20https://www.researchgate.net/profile/B_Park/publication/8635488_Polarization-sensitive_optical_coherence_tomography_of_invasive_basal_cell_carcinoma/links/53ecf88a0cf23733e804e916.pdf.

[16] J. De Boer, S. Srinivas, A. Malekafzali, Z. Chen, and J. Nelson, "Imaging thermally damaged tissue by polarization sensitive optical coherence tomography", *Optics express*, vol. 3, no. 6, pp. 212–218, 1998. [Online]. Available: https://www.osapublishing.org/abstract.cfm?uri=oe-3-6-212;%20https://www.osapublishing.org/oe/fulltext.cfm?uri=oe-3-6-212.

[17] M. C. Pierce, R. L. Sheridan, B. H. Park, B. Cense, and J. F. de Boer, "Collagen denaturation can be quantified in burned human skin using polarization-sensitive optical coherence tomography", *Burns*, vol. 30, no. 6, pp. 511–517, 2004. [Online]. Available: http://www.sciencedirect.com/science/article/pii/S0305417904000592;%20http://www.journals.elsevierhealth.com/article/S0305-4179(04)00059-2/fulltext.

[18] S. M. Srinivas, J. F. de Boer, H. Park, K. Keikhanzadeh, L. H. Huai-en, J. Zhang, W. Q. Jung, Z. Chen, and J. S. Nelson, "Determination of burn depth by polarization-sensitive optical coherence tomography", *Journal of Biomedical Optics*, vol. 9, no. 1, pp. 207–212, 2004. [Online]. Available: http://biomedicaloptics.spiedigitallibrary.org/article.aspx?articleid=1101685;%20http://pubs.bli.uci.edu/sites/default/files/publications/429..pdf.

[19] K. H. Kim, M. C. Pierce, G. Maguluri, B. H. Park, S. J. Yoon, M. Lydon, R. Sheridan, and J. F. de Boer, "In vivo imaging of human burn injuries with polarization-sensitive optical coherence tomography", *Journal of biomedical optics*, vol. 17, no. 6, pp. 066 012–066 012, 2012. [Online]. Available: https://biomedicaloptics.spiedigitallibrary.org/article.aspx?articleid=1199115.

[20] M. Zurauskas and A. G. Podoleanu, "Multiplexing-based polarization sensitive en-face optical coherence tomography", *Journal of biomedical optics*, vol. 18, no. 10, pp. 106 010–106 010, 2013. [Online]. Available: http://

reviews.spiedigitallibrary.org/article.aspx?articleid=1760313.

[21] A. Baumgartner, S. Dichtl, C. Hitzenberger, H. Sattmann, B. Robl, A. Moritz, A. Fercher, and W. Sperr, "Polarization–sensitive optical coherence tomography of dental structures", *Caries research*, vol. 34, no. 1, pp. 59–69, 2000. [Online]. Available: http://www.karger.com/Article/Abstract/16571.

[22] X.-J. Wang, T. E. Milner, J. F. De Boer, Y. Zhang, D. H. Pashley, and J. S. Nelson, "Characterization of dentin and enamel by use of optical coherence tomography", *Applied Optics*, vol. 38, no. 10, pp. 2092–2096, 1999. [Online]. Available: https://www.osapublishing.org/abstract.cfm?uri=ao-38-10-2092;%20https://www.researchgate.net/profile/Xiaojun_Wang5/publication/5532035_Characterization_of_Dentin_and_Enamel_by_use_of_Optical_Coherence_Tomography/links/0c96051cdea54e0f46000000.pdf.

[23] S. D. Giattina, B. K. Courtney, P. R. Herz, M. Harman, S. Shortkroff, D. L. Stamper, B. Liu, J. G. Fujimoto, and M. E. Brezinski, "Assessment of coronary plaque collagen with polarization sensitive optical coherence tomography (ps-oct)", *International journal of cardiology*, vol. 107, no. 3, pp. 400–409, 2006. [Online]. Available: http://www.sciencedirect.com/science/article/pii/S0167527305013367;%20http://www.internationaljournalofcardiology.com/article/S0167-5273(05)01336-7/abstract.

[24] W.-C. Kuo, N.-K. Chou, C. Chou, C.-M. Lai, H.-J. Huang, S.-S. Wang, and J.-J. Shyu, "Polarization-sensitive optical coherence tomography for imaging human atherosclerosis", *Applied optics*, vol. 46, no. 13, pp. 2520–2527, 2007. [Online]. Available: https://www.osapublishing.org/abstract.cfm?uri=ao-46-13-2520.

[25] S. K. Nadkarni, M. C. Pierce, B. H. Park, J. F. de Boer, P. Whittaker, B. E. Bouma, J. E. Bressner, E. Halpern, S. L. Houser, and G. J. Tearney, "Measurement of collagen and smooth muscle cell content in atherosclerotic plaques using polarization-sensitive optical coherence tomography", *Journal of the American College of Cardiology*, vol. 49, no. 13, pp. 1474–1481, 2007. [Online]. Available: http://content.onlinejacc.org/article.aspx?articleid=1188870;%20/scholar?output=instlink&q=info:V21PItRfEl8J:scholar.google.com/&hl=en&as_sdt=0,5&as_

ylo=2007&as_yhi=2007&as_vis=1&scillfp=4619160341505647109&oi=lle.

[26] B. H. Park and J. F. de Boer, "Polarization sensitive optical coherence tomography", in *Optical Coherence Tomography: Technology and Applications*, W. Drexler and J. G. Fujimoto, Eds., 2nd ed., Springer, 2015, ch. 33.

[27] E. Hecht, *Optics*, 4th ed. Addison Wesley, 2002, ch. 8.

[28] C. K. Hitzenberger and M. Pircher, "Muw approach of ps oct", in *Optical Coherence Tomography: Technology and Applications*, W. Drexler and J. G. Fujimoto, Eds., 2nd ed., Springer, 2015, ch. 34.

[29] W. L. Bragg and A. B. Pippard, "The form birefringence of macromolecules", *Acta Cryst.*, vol. 6, no. 11, pp. 865–867, Nov. 1953, ISSN: 0365-110X. DOI: 10.1107/s0365110x53002519. [Online]. Available: http://dx.doi.org/10.1107/S0365110X53002519.

[30] S.-Y. Lu and R. A. Chipman, "Interpretation of mueller matrices based on polar decomposition", *J. Opt. Soc. Am. A*, vol. 13, no. 5, p. 1106, May 1996, ISSN: 1520-8532. DOI: 10.1364/josaa.13.001106. [Online]. Available: http://dx.doi.org/10.1364/JOSAA.13.001106.

[31] J. W. Mishchenko M. I.; Hovenier, "Depolarization of light backscattered by randomly oriented nonspherical particles", *Optics Letters*, vol. 20, 12 1995. DOI: 10.1364/OL.20.001356.

[32] R. C. Jones, "A new calculus for the treatment of optical systemsi. description and discussion of the calculus", *JOSA*, vol. 31, no. 7, pp. 488–493, 1941.

[33] B. Cense, T. C. Chen, B. H. Park, M. C. Pierce, and J. F. de Boer, "In vivo birefringence and thickness measurements of the human retinal nerve fiber layer using polarization-sensitive optical coherence tomography", *Journal of Biomedical Optics*, vol. 9, no. 1, p. 121, 2004, ISSN: 1083-3668. DOI: 10.1117/1.1627774. [Online]. Available: http://dx.doi.org/10.1117/1.1627774.

[34] S. Guo, J. Zhang, L. Wang, J. S. Nelson, and Z. Chen, "Depth-resolved birefringence and differential optical axis orientation measurements with fiber-based polarization-sensitive optical coherence tomography", *Opt. Lett.*, vol. 29, no. 17, p. 2025, Sep. 2004, ISSN: 1539-4794. DOI: 10.1364/ol.29.002025. [Online]. Available: http://dx.doi.org/10.1364/OL.29.002025.

[35] S. Makita, M. Yamanari, and Y. Yasuno, "Generalized jones matrix optical coherence tomography: performance and local birefringence imaging", *Optics Express*, vol. 18, no. 2, p. 854, Jan. 2010, ISSN: 1094-4087. DOI: 10.1364/oe.18.000854. [Online]. Available: http://dx.doi.org/10.1364/OE.18.000854.

[36] C. Fan and G. Yao, "Mapping local retardance in birefringent samples using polarization sensitive optical coherence tomography", *Opt. Lett.*, vol. 37, no. 9, p. 1415, Apr. 2012, ISSN: 1539-4794. DOI: 10.1364/ol.37.001415. [Online]. Available: http://dx.doi.org/10.1364/OL.37.001415.

[37] D. Kasaragod, S. Makita, S. Fukuda, S. Beheregaray, T. Oshika, and Y. Yasuno, "Bayesian maximum likelihood estimator of phase retardation for quantitative polarization-sensitive optical coherence tomography.", *Opt Express*, vol. 22, no. 13, pp. 16 472–92, Jun. 2014.

[38] E. Götzinger, M. Pircher, W. Geitzenauer, C. Ahlers, B. Baumann, S. Michels, U. Schmidt-Erfurth, and C. K. Hitzenberger, "Retinal pigment epithelium segmentation by polarization sensitive optical coherence tomography", *Optics express*, vol. 16, no. 21, pp. 16 410–16 422, 2008. [Online]. Available: https://www.osapublishing.org/abstract.cfm?uri=oe-16-21-16410.

[39] N. Lippok, M. Villiger, and B. E. Bouma, "Degree of polarization (uniformity) and depolarization index: unambiguous depolarization contrast for optical coherence tomography", *Opt. Lett.*, vol. 40, no. 17, p. 3954, Aug. 2015, ISSN: 1539-4794. DOI: 10.1364/ol.40.003954. [Online]. Available: http://dx.doi.org/10.1364/OL.40.003954.

[40] M. R. Hee, E. A. Swanson, J. G. Fujimoto, and D. Huang, "Polarization-sensitive low-coherence reflectometer for birefringence characterization and ranging", *JOSA B*, vol. 9, no. 6, pp. 903–908, 1992.

[41] A. Gerrard and J. M. Burch, *Introduction to matrix methods in optics*. New York: Dover Publications, 1994.

[42] K. Schoenenberger, B. W. Colston, D. J. Maitland, L. B. Da Silva, and M. J. Everett, "Mapping of birefringence and thermal damage in tissue by use of polarization-sensitive optical coherence tomography", *Applied Optics*, vol. 37, no. 25, p. 6026, Sep. 1998, ISSN: 1539-4522. DOI: 10.1364/ao.37.006026. [Online]. Available: http://dx.doi.org/10.1364/AO.37.006026.

[43] C. K. Hitzenberger, E. Götzinger, M. Sticker, M. Pircher, and A. F. Fercher, "Measurement and imaging of birefringence and optic axis orientation by phase resolved polarization sensitive optical coherence tomography", *Optics Express*, vol. 9, no. 13, pp. 780–790, 2001.

[44] D. R. H. Craig F. Bohren, *Absorption and scattering of light by small particles*. John Wiley & Sons, 1983, ISBN: 9780471057727.

[45] W. A. Shurcliff, *Polarized light. Production and use*. Cambridge, Mass: Harvard University Press, 1966.

[46] H. G. Jerrard, "Transmission of light through birefringent and optically active media: the poincaré sphere", *J. Opt. Soc. Am.*, vol. 44, no. 8, p. 634, Aug. 1954, ISSN: 0030-3941. DOI: 10.1364/josa.44.000634. [Online]. Available: http://dx.doi.org/10.1364/JOSA.44.000634.

[47] S. Jiao, G. Yao, and L. V. Wang, "Depth-resolved two-dimensional stokes vectors of backscattered light and mueller matrices of biological tissue measured with optical coherence tomography", *Applied Optics*, vol. 39, no. 34, pp. 6318–6324, 2000. [Online]. Available: https://www.osapublishing.org/abstract.cfm?uri=ao-39-34-6318;%20http://citeseerx.ist.psu.edu/viewdoc/download?doi=10.1.1.461.2112&rep=rep1&type=pdf.

[48] J. F. De Boer, T. E. Milner, M. J. van Gemert, and J. S. Nelson, "Two-dimensional birefringence imaging in biological tissue by polarization-sensitive optical coherence tomography", *Optics letters*, vol. 22, no. 12, pp. 934–936, 1997. [Online]. Available: https://www.osapublishing.org/abstract.cfm?uri=ol-22-12-934;%20http://dare.uva.nl/document/2/2960.

[49] R. G. Cucu, A. G. Podoleanu, R. B. Rosen, A. B. Boxer, and D. A. Jackson, "En-face polarization-sensitive optical coherence tomography", W. Drexler, Ed., SPIE-Intl Soc Optical Eng, Oct. 2003. DOI: 10.1117/12.500779. [Online]. Available: http://dx.doi.org/10.1117/12.500779.

[50] M. K. Al-Qaisi and T. Akkin, "Polarization-sensitive optical coherence tomography based on polarization-maintaining fibers and frequency multiplexing", *Optics express*, vol. 16, no. 17, pp. 13 032–13 041, 2008. [Online]. Available: http://www.osapublishing.org/oe/fulltext.cfm?uri=oe-16-17-13032&id=170503.

[51] E. Götzinger, M. Pircher, and C. K. Hitzenberger, "High speed spectral domain polarization sensitive optical coherence tomography of the human retina", *Optics express*, vol. 13, no. 25, pp. 10 217–10 229, 2005. [Online]. Available: https://www.osapublishing.org/abstract.cfm?uri=OE-13-25-10217.

[52] W. Trasischker, S. Zotter, T. Torzicky, B. Baumann, R. Haindl, M. Pircher, and C. K. Hitzenberger, "Single input state polarization sensitive swept source optical coherence tomography based on an all single mode fiber interferometer", *Biomed. Opt. Express*, vol. 5, no. 8, pp. 2798–2809, 2014. DOI: 10.1364/BOE.5.002798. [Online]. Available: http://www.osapublishing.org/boe/abstract.cfm?URI=boe-5-8-2798.

[53] N. Lippok, M. Villiger, C. Jun, and B. E. Bouma, "Single input state, single-mode fiber-based polarization-sensitive optical frequency domain imaging by eigenpolarization referencing.", *Optics Letters*, vol. 40, no. 9, pp. 2025–8, 2015.

[54] M. J. Marques, S. Rivet, A. Bradu, and A. Podoleanu, "Polarization-sensitive optical coherence tomography system tolerant to fiber disturbances using a line camera", *Opt. Lett.*, vol. 40, no. 16, pp. 3858–3861, 2015.

[55] J. F. De Boer, T. E. Milner, and J. S. Nelson, "Determination of the depth-resolved stokes parameters of light backscattered from turbid media by use of polarization-sensitive optical coherence tomography", *Optics Letters*, vol. 24, no. 5, pp. 300–302, 1999. [Online]. Available: https://www.osapublishing.org/abstract.cfm?uri=ol-24-5-300.

[56] C. E. Saxer, J. F. de Boer, B. H. Park, Y. Zhao, Z. Chen, and J. S. Nelson, "High-speed fiber–based polarization-sensitive optical coherence tomography of in vivo human skin", *Optics Letters*, vol. 25, no. 18, pp. 1355–1357, 2000. [Online]. Available: https://www.osapublishing.org/abstract.cfm?uri=ol-25-18-1355;%20http://www.ece.ucr.edu/~hylepark/publications/2/Saxer%20FiberPSOCT%20OL25(18)1355(2000).pdf.

[57] J. E. Roth, J. A. Kozak, S. Yazdanfar, A. M. Rollins, and J. A. Izatt, "Simplified method for polarization-sensitive optical coherence tomography", *Optics Letters*, vol. 26, no. 14, pp. 1069–1071, 2001. [Online]. Available: http://www.osapublishing.org/fulltext.cfm?uri=ol-26-14-1069&id=64718;%20ftp://ftp.chara.gsu.edu/pub/users/shure/papers/downld2/article15.pdf.

[58] J. Zhang, W. Jung, J. Nelson, and Z. Chen, "Full range polarization-sensitive fourier domain optical coherence tomography", *Optics Express*, vol. 12, no. 24, pp. 6033–6039, 2004. [Online]. Available: https://www.osapublishing.org/abstract.cfm?uri=oe-12-24-6033;%20https://www.osapublishing.org/oe/fulltext.cfm?uri=oe-12-24-6033.

[59] B. Cense, T. C. Chen, M. Mujat, C. Joo, T. Akkin, B. H. Park, M. C. Pierce, A. Yun, B. E. Bouma, G. J. Tearney, *et al.*, "Spectral domain polarization-sensitive optical coherence tomography at 850 nm", in *Biomedical Optics 2005*, International Society for Optics and Photonics, 2005, pp. 159–162. [Online]. Available: http://proceedings.spiedigitallibrary.org/proceeding.aspx?articleid=858695.

[60] G. Yao and L. V. Wang, "Two-dimensional depth-resolved mueller matrix characterization of biological tissue by optical coherence tomography", *Optics Letters*, vol. 24, no. 8, pp. 537–539, 1999. [Online]. Available: https://www.osapublishing.org/abstract.cfm?uri=ol-24-8-537.

[61] B. H. Park, M. C. Pierce, B. Cense, and J. F. de Boer, "Jones matrix analysis for a polarization-sensitive optical coherence tomography system using fiber-optic components", *Optics letters*, vol. 29, no. 21, pp. 2512–2514, 2004. [Online]. Available: https://www.osapublishing.org/abstract.cfm?uri=OL-29-21-2512;%20http://www.ncbi.nlm.nih.gov/pmc/articles/pmc2693253/.

[62] M. Yamanari, S. Makita, V. D. Madjarova, T. Yatagai, and Y. Yasuno, "Fiber-based polarization-sensitive fourier domain optical coherence tomography using b-scan-oriented polarization modulation method", *Optics Express*, vol. 14, no. 14, pp. 6502–6515, 2006. [Online]. Available: https://www.osapublishing.org/abstract.cfm?uri=OE-14-14-6502.

[63] Y. Yasuno, M.-J. Ju, Y. J. Hong, S. Makita, Y. Lim, and M. Yamanari, "Jones matrix based polarization sensitive optical coherence tomography", in *Optical Coherence Tomography: Technology and Applications*, W. Drexler and J. G. Fujimoto, Eds., 2nd ed., Springer, 2015, ch. 35, p. 1137.

[64] B. Baumann, M. Pircher, C. K. Hitzenberger, *et al.*, "Single camera based spectral domain polarization sensitive optical coherence tomography", *Optics express*, vol. 15, no. 3, pp. 1054–1063, 2007. [Online]. Available: https://www.osapublishing.org/abstract.cfm?uri=OE-15-3-1054.

[65] B. Cense, M. Mujat, T. C. Chen, B. H. Park, and J. F. de Boer, "Polarization-sensitive spectral-domain optical coherence tomography using a single line scan camera", *Optics Express*, vol. 15, no. 5, pp. 2421–2431, 2007. [Online].

Available: http://www.osapublishing.org/vjbo/fulltext.cfm?uri=oe-15-5-2421&id=130598.

[66] C. Fan, Y. Wang, and R. K. Wang, "Spectral domain polarization sensitive optical coherence tomography achieved by single camera detection", *Optics express*, vol. 15, no. 13, pp. 7950–7961, 2007. [Online]. Available: https://www.osapublishing.org/abstract.cfm?uri=OE-15-13-7950.

[67] S. C. Rashleigh, "Acoustic sensing with a single coiled monomode fiber", *Optics letters*, vol. 5, no. 9, pp. 392–394, 1980. [Online]. Available: http://www.osapublishing.org/ol/fulltext.cfm?uri=ol-5-9-392.

[68] S. Rivet, M. J. Marques, A. Bradu, and A. G. Podoleanu, "Optical module to extend any fourier-domain optical coherence tomography system into a polarisation-sensitive system", In press. 2016.

[69] J. A. Rogers, A. Bradu, and A. G. Podoleanu, "Polarization maintaining multiple-depth en face optical coherence tomography system using active re-circulation loops in the non-stationary state", *Optics Express*, vol. 20, no. 28, p. 29 196, Dec. 2012, ISSN: 1094-4087. DOI: 10.1364/oe.20.029196. [Online]. Available: http://dx.doi.org/10.1364/OE.20.029196.

[70] A.-H. Dhalla, D. Nankivil, T. Bustamante, A. Kuo, and J. A. Izatt, "Simultaneous swept source optical coherence tomography of the anterior segment and retina using coherence revival", *Opt. Lett.*, vol. 37, no. 11, p. 1883, May 2012, ISSN: 1539-4794. DOI: 10.1364/ol.37.001883. [Online]. Available: http://dx.doi.org/10.1364/OL.37.001883.

Part II

Experimental Work

Chapter 5

Simultaneous and sequential Sp-OCT and SLO imaging with Talbot bands

Author's note: portions of this chapter are based on work which has been reported in a peer-reviewed publication [1] and presented at an international conference (*Frontiers in Optics)* in October 2014 [2].

Contents

WHEN performing *in-vivo* OCT retinal imaging it is important to have a "bird's eye" perspective (an *en-face* view) of the retina. However, FD-OCT methods obtain depth profiles which must then be combined together in a 3-D volume. This volume will then have to be computationally sliced, normally by employing a summed voxel projection [3] (SVP) in order to obtain an *en-face* image. All these operations lead to a slowing down of the overall frame rate, thus increasing the occurrence of motion artefacts with consequences in image degradation.

Another option which is currently being marketed by Topcon [4] is to employ a SLR camera to provide an image of the retinal fundus, in parallel with the OCT

image. Even though this approach allows a faster system to be implemented, it is difficult to secure pixel-to-pixel correspondence between the two images obtained, since different optics are used by the SLR camera and the OCT scanning head.

One way of obtaining a "bird's eye" perspective is to integrate a confocal microscope into the existing OCT system. In the case of retinal imaging, and because the focal spot is raster-scanned over the retina, such a confocal device is often called a scanning laser ophthalmoscope (SLO) in the literature. Such an approach requires diverting some of the light as it returns from the retina towards a different photo-detector [5–7] to obtain a combined OCT/SLO instrument. A version of OCT/SLO is marketed by Optos [8], where the two channels share the same scanning head. An SLO image is produced sequentially with a cross-section OCT image [9]. Vienola *et al.* [10] employ a different principle, whereby separate scanners are used by the two channels, which operate at different wavelengths via a dichroic splitter. The SLO channel in this case may be employed for imaging, but it can also function as a retinal tracker, effectively compensating for the patient's involuntary movements. A similar concept was implemented in a hand-held probe, which is appropriate for imaging subjects with a lower degree of fixation, such as children, and in this case a spectrometer was used as the OCT detection block [11]. An en-face SLO channel using a line array detector was added to a B-scan TD-OCT set-up to create a sequential SLO/OCT system [12]. Sequential production of B-scans and confocal microscopy images has also been reported by means of fluorescence-based microscopy [13, 14]. By interlacing a spectrally-encoded confocal SLO (SECSLO) frame and an OCT B-scan in alternating fashion [15], a fundus image is generated during the same time interval required to acquire a B-scan.

All of the aforementioned methods and systems allow the operator to relate the features seen in the *en-face* image to those in the OCT B-scan image, with various degrees of pixel-to-pixel correspondence and simultaneity. The considerable number of reports on such systems demonstrate the interest in finding the best solution for presenting a guiding *en-face* image and a high axial resolution B-scan image together.

5.1 The experimental set-up

The Applied Optics Group has previously built a spectrometer-based OCT (Sp-OCT) system operating at $830\,\mathrm{nm}$, specifically designed to image the retina. The spectrometer arm from a standard Sp-OCT set-up was modified [16, 17] to achieve

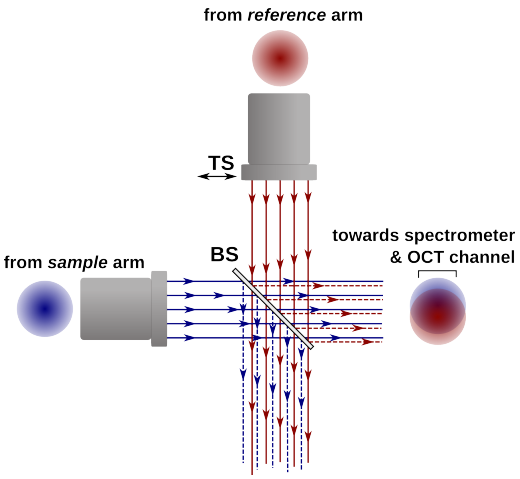

(A) Slight gap introduced between the two beams using *TS*: Talbot bands are generated and the visibility profile C_{TB} is shifted.

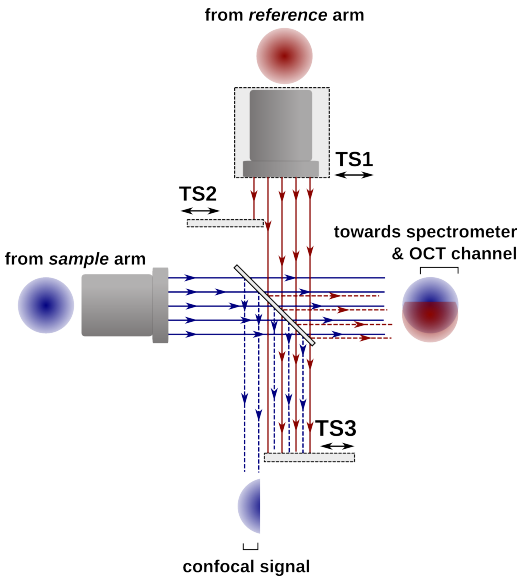

(B) By taking the second output of the bulk beam-splitter (bottom part of the diagram) and introducing a pair of spatial filters attached to *TS2* and *TS3* an additional channel can be implemented, receiving optical power exclusively from the sample arm.

FIGURE 5.1: Coupling the outputs of interferometer arms by employing a bulk beam-splitter.

the functionality of exhibiting Talbot bands, which allows the control of the OCT visibility profile, as explained in Section 3.2.1.

The nature of this implementation requires independent control over the relative positions of the two beams. These beams have to be superposed and directed to the spectrometer. Superposition of the two beams is achieved by using a bulk beam-splitter. This operates as a 2-input/2-output device, as shown in Figure 5.1a. However, only one of the outputs is effectively used by the OCT set-up, while the other pair of beams is usually discarded.

The sample beam part of the pair of beams that would otherwise be discarded can be used to drive a photodetector in a SLO channel. This can be achieved by using a pair of screens placed at appropriate positions, as depicted in Figure 5.1b. The main task of the screens is to prevent the strong reference arm beam from reaching the SLO photodetector.

The interferometric optical system

The OCT/SLO system developed is depicted schematically in Figure 5.2. Light from a super-luminiscent diode SLD (Superlum SLD-381-HP1-DIL-SM-PD, Cork,

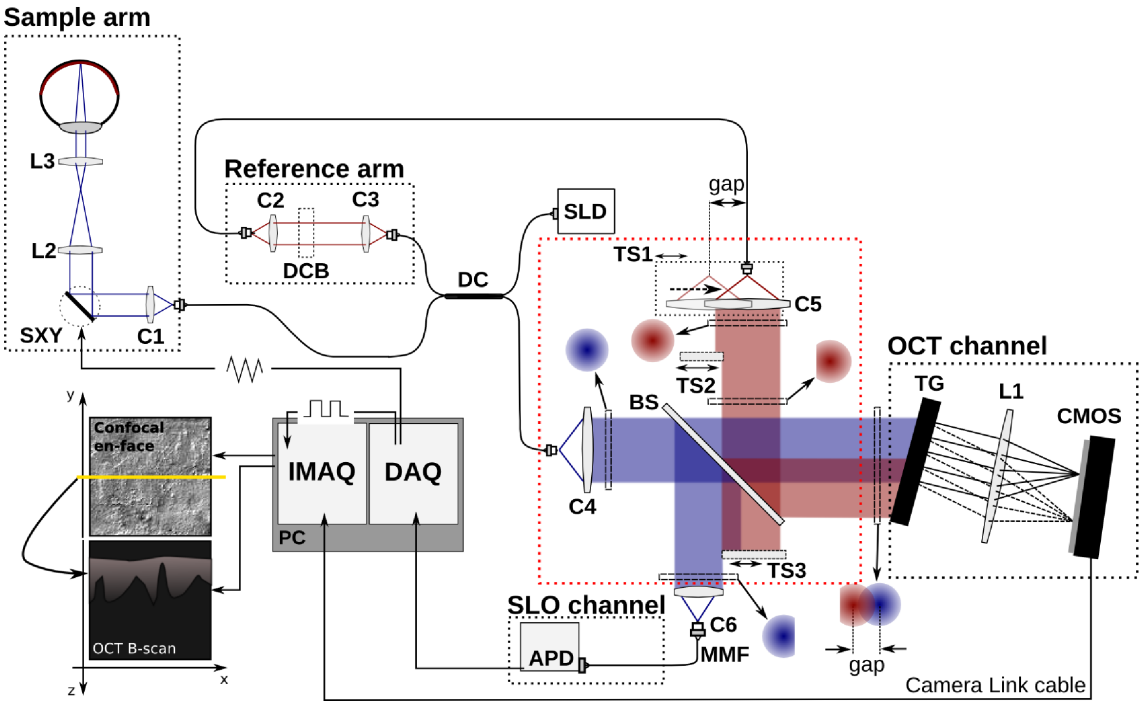

FIGURE 5.2: Dual channel Sp-OCT/SLO set-up. **C1-6**: fibre collimators; **SLD**: super-luminescent diode; **DC**: fibre-based directional coupler; **DCB**: dispersion compensation block (adjustable length, depending on the sample being imaged); **TS1-3**: translation stages; **SXY**: pair of orthogonal galvo-scanners; **TG**: transmission grating; **L1-3**: achromatic lenses; **BS**: bulk beam-splitter; **MMF**: multimode fibre; **CMOS**: line camera; **APD**: avalanche photo-diode; **IMAQ**: Camera Link-based image acquisition board; **DAQ**: multi-function data acquisition board. Region delimited by the red box shows the lateral gap between the two beams reaching *TG*, which is essential to create a Talbot bands effect. Cross-sections of the beams incident on the *TG* (OCT) and on the fibre collimator *C6* (SLO) are shown for the sample beam in red and for the reference beam in blue (taken from Marques *et al.* [1]).

Ireland - central wavelength $\lambda_0 = 830$ nm, and spectral bandwidth $\Delta\lambda \sim 20$ nm) is directed towards the two interferometer arms (reference and sample) through a fused optical fibre coupler, DC (AC Photonics, Santa Clara CA, United States of America). Given the optical bandwidth of the SLD and its central wavelength, the axial resolution due to the autocorrelation of the source's spectrum was measured to be around $15\,\mu$m.

A 20% fraction of the optical source power is directed to the sample arm, where it traverses a pair of galvo-scanners *SXY* (Crisel Instruments Galvoline G1432, Italy). The resulting beam is used to angularly scan the retina after passing through lenses *L2* and *L3* with focal lengths $f[L2] = 7.5\,\mathrm{cm}$ and $f[L3] = 3\,\mathrm{cm}$, whose role is to reduce the beam diameter at the eye pupil to $\sim 3\,\mathrm{mm}$.

The output of both interferometer arms is reunited at the bulk beam-splitter *BS*, which features an 80/20 splitting ratio. 80% of the power returning from the sample arm is directed to the spectrometer, and the remaining 20% is transferred to the orthogonal direction which encompasses the SLO channel. Additionally, the beam-splitter *BS* transmits 80% of the reference arm power towards the SLO channel collimator *C6*. Given that a gap has been introduced between the two beams for the Talbot bands implementation (by shifting the reference arm launcher *C5* using *TS1*), there is enough spatial separation to ensure that only the contribution from the sample arm is injected into the multi-mode fibre *MMF* through the collimator *C6*.

For better attenuation of the stray signal caused by the edge of the strong reference beam, a specially-devised spatial filter has been implemented (Figure 5.1b), consisting of a pair of opaque screens introduced before and after the beam-splitter *BS* along the path of the reference beam. These screens are attached to micrometre-precision translation stages *TS2-3* allowing very fine adjustments over the beam profiles. The first screen (attached to *TS2*) cuts off the edge of the reference beam on the side of the sample beam directed towards *C6*. Due to diffraction registered at the edge of the beam caused by the introduction of this screen, some stray light is still directed towards *C6*, hence a second screen attached to *TS3* is necessary. For better rejection of the reference signal, the screen is pushed towards the centre of the collimator *C6*, and a small fraction of optical power from the edge of the sample beam is blocked, as shown exaggerated in the region bounded by the red box in Figure 5.2.

Due to the combined action of moving the collimator *C5* and positioning the screen attached to *TS2*, the distribution of power in the transversal section of the reference beam results in a trimmed Gaussian profile. This affects the symmetry of the OCT sensitivity profile versus OPD, as documented in [18, 19]. However,

given that the trimmed region corresponds to one of the side wings of the reference beam profile (which carries less power), such asymmetry will have little influence on the shape of the final visibility profile.

The OCT channel detection is performed by a custom-designed spectrometer, comprising of a diffraction grating *TG* (whose grooves are orthogonal to the plane of Figure 5.2) working in transmission (Wasatch Photonics, Logan UT, United States of America) with 1200 lines/mm blazed at $830\,\mathrm{nm}$, a *CMOS* line camera (Basler sprint spl-4096km, Ahrensburg, Germany) scanning at a maximum of 140,000 lines/second, and an achromatic lens *L1* with $f = 150\,\mathrm{mm}$ to focus the diffracted light onto the camera array. The spectrum projection covers $\sim 1\,\mathrm{cm}$ of the array, which corresponds to about 1024 out of the available 4096 pixels. Using a reduced number of pixels enables the camera to operate at a higher line rate.

Each lateral scan is comprised of N_x arrays of 1024 spectral points, which have been digitised with a 12-bit resolution. After acquisition, these spectra undergo software-based processing, encompassing re-sampling in k-domain (using the method described in [20], as covered in Section 3.2.3), zero padding and inverse FFT to retrieve the depth profile (A-scans). By adding all these N_x arrays, a B(A)-scan is formed. Given the properties of the Fourier transform, this image has a size of $N_x \times 512$ pixels (width $\times$ depth).

In the SLO detection channel, light reflected from the sample arm is injected into the multi-mode fibre *MMF* through the collimator *C6*, and then directed to an avalanche photo-diode *APD* plus amplifier (Hamamatsu C5460-01, Japan) with a cut-off frequency $f_c = 100\,\mathrm{kHz}$. The electronic output of this photo-detector is then digitised by an analogue-to-digital converter within a data acquisition device *DAQ* (National Instruments PCI-6110, Austin TX, United States of America).

The SLO channel delivers *en-face* images made from T-scans. Each SLO T-scan and OCT B(A)-scan are acquired during the half-period of a triangular waveform applied to the fast scanner (x-axis).

Control system

The control system for the set-up presented is schematically represented in Figure 5.3. The Intel-based workstation is equipped with two distinct cards, a multi-function (I/O) data acquisition device *DAQ* (National Instruments PCI-6110, Austin TX, USA) and a CameraLink bus frame grabber card *IMAQ* (National Instruments PCIe-1429, Austin TX, USA). The former drives the transversal scanners and acquires the SLO signal to produce the SLO image, whereas the latter interfaces the CMOS line camera in the spectrometer with the PC, buffering the optical spectra which will then yield the OCT frames.

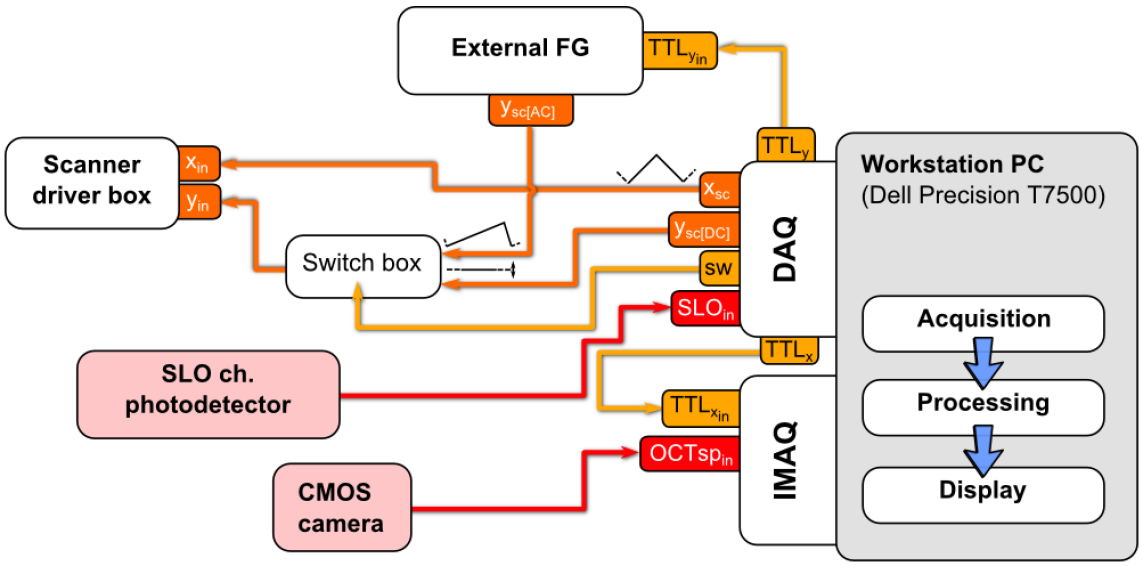

FIGURE 5.3: Schematic diagram of the control system of the OCT/SLO set-up to achieve the three modes of operation. The data acquisition card (DAQ) and the External Function Generator deliver signals to the X- and Y-scanners via the Scanner driver box. The Switch box is only used in the sequential modes. The detected spectra from the CMOS camera are sent through a Camera Link bus to the image acquisition (IMAQ) card while the analog SLO signal is sent to the DAQ card. (taken from Marques *et al.* [1])

The line scanner (corresponding to the x-axis) is driven by a triangular waveform x_{sc} which is generated by the control software running on the workstation PC. The frame scanner (corresponding to the y-axis) can either be driven by an external function generator box (Hewlett-Packard 8116A, Palo Alto CA, USA) outputting a saw-tooth waveform, or through an adjustable DC voltage supplied by another of the DAQ's analogue outputs ($y_{\mathrm{sc}}\,[\mathrm{DC}]$). The external function generator is employed to synchronise the LabVIEW frame acquisition loop with the saw-tooth waveform generation.

Swapping between the two possible outputs is enabled through the use of a switch box, which is triggered by a TTL signal $\mathrm{TTL}_{\mathrm{sw}}$ created by the workstation and outputted through one of the DAQ's digital ports. The adjustable DC comes into effect when a single Oxz frame is needed on the OCT channel (B-scan), as this allows the user to map the position of the cursor placed over the SLO image to the corresponding B-scan being acquired. This implementation may or may not be needed, depending on the mode of operation chosen, as explained over the course of the next section.

Through another TTL line (TTL_x), the DAQ also drives the buffering of the spectra which will be used to form the B-scans. Both this TTL line and the SLO acquisition trigger are linked, which ensures that the two frames (OCT and SLO) are synced along one of their axes.

5.1.1 Timing and acquisition speed constraints

The operation of the OCT/SLO instrument depends on a set of constraints introduced by currently available hardware, whose parameters can be manipulated to sacrifice resolution for speed and vice-versa.

Line camera

The CMOS camera used in the OCT spectrometer allows for various acquisition settings [21]. The absolute maximum line rate attainable with this camera is $312\,\mathrm{kHz}$. This value is only attainable when several signal-enhancing features of the camera are turned off, namely: (1) the vertical and horizontal binning which, when combined, increase the effective size of the pixels in the detector array, quadrupling their area; and (2) the requirement to use a subset of the full 4096 range of pixels [21], therefore constricting the size of the projected spectrum onto the camera plane. Furthermore, at high line rates, the signal-to-noise ratio (SNR) diminishes, hence the choice of the line acquisition rate is decided as a trade-off between speed and sensitivity. Throughout all of the experimental work carried out, the camera was run at rates of between 50 and $100\,\mathrm{kHz}$, which allowed us to use several of the aforementioned features of the camera. Such rates determine an acquisition time per spectra of $\delta t_{\mathrm{OCT}} \sim 10 - 20\,\mu\mathrm{s}$.

Galvo-scanners

The inertia of the galvo-scanners *SXY* constrains the speed of the lateral scanning, hence the triangular waveform driving the line scanner (x) is limited to a frequency of $500\,\mathrm{Hz}$ to prevent heat and reliability issues [22].

Lateral resolution and maximum lateral range

Finally, there is also the issue of lateral resolution, which was discussed earlier in Section 3.4.2. Let us consider a beam focused on the patient's retina on a spot with a diameter of D_0, as determined by the Airy disc diameter. Then the maximum lateral size of the image is:

$$\Delta X = D_0 N_x. \tag{5.1}$$

Using Gaussian optics, D_0 can be approximated by the waist diameter w_0 at the centre of the Raleigh range. From Equation (3.43) it is possible to relate the numerical aperture of the eye with w_0. Assuming a scanning beam diameter of $D = 3\,\mathrm{mm}$ (and that the entrance pupil is wider than D), and an eye length of $f = 25\,\mathrm{mm}$, one obtains $\mathrm{NA} = n\frac{D}{2f} = 0.08$, where $n = 1.33$ (refractive index of water

at $\lambda_0 = 840\,\mathrm{nm}$). Substituting in Equation (3.43), a value of $w_0 = D_0 = 3.5\,\mu\mathrm{m}$ is obtained. This figure will necessarily be higher due to the aberrations present in the eye, hence we can assume $D_0 \sim 10\,\mu\mathrm{m}$.

If we consider a line scanning frequency of $500\,\mathrm{Hz}$, this means that a half-period is $1\,\mathrm{ms}$. Assuming that the line camera runs at $100\,\mathrm{kHz}$, one can only retrieve $N_x = N_S = 100$ adjacent A-scans during a half-period, which limits the lateral range to $N_S D_0 = 1\,\mathrm{mm}$. If the galvo-scanner amplitude is set to a value such that the scanning range is increased beyond $N_S D_0$, the system will undersample the object in terms of the optical resolution. In other words, the width of each electronic pixel along the lateral coordinate (i.e., the width of the A-scan column) is larger than the Airy disc diameter.

The SLO channel also introduces a limit to the lateral size, albeit a less constrained one: the photo-diode used has a bandwidth $f_{3\,\mathrm{dB}}$ of $100\,\mathrm{kHz}$, which determines a rise time $t_{\mathrm{rise}} = 3.5\,\mu\mathrm{s}$ for the impulses at the APD output. Considering the same line scanner speed ($500\,\mathrm{Hz}$) as before, this allows a greater number of lines $N_x\,[\mathrm{SLO}] = 280$ than the OCT channel, which is capped at $N_x = N_S = 100$ for CMOS camera acquisition time δt_{OCT} considered. This may be of interest if higher resolution SLO images are desired, even without pixel-to-pixel correspondence between the frames in the two channels.

5.1.2 Modes of operation

By taking all the constraints described over the previous section into consideration, we have devised three different modes of operation, each of them having varying degrees of pixel-to-pixel correspondence and allowable acquisition times. They are:

- a purely *simultaneous* mode, where the OCT frame is buffered during the acquisition of each of the confocal T-scans making up the SLO frame;
- a purely *sequential* mode, where the user can manually alternate "on-demand" between OCT and SLO acquisition;
- a *hybrid* mode, sequential in nature, but switching automatically between the acquisition of either channel and refreshing the two frames at the same time.

A schematic diagram of the timing and behaviour of these three different modes is shown in Figure 5.4.

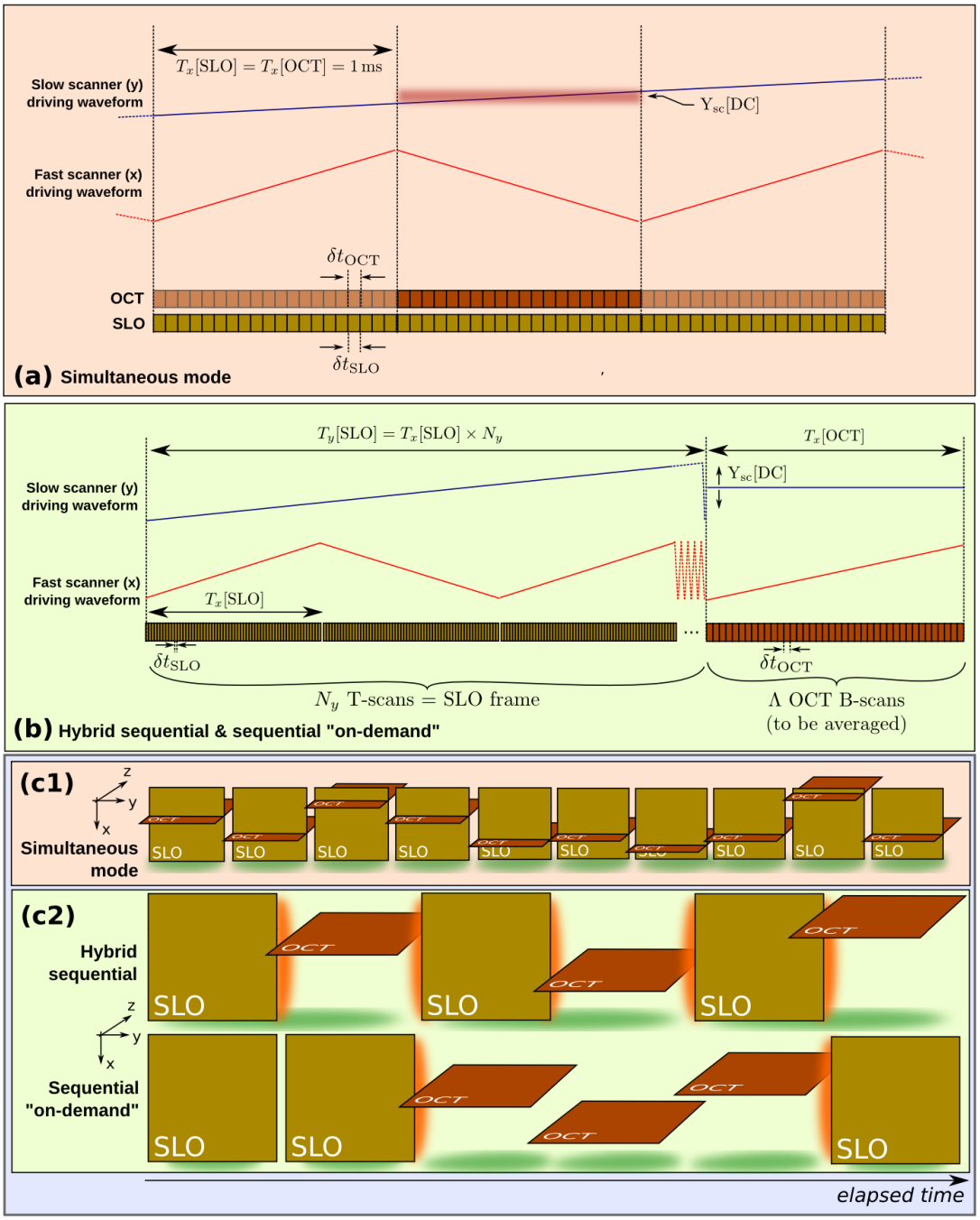

FIGURE 5.4: Diagram illustrating the timing and operation of the three different modes of operation: simultaneous (**(a)** and **(c1)**), sequential and hybrid (**(b)** and **(c2)**).

(a) and **(b)**: Scanner waveforms (x- and y-axis), with the sampling events for both OCT and SLO channels represented as orange/brown blocks corresponding, respectively, to the acquisition time δt_{OCT} for an OCT A-scan and δt_{SLO} for the SLO T-scan.

(c1) and **(c2)**: sequence of frames for all three regimes, where the green shadows show the frame refresh period, and the orange glow shows the instances when the system is switched between the two regimes (taken from Marques *et al.* [1]).

5.1.2.1 Simultaneous mode

In this mode, the system acquires an OCT B-scan frame *during* the SLO frame acquisition. In effect, the A-scans making up the B-scan are buffered at the same time as one of the confocal T-scans making up the full SLO image, as shown in Figure 5.4 (a).

The B-scan OCT image exhibits pixel-to-pixel correspondence with a line placed by a cursor over the *en-face* SLO image, whose y-coordinate is used to select the instant when the B-scan is buffered amongst all the confocal T-scans. The lateral size of either frame is equal, that is $N_x\,[\mathrm{SLO}] = N_x\,[\mathrm{OCT}] = N_S$. The frames corresponding to the data acquired over the two channels then refresh simultaneously.

This means, however, that the line/frame acquisition times in both channels are interdependent. Running the line camera present in the OCT spectrometer at $100\,\mathrm{kHz}$ yields $\delta t_{\mathrm{OCT}} = 10\,\mu\mathrm{s}$, and with a triangular signal of period $T_x = 2\,\mathrm{ms}$ being supplied to the line scanner, a total of 100 adjacent OCT A-scans are possible (each half of the waveform's period produces a B-scan), thus yielding an OCT frame with a 100×512 pixel resolution. The overall frame rate $f_y = 1/T_y$ is determined by the number of adjacent SLO T-scans acquired. If a square aspect ratio is desired then 100 T-scans are needed, producing a 100×100 pixel SLO image. T_y is then $1/2 T_x N_S = 100\,\mathrm{ms}$, which results in a frame rate of $10\,\mathrm{Hz}$. In reality, the frame rate has to be lowered to about $8\,\mathrm{Hz}$ due to the signal processing time.

As mentioned in Section 5.1.1 and detailed in Equation (5.1), by reducing the scanning time the transversal range is limited due to the resolution of the interface optics. Assuming $D_0 \sim 10\,\mu\mathrm{m}$, our lateral range under this mode of operation is limited to $\lesssim 1\,\mathrm{mm}$.

This mode of operation allows simultaneous imaging with pixel-to-pixel correspondence at fairly high refresh rates, but at the expense of the transversal size. It is more suitable, then, for small-scale retinal imaging, covering photoreceptor cells as shown in [23], with or without adaptive optics. If the lack of lateral resolution is not a concern, then the area covered by the scanning beam can be increased and this mode can be used as an assistive technique for retinal tracking, where only the major features (such as the fovea, optic nerve...) need to be recognisable, as their position will then be supplied to the tracking algorithm which will adjust the beam positioning accordingly, or suppress motion artefacts already present in the images. The frame rate achievable (up to $\sim 8\,\mathrm{Hz}$) makes this mode of operation tolerant to patient movement.

However, if a larger lateral size ($N_x > N_S$) is desired without compromising the optical resolution, or if the SNR needs to be increased (by relaxing the line camera acquisition constraints), this mode is no longer suitable. Achieving the

same lateral size in both channels beyond $N_x = N_S$ is only possible by allocating different time durations to each channel. This leads to two additional possible modes of operation, whereby the system operates in a single regime at any given time, as can be seen in Figure 5.4 (b).

For better SNR in the OCT channel, the line camera integration time was raised to $\delta t_{\mathrm{OCT}} = 20\,\mu$s. In addition, averaging can be performed at the expense of acquisition time by a factor of Λ, given by the number of averaged frames. Using $N_x \sim 100 - 1000$, with $\delta t_{\mathrm{OCT}} = 20\,\mu$s, $T_x\,[\mathrm{OCT}] \sim 2 - 20\,\mathrm{ms}$.

5.1.2.2 Sequential mode

In this mode of operation (schematically presented in Figure 5.4 (c2)), the system continuously alternates between different scanning speeds to acquire either SLO or OCT signals. Two sub-modes of operation have been implemented which differ in the fact that the switch can be either done automatically (top diagram, "*hybrid sequential*") or manually, given user input (bottom diagram, "*sequential on-demand*").

During the SLO regime (with a periodicity of $T_y\,[\mathrm{SLO}]$) the frame scanner is driven by a ramp which is part of a saw-tooth waveform and is generated by the external *FG* (Figure 5.3), with a 90% duty cycle to minimise the return dead time, since the SLO data does not require a comparable amount of time for processing (Figure 5.4 (b)).

When the system is switched to the OCT regime (either by user input or automatically by the acquisition software), the frame scanner is stopped at a vertical position selected by $Y_{sc}\,[\mathrm{DC}]$ which determines the y-coordinate of each B(A)-scan being displayed. In addition, the speed of the line scanner is reduced to allow for a larger N_x and an increased δt_{OCT}. Considering the maximum number of pixels $N_x = 280$ allowed by the APD bandwidth, the line scanner speed in the OCT regime is reduced to $f'_x = \dfrac{N_S}{N_x} f_x = 180\,\mathrm{Hz}$. If longer spectrometer exposure times are required, even lower frequency f'_x values are needed.

The "*sequential on-demand*" mode presents the obvious drawback of reduced tolerance to eye movements, given that the SLO image is no longer refreshed when the system is switched to OCT mode. However, this mode of operation allows for more freedom in setting the lateral image size and the OCT channel parameters, since the timing of each frame is not tied to the time constraints of the SLO channel. In essence, in this mode the system operates at independent frame rates, which may make it flexible enough to perform in an array of clinical

scenarios, where image quality and size in both channels are more important than the exact correspondence between the two images.

In the *"hybrid sequential"* mode, the pixel-to-pixel correspondence between the OCT and the SLO frames is improved by automatically switching between the two modes at the end of each period of the frame scanner, which reduces the occurrence of the aforementioned moving artefacts. Given that the time required to acquire one B(A)-scan $T_x\,[\mathrm{OCT}]$ is much smaller than the overall time necessary to buffer all the T-scan SLO lines (even when considering the transition between the two line scanning rates) an averaging feature is introduced whilst in the OCT regime, where an arbitrary number Λ of frames is acquired. $T_x\,[\mathrm{OCT}]$ increases linearly with Λ, and the maximum for this parameter is dependent on the period of the SLO regime, $T_y\,[\mathrm{SLO}]$, in order to satisfy the condition $\Lambda T_x\,[\mathrm{OCT}] < T_y\,[\mathrm{SLO}]$.

Moving artefacts notwithstanding, some variations in pixel-to-pixel correspondence may be observed due to the change in image size when switching from 500 to $180\,\mathrm{Hz}$ signal frequencies applied to the line scanner. This can be compensated for by a corresponding decrease in the voltage V_x applied to the line scanner in the OCT regime, in comparison with the value employed in the SLO regime. Such correction can be accurately calculated by using the position sensing signal outputted by the scanners' driver board.

5.1.3 Lateral size constraints

Depending on the mode of operation chosen, the maximum lateral image size attainable without loss of resolution varies according to the graph in Figure 5.5. The line across the graph corresponds to the special case where the lateral electronic pixel size δx matches the Airy disc diameter D_0. Above this line, the electronic pixel size is smaller than D_0, with the system over-sampling the signals captured; conversely, below the line $\delta x > D_0$ and the system under-samples the signals received. Note that the line scanner period is maintained at $1\,\mathrm{ms}$ for all SLO operations, but it might be modified during the OCT regime depending on the mode of operation chosen.

True pixel-to-pixel correspondence (red shaded region) is only attainable when operating in simultaneous mode, which limits the lateral image size to less than $1\,\mathrm{mm}$.

A degree of pixel-to-pixel correspondence is still achievable for $N_S < N_x < N_{\mathrm{SLO}}$, i.e. for $100 < N_x < 280$, if the correction to the lateral image size presented in Section 5.1.2.2 is employed to compensate for the swing variation of the line scanner with the changing frequency of the applied signal.

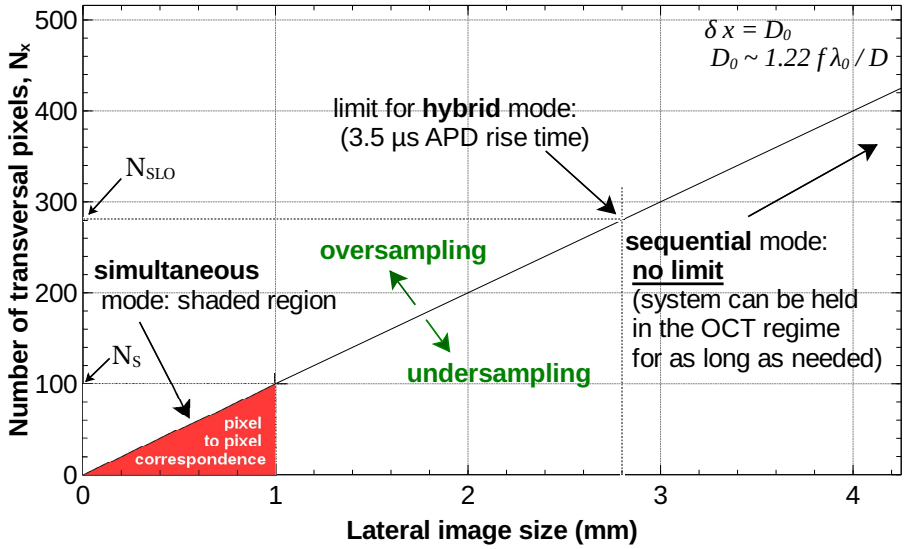

FIGURE 5.5: Relation between the number of pixels, N_x and the lateral image size, depending on the mode of operation applicable. The red shaded region corresponds to the settings which allow pixel-to-pixel correspondence between the OCT and SLO images, regime limited by $N_x = N_S$. Lateral image size is calculated using $N_x \cdot D_0$, with $D_0 \approx 10\,\mu\text{m}$ (taken from Marques *et al.* [1]).

For $N_x > 280$ the APD amplifier starts behaving as a low-pass filter due to its finite rise time, hence the line rate must be reduced in order to maintain the lateral resolution whilst allowing for a larger lateral size. This will however have an impact on the frame refresh rate, making the system more prone to motion-induced artefacts.

5.2 Results

The apparatus described in this chapter was first of all benchmarked in terms of the optical power arriving at each detector. Then, the effect of the spatial filter adjustment on the OCT channel visibility profile was evaluated. Afterwards, retinal images were obtained in both simultaneous and sequential modes of operation with varying degrees of lateral size range, frame rate, and pixel-to-pixel correspondence.

5.2.1 Optical power considerations

The beam-splitter *BS* employed to couple the beams from the two arms of the interferometer (Figure 5.2) has a splitting ratio of 80/20. As mentioned in Section

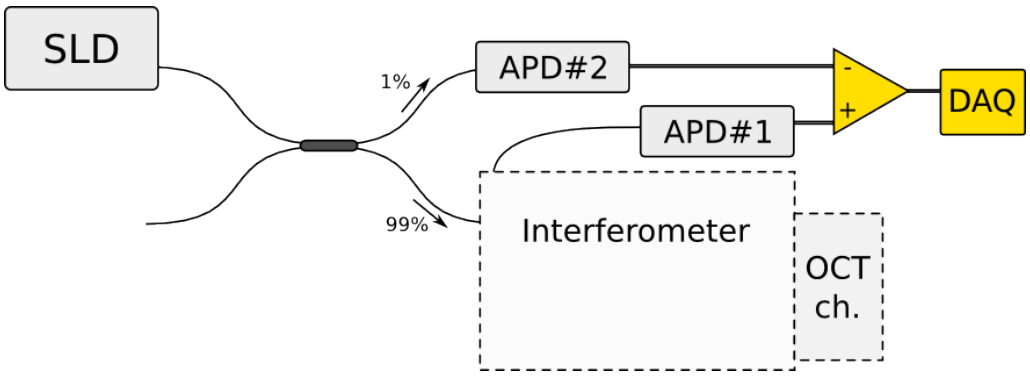

FIGURE 5.6: Balanced configuration for the SLO channel, where 1% of the source optical power was subtracted from the signal arriving at the SLO detector (APD#1) in order to prevent the occurrence of DC noise on the SLO signal.

5.1, 80% of the optical power from the sample arm is directed toward the spectrometer, hence the 20% fraction, which is diverted towards *C6*, will be employed to create the SLO frame.

When performing retinal imaging, the typical figures for the optical power returning from the patient's eye are in the μW range, hence the necessity to employ an avalanche photo-diode (*APD*) to detect such low powers.

Beyond the fact that only 20% of the returning optical power is directed to the SLO channel, there is also the issue of the spatial filter that may leak some of the large power from the reference arm beam. Moreover, the actual injection of the collimated beam into the multi-mode fibre *MMF* is subject to additional losses (power efficiency is around 70%). This configuration, using a multi-mode fibre and spatial filtering, was preferred over that of direct illumination of the *APD*, as it allows more flexibility in the imaging procedure. In free space, the *APD* would normally be picking up some of the ambient light and introducing an offset on the acquired signal.

In order to try to remove part of the DC noise from the source, which would otherwise degrade the SLO signal, a balanced configuration was devised (Figure 5.6). A 99/1 coupler was placed between the optical source and the interferometer, with a very small amount of power being directed to an additional *APD* (identical to the first one). The difference between the output of these two APDs was then acquired by the digitiser, effectively placing the confocal component within the dynamic range of the detector.

With regards to the OCT channel, it was necessary to ensure that the spot size (corresponding to a single wavelength) on the *CMOS* array matched the size of the pixel ($10 \times 20\,\mu$m if no horizontal averaging is performed on the camera).

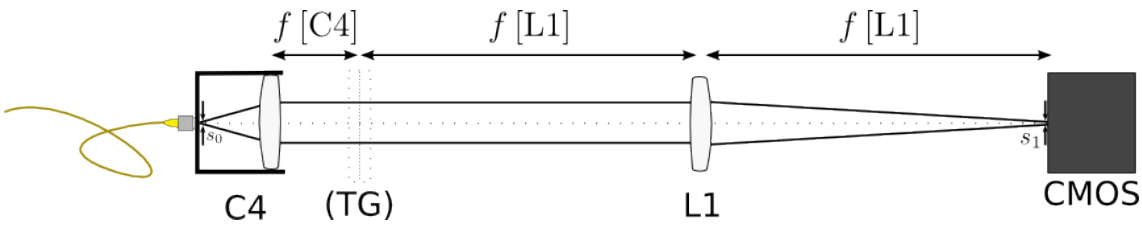

FIGURE 5.7: Magnification of the spot size s_1 on the vertical plane (no diffraction) due to different focal lengths in the collimating and focusing lenses, f [C4] and f [L1] respectively.

Departing from a single-mode fibre core ($s_0 \sim 8\,\mu$m), the diverging beam is collimated with a $f[\mathrm{C4}] = 18\,$mm aspheric collimator (*C4*), with the resulting collimated beam traversing the diffraction grating and being refocused on the *CMOS* array via *L1*. In other words, the core size s_0 is projected onto the camera with a spot size s_1, given by the magnification M, which is calculated from the ratio of the focal lengths of the two lenses, *C4* and *L1*, $M = \dfrac{f\,[\mathrm{L1}]}{f\,[\mathrm{C4}]}$ (Figure 5.7).

By increasing the focal length of *L1* it is possible to increase the overall depth axial range by narrowing the transfer function of the spectrometer (lower optical spectral bandwidth per pixel), but at the same time this increases the spot size s_1 on the camera due to the change in the magnification M of the optical system. Thus, the spot size for a single wavelength is $s_1 = M \cdot s_0$, and this value should be kept under $20\,\mu$m. A compromise has to be found between the fall-off depth and the spectrum projection efficiency. Ultimately, $f\,[\mathrm{L1}]$ was chosen to be $150\,$mm, which gives $s_1 \sim 60\,\mu$m. There is still a significant loss in optical power, however, given that the beam shape is Gaussian, the edges present considerably less power than the centre; moreover, the value of $f\,[\mathrm{C4}]$ has to be kept small due to the fact that narrow beam widths ($\sim 2 - 3\,$mm) are needed to ensure total separation between the beams, and in this way to have only the sample arm power arriving at the SLO channel detector.

5.2.2 OCT sensitivity with the spatial filter in place

Figure 5.8 (i) shows the sensitivity profile versus OPD. The launcher *TS1* was laterally moved by $\sim 0.25\,$mm to create the gap necessary for TB implementation, which will produce a shift in the sensitivity peak from $\mathrm{OPD} = 0$ to $-1.8\,$mm as shown by the red circles and green triangles in the graph. The TB sensitivity profile conserves its width from the non-TB case, but the maximum sensitivity reduces by about $2\,$dB. However, at larger depths the gain in relation to the standard Sp-OCT case exceeds $6\,$dB.

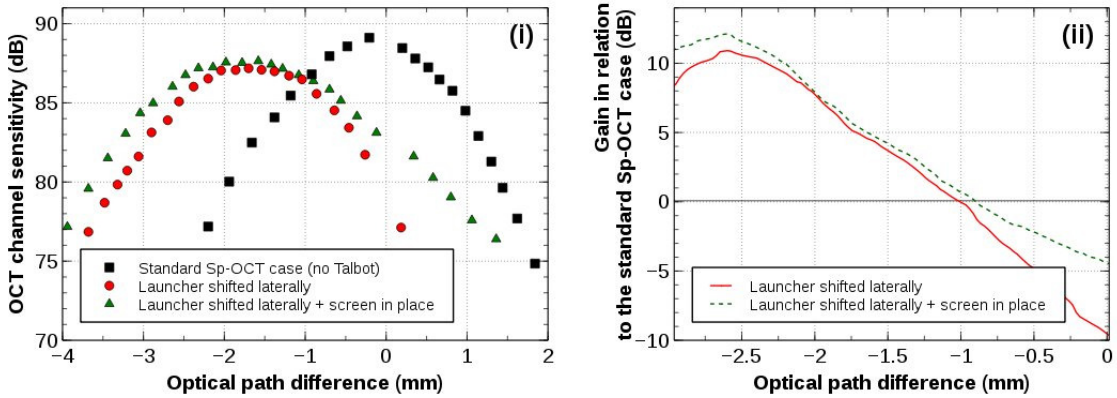

FIGURE 5.8: **(i)** OCT channel sensitivity. Black squares: conventional Sp-OCT, with the beam centres spatially coinciding; Red circles: one of the launchers was moved by $\sim 0.25\,\mathrm{mm}$ to produce Talbot bands; Green triangles: one of the launchers was moved by $\sim 0.25\,\mathrm{mm}$ to produce Talbot bands and a screen (attached to *TS2*) was placed on the edge of the laterally-shifted reference arm beam, as shown in Figure 5.2;
(ii) Relative sensitivity for the Talbot bands configurations with respect to the conventional Sp-OCT for: launcher shifted laterally (red solid line), launcher shifted laterally and screen in place (green dashed line). (taken from Marques *et al.* [1])

The green curve shows the TB sensitivity versus OPD with the screen attached to *TS2* in place. As demonstrated in Section 3.2.1.3, the sensitivity profile is given by the correlation of the power distribution within the footprints of the two beams incident on the diffraction grating (not considering the effects of the detector's sampling resolution, the *sinc* function). Due to the existence of diffraction on the screen edge, the power distribution of the reference beam is changed to a wider footprint with secondary lobes. Such behaviour was documented in [18], where a screen was also used to modify the distribution of power in the reference beam across the grating. Therefore, a slight improvement in the sensitivity profile width is observed.

The peak sensitivity value was measured following the procedure described in [24] for the non-TB case (black curve, Figure 5.8 (i)) and with the OPD set at $-1\,\mathrm{mm}$. For the two integration time settings used in this study, $\delta t_{\mathrm{OCT}} = 10$ and $20\,\mu\mathrm{s}$, sensitivities of $82\,\mathrm{dB}$ and $87\,\mathrm{dB}$ are obtained, respectively.

5.2.3 Imaging the human retina with the two modes of operation

Figures 5.9 and 5.10 present images obtained with the system running under both modes of operation, simultaneous and hybrid sequential, respectively. These images were obtained *in-vivo* from the eye of a volunteer, and cover different

features in the eye, those being the foveal and optic nerve regions. Ethical approval was obtained from the Faculty of Sciences' Ethics Committee, and the optical power at eye level was less than $750\,\mu\mathrm{W}$ (on a single point, without raster-scanning the beam), in accordance with the ANSI standards [25].

In Figure 5.9, the system is being refreshed at $3\,\mathrm{Hz}$, with the line scanner being driven by a triangular signal of period $2\,\mathrm{ms}$ and the CMOS camera's integration time set at $10\,\mu\mathrm{s}$. Two possibilities are presented: small-size imaging with a lateral size equal to or lower than the optical transversal resolution limit, which is constrained by the limited number of lateral pixels achievable as explained above; and large scale imaging, whereby the system still operates with the same number of pixels and therefore the images are under-sampled in the transversal direction.

In each of the boxes in Figure 5.9, SLO frames are shown at the top with a (digital) resolution of 100×280 pixels (width $\times$ height). OCT frames are shown in the bottom part with a resolution of 100×150 pixels (width $\times$ depth; the depth-dimension was cropped from the original 512 axial pixels in order to emphasise the region under analysis).

In Figure 5.9 (i) to (iii) the SLO images have a lateral size of about $500 \times 500\,\mu\mathrm{m}^2$, therefore the pixel mesh is denser than the actual optical resolution of the system. In (i) the edge of the optical nerve head is shown (top left corner).

In (ii) the volunteer looked half-way between the fovea and the optic nerve. The small-size imaging allows one to distinguish individual photo-receptor cells when the eccentricity of the location on the retinal image exceeds 5 degrees. For such eccentricity, the cone spacing is larger than $\sim 10\,\mu\mathrm{m}$ [26]. In (iii) the photo-receptor cells are still visible, along with the choroid layer (yellow arrow).

Larger values for the lateral image size were also considered. In Figure 5.9 (iv), the line scanner was driven with $\sim 600\,\mathrm{mVpp}$ determining about $2\,\mathrm{mm}$ lateral size. This size is larger than that obtained by multiplying the Airy disc diameter $D_0 \sim 10\,\mu\mathrm{m}$ with the number of transversal pixels $N_x = 100$, as employed in the acquisition procedure, hence the image is obviously under-sampled in the lateral direction, as commented above in connection to Figure 5.5.

Figure 5.9 (v) contains an optically under-sampled OCT image as well, since the lateral size is over $1\,\mathrm{mm}$ in the line scanner's direction. The focal region lays on the shallower retinal tissue, hence the corresponding OCT profile only maps the x-coordinates where the optic nerve is situated.

Features are sufficiently well seen in both columns, however due to the high speed at which the CMOS camera was run the OCT images are considerably noisier. Even so, contours and main layers are easily identified whilst operating at this frame rate.

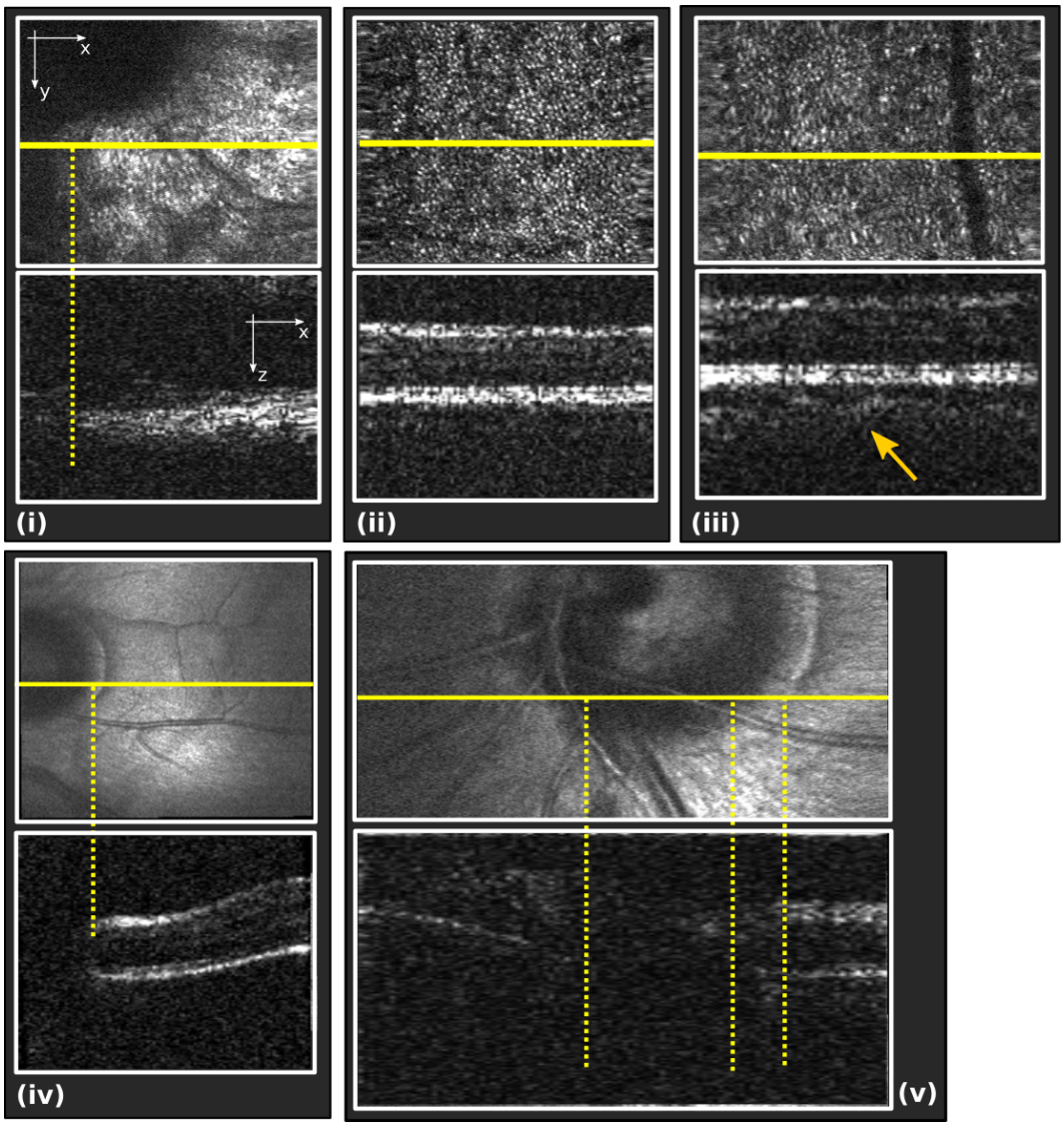

FIGURE 5.9: Retinal images obtained while running the system in the simultaneous mode of operation at a frame rate of $\approx 3\,\mathrm{Hz}$. SLO frames (top image in each frame) are 100×280 pixels and OCT frames (bottom image in each frame) are 100×512 pixels (here cropped to 100×150 pixels to emphasise the region under analysis).
(i) edge of the optic nerve head, lateral size $\approx 500 \times 500\,\mu\mathrm{m}^2$; **(ii)** region between the optic nerve and the fovea, in an area showing larger photo-receptors ($\approx 10\,\mu\mathrm{m}$), lateral size $\approx 500 \times 500\,\mu\mathrm{m}^2$; **(iii)** pair of SLO and OCT images (lateral size $\approx 500 \times 500\,\mu\mathrm{m}^2$) featuring a blood vessel; the choroid (yellow arrow) is visible below the nerve fibre layer; **(iv)** optically under-sampled OCT image of the area between the foveal region and the optic nerve, lateral image size $\approx 2 \times 2.5\,\mathrm{mm}^2$; **(v)** optically under-sampled OCT image of the optic nerve, the region in focus is the shallower retinal layer, lateral size $\approx 1.5 \times 0.8\,\mathrm{mm}^2$. The OCT B-scans correspond to the location of the horizontal lines overlaid on the SLO C-scans (taken from Marques *et al.* [1]).

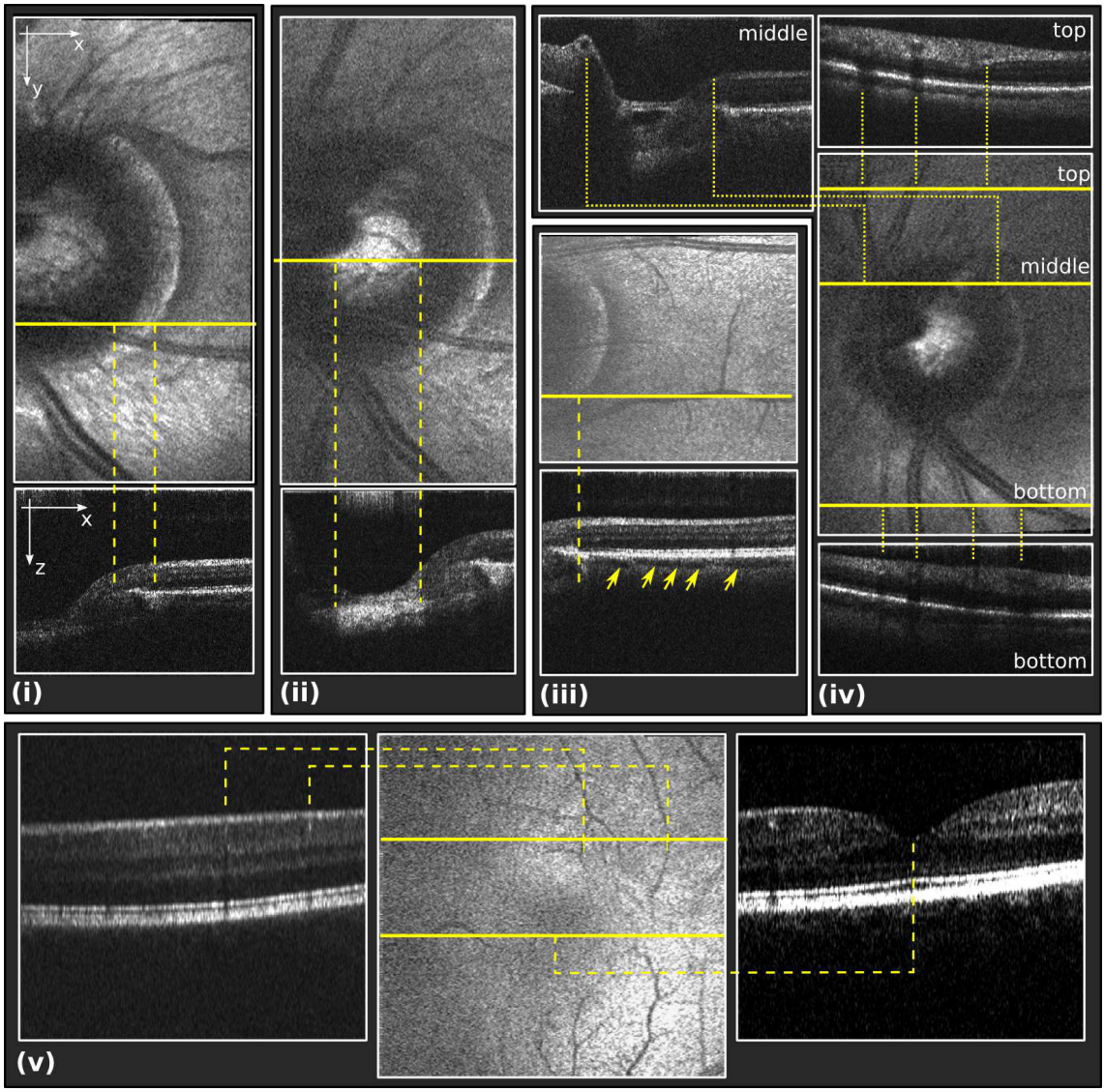

FIGURE 5.10: Images obtained with the OCT/SLO set-up operating in hybrid sequential mode (SLO top, OCT bottom). The images in (i), (ii) and (iii) have sufficient sampling whilst the images in (iv) and (v) are under-sampled in the transversal direction.

(i) and **(ii)**: area between the optic nerve and the shallower retinal tissue (lateral size $2.6 \times 5.2\,\mathrm{mm}^2$); **(i)**: focus on shallow layers; **(ii)**: focus at the *lamina cribrosa*'s depth; **(iii)**: area located in the vicinity of the optic nerve, the OCT B-scan cut intercepts a blood vessel along its course (yellow arrows), lateral size $2.6 \times 5.2\,\mathrm{mm}^2$; **(iv)**: detail of the optic nerve region ($5 \times 6\,\mathrm{mm}^2$ lateral size) emphasizing several positions of the cursor with varying features selecting the associated OCT B-scans; **(v)**: fovea region, lateral size $5 \times 5\,\mathrm{mm}^2$.

The OCT B-scans are obtained from an average of $\Lambda = 4$ OCT frames. The positions of the OCT cuts along the y-axis correspond to the locations of the horizontal lines overlaid on the SLO C-scans (taken from Marques *et al.* [1]).

Figure 5.10 features the results obtained with the OCT/SLO system operating in the hybrid sequential mode. During the OCT regime, the lateral scanning duration of the line scanner is $20\,\mathrm{ms}$ and the camera's integration time was increased to $20\,\mu\mathrm{s}$ (acquisition rate set at $50\,\mathrm{klines/s}$), which enabled more pixels to be used in the lateral dimension of the OCT B-scans. Images of the foveal and optic nerve regions are presented, again with two different sizes being employed: a medium lateral size of $2.6\,\mathrm{mm}$, where the lateral pixel size in the SLO image is of the same order of magnitude as the optical transversal resolution and a larger lateral size of $5\,\mathrm{mm}$, where the SLO images are under-sampled. For both sizes, the same number of lateral electronic pixels $N_x \sim 500$ are used for both OCT and SLO regimes.

Figures 5.10 (i) and (ii) differ mostly on the location of the focal point (in depth) - the former presents better defined retinal surfaces, whereas the latter emphasises the *lamina cribosa*, deep within the optic nerve. The lateral size of these images ($2.6 \times 5.2\,\mathrm{mm}^2$) meets the sampling criteria, and the corresponding OCT images are better defined than in the previous case since the exposure time is twice as large, thus improving the SNR.

In Figure 5.10 (iv) several OCT B-scan slices taken at different y positions are shown with their corresponding SLO image. These cover the optic nerve region with a large lateral size of $\sim 5 \times 6\,\mathrm{mm}^2$.

A good match was found between the features visible in the SLO image and those seen in the corresponding OCT B-scans. The correspondence is also clear in (iii) and (v), the former with a significant intercept of a sub-retinal blood vessel (highlighted by the yellow arrows overlaid on the image) and the latter with a good correspondence of features from the foveal region.

5.3 Final conclusions

A spectrometer-based Talbot Bands OCT system with SLO technology was devised and characterised in this chapter. This system is compatible with the limitations imposed by the current technology in terms of the speed attainable by line cameras employed in the spectrometer. While resonant transversal scanners can work faster than the galvo-scanners used in the system here presented, the bottleneck of the operation is still the A-scan rate of the line camera. Moreover, even though resonant scanners and polygon mirrors can attain higher scanning speeds, they are limited to a fixed rate throughout the acquisition. This prevents the implementation of the sequential methods described in Section 5.1.2.2, where

the scanners need to be slowed down in the OCT regime (in comparison with the rates for the SLO regime) in order to acquire an increased number of A-scans.

The bandwidth of the SLO channel can in principle be increased, allowing more optical pixels to be scanned within the same $1\,\mathrm{ms}$ ramp. However, such increase would have ruled out simultaneous operation with the OCT channel.

The Talbot Bands configuration presented here allows the deflection of optical signal towards the SLO channel with little loss introduced in the OCT channel, however the three modes of operation presented in this chapter can also be implemented in any other spectrometer-based OCT system coupled with an SLO channel. In addition, the Talbot Bands configuration breaks the symmetry of the visibility profile (as explained in Section 3.2.1) by shifting the peak of the C_{TB} profile to larger depths, attenuating the mirror terms in the same process. Given that the spectrometer's resolution is unaffected by this procedure (which is responsible for the *sinc*-shaped profile, as explained in the same section), the overall sensitivity is reduced by $\approx 10\,\mathrm{dB}$ at depths below $0.5\,\mathrm{mm}$. This, however, does not present a disadvantage when comparing this approach to conventional Sp-OCT systems, since in these systems one normally avoids the region close to OPD=0, keeping it as a buffer to cover fluctuations of the axial eye position. What this actually means is that the region where the sensitivity is at its largest value in conventional systems is avoided, hence a compromise on the maximum sensitivity attainable by using Talbot bands, factoring in the drop-off caused by the spectrometer, is adequate for this approach.

Some additional loss of sensitivity is also incurred in practice when moving from conventional Sp-OCT to a Talbot Bands configuration, given that one needs to secure similar polarisation and dispersion in the two arms which are coupled in bulk at the beam-splitter. Such problems do not usually arise in conventional systems since they often employ fibre-based couplers to combine the output of the two arms of the interferometer. More work is necessary to optimise Talbot Bands configurations in order to achieve similar efficiency to that of conventional Sp-OCT configurations. It would be ideal if the output of the two arms could be coupled without resorting to a bulk beam-splitter while keeping the Talbot bands functionality, which is a feature to be addressed in the next chapter (Chapter 6), where a novel spectrometer design coupling the two beams within the spectrometer itself is presented.

References

[1] M. J. Marques, A. Bradu, and A. G. Podoleanu, "Towards simultaneous talbot bands based optical coherence tomography and scanning laser ophthalmoscopy imaging", *Biomed. Opt. Express*, vol. 5, no. 5, p. 1428, Apr. 2014, ISSN: 2156-7085. DOI: 10.1364/BOE.5.001428.

[2] M. J. Marques, A. Bradu, and A. G. Podoleanu, "Optical coherence tomography and scanning laser ophthalmoscopy: approaches to dual-channel retinal tissue imaging", in *Frontiers in Optics*, Optical Society of America, 2014, FTu2F–3. [Online]. Available: http://www.osapublishing.org/abstract.cfm?uri=FiO-2014-FTu2F.3.

[3] L. D. Harris, R. A. Robb, T. S. Yuen, and E. L. Ritman, "Display and visualization of three-dimensional reconstructed anatomic morphology: experience with the thorax, heart, and coronary vasculature of dogs.", *J. Comput. Assist. Tomogr.*, vol. 3, no. 4, pp. 439–46, Aug. 1979, ISSN: 0363-8715. [Online]. Available: http://www.ncbi.nlm.nih.gov/pubmed/379055.

[4] *3d oct-2000 spectral domain oct — topcon medical systems, inc.* [Online]. Available: http://www.topconmedical.com/products/3doct2000.htm.

[5] A. G. Podoleanu and D. A. Jackson, "Combined optical coherence tomograph and scanning laser ophthalmoscope", *Electron. Lett.*, vol. 34, no. 17, pp. 1088–1090, 1998. [Online]. Available: http://ieeexplore.ieee.org/xpls/abs%5C_all.jsp?arnumber=684353.

[6] A. G. Podoleanu and R. B. Rosen, "Combinations of techniques in imaging the retina with high resolution", *Prog. Retin. Eye Res.*, vol. 27, no. 4, pp. 464–499, 2008.

[7] M. Pircher, E. Götzinger, and H. Sattmann, "In vivo investigation of human cone photoreceptors with slo/oct in combination with 3d motion correction on a cellular level", *Opt. Express*, vol. 18, no. 13, pp. 13 935–13 944, 2010. [Online]. Available: http://www.ncbi.nlm.nih.gov/pmc/articles/PMC2976031/.

[8] "Oct/slo - optos", [Online]. Available: http://www.optos.com/en-GB/Products/Ultra-widefield-imaging/OCT-imaging/OCTSLO.

[9] S. N. Markowitz and S. V. Reyes, "Microperimetry and clinical practice: an evidence-based review", *Can. J. Ophthalmol. / J. Can. d'Ophtalmologie*, 2012. [Online]. Available: http://www.sciencedirect.com/science/article/pii/S0008418212001202.

[10] K. V. Vienola, B. Braaf, C. K. Sheehy, Q. Yang, P. Tiruveedhula, D. W. Arathorn, J. F. de Boer, and A. Roorda, "Real-time eye motion compensation for oct imaging with tracking slo.", *Biomed. Opt. Express*, vol. 3, no. 11, pp. 2950–63, Nov. 2012, ISSN: 2156-7085. DOI: 10.1364/BOE.3.002950. [Online]. Available: http://www.pubmedcentral.nih.gov/articlerender.fcgi?artid=3493227%5C&tool=pmcentrez%5C&rendertype=abstract.

[11] F. Larocca, D. Nankivil, S. Farsiu, and J. A. Izatt, "Handheld simultaneous scanning laser ophthalmoscopy and optical coherence tomography system.", *Biomed. Opt. Express*, vol. 4, no. 11, pp. 2307–21, Jan. 2013, ISSN: 2156-7085. DOI: 10.1364/BOE.4.002307. [Online]. Available: http://www.pubmedcentral.nih.gov/articlerender.fcgi?artid=3829529%5C&tool=pmcentrez%5C&rendertype=abstract.

[12] D. X. Hammer, N. V. Iftimia, T. E. Ustun, J. C. Magill, and R. D. Ferguson, "Dual oct/slo imager with three-dimensional tracker", in *Ophthalmic Technol. XV*, F. Manns, P. G. Soederberg, A. Ho, B. E. Stuck, and M. Belkin, Eds., vol. 5688, Proceedings of SPIE Vol. 5688, Apr. 2005, pp. 33–44. DOI: 10.1117/12.592762. [Online]. Available: http://proceedings.spiedigitallibrary.org/proceeding.aspx?articleid=1323404.

[13] A. Bradu, L. Ma, J. W. Bloor, and A. G. Podoleanu, "Dual optical coherence tomography/fluorescence microscopy for monitoring of drosophila melanogaster larval heart", *J. Biophotonics*, vol. 2, no. 6-7, pp. 380–388, 2009.

[14] K. Komar, P. Stremplewski, M. Motoczyńska, M. Szkulmowski, and M. Wojtkowski, "Multimodal instrument for high-sensitivity autofluorescence and spectral optical coherence tomography of the human eye fundus", *Biomed. Opt. Express*, vol. 4, no. 11, p. 2683, Oct. 2013, ISSN: 2156-7085. DOI: 10.1364/BOE.4.002683. [Online]. Available: http://www.opticsinfobase.org/abstract.cfm?URI=boe-4-11-2683.

[15] Y. K. Tao, S. Farsiu, and J. a. Izatt, "Interlaced spectrally encoded confocal scanning laser ophthalmoscopy and spectral domain optical coherence tomography.", *Biomed. Opt. Express*, vol. 1, no. 2, pp. 431–440, Jan. 2010, ISSN: 2156-7085. DOI: 10.1364/BOE.1.000431. [Online]. Available: http://www.pubmedcentral.nih.gov/articlerender.fcgi?artid=3017990%5C&tool=pmcentrez%5C&rendertype=abstract.

[16] A. Bradu and A. G. Podoleanu, "Attenuation of mirror image and enhancement of the signal-to-noise ratio in a talbot bands optical coherence tomography system", *J. Biomed. Opt.*, vol. 16, p. 76 010, 2011.

[17] P. Bouchal, A. Bradu, and A. G. Podoleanu, "Gabor fusion technique in a talbot bands optical coherence tomography system", *Opt. Express*, vol. 20, no. 5, pp. 5368–5383, 2012.

[18] M. Hughes, D. Woods, and A. G. Podoleanu, "Control of visibility profile in spectral low-coherence interferometry", *Electron. Lett.*, vol. 45, no. 3, pp. 182–183, 2009.

[19] D. Woods and A. G. Podoleanu, "Controlling the shape of talbot bands' visibility", *Opt. Express*, vol. 16, no. 13, pp. 9654–9670, 2008.

[20] S. Makita, T. Fabritius, and Y. Yasuno, "Full-range, high-speed, high-resolution 1-μm spectral-domain optical coherence tomography using bm-scan for volumetric imaging of the human posterior eye", *Optics express*, vol. 16, no. 12, pp. 8406–8420, 2008. [Online]. Available: https://www.osapublishing.org/abstract.cfm?uri=oe-16-12-8406.

[21] B. Potsaid, I. Gorczynska, V. J. Srinivasan, Y. Chen, J. Jiang, A. Cable, and J. G. Fujimoto, "Ultrahigh speed spectral/fourier domain oct ophthalmic imaging at 70,000 to 312,500 axial scans per second", *Opt. Express*, vol. 16, no. 19, pp. 15 149–15 169, 2008.

[22] V.-F. Duma, K.-s. Lee, P. Meemon, and J. P. Rolland, "Experimental investigations of the scanning functions of galvanometer-based scanners with applications in oct.", *Appl. Opt.*, vol. 50, no. 29, pp. 5735–49, Oct. 2011, ISSN: 1539-4522. [Online]. Available: http://www.ncbi.nlm.nih.gov/pubmed/22015369.

[23] M. Pircher, B. Baumann, E. Götzinger, and C. K. Hitzenberger, "Retinal cone mosaic imaged with transverse scanning optical coherence tomography.", *Opt. Lett.*, vol. 31, no. 12, pp. 1821–3, Jun. 2006, ISSN: 0146-9592. [Online]. Available: http://www.pubmedcentral.nih.gov/articlerender.fcgi?artid=2956974%5C&tool=pmcentrez%5C&rendertype=abstract.

[24] R. Leitgeb, C. K. Hitzenberger, A. F. Fercher, *et al.*, "Performance of fourier domain vs. time domain optical coherence tomography", *Opt. Express*, vol. 11, no. 8, pp. 889–894, 2003.

[25] A.N.S.Institute, "Safe use of lasers", ANSI Z 136.1–2000, American National Standards Institute, Tech. Rep., 2007, ANSI Z 136.1–2000.

[26] D. Merino, J. L. Duncan, P. Tiruveedhula, and A. Roorda, "Observation of cone and rod photoreceptors in normal subjects and patients using a new generation adaptive optics scanning laser ophthalmoscope.", *Biomed. Opt. Express*, vol. 2, no. 8, pp. 2189–201, Aug. 2011, ISSN: 2156-7085. DOI: 10.1364/BOE.2.002189. [Online]. Available: http://www.pubmedcentral.nih.gov/articlerender.fcgi?artid=3149518%5C&tool=pmcentrez%5C&rendertype=abstract.

Chapter 6

Dual-input spectrometer for White Light Interferometry

Author's note: some parts of this Chapter are based on a peer-reviewed publication [1] published by the author in 2015.

Contents

THIS project involved developing a novel Talbot Bands WLI configuration in which two tilted gratings replaced the splitter normally used for recombining the beams from the two interferometer arms.

These two beams are launched by two fibre leads tightly brought together whose bare ends are placed at the front focal plane of a single collimating lens. As a particularity of the configuration, the two fibre ends are slightly off-axis, and therefore the collimated beams emerging from a lens behind them are not parallel. Thus, a gap between them is created, and the larger the distance the two diffraction gratings are placed from the lens, the larger the gap. This is used to create a configuration to perform Talbot Bands, similar to those observed in previous publications [2–5] and described in detail in Section 3.2.1.

In addition to the Talbot Bands, given the geometry of the configuration a total elimination of mirror terms is achieved. The effects of several geometrical parameters on the visibility profiles *versus* the optical path difference (OPD) between the two interferometer arms are studied and the results obtained are compared to a theoretical model.

6.1 Introduction

As presented in Section 3.2.1 and documented in many previous reports [6–9], Talbot bands (TB) represent a particular case of modulation of the channelled spectrum at the output of an interferometer illuminated by a broadband optical source. Provided that no overlap is present between the two beams, a TB configuration can determine which optical path of the two interfering beams is shorter (or longer) than the other one, thus addressing the ambiguity specific to frequency-domain WLI as described in Section 3.1. Moreover, unlike the other methods described in the same Section, a TB configuration only requires a single spectral acquisition and no post-processing.

A Mach-Zehnder (MZ) configuration may be employed for WLI if modulators are to be used in its arms [10]. Additionally, in order to implement a TB-based system such as the ones described in [2–5] a MZ configuration *must* be used, as independent control over the degree of overlapping of the projections of the two beams over the diffraction grating is required. In all cases described, a splitter or a combination of splitters are required to direct the output of the two interferometer arms towards the spectrometer.

In this chapter, a configuration which removes the need for the last splitter before the spectrometer is presented. This is achieved by replacing the splitter with a pair of tilted diffraction gratings which are being illuminated by the two collimated beams arising from the two arms of the interferometer. Since these beams originated from two fibre ends which are slightly off-axis, their paths diverge from each other, and by adjusting the distance between the fibre ends and the two diffraction gratings it is possible to adjust the separation between the two beam spots on the gratings, as an essential parameter in controlling the Talbot bands.

Not only that it is possible to create an equivalent TB configuration to those presented in [2–5], but given the fact that each diffraction grating has its angle adjusted to one of the beams, if the distance between the fibre ends and the diffraction gratings is such that the projected spots partly overlap, mirror terms are not observed, which is not the case with previously reported [2–5] TB systems.

6.2 Set-up description

As shown in Figure 6.1, a MZ interferometer has been implemented to validate this configuration. The interferometer employs two directional couplers: S1 splits the optical power from the source (SLD, Superlum, Cork, Ireland, $\lambda_0 = 831.1$ nm,

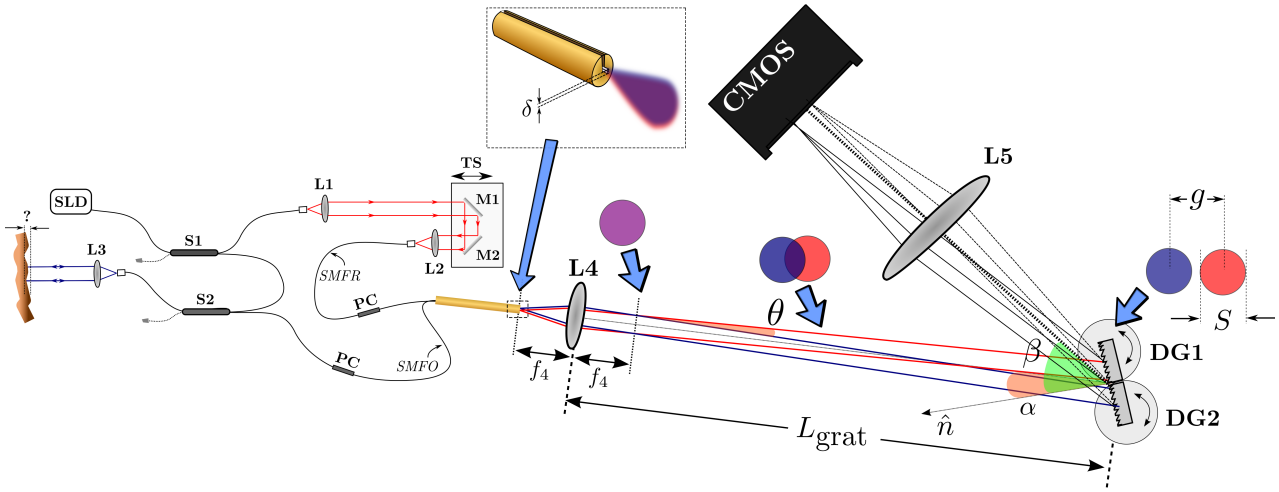

FIGURE 6.1: Experimental set-up. **SLD**, super-luminiscent diode (Superlum SLD-381-HP1-DIL-SM-PD, $\lambda_0 = 831.1\,\mathrm{nm}$, $\Delta\lambda = 16\,\mathrm{nm}$, $\sim 10\,\mathrm{mW}$ output power); **S1-2**, fibre-based directional couplers; **L1-5**, achromatic lenses; **TS**, translation stage (Aerotech Unidex 11); **M1-2**, flat silver mirrors; **PC**, fibre-based polarisation controllers; **DG1-2**, ruled diffraction gratings operating in reflection, detailed in Figure 6.2 (Thorlabs GR25-1210, $1200\,\mathrm{l/mm}$ at $1\,\mu\mathrm{m}$); **CMOS**, line camera pixel array (Basler sprint spl-140km, $140\,\mathrm{kHz}$ maximum line rate at full range). Inset: the two output fibres (*SMFO* and *SMFR*) aligned inside the groove, with a distance δ between the two fibre cores. (taken from Marques *et al.* [1])

$\Delta\lambda = 16$ nm, ~ 10 mW maximum output power) between the two arms, object and reference, and S2, which diverts and collects the light from the object via achromatic lens L3. In the reference arm, achromatic lenses L1 and L2 are used to route a collimated beam between two silver mirrors, M1 and M2, which are placed on a motorised translation stage TS (Aerotech Unidex II, Hampshire, England), employed to adjust the reference arm length and thus vary the frequency modulation of the channelled spectrum, enabling the study of the visibility profile of the spectrometer for different OPD values.

Lens L2 focuses the collimated beam into a single-mode optical fibre, SMFR, which is placed in a groove (see inset in Figure 6.1) together with the object arm fibre SMFO, brought from S2. Both fibres are closely laid together inside the groove, with their plastic buffers removed to minimise the distance δ between their tips. These are placed at the front focal plane of lens L4, so that two collimated beams emerge from the lens with their paths slightly diverging from each other. Each beam then travels to a diffraction grating wherefrom the diffracted fan of rays is made convergent for each individual spectral component on a subset of the pixel array of the line camera CMOS via lens L5.

Due to the gap δ between the two fibre apertures, the two beams intersect at a distance f_4 from lens L4, corresponding to its back focal plane. Due to the fact that

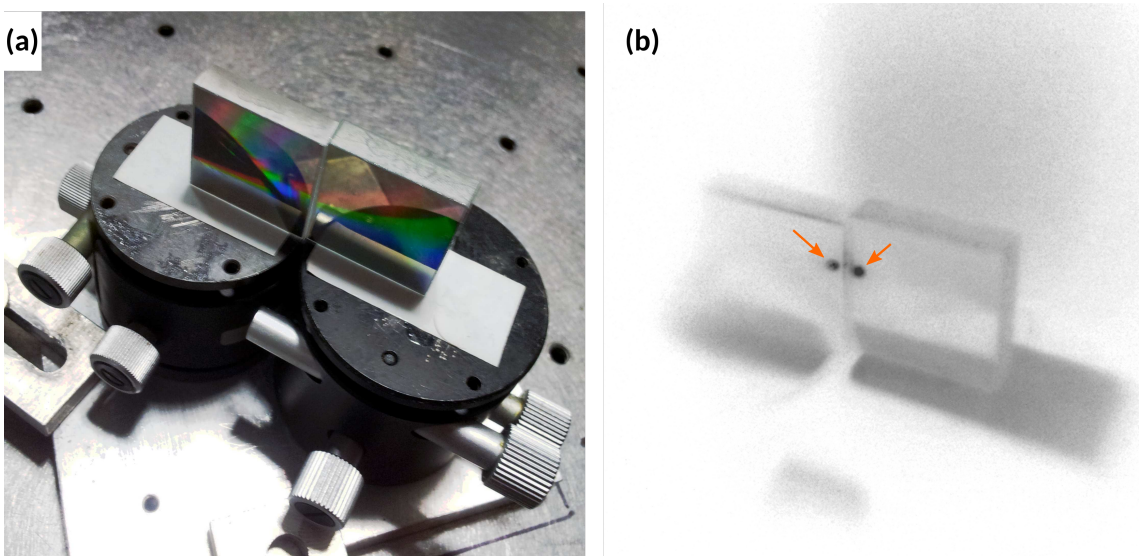

FIGURE 6.2: Detail of the assembly containing the two individually adjustable diffraction gratings, DG1,2: **(a)** colour photograph and **(b)** photograph taken through the infra-red viewer (FJW Find-R-Scope, Palatine, Illinois, USA) showing the two beam profiles (orange arrows) at the edge of each respective grating (for the $f_4 = 30\,\mathrm{mm}$ configuration). Each square-shaped diffraction grating has 1200 lines/mm, blazed at 1 μm, with dimensions 25×25 mm.

the paths of the two beams are divergent from each other, if a single grating was to be used, rays of the same wavelength in the two beams would not superpose on the same pixel of the line camera. Therefore, a specific assembly with two independently adjustable diffraction gratings (DG1,2, detailed in Figure 6.2 (a)) is used for each beam. By tilting the diffraction gratings in relation to each other and monitoring the resulting spectrum being detected by the line camera, it is possible to determine the setting in which the rays of the same wavelength from either arm are superposed on the line camera, since, provided a slight OPD is present between the two arms of the interferometer, a modulated spectrum will arise once the position adjustments of DG1,2 ensure the superposition mentioned before.

Let us consider the angle θ between the two collimated beams emerging from L4, as depicted in the diagram in Figure 6.1. Following a trigonometric analysis, such angle can be approximated by $\tan\theta \approx \dfrac{\delta}{2f_4}$. Given that throughout this implementation, $f_4 \gg \delta$ and $\theta \ll 1$, effectively the correction required for the angle between the two gratings is slightly less than 1 degree, which is why such angle is not evident in both the sketch in Figure 6.1 and in the photograph of the actual assembly in Figure 6.2.

Beyond the back focal plane of L4, the two beams no longer overlap but diverge in their paths; the distance between their centres scales with the distance L_{grat} between L4 and the pair of diffraction gratings DG1,2.

In order to employ the same theory developed in [4, 11] to analyse the shift in the visibility profile caused by the Talbot bands configuration, it is necessary to infer an equivalent gap g from the present configuration, which is linked to the distance between the two beam centres. This gap can be written as a function of the grating angle α and also of the correction θ between the two diffraction gratings. If the two gratings are placed perpendicularly to the propagation direction of the two beams, as shown for gap g'' in Figure 6.3 , the gap is:

$$g'' = \frac{\delta}{2f_4}\left(L_{\text{grat}} - f_4\right). \tag{6.1}$$

Given that the correction for the angle between the two diverging beams is very small, i.e., $\theta \ll 1$, $g' = g''/\cos\theta \approx g''$. Lastly, if the grating angle α is now considered, as represented in red in Figure 6.3, g will be given by

$$g = \frac{1}{\cos\alpha}\frac{\delta}{2f_4}\left(L_{\text{grat}} - f_4\right). \tag{6.2}$$

This expression for the equivalent gap g allows us to use the same Talbot Bands theory as presented in Section 3.2.1. Therefore, it is possible to relate the shift of the OPD for the maximum visibility OPD_{max} to g,

$$\text{OPD}_{\text{max}} = \frac{g}{a}\lambda_0, \tag{6.3}$$

where a is the grating pitch and λ_0 the central wavelength of the optical source spectrum. Given that $a \sim 0.833\,\mu$m and $\lambda_0 = 831$ nm, $\lambda_0/a \approx 1$, hence $\text{OPD}_{\text{max}} \sim g$.

The number of illuminated grating lines dictates the width of the C profile versus OPD, which in Section 3.2.2 is defined as the cross-convolution of the two beam profiles at the diffraction grating, $\mathfrak{F}(B)$ (Figure 3.20). By varying the focal length f_4 of L4, it is possible to change the width of the collimated beams and consequently the number of illuminated grating lines.

Hence, by varying both f_4 and L_{grat} it is possible to achieve the same functionality as the system reported in Chapter 5 and in previous publications [3, 4] in terms of controlling the position and shape of the visibility profile.

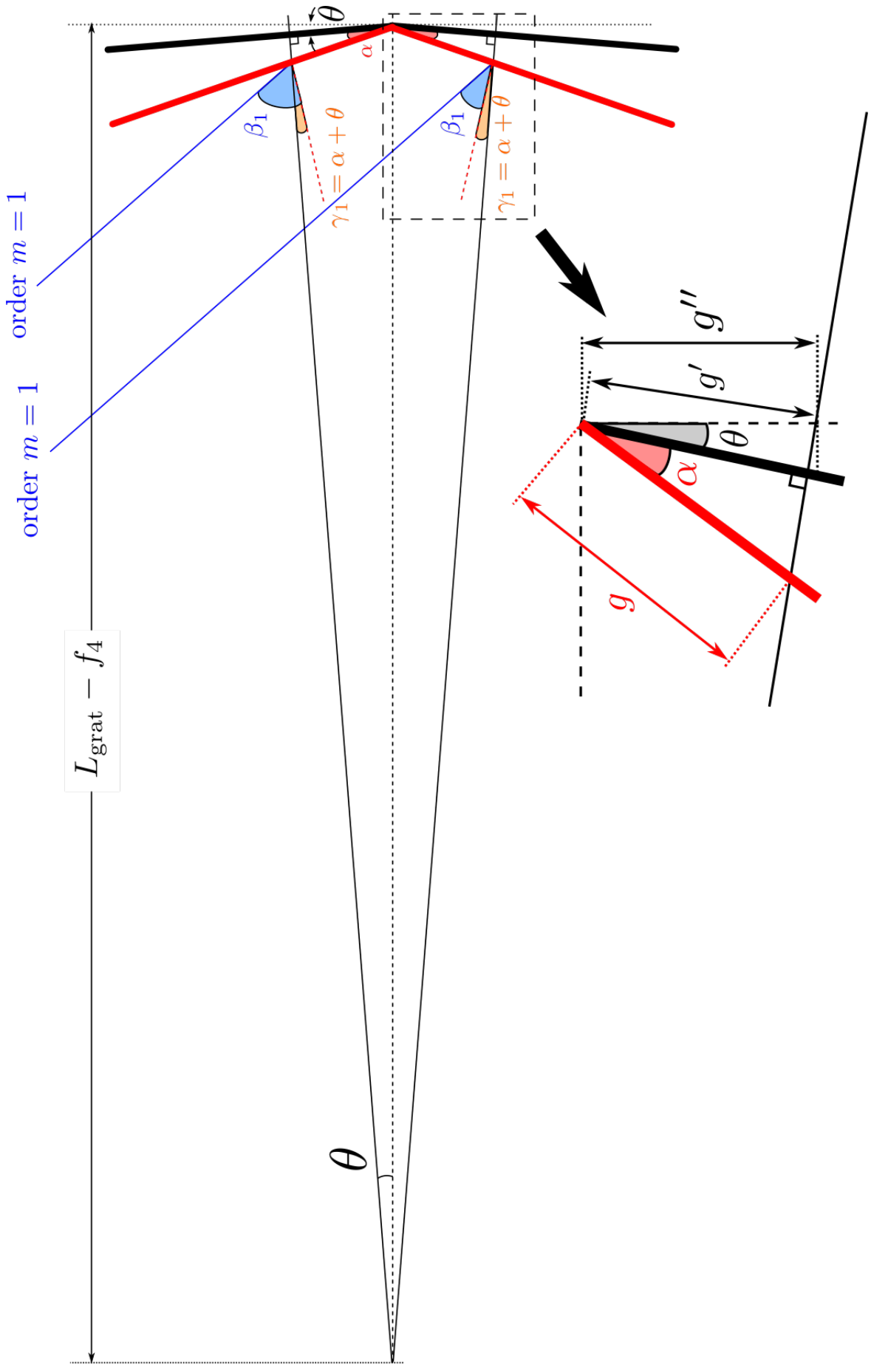

FIGURE 6.3: Analysis of the different angles considered for the equivalent gap g calculation. θ is the correction between the two diffraction gratings in order to compensate for the diverging beam propagation directions, and α is the grating angle for optimum diffraction performance.

6.3 Visibility profile characterisation

In order to characterise the visibility curves of the experimental system, several sets of measurements relating the channelled spectrum modulation to the OPD between the two arms of the interferometer were carried out for different values of the gap g and also for different widths of the C profile. These values were obtained by varying the focal length f_4 of lens L4 and the distance L_{grat} between L4 and the diffraction gratings DG1,2. Such changes allow g to be adjusted in the range of 1 to several mm; however, an exact value for g is difficult to ascertain since the edges of the two diffraction gratings introduce an additional error in the determination of g.

The visibility profile measurements are performed by recording the amplitude of the channelled spectrum modulation (obtained from the Fourier transform of the $\vec{k}$ re-sampled spectrum) for an ordered set of OPD values, which are varied in $20\,\mu\mathrm{m}$ increments using the TS.

Estimation of the effective gap values was possible by fitting the channelled spectrum visibility curves obtained by simulations based on the theory presented in Section 3.2.1.3; the code used for the simulations was based on code written by Michael Hughes during his PhD [12] and is presented in Appendix A . This code performs a cross-correlation of the Gaussian beam profiles from the two arms of the interferometer (with or without a gap g between them), whose result is multiplied by the *sinc* factor adjusted to the spectrometer resolution.

According to Equation (6.2), the larger L_{grat}, the larger the value of g and consequently the larger the intrinsic delay between the two diffracted beams, leading to a shift towards longer OPDs in the visibility profile. On the other hand, varying f_4 changes both $\mathrm{OPD}_{\mathrm{max}}$ through g (since $g \propto 1/f_4$) but also the width of the visibility profile, as the number of illuminated lines differ. Two different sets of measurements are carried out: the first with two different values of L_{grat} for the same collimating lens L4, and the second set with two values of f_4 for a constant L_{grat}.

6.3.1 Varying beam propagation distance

In this set of measurements, only the gap g is modified by opting for two L_{grat} values separated by approximately $40\,\mathrm{cm}$, accomplished by moving the group comprising the pair of diffraction gratings DG1,2 (Figure 6.2), the CMOS camera and the lens L5 along a direction given by the axis of L4. The results obtained are shown in Figure 6.4.

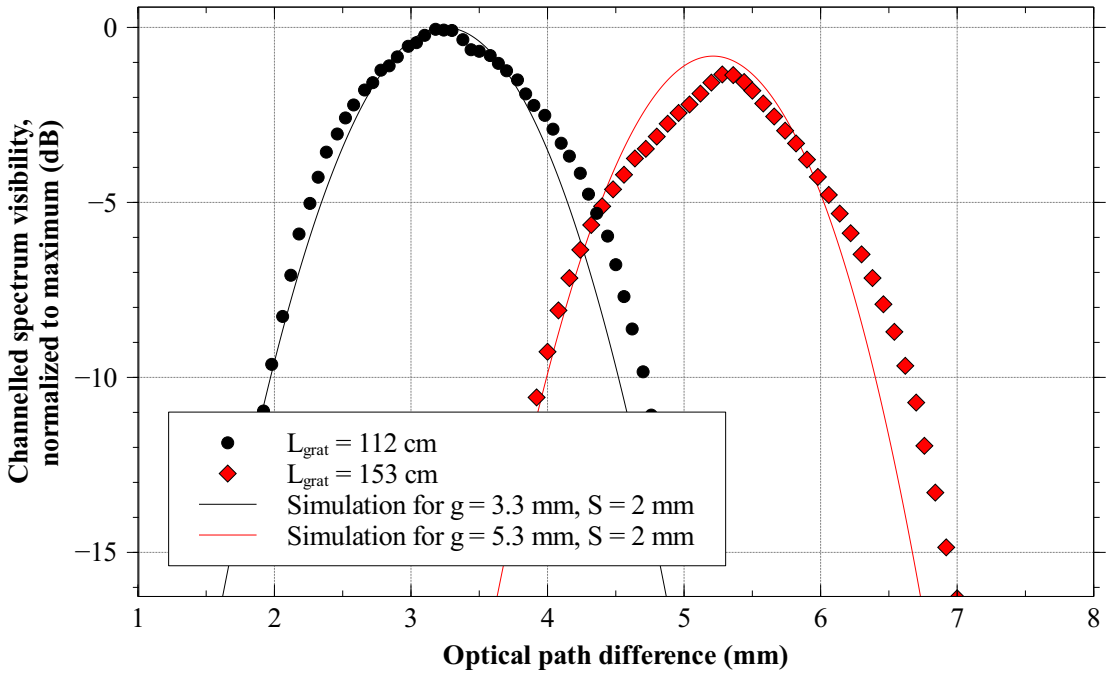

FIGURE 6.4: Visibility profile *versus* OPD for the configuration studied, using $f_4 = 30$ mm and two different values of L_{grat}: 112 cm, black circles; 153 cm, red diamonds. These correspond to a g value of ~ 3.25 mm and ~ 5.25 mm, respectively. The solid line plots correspond to simulations carried out using the code in Appendix A for two different gap g settings and the same beam width S. (taken from Marques *et al.* [1])

Considering the focal length of L4 as $f_4 = 30\,\text{mm}$ and the grating angle $\alpha \sim 18\,\text{deg}$, the spot diameter of each beam on each grating is approximately $S \sim 2\,\text{mm}$. If the beam profiles are approximated as top hats [7], the number of illuminated grating lines by each beam is $N = S/a = 2,400$. The cross-correlation of these two profiles, each of width $N\lambda_0$, yields a triangular profile which covers a $2N\lambda_0$ base of $\sim 4\,\text{mm}$. As expected, when considering more realistic Gaussian footprints, the width of the resulting profile is smaller than $2N\lambda_0$, as shown by the $-10\,\text{dB}$ width ($3\,\text{mm}$) of the simulated profiles in solid line overlaid on the experimental data in Figure 6.4.

The second plot in Figure 6.4 corresponds to a larger value of L_{grat} which determines a gap g larger than the beam width S. This curve shows that due to a larger gap, the C profile moves to larger OPD values, as expected. However, this shift also slightly decreases the peak visibility profile due to the limited spectrometer resolution, which introduces a sampling limit at larger modulation frequencies, as described in Section 3.2.2.

The gap settings for the theoretical simulations (plotted as solid lines in Figure 6.4) are adjusted to fit the experimental curves, with a value of $3.3\,\text{mm}$ for the $L_{\text{grat}} = 112\,\text{cm}$ case and a value of $5.3\,\text{mm}$ for the $L_{\text{grat}} = 153\,\text{cm}$ case. Both

experimental and theoretical data sets are normalised to the maximum peak visibility of their respective data set. The $L_{\mathrm{grat}} = 153\,\mathrm{cm}$ experimental data set has a peak value $\sim 1\,\mathrm{dB}$ lower than its simulated counterpart, which may be due to an imperfect alignment of the spectrometer after being reassembled following the change in L_{grat}.

6.3.2 Varying collimator focal length

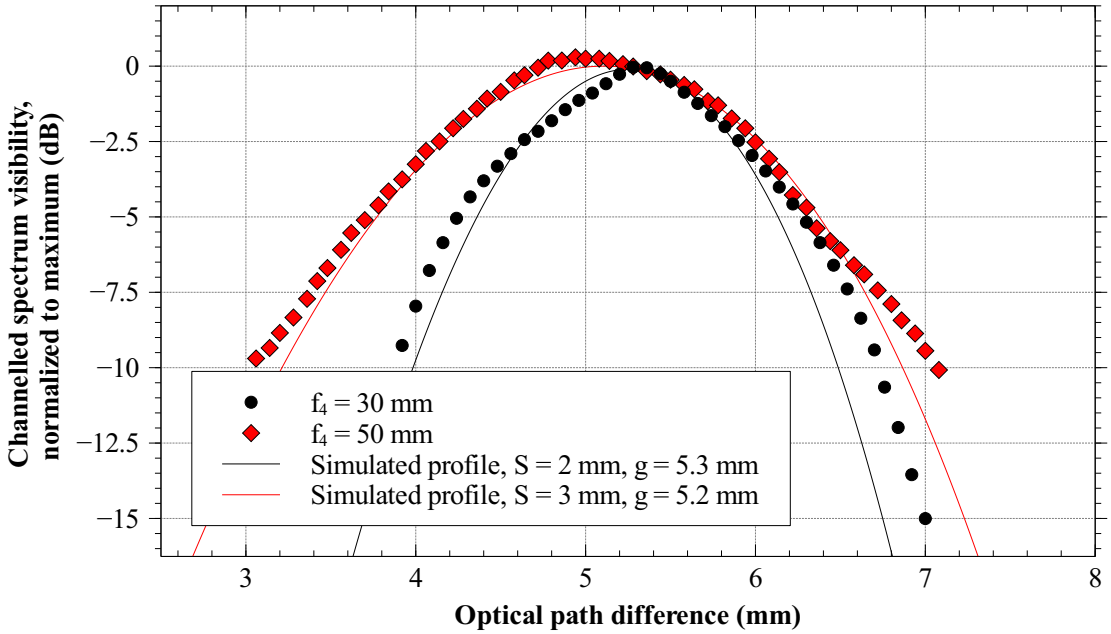

FIGURE 6.5: Visibility profile *versus* OPD for the configuration studied, using $L_{\mathrm{grat}} = 153$ cm and two different values of f_4: 30 mm, black circles; 50 mm, red diamonds. Both experimental and theoretical data sets have been normalised to the peak value for the profile closer to OPD = 0. (taken from Marques *et al.* [1])

A second set of experiments refer to the effect of the focal length f_4 of lens L4 on the visibility profile versus OPD. Figure 6.5 illustrates the visibility decay with OPD for two values of f_4 ($f_4 = 30$ and $50\,\mathrm{mm}$), using $L_{\mathrm{grat}} = 153\,\mathrm{cm}$.

The profile corresponding to $f_4 = 50\,\mathrm{mm}$ displays a slight shift towards OPD = 0. Given that the gap g between beams is inversely proportional to f_4 (Equation (6.2)), a larger focal length yields a smaller gap between the beams.

However, by increasing f_4 the collimated beam profiles will increase their width, and for the same value of L_{grat} this will mean that they might overlap, with a portion of one of the beams illuminating the grating adjusted for the other beam, and vice-versa. This would lead to some parts of both beams being diffracted by

both gratings, which would not interfere and therefore would reduce the overall interferometer performance.

The gap setting supplied to the simulations for the $f_4 = 50\,\mathrm{mm}$ configuration is $g = 5.2\,\mathrm{mm}$. Due to implementation challenges, it proved difficult to ensure that the beam centres remained in the same relative positions during the spatial adjustments of the components. Also, as mentioned before, the effective areas of the diffraction gratings do not extend up to their support edges, and this contributes to increasing the gap between the beams. All these aspects make it challenging to accurately measure the gap g experimentally.

The beam diameter for $f_4 = 50\,\mathrm{mm}$, assumed to be $S = 3\,\mathrm{mm}$ in the simulations, matches the experimental data, yielding a visibility profile width of around $2\,\mathrm{mm}$ (FWHM). The peak location shifts toward smaller OPD values by $\sim 0.4\,\mathrm{mm}$, as shown in Figure 6.5.

6.4 Conclusions

In conclusion, a novel Talbot bands configuration has been presented and validated in this Chapter, where the launching of the two beams from the object and reference arms uses a single lens, and where the splitter before the spectrometer is eliminated by employing two tilted diffraction gratings. The gratings perform two functions:

1. Allow superposition of the two diffracted beams on the line camera, effectively "closing" the two arms of the Mach-Zehnder inteferometer without resorting to an additional splitter;

2. Due to the tilt θ introduced between the gratings, the overlapped portions of the two beams will not contribute to the interference, leading to a total elimination of the mirror terms.

The adjustment of the relative tilt of the gratings is not more difficult than the alignment of the beam-splitter conventionally used in the Talbot bands configurations presented in previous reports [2–4].

Elimination of the final splitter also brings advantages in terms of power efficiency, as all the optical power arriving at the diffraction gratings from both beams can be directed towards the detector array. In a conventional M-Z interferometer, some optical power will necessarily be lost via the unused port, unless a configuration with an additional channel, such as the one [2] presented in Chapter 5 is employed. However, even in this configuration part of the reference arm

power will need to be attenuated in order not to saturate the confocal channel photo-detector.

In the configuration presented in this Chapter, the two beams will encounter optical elements with similar properties, which may present an extra advantage when handling large bandwidth signals as the splitting ratio depends on wavelength. Furthermore, any polarisation diattenuation which would be potentially introduced by the splitter will be removed, which makes this configuration attractive for polarisation-sensitive WLI/OCT systems.

From previous studies of Talbot bands configurations [4, 5], it is known that a smaller gap between the beams is desired to shift the visibility curve to a region closer to OPD = 0, for a higher SNR, while still ensuring mirror term attenuation. Shifting the sensitivity curve towards OPD = 0 means shifting it away from the spectrometer resolution limit (determined by the *sinc* profile). Also, if a large axial range is desired, the width of the visibility profile needs to be increased; this is accomplished with larger beam diameters, i.e., with larger values of f_4. However, fulfilling these two requirements may lead to some overlap of the two beams on the grating surfaces, which, as presented before, reduces the interferometer performance since the power diffracted from the overlapped regions does not contribute to the interference. This particularity effectively impedes mirror terms from arising at all, hence it is not be possible to observe curves similar to those found in Figure 5.8 in the previous Chapter, where part of the visibility profile still lies in the symmetric OPD side.

Therefore, a compromise has to be made with regards to the size of the gap between the two beams, in order to ensure complete separation when projected on the diffraction gratings and in this way maximise the interferometer performance. This necessarily introduces a lower peak visibility due to the shift to larger OPDs; however, it is believed that the gain in efficiency introduced by the elimination of the final splitter somewhat compensates for that drawback.

To ensure complete separation between the two beams as they illuminate the two diffraction gratings, L_{grat} has to be large (over $1\,\text{m}$), which may not be feasible and introduces additional design challenges. One can rewrite Equation 6.2 for L_{grat}, assuming $g = S$ (complete beam separation) and using the identity $\tan\theta \sim \frac{\delta}{2f_4} \sim \frac{g}{L_{\text{grat}}}$:

$$L_{\text{grat}} = f_4 \left(1 + \frac{2}{\delta}\cos\alpha\right). \tag{6.4}$$

Hence, if one wishes to reduce L_{grat} but still maintain the same interferometer performance (by ensuring $g \geq S$, that is, complete beam separation), f_4 can be

reduced or δ can be increased. The former determines the size of the footprint on each grating, which consequently influences the width of the visibility profile, as covered before; by reducing it, the axial range is necessarily compromised. The latter (δ) can be increased by separating the fibres in the launcher; however, there is a limit to this increase, since the larger the value of δ, the larger the geometrical aberrations on the beam profiles introduced by lens L4 due to the beams originating from off-axis-placed cores.

References

[1] M. J. Marques, A. Bradu, and A. Podoleanu, "Two-grating talbot bands spectral-domain interferometer", *Optics letters*, vol. 40, no. 17, pp. 4014–4017, 2015.

[2] M. J. Marques, A. Bradu, and A. G. Podoleanu, "Towards simultaneous talbot bands based optical coherence tomography and scanning laser ophthalmoscopy imaging", *Biomed. Opt. Express*, vol. 5, no. 5, p. 1428, Apr. 2014, ISSN: 2156-7085. DOI: 10.1364/BOE.5.001428.

[3] P. Bouchal, A. Bradu, and A. G. Podoleanu, "Gabor fusion technique in a talbot bands optical coherence tomography system", *Opt. Express*, vol. 20, no. 5, pp. 5368–5383, 2012.

[4] A. Bradu and A. G. Podoleanu, "Attenuation of mirror image and enhancement of the signal-to-noise ratio in a talbot bands optical coherence tomography system", *J. Biomed. Opt.*, vol. 16, p. 76 010, 2011.

[5] D. Woods and A. G. Podoleanu, "Controlling the shape of talbot bands' visibility", *Opt. Express*, vol. 16, no. 13, pp. 9654–9670, 2008.

[6] H. F. Talbot, "An experiment on the interference of light", *Philos. Mag*, vol. 10, p. 364, 1837.

[7] A. G. Podoleanu, "Unique interpretation of talbot bands and fourier domain white light interferometry", *Opt. Express*, vol. 15, no. 15, pp. 9867–9876, 2007.

[8] A. L. King and R. Davis, "The curious bands of talbot", *American Journal of Physics*, vol. 39, no. 10, pp. 1195–1198, 1971. [Online]. Available: http://scitation.aip.org/content/aapt/journal/ajp/39/10/10.1119/1.1976602.

[9] Z. Benkö, M. Hilbert, and Z. Bor, "New considerations on talbot's bands", *American Journal of Physics*, vol. 68, no. 6, pp. 513–520, 2000. [Online]. Available: http://scitation.aip.org/content/aapt/journal/ajp/68/6/10.1119/1.19477.

[10] M. E. Brezinski, *Optical Coherence Tomography: Principles and Applications*. Academic Press, 2006, ISBN: 9780080464947.

[11] M. Hughes, D. Woods, and A. G. Podoleanu, "Control of visibility profile in spectral low-coherence interferometry", *Electron. Lett.*, vol. 45, no. 3, pp. 182–183, 2009.

[12] M. Hughes, "Optical coherence tomography for art conservation and archaeology: methods and applications", PhD thesis, University of Kent, 2010.

Chapter 7

Fibre-based, polarisation-sensitive OCT insensitive to fibre-induced disturbances

Author's note: portions of this chapter are based on two peer-reviewed publications [1, 2], with one of which having been presented at an international conference (*Photonics West 2016 BiOS)* in February 2016 [3]. All the work described in this chapter has been done in collaboration with Dr Sylvain Rivet from the Université de Bretagne Occidentale (France) on a Marie Curie Intra European Fellowship in our group (2015-2016).

Contents

THE work presented in this Chapter covers a series of different designs for a fibre-based, polarisation-sensitive OCT (PS-OCT) system whose key feature is the avoidance of any fibre-based disturbances in the sample's polarimetric measurements by performing the actual measurement before the collecting fibre.

As mentioned in Section 4.2, fibre-based implementations are useful in the OCT practice due to their advantages in terms of ease of alignment and handling [4, 5], and also due to their enhanced flexibility in the sample arm designs [6]. All the designs presented in the following sections belong to this category.

Polarisation-maintaning (PM) fibres are often used in fibre-based PS-OCT systems [7] due to their ability to avoid polarisation state disturbances due to fibre deformations. Such fibres are however not perfect and a manifested problem is that of cross-talk between the polarisation eigenmodes of the fibre that introduces artefacts [8]. Single-mode fibres, on the other hand, avoid such artefacts but external factors such as temperature and mechanical stress can affect their birefringence, introducing disturbances [9] in the measured polarisation.

One way of bypassing the disturbances due to the birefringence variations in SM fibres consists in performing the polarisation selection before the collecting fibre. Roth *et al.* [6] devised such a system, operating in time-domain, which employed a liquid-crystal modulator in the sample arm to vary the polarisation state of the light, probing the medium according to three polarisation states generated sequentially. Fibre-based polarisation controllers are present in this design, but only to maximise signal amplitude. This particular implementation, however, means that the input polarisation of the light is not circular, which has an impact on the SNR of the images corresponding to the different polarisation state settings. Moreover, three sequential measurements are needed, which impacts the frame rate attainable.

Al-Qaisi *et al.* [7] reported on a fibre-based PS-OCT system which illuminates the sample with circularly polarised light. This is again a time-domain system with a single detector, which required the use of polarisation-maintaining (PM) optical fibres and couplers. This system does not detect the polarisation components sequentially; instead, the orthogonal polarisation states are modulated in the interferometric signal, multiplexing the polarimetric information in a single detector reading.

SMFs can be employed in a spectral-domain system such as the one presented in Cense *et al.* [10], where a Wollaston prism separates the two orthogonal polarisation states and projects them onto different parts of the same linear detection array. While allowing for simultaneous acquisition of both polarisation states using a single spectrometer, this approach requires fine tuning (and potentially

periodic recalibration) of the polarisation state of the light using fibre-based polarisation controllers. Additionally, by projecting the two polarisation components onto different sections of the camera pixel array the effective spectrometer resolution is reduced, since the number of pixels per polarisation component is smaller. This will have an impact on the OCT axial range, as presented earlier in Section 3.2.2.

More recently, Lippok *et al.* [8] have reported a system which employs a single input polarisation state and a full SMF implementation with no need for periodic recalibration. It applies a correction for the fibre birefringence by introducing a reference in the sample arm which can be used to determine the Jones matrix of the collecting fibre. The system is therefore able to correct for the effects of the fibre birefringence. However, this method requires post-processing to take place since it is not a fully hardware-based method.

All the configurations presented in Sections 7.1, 7.2 and 7.3 of this chapter meet three fundamental requirements:

1. Insensitivity to fibre birefringence: several approaches have already been mentioned above. All designs presented in this chapter perform the polarimetric measurement before the fibre aperture (philosophically speaking, in a manner similar to that presented by Roth *et al.* [6]), thus removing the need for careful pre-calibration or extensive post-processing.

2. Characterisation of the retardance and fast axis orientation with a minimal amount of measurements: this requires illumination of the sample with circularly polarised light, placing the systems proposed into the "Hee - Hitzenberger" category, as described in Section 4.2. A large number of PS-OCT systems reported in the literature belong to this category [7, 11–13].

3. Single detector: it is important to minimise the system complexity to diminish the number of detectors used, especially if using SD-OCT (spectrometer-based); this requires that the two orthogonal polarisation components have to be sequentially detected or multiplexed into the channelled spectrum modulation.

The first design (configuration A), along with its experimental validation has been published in a peer-reviewed publication [1] (and presented at an international conference in February 2016 [3]) and is described in detail in Section 7.1. The polarimetric measurements are carried out before the collecting fibre; this is achieved by rotating the polarisation state of the returned probing beam between two alternating settings (either no rotation or a 90 degree rotation) and projecting

it against a linear polariser before injection into the collecting fibre, thus meeting requirement (1). A sequential approach was used here, to meet requirement (3). The rotation was performed using a liquid crystal rotator which limited the B-scan refresh rate to a few Hz. In order to meet requirement (2) whilst still observing requirement (3), the probe and return paths in the sample arm are spatially separated, in this way ensuring a constant circular polarisation state illuminating the sample, regardless of the state of the liquid crystal rotator.

The second (conceptual) design (configuration B) has been published in a peer-reviewed journal [2] and is described in detail in Section 7.2. All three requirements listed above are satisfied; requirement (1) is met in the same way as in configuration A, by performing the polarimetric measurement before the collecting fibre. Moreover, this design also relies on a sequential approach to fulfil requirement (3), employing electro-optical polarisation modulators which allow for larger frame rates to be attained. Unlike configuration A though, in this configuration an additional requirement is imposed: that the probe and return paths must be the same, hence an in-line design is considered. This configuration is thus attractive for implementation in any existing OCT system (without further modifications of the interferometer). In order to attain that whilst still fulfilling requirement (1), the reciprocity has to be broken; that is achieved by the introduction of a Faraday rotator, that is used to maintain the input polarisation state constant and circular regardless of the state of the electro-optical polarisation modulator, thus observing requirement (2).

Lastly, the third design (configuration C)[1] fulfils all four requirements previously listed, and introduces a fifth one: the two orthogonal polarisation states must be sampled simultaneously (i.e. performing a "snapshot" measurement). In order to do so whilst still meeting requirement (3), the two orthogonal polarisation states are encoded on different OPD values, in a similar manner to the procedure described in [14].

Scanning of the sample is performed by two galvo-scanning mirrors *SXY* placed just before the sample. Since the angles of incidence of the beam on the two mirrors in the galvanometer scanning head are relatively large ($\sim$ 45 degrees), the Fresnel coefficients differ for perpendicular and parallel components in relation to the incidence plane of the wave incident on each galvanometer scanner. Having two galvanometer scanners at 90 degrees in sequence leads to no disturbances on the polarisation state after reflection of light on both mirrors. This can be simply demonstrated using the Fresnel coefficients, as the wave oscillating

[1] At the time of the submission of this thesis, this design has not been fully implemented, hence only a brief description of it will be presented in Section 7.3.

in the incident plane of the first mirror oscillates perpendicularly to the incident plane of the second mirror. Therefore, SXY should not introduce any effect on the polarisation state. However, if only one mirror would be used, then its effect must be taken into account.

7.1 Configuration A: Sequential, split-path design

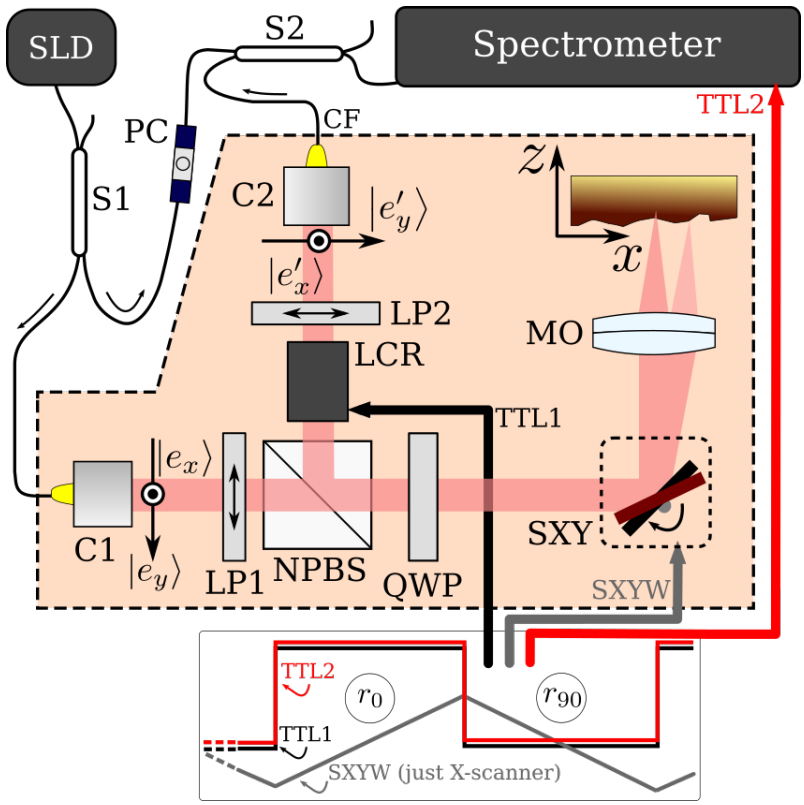

FIGURE 7.1: Sequential, fibre-based PS-OCT system (first design). **C1-2**, fibre collimators; **PC**, fibre-based polarisation controller; **LP1-2**, dichroic linear polarisers; **NPBS**, non-polarising beam-splitter; **QWP**, quarter-wave plate (oriented at 45° in respect to the direction of the linear polarisation state selected by LP1); **SXY**, pair of galvo-scanners; **MO**, microscope objective; **CF**, collecting fibre; **LCR**, liquid-crystal polarisation rotator switching between states r_0 and r_{90}; **SXYW**, waveforms driving the pair of galvo-scanners, with the X-scanner deflecting back and forth, performing acquisition of two horizontally flipped images during each period, which in turn correspond to the two states r_0 and r_{90} respectively; **TTL1-2**, driving signals for the LCR switching and the spectrometer acquisition trigger, respectively. (adapted from Marques *et al.* [1])

The configuration proposed (and experimentally demonstrated) is schematically represented in Figure 7.1. Light from a superluminiscent diode (SLD, Superlum, Cork, Ireland, central wavelength $830\,\mathrm{nm}$, spectral bandwidth $\sim 20\,\mathrm{nm}$, output peak power $\sim 10\,\mathrm{mW}$) is split between the two arms of a Mach-Zehnder

interferometer by the directional splitter S1, 20% of which is directed to the reference arm and 80% to the sample arm.

In the sample arm, which corresponds to the shaded region in Figure 7.1, a liquid-crystal polarisation rotator (LCR, Meadowlark LPR-100-800, Frederick, Colorado, USA) is employed to rotate the returned field from the sample between two states, corresponding to either no rotation or to a 90 degree rotation. Switching between these two states is performed by the computer's DAQ card, which generates a TTL signal represented in Figure 7.1 as TTL1.

The two arms of the interferometer are re-coupled at S2, with the resulting signal being directed toward a custom-built spectrometer, comprised by a $1200\,\mathrm{l/mm}$ transmissive diffraction grating (Wasatch Photonics, Logan, Utah, USA), a focusing achromatic lens, a Basler sprint line camera (Basler AG, Ahrensburg, Germany) set to $400\,\mu\mathrm{s}$ acquisition time, and a CameraLink frame grabber (National Instruments PCIe-1429, Austin, Texas, USA) with a syncing signal TTL2 triggering the start of each frame acquisition. An in-line fibre polarisation controller (PC, Newport F-POL-IL, Irvine, California, USA) in the reference arm is used to maximise the interferometric signal.

After acquisition, the channelled spectra are re-sampled linearly in $\vec{k}$ (using the algorithm described in [15, 16] and detailed in Section 3.2.3), an inverse Fourier transform (IFT) is performed, and the A-scans are bundled together to form a B-scan. The two TTL signals represented at the bottom of Figure 7.1 are in phase; therefore, a 1024 pixel-wide B-scan contains two identically sized B-scan images (each 512 pixel-wide) corresponding to the two rotation states of the liquid-crystal rotator LCR, r_0 and r_{90}. The pair of images is refreshed at $2.5\,\mathrm{Hz}$.

7.1.1 Theoretical model

To describe the theoretical model corresponding to this configuration, it has been assumed that the polarisation rotator is a pure one (ie, no chromaticity has been taken into consideration, and there is no ellipticity added to the resulting polarisation state). One can implement this system by either using a liquid-crystal rotator (which is what was used in the experimental demonstrator) or by employing an electro-optic polarisation modulator oriented at 45 degrees in relation to the vector basis $\left\{\left|e'_x\right\rangle, \left|e'_y\right\rangle\right\}$ in Figure 7.1. In this case, the state r_0 could correspond to a retardance equal to 0 degrees and the state r_{90} to a retardance equal to 180 degrees, with the polarisation rotator device effectively behaving as a switchable half-wave plate.

A realistic polarisation rotator is however non-ideal and therefore introduces errors in the measurement of the sample retardance. Still, the non-ideal behaviour

does not affect the insensitivity to the disturbances in the collecting fibre, as will be shown below.

After re-sampling the spectra in $\vec{k}$-domain, the intensity $I(\nu)$ versus the optical frequency ν at the spectrometer is given by

$$I(\nu) = I_{DC}(\nu) + A_z e^{j\frac{\pi}{c}\nu \cdot z} + A_z e^{-j\frac{\pi}{c}\nu \cdot z}, \tag{7.1}$$

where A_z describes the amplitude of the interference between the field returning from the sample measured at the output of the collecting fibre CF, and the field $|r_{\text{out}}\rangle$ from the reference arm; c is the speed of light, and z is the depth of the medium measured from zero optical path difference (OPD = 0). The returning wave from the sample arm is given by $r(z)\,|S_{\text{out}}(z)\rangle$, where $r(z)$ is the complex amplitude reflection coefficient for a scattering centre located at a depth z. By taking the IFT of $I(\nu)$, we obtain the absolute value of A_z, which is given by

$$I_{\text{interf}} = |A_z| \propto |\langle r_{\text{out}} \,|\, S_{\text{out}}(z)\rangle| \cdot |r(z)|\,, \tag{7.2}$$

where $\langle r_{\text{out}} \,|\, S_{\text{out}}(z)\rangle$ denotes the dot product between the complex conjugate of the field $|r_{\text{out}}\rangle$ and the field $|S_{\text{out}}(z)\rangle$, the latter containing both the phase retardance information of the sample under analysis and the polarimetric response of the collecting fibre CF and coupler S2 combined together. Thus, the ability to de-couple these two contributions enables the identification of the polarimetric response of the sample independently from that of the fibres/couplers which vary greatly with environmental parameters.

In the sample arm (shaded region of Figure 7.1), the linearly polarised wave $|e_1\rangle = |e_y\rangle$ oriented parallel to the figure plane is shown traversing the non-polarising beam splitter (NPBS). The polarisation state is converted into circularly polarised light by means of a quarter-wave plate (QWP, Thorlabs, Newton, NJ, USA) oriented at 45 degrees in relation to the axis of LP1. The beam is then laterally scanned with the pair of galvo-scanners SXY over the surface of the sample. Light returning from the sample goes through the QWP a second time, and before crossing the liquid-crystal polarisation rotator (operating at $5\,\text{Hz}$), the returning field $|e_2\rangle$ contains the information of the (net) retardance $\Phi(z)$ and optical axis orientation $\theta(z)$ of the sample. This field can be expressed on a vector basis $\left\{\, |e'_x\rangle\,, |e'_y\rangle \,\right\}$ (refer to Figure 7.1), as:

$$|e_2\rangle = \cos\Phi(z)\,|e'_x\rangle + \sin\Phi(z) e^{2j\theta(z)}\,|e'_y\rangle\,. \tag{7.3}$$

The beam then passes through another linear polariser, LP2, which is oriented along $\left|e'_y\right\rangle$. The resulting field at the input of the collecting fibre CF is defined by $|S_{\text{in}}(z)\rangle$. According to the rotation states r_0 and r_{90} of the LCR, $|S_{\text{in}}(z)\rangle$ can be defined as follows:

$$|S_{\text{in}}\rangle = \begin{cases} \sin\Phi(z)\exp\left[j\left(2\theta(z)+\varphi_{r0}\right)\right]\left|e'_y\right\rangle & = |S_{\text{in}}^{r0}(z)\rangle \\ \cos\Phi(z)\exp\left[j\varphi_{r90}\right]\left|e'_y\right\rangle & = |S_{\text{in}}^{r90}(z)\rangle \end{cases}, \tag{7.4}$$

where φ_{r0} and φ_{r90} correspond to the additional phase introduced by the LCR in each case being considered. The two states are presented sequentially to the fibre input. They are similar to the components simultaneously measured according to the theoretical analysis developed in Section 4.1.1 (on the first PS-OCT system by Hee *et al.* [11]), following the formalism described by Pircher and Hitzenberger [5].

As described in Section 7.1.2, due to the polarimetric response of the collecting fibre CF and coupler S2, $|S_{\text{in}}\rangle$ and $\left|e'_y\right\rangle$ are respectively transformed into $|S_{\text{out}}\rangle$ and $|e_{\text{out}}\rangle$:

$$|S_{\text{out}}(z)\rangle = \begin{cases} \sin\Phi(z)\exp\left[j\left(2\theta(z)+\varphi_{r0}\right)\right]|e_{\text{out}}\rangle & = |S_{\text{out}}^{r0}(z)\rangle \\ \cos\Phi(z)\exp\left[j\varphi_{r90}\right]|e_{\text{out}}\rangle & = |S_{\text{out}}^{r90}(z)\rangle \end{cases}. \tag{7.5}$$

By replacing the equation above in Equation (7.2), one can obtain an expression for the interferometric component I_{interf}:

$$I_{\text{interf}} = \begin{cases} \left|\sin\Phi(z)\right|\left|\langle r_{\text{out}}\,|\,e_{\text{out}}\rangle\, r(z)\right| & = I^{r0} \\ \left|\cos\Phi(z)\right|\left|\langle r_{\text{out}}\,|\,e_{\text{out}}\rangle\, r(z)\right| & = I^{r90} \end{cases}, \tag{7.6}$$

and, as presented before in Equation (4.17) in Section 4.1.1, one can obtain the absolute value of the net phase retardance in the medium $|\Phi|$, as

$$|\Phi| = \arctan\left[\frac{I^{r0}}{I^{r90}}\right]. \tag{7.7}$$

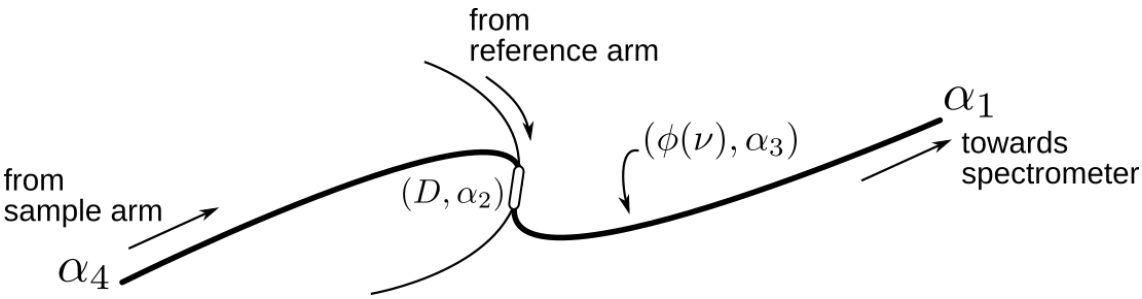

FIGURE 7.2: Schematic representation of the collecting fibre from the Michelson/Mach-Zehnder interferometer, detailing the several elements of the in-fibre path which may influence the polarimetric measurement: orientation angle of the SM fibre ends (α_1 and α_4), diattenuation D of the fibre coupler (modelled as a diattenuator oriented at α_2), and the phase retardance $\phi_(\nu)$ of the fibre, which has been modelled as a linear retarder with orientation α_3 and a polarisation-mode dispersion ΔT.

Given that it is actually necessary to consider a broadband spectrum, the chromatic behaviour of the fibres must be considered, with $|r_{\text{out}}\rangle$ and $|S_{\text{out}}\rangle$ being dependent on ν. Equation (7.6) then becomes

$$I_{\text{interf}} = \begin{cases} |\sin\Phi(z)| \left| \int \langle r_{\text{out}}(\nu) \,|\, e_{\text{out}}(\nu)\rangle \, r(z) d\nu \right| & = I^{r0} \\ |\cos\Phi(z)| \left| \int \langle r_{\text{out}}(\nu) \,|\, e_{\text{out}}(\nu)\rangle \, r(z) d\nu \right| & = I^{r90} \end{cases}, \tag{7.8}$$

where $\left| \int \langle r_{\text{out}}(\nu) \,|\, e_{\text{out}}(\nu)\rangle \, r(z) d\nu \right|$ yields the value of the FT corresponding to a single layer at depth z, equivalent to the $|\gamma(\Delta z)|$ term in Equations (4.12) and (4.13). By taking these two terms (I^{r0} and I^{r90}) and calculating the ratio between them, the value of $|\Phi|$ becomes insensitive to the effects of both fibres and couplers, which comprise their birefringence, diattenuation, and chromatic behaviour. Moreover, regardless of the rotator's imperfections, the system will always exhibit tolerance to these effects.

7.1.2 Demonstration of insensitivity to the polarimetric disturbances introduced by the collecting fibre/coupler

In order to numerically demonstrate how this configuration is insensitive to the disturbances in the collecting fibre and final coupler, the effects of these two elements are modelled via a product of Jones matrices describing a linear retarder whose birefringence exhibits chromaticity, a linear diattenuator and also the orientation of the two fibre ends, as depicted in Figure 7.2.

In these simulations, the system is assumed to be illuminated with an optical source at $\lambda_0 = 850\,\text{nm}$ having a Gaussian-shaped spectrum with a FWHM

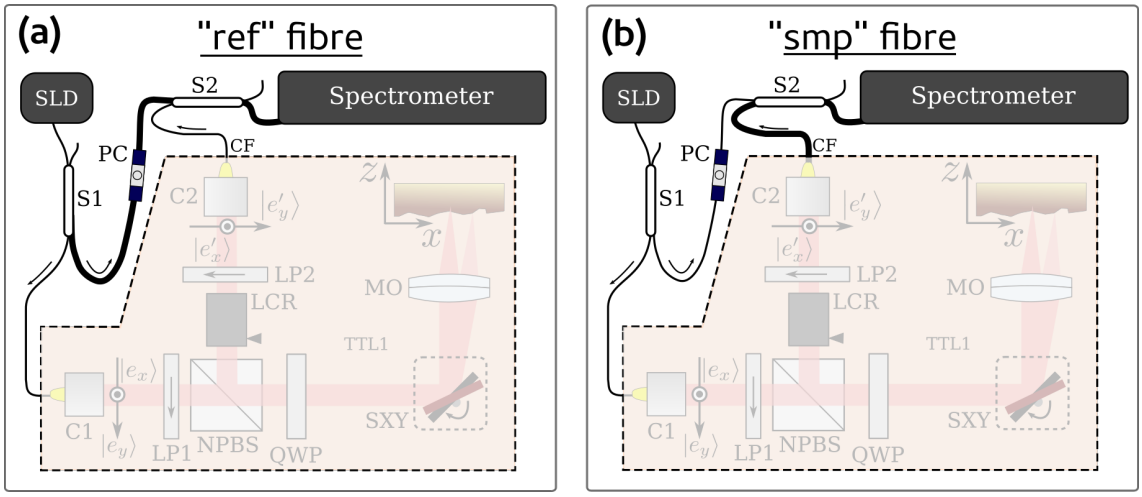

FIGURE 7.3: Schematic representation of the different fibre paths employed in the simulations. **(a)** wave propagation from the splitter S1 along the reference arm fibre, and then from it to the detector; **(b)** wave propagation from the sample arm to the detector;

of $\Delta\lambda = 100\,\mathrm{nm}$. Moreover, the output spectra have been re-sampled in the $\vec{k}$-domain with 1,000 points. The aforementioned product of Jones matrices modelling the collecting fibre+coupler system is defined as follows (each of the matrices is described in detail in Appendix B):

$$J_F^{smp} = J_{Rot(\alpha 1)} \cdot J_{Diat(D,\alpha 2)} \cdot J_{Bir(\phi(\nu),\alpha 3)} \cdot J_{Rot(\alpha 4)}, \tag{7.9}$$

where $J_{Rot(\alpha)}$ is the Jones matrix for a rotator which rotates the incident polarisation by an angle α, $J_{Bir(\phi(\nu),\alpha)}$ corresponds to a linear retarder oriented at an angle α with retardance $\phi(\nu)$, and $J_{Diat(D,\alpha)}$ corresponds to a diattenuator with diattenuation D and oriented at an angle α. To account for the chromaticity of the fibre, in the simulation it has been considered that the retardance $\phi(\nu)$ is expressed according to a mean retardance $\phi\,(\nu_0)$ and a parameter ΔT to account for the polarisation mode dispersion (PMD) of the fibre, as follows:

$$\phi(\nu) = \phi\,(\nu_0) + 2\pi\Delta T\,(\nu - \nu_0)\,, \tag{7.10}$$

with ν_0 corresponding to the central optical frequency of the source spectrum.

If we consider the field coming from the sample and being injected into the fibre as $|S_{in}(z,\nu)\rangle$ (as presented in Equation (7.4)), the actual field arriving at the spectrometer is given by

$$|S_{out}(z,\nu)\rangle = J_F^{smp}\,|S_{in}(z,\nu)\rangle\,. \tag{7.11}$$

The Jones matrix J_F^{smp} will affect the propagation in the "out" fibre path (Figure 7.3 (b)). The reference path (Figure 7.3 (a)) will be affected in a similar way, with the contribution from the reference arm at the detector being given by

$$|r_{out}(\nu)\rangle = e^{j\frac{2\pi\nu}{c}2z} J_F^{ref}(\nu)\,|e_0\rangle\,, \tag{7.12}$$

where J_F^{ref} is the Jones matrix associated with the full propagation in fibre (Figure 7.3 (c)), $|e_0\rangle$ is the field from the optical source and $2z$ is the OPD between the lengths of the two arms of the interferometer.

By taking the Fourier transform of the detected interferometric signal $I_{\text{interf}}(\nu)$ (as defined in Equation (7.8) for the two states of the LCR) and evaluating the complex amplitude associated with the peak present at depth z, one can retrieve the intensities for each of the sequential steps and thus recover the polarimetric information as presented earlier.

	Length (m)	**D**	$\phi(\nu_0)$ **(rad)**	**ΔT (fs)**	α_1 **(rad)**	α_2 **(rad)**	α_3 **(rad)**	α_4 **(rad)**
"smp" fibre	10	0,D_{out}	$\pi/8, \phi(\nu_0)_{out}$	10, ΔT_{out}	0	0.5	$\pi/12$	$\pi/2$
"ref" fibre	20	0	$\pi/4$	14	$\pi/4$	0	$\pi/4$	$\pi/4$

TABLE 7.1: Coefficients for the fibres in the OCT system. PMD is considered to be equal to $0.1\,\text{ps}/\sqrt{\text{km}}$ for a single-mode fibre, which corresponds to a delay of $\Delta T = 10\,\text{fs}$ for a $10\,\text{m}$ fibre. Coefficients D, $\phi(\nu_0)$, α_1, α_2, α_3 and α_4 are arbitrarily chosen. D_{out}, $\phi(\nu_0)_{out}$ and ΔT_{out} are independently varied in the simulations to assess the effect of each one in the polarimetric measurements.

Table 7.1 lists the parameters used in the fibres present in the system, which are linked to the propagation paths listed in Figure 7.3. Here, the PMD is considered to be $0.1\,\text{ps}/\sqrt{\text{km}}$ for a single-mode fibre, which for a 10-metre fibre corresponds to a delay of $\Delta T = 10\,\text{fs}$, with this value being then used in Equation (7.10).

The remaining values in Table 7.1 are arbitrarily chosen, with some parameters (D_{out}, $\phi(\nu_0)_{out}$ and ΔT_{out}) being independently varied to mimic the disturbances the fibre and the coupler may introduce, and therefore prove the insensitivity of the retardance and optical axis orientation measurements to these disturbances.

To verify this behaviour, a sample modelled as a linear retarder oriented at 45 degrees with a phase retardance of 10 degrees is employed, and no other chromatic effects are assumed. Figure 7.4 shows the bias of the retardance $\Delta\varphi_{\text{bias}}$ and optical axis orientation $\Delta\theta_{\text{bias}}$ measurements for fluctuations in the properties of the "out" fibre. Let us assume that the fibre properties do not vary during the

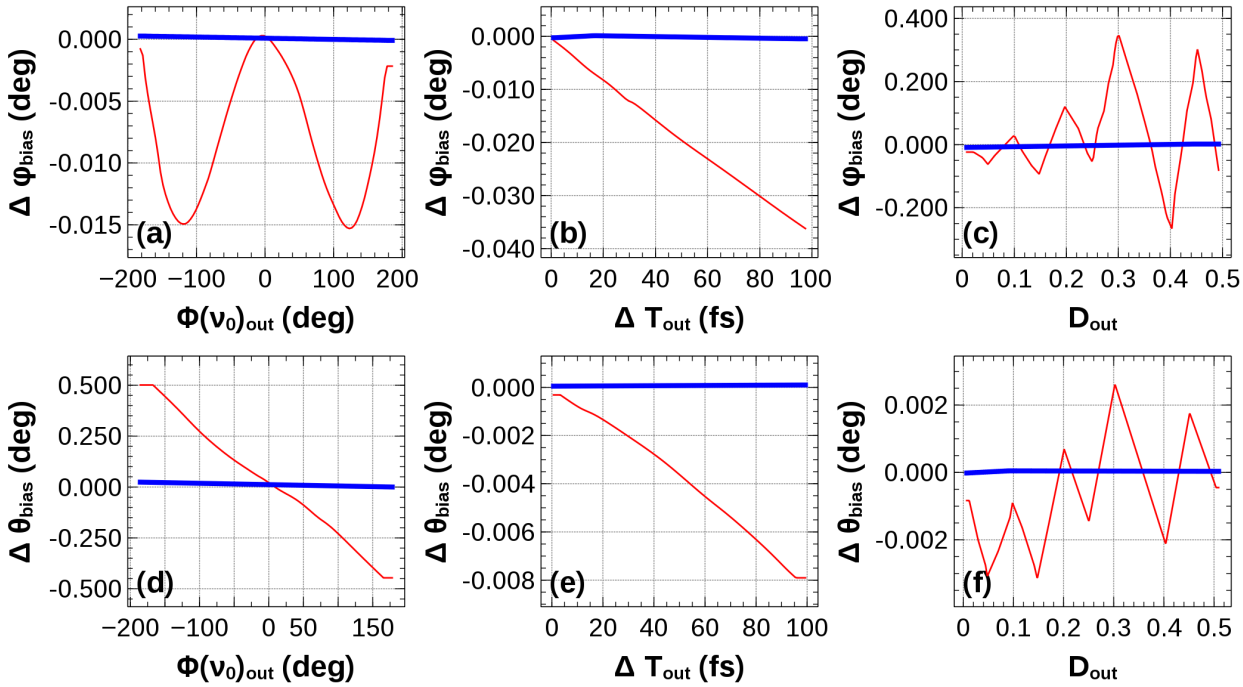

FIGURE 7.4: Simulation of the bias on the retardance φ_{sample} (top row) and on the orientation angle θ_{sample} (bottom row) of a sample. Thick blue lines: the characteristics of the "out" fibre are identical for the two sequential measurements. **(a)** and **(d)**, thin red lines: the retardance of the "out" fibre is $\phi(\nu_0)_{out}$ during the first measurement step, and $1.01 \times \phi(\nu_0)_{out}$ during the second measurement step; **(b)** and **(e)**, thin red lines: the PMD of the "out" fibre is ΔT_{out} during the first measurement step, and $1.01 \times \Delta T_{out}$ during the second measurement step; **(c)** and **(f)**, thin red lines: the diattenuation of the "out" fibre is D_{out} during the first measurement step, and $1.01 \times D_{out}$ during the second measurement step. (adapted from Rivet *et al.* [2])

time it takes to perform a *single* polarimetric measurement (but they are allowed to vary at a longer time scale), both biases $\Delta\varphi_{\text{bias}}$ and $\Delta\theta_{\text{bias}}$ are equal to zero, as shown by the thick blue lines in all the plots in Figure 7.4.

However, one has to consider the possibility that the properties of the "smp" fibre may vary during the time it takes to switch from one measurement to the other; this has been shown in the thin red traces in Figure 7.4, where the parameters D_{out}, $\phi(\nu_0)_{out}$ and ΔT_{out} have been increased by 1% between the two sequential measurements.

The biases reported by the simulations are weak ($< 1\%$); however, additional effects such as the chromaticity of the optical elements used have not been considered at this stage. For a switching rate comparable to the A-line rate this would mean that the fibre properties would have to change in a period of micro-seconds; since it is commonly assumed in PS-OCT systems that fibres remain stable during sequential measurements [17, 18], this effect will not be dominant.

7.1.3 Experimental results

This configuration has been implemented and thus experimentally validated. Firstly, the accuracy of the system was assessed by means of a calibrated reference wave plate, in the form of a Berek wave plate [19] (Newport model 5540, Newport Corporation, Irvine CA, USA). This consists of a slab of a uniaxial crystalline medium with its optical axis perpendicular to the faces of the slab. By tilting the slab, phase differences are introduced between the ordinary and the extraordinary rays [20], which can be quantified precisely when measuring the tilting angle.

According to the manufacturer [21], the one-pass phase retardation R (in fractions of the central wavelength λ_0) introduced by the wave plate can be related to its tilting angle θ_R by

$$\theta_R = \arcsin\left(0.284\sqrt{\lambda_0 R}\right). \tag{7.13}$$

The wave plate housing dictates the relation between the tilting angle θ_R and the adjustable indicator setting J, defined as [21]

$$J = 50.22 - 71\sin\left(\frac{\pi}{4} - \theta_R\right). \tag{7.14}$$

By varying J it is then possible to introduce different phase retardation settings in the sample arm and thus quantify the accuracy of the polarimetric measurements.

In order to prove the insensitivity to the disturbances caused by the collecting fibre and coupler, an additional experiment has been devised. A second in-line fibre polarisation controller has been installed in the collecting fibre CF (Figure 7.1) which can be adjusted to mimic the mechanical stress effect which can result in a change in the polarimetric properties of the fibre. As a sample, a highly birefringent plastic phantom has been imaged under two different settings of the polarisation controller. The results are shown in Figure 7.7 in Section 7.1.3.2.

7.1.3.1 Validation with a calibrated reference

Prior to its installation in the PS-OCT system, the Berek wave plate was characterised in terms of its polarimetric response using a Müller polarimeter which has been implemented in the group [22]. This device allows for the complete characterisation of the polarimetric response of the Berek wave plate since it relies on an incoherent detection method, obtaining its full Müller matrix. From this matrix,

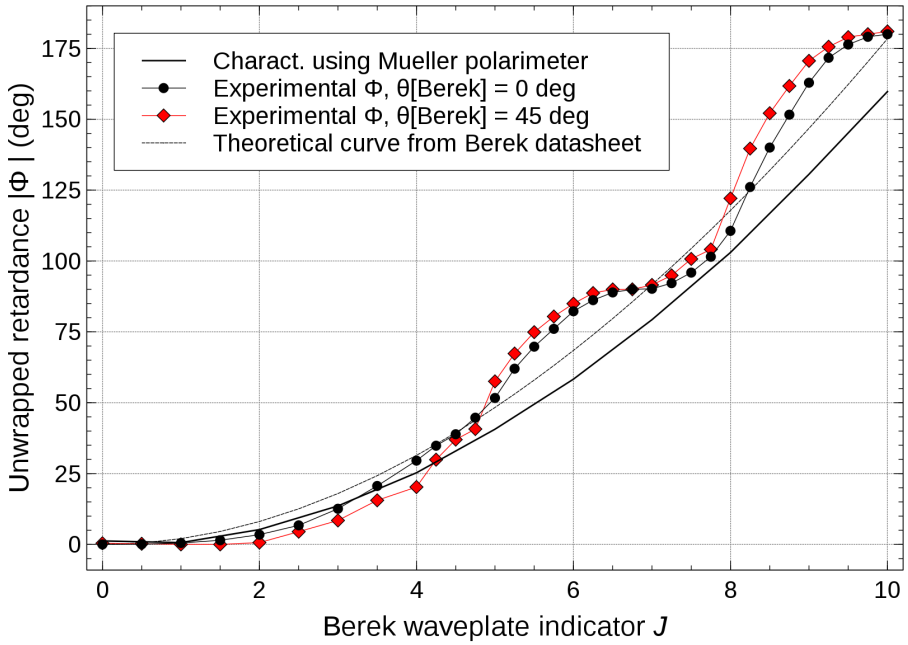

FIGURE 7.5: Phase retardance Φ measurements of a Berek wave plate, placed in the sample arm, versus the indicator setting J, which is proportional to its retardance. Between the two experimental data sets (shown as black circles and red crosses), the Berek compensator was rotated by 45º around the axis of propagation. Also represented are the polarimetric response of the Berek wave plate as measured by a Müller polarimeter [22] (thick black line) and the theoretical response of the Berek wave plate (thin dashed black line) as reported by the manufacturer's data sheet [21] for $\lambda_0 = 830\,\mathrm{nm}$. (adapted from Marques *et al.* [1])

it is possible to extract the phase retardance versus the indicator setting J on the wave plate which is plotted in Figure 7.5 as a thick black line.

Using a combination of Equations (7.13) and (7.14) it is possible to obtain the representation of the net retardance $|\Phi|$ versus the indicator setting J for a given wavelength λ_0. In Figure 7.5 such representation is plotted as a thin dashed curve for $\lambda_0 = 830\,\mathrm{nm}$.

The two aforementioned curves are not overlapping, although their overall behaviour is similar; the reason behind it might be linked with the fact that the Müller polarimeter used a wider bandwidth source for the characterisation (Superlum Broadlighter S840, $\lambda_0 \sim 840\,\mathrm{nm}$, $\Delta\lambda \sim 50\,\mathrm{nm}$) and the theoretical model considered a single wavelength $\lambda_0 = 830\,\mathrm{nm}$.

Experimental data sets are also plotted in the graph in Figure 7.5; these correspond to polarimetric measurements made with the PS-OCT system with the Berek placed in its sample arm. No scanning was performed in this case. Two data sets are represented in the figure (as black dots and red diamonds), corresponding to two orientation angles of the wave plate separated by 45 degrees.

Some discrepancies are observed between the experimental data sets and the two curves (theoretical and Müller matrix characterisation), which may be due to the fact that the LCR is not a pure rotator at the central wavelength $\lambda_0 = 830\,\mathrm{nm}$ of the SLD (instead, it may introduce some ellipticity in the polarisation state). This deviation induces systematic errors in the retardance measurement which depend slightly on the orientation of the sample; however, the deviation between the two experimental data sets is never larger than 10 degrees.

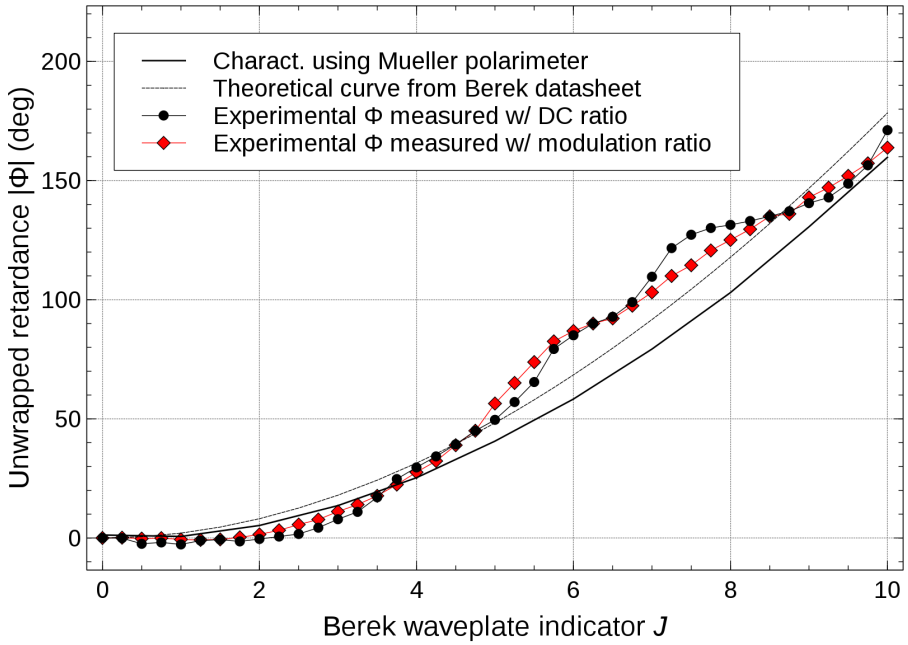

FIGURE 7.6: Phase retardance Φ measurements of a Berek wave plate, placed in the sample arm, versus the indicator setting J, which is proportional to the retardance introduced by the compensator. Black dots correspond to the polarimetric measurements performed using the DC intensity from the sample arm, whereas red diamonds correspond to the polarimetric measurements performed using the interferometric modulation. Also represented are the polarimetric response of the Berek wave plate as measured by a Müller polarimeter [22] (thick black line) and the theoretical response of the Berek wave plate (thin dashed black line) as reported by the manufacturer's data sheet [21] for $\lambda_0 = 830\,\mathrm{nm}$.

In order to show that the polarimetric measurements are independent from the polarisation state of the reference arm (one must reinforce the fact that this is a purely intensity-based measurement amplified by the interferometric component), a different study has been carried out. Again, the Berek wave plate has been placed in the sample arm and the indicator setting J varied. The retardance measurements were then made resorting to the values of $I^{r0}(z)$ and $I^{r90}(z)$ (for a non-zero modulation frequency of the channelled spectrum), but also done using the DC intensity level exclusively from the sample arm. The comparison between these data sets is plotted in Figure 7.6. There is a slight difference between the

two sets of experimental points, potentially due to the limited extinction ratio of the linear polariser letting some of the otherwise blocked orthogonal polarisation state through. In this case, the assumption that a single polarisation state propagates through the collecting fibre, regardless of the setting on the rotator device, no longer holds.

The oscillating pattern in the experimental data sets in Figure 7.6 differs from that of Figure 7.5 most likely due to the fact that the sample arm has been realigned between the moments when these measurements were taken: readjustment of the LCR affected its orientation and hence its effects on the light transmitted.

7.1.3.2 Demonstration of independence of B-scan images to fibre-based disturbances

PS-OCT imaging has been carried out on a plastic phantom which exhibited strong birefringence. In Figure 7.7, the B(A)-scans corresponding to the two LCR rotation states (r_0 and r_{90}) are represented, along with the corresponding retardance maps $|\Phi|$.

To experimentally demonstrate the insensitivity of the system to the perturbations caused by the collecting fibre, two sets of images were generated, corresponding to Case 1 and Case 2. Between these two cases, the fibre-based polarisation controller in the collecting fibre was adjusted to mimic such perturbations. Case 1 is represented in Figure 7.7 (a)–(c), with frame I_1^{r0} depicting the 2-D structural map for the state r_0, I_1^{r90} the 2-D structural map for the state r_{90}, and Φ_1 the net retardance $|\Phi|$ map resulting from the ratio I^{r0}/I^{r90} (from Equation (7.7)). In the same way, Figure 7.7 (d)–(f) correspond to the same frames but in Case 2. The lateral size in all images is $3.5\,\mathrm{mm}$, and the usable depth range is $\sim 1.6\,\mathrm{mm}$.

One issue that arises when calculating $|\Phi|$ with the method presented is that the regions within the images being analysed with no or little signal (which can be caused by either $r(z) \sim 0$ or $\langle e_{\mathrm{out}} \,|\, r_{\mathrm{out}} \rangle \sim 0$) lead to erroneous values of $|\Phi|$ in the range of 0 to $\pi/2$. Effectively, if the noise floor is of the same order of magnitude in either image, a region with no signal yields a ratio $I^{r0}/I^{r90} \sim 1$, which in turn corresponds to a phase retardance in that region $|\Phi| \sim \pi/4$, which is clearly incorrect (since there are no reflectors at that depth). These artefacts are prevented by introducing a threshold value before the calculations are carried out, with the pixels whose values lie under the threshold not being taken into consideration in the calculations; instead, they are set to zero in the final retardance map.

In Figure 7.8 the A-scans along the shaded regions (centred at $x \sim 2.6\,\mathrm{mm}$, laterally averaged within the region) drawn over the frames of Figure 7.7 have

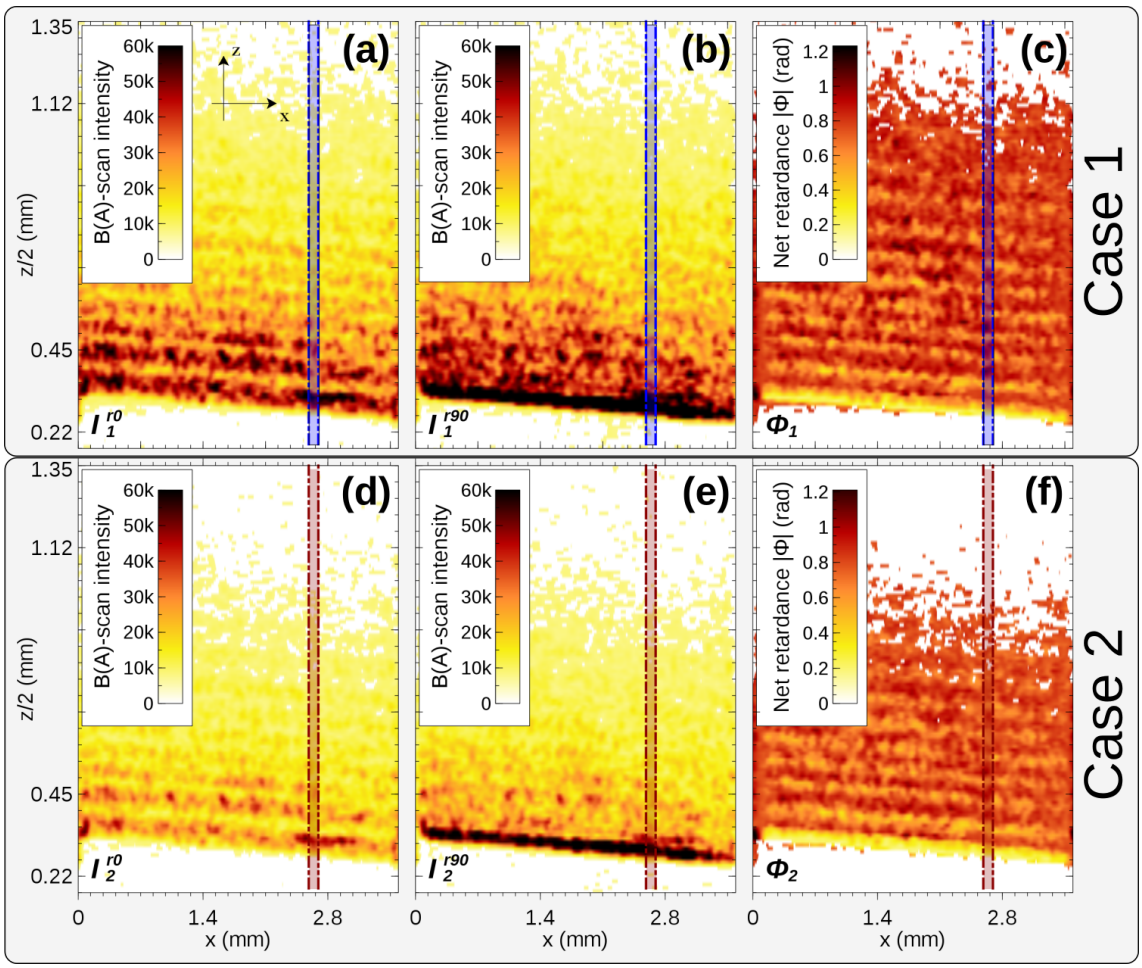

FIGURE 7.7: B(A)-scans of a plastic phantom exhibiting strong birefringence. Between the top (Case 1) and bottom rows (Case 2), the additional in-line fibre polarisation controller in the collecting fibre has been adjusted in terms of both pressure and rotation to create different fibre-induced polarisation states, and in this way replicate polarisation disturbances. **(a)**, **(b)**, **(d)**, and **(e)** correspond to the OCT B(A)-scans of the two rotation states; **(c)** and **(f)** depict the retardance maps for the two cases considered. The shaded regions (both the blue and the red-coloured ones) correspond to the averaged A-scans represented in Figure 7.8. (adapted from Marques *et al.* [1])

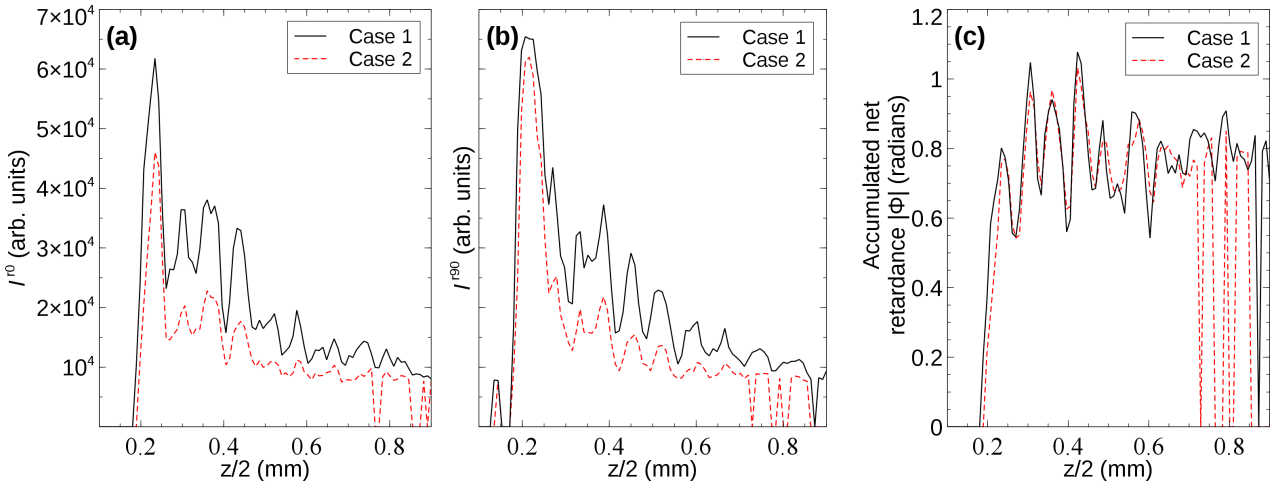

FIGURE 7.8: A-scan comparison for the two cases considered taken within the shaded regions represented in Figure 7.7. **(a)** and **(b)** correspond to A-scans of the OCT images concerning the two orthogonal polarisation states (I_i^{r0} and I_i^{r90}, for $i = 1, 2$). **(c)** is the accumulated (net) phase retardance for the two cases. (adapted from Marques *et al.* [1])

been plotted. Focusing on the plots corresponding to the OCT images ((a) and (b)), it is clear that the SNR for Case 2 is lower than that of Case 1; this results from the polarisation disturbances deliberately introduced in the collecting fibre, which create a mismatch between the polarisation states of the two interferometer arms, lowering the interferometric modulation. Even so, the resulting retardance maps in Figure 7.7 (c) and (f) show similar levels of phase retardance despite the disturbances induced in the collecting fibre. This can be further confirmed when analysing the A-scan cut in Figure 7.8 (c), with the two curves overlapping until $z/2 \sim 0.7\,\mathrm{mm}$.

One has to set the threshold level carefully, since this impacts the axial range of the phase retardance maps. Between Case 1 and 2 there is a significant reduction of the SNR on the OCT images, and if similar threshold settings are applied to both, then this results in differently-sized regions where the value of $|\Phi|$ matches. One has to stress out that this has nothing to do with the measurement itself, it is only a matter of optimising the contrast by adjusting the polarisation controllers as one would do in any OCT system, polarisation-sensitive or not.

In Figure 7.9 a comparison of several threshold settings is presented. The curves correspond to the depth distribution of the net phase retardance along the shaded region in Figure 7.7 (c) and (f) (in the same way as in Figure 7.8 (c)). The threshold setting chosen for the previous plot was 7500, which is represented in red in Figure 7.9; the box on both plots represents the region where the values of $|\Phi|$ for the two cases overlap fully for the 7500 threshold setting. Raising that

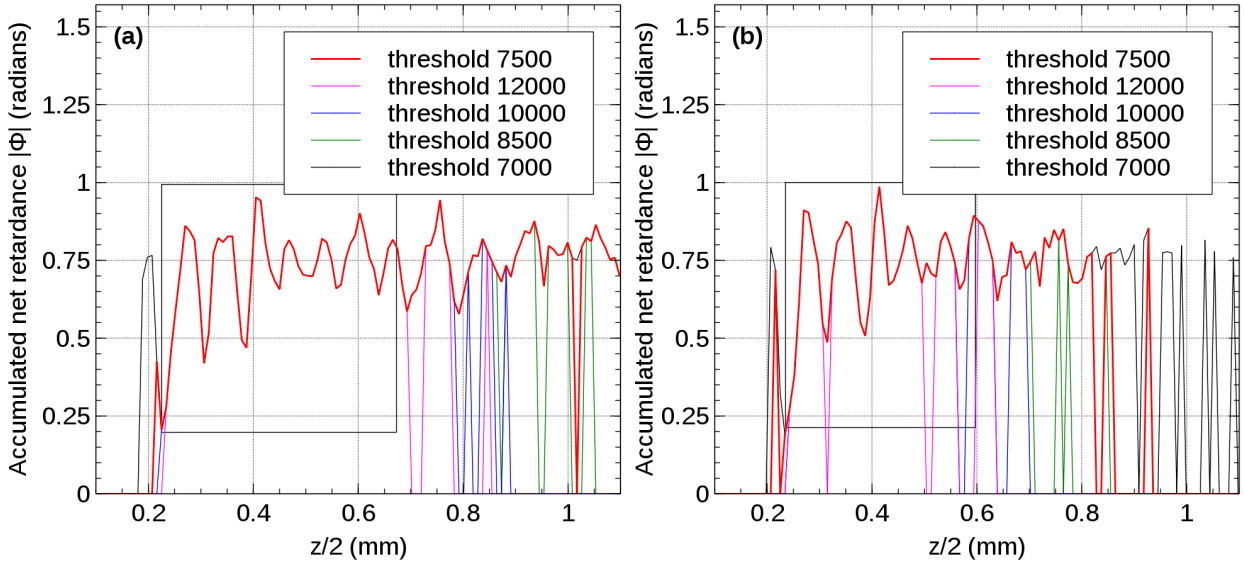

FIGURE 7.9: Comparison of different threshold settings for the accumulated (net) retardance measurements along an A-scan for the two cases, **(a)**: Case 1; **(b)**: Case 2. The region delimited by the box corresponds to the extent where the two cases have the same net retardance measurements for a threshold setting of $7,500$.

value leads to artefacts at larger depths, with the effect being particularly dramatic for Case 2, which exhibits a lower SNR to start with. Conversely, decreasing the threshold setting decreases the occurrence of artefacts at larger depths, but this gives rise to erroneous values in regions with no signal, as mentioned before.

7.2 Configuration B: Sequential, in-line design

This configuration aims to improve Configuration A by turning the sample arm design into an in-line configuration; this will mean that the original OCT system (Figure 7.10 (a)) can be transformed into a PS-OCT by adding such an in-line configuration, considered as an optical module which is inserted after the sample arm fibre. For the purpose of this analysis, only the SD-OCT implementation is considered, but the module is equally applicable to a SS-OCT system, as well as to TD-OCT.

7.2.1 Theoretical model

Following a similar approach to that presented in Section 7.1.1, the amplitude of the interferometric signal A_z caused by a single reflector at depth z is expressed

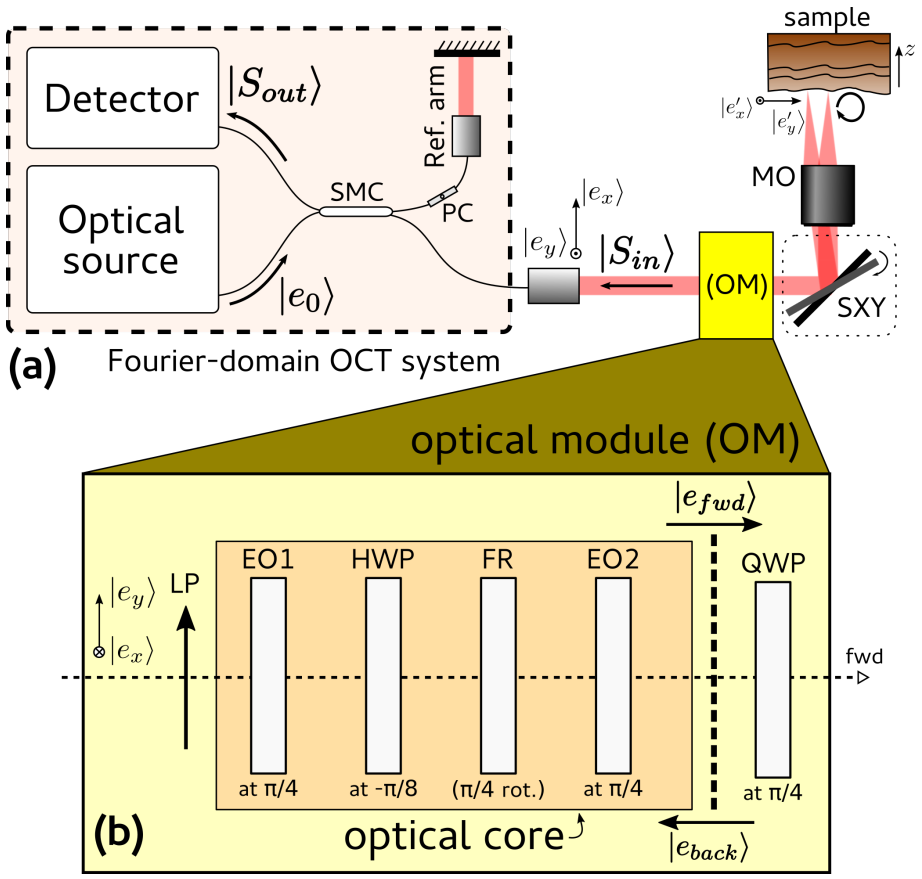

FIGURE 7.10: **(a)** Schematic representation of a Fourier-domain, PS-OCT system with the second drop-in optical module (OM) design (configuration B). The dashed rectangle corresponds to a fibre-based implementation of a Fourier-domain OCT system (minus the sample arm). **SXY**, scanning head with two galvanometer scanners with axes oriented at 90º in relation to each other; **MO**, microscope objective; **PC**, fibre-based polarisation controller; **SMC**, single-mode fibre coupler. Only single-mode fibres are used in the system. The field generated by the optical source is given by $|e_0\rangle$. The sample is probed with a circular polarisation state. $|S_{in}\rangle$ describes the field returning to the fibre-based part of the interferometer, and $|S_{out}\rangle$ describes the same field after propagation through the fibres and the SMC.

Inset **(b)**: Second optical module (OM) design. **LP**, linear polariser oriented along $|e_y\rangle$; **QWP**, quarter-wave plate oriented at $\pi/4$ in relation to $|e_x\rangle$. Inside the OM, another optical block is defined as the optical core of the OM, which consists of two electro-optic polarisation modulators (**EO1** and **EO2**) oriented at $\pi/4$ according to $|e_x\rangle$, a half-wave plate **HWP** oriented at $-\pi/8$ and a Faraday rotator **FR** that induces a polarisation state rotation of $\pi/4$. The operation of the optical core is described in the text. $|e_{fwd}\rangle$ describes the polarisation state of the light probing the sample before the QWP of the OM. $|e_{back}\rangle$ describes the polarisation state of the light returning from the sample after passing through the QWP. (adapted from Rivet *et al.* [2])

in the same way as in Equation (7.2), as a product between the fields $|r_{out}\rangle$ from the reference arm and $|S_{\text{out}}\rangle$ from the sample arm. Again, in this analysis the chromatic behaviour of the fibres is considered, hence A_z is effectively identified as $A(z,\nu)$, and described by:

$$A(z,\nu) = r(z)\,\langle r_{\text{out}}(\nu)\,|\,S_{\text{out}}(z,\nu)\rangle\,. \tag{7.15}$$

Throughout the analysis carried out in this section, the spectral shape is taken as flat in ν throughout the optical bandwidth of the source.

By Fourier transforming $I(\nu)$ (Equation (7.1)), an A-scan is obtained, which will contain a complex-valued peak corresponding to the single reflector located at depth z. Let $\hat{A}(z)$ be the complex value at the maximum of this peak. $\hat{A}(z)$ is related to $A(z,\nu)$ as follows:

$$\hat{A}(z) = \int A(z,\nu)d\nu, \tag{7.16}$$

and its absolute value $\hat{I}_{\text{interf}}$ can be written as

$$\hat{I}_{\text{interf}} = \left|\hat{A}(z)\right| = \left|r(z)\int \langle r_{\text{out}}(\nu)\,|\,S_{\text{out}}(z,\nu)\rangle\,d\nu\right|. \tag{7.17}$$

As before, the field $|S_{\text{out}}(z,\nu)\rangle$ contains both the retardance of the sample under analysis and the polarimetric properties of the fibre and couplers, which may be subject to environmental-induced changes. If the contributions from the sample and the fibre/couplers are de-coupled, then the polarimetric response of the sample can be measured independently from that of the fibres/couplers.

The optical module (OM) design is detailed in inset (b) of Figure 7.10. This design comprises a total of six elements, starting with a linear polariser *LP* and ending with a quarter-wave plate *QWP*, ensuring in this way a circular polarisation state in front of the sample.

Performing polarimetric measurements on the sample requires the analysis of the two orthogonal polarisation components. The *LP*, however, favours a single polarisation state – therefore, to circumvent this limitation, an optical core comprising two electro-optic polarisation modulators *EO1* and *EO2*, a half-wave plate *HWP* and a Faraday rotator *FR* are used. The arrangement of these components within the optical core ensures that the polarisation state of the beam will be altered differently depending on the direction of propagation: in the forward direction, regardless of the sequential step present in the optical core, the output polarisation state is always circular; while on the backward direction the returned

polarisation state (after the *QWP*) is rotated by either 0 or 90 degrees, depending on the sequential step considered.

Analysing the OM's behaviour in more detail, linearly polarised light after the *LP* is oriented along $|e_y\rangle$ and propagates through the optical core. Inside it (Figure 7.10 (b)), and following the forward propagation direction, the following optical elements are present: an electro-optic polarisation modulator *EO1* oriented at $\pi/4$, a half-wave plate *HWP* oriented at $-\pi/8$, a Faraday rotator *FR* which rotates the incident polarisation state by $\pi/4$, and a second electro-optic polarisation modulator *EO2* also oriented at $\pi/4$. *EO1* and *EO2* are driven to exhibit the same retardance ϕ_{EO}. The orientation of their fast axes is defined in respect to $|e_x\rangle$ in the basis $\{\,|e_x\rangle\,, |e_y\rangle\,\}$.

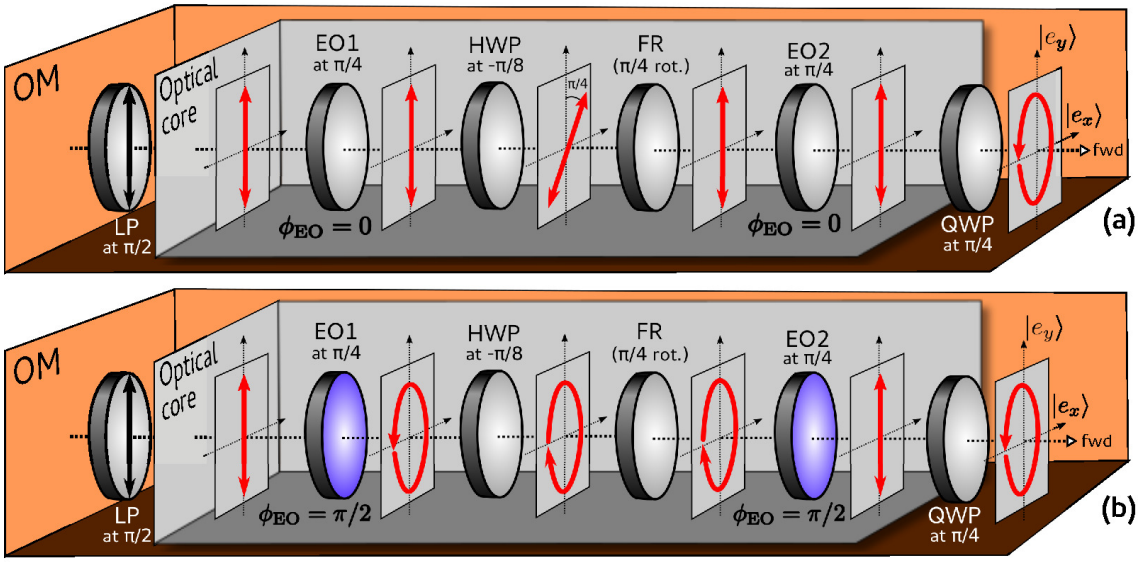

FIGURE 7.11: Orientation of the polarisation states within the OM (Figure 7.10 (b)) for $\phi_{EO} = 0$ (a) and $\phi_{EO} = \pi/2$ (b) for forward propagation (left to right). Regardless of the value ϕ_{EO} of the EO's retardance, the output polarisation state is always circular. (adapted from Rivet *et al.* [2])

In order to visualise the change of the polarisation states induced by the optical core when the forward propagation is considered, the retardance ϕ_{EO} is set to 0 or $\pi/2$, as shown in Figure 7.11. For the field going forward through the optical core, there is no change in the polarisation state of the light and this result can be generalised irrespective of the values of ϕ_{EO} introduced by *EO1* and *EO2*. Indeed, the Jones matrix of the optical core in the forward propagation direction, J^{fwd}_{core}, is

$$J^{fwd}_{core}\left(\phi_{EO}\right) = -j \begin{pmatrix} -1 & 0 \\ 0 & 1 \end{pmatrix}. \tag{7.18}$$

Therefore, the field $|e_{fwd}\rangle = J_{core}^{fwd}\,|e_y\rangle$ is given by $-j\,|e_y\rangle$ after *EO2*, making it linearly polarised along $|e_y\rangle$. Then the electric field is converted into a circular polarisation state by the *QWP* oriented at 45 degrees.

For the purpose of this analysis, the sample is modelled as a linear retarder with a net (double-pass) retardance $2\varphi(z)$ and a fast axis orientation given by $\theta(z)$ in respect to the sample basis $\{\,|e'_x\rangle\,,|e'_y\rangle\,\}$, as defined in Figure 7.10 (a). This basis results from the transformation of the original $\{\,|e_x\rangle\,,|e_y\rangle\,\}$ basis via reflections occurring on the two mirrors of the galvo-scanners *SXY*.

Light back-reflected by the birefringent sample travels towards the *QWP* within the OM. The corresponding field $|e_{back}\rangle$ (Figure 7.10 (b)) can be expressed as a product of the various Jones matrices and as a function of the forward propagating wave leaving the optical core, $|e_{fwd}\rangle$:

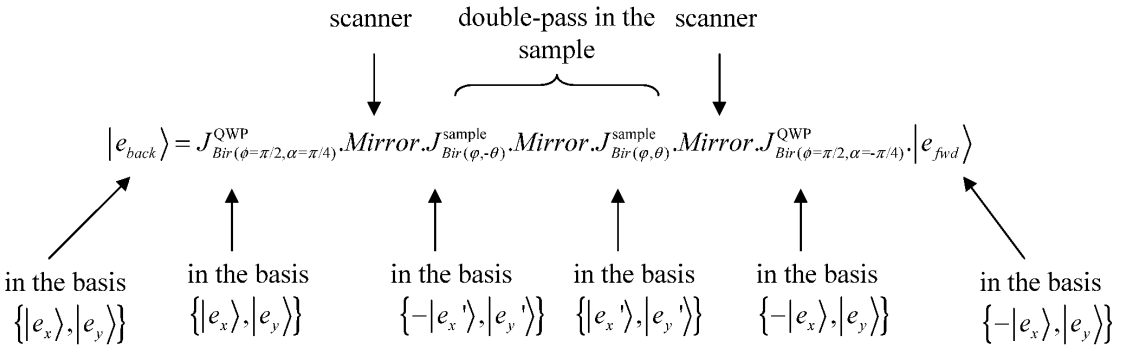

(7.19)

All these calculations have been carried out considering the point of view of the optical source, meaning that the basis for $|e_{fwd}\rangle$ is given by $\{-|e_x\rangle\,,|e_y\rangle\,\}$. $J_{\mathrm{Bir}(\phi,\alpha)}$ is defined in Equation (B.2) in Appendix B, and the Jones matrix for the mirrors present is defined in Equation (B.5) of the same Appendix. Developing the product of matrices, $|e_{back}\rangle$ can be written as

$$|e_{back}\rangle = \cos\varphi(z)\,|e_x\rangle - \sin\varphi(z)e^{-2i\theta(z)}\,|e_y\rangle\,, \tag{7.20}$$

which is a similar result to that obtained for the first design, as shown in Equation (7.3). The range for the one-pass retardance $\varphi(z)$ is considered from 0 to $\pi/2$, while the range for the fast axis orientation $\theta(z)$ is measured between 0 and π.

In the backward propagation direction, the optical core modifies the polarisation state according to the retardance ϕ_{EO} imprinted by the two *EO*s. In particular, the optical core acts as a rotator of the polarisation state, as shown in Figure 7.12 for ϕ_{EO} set either at 0 (a) or at $\pi/2$ (b).

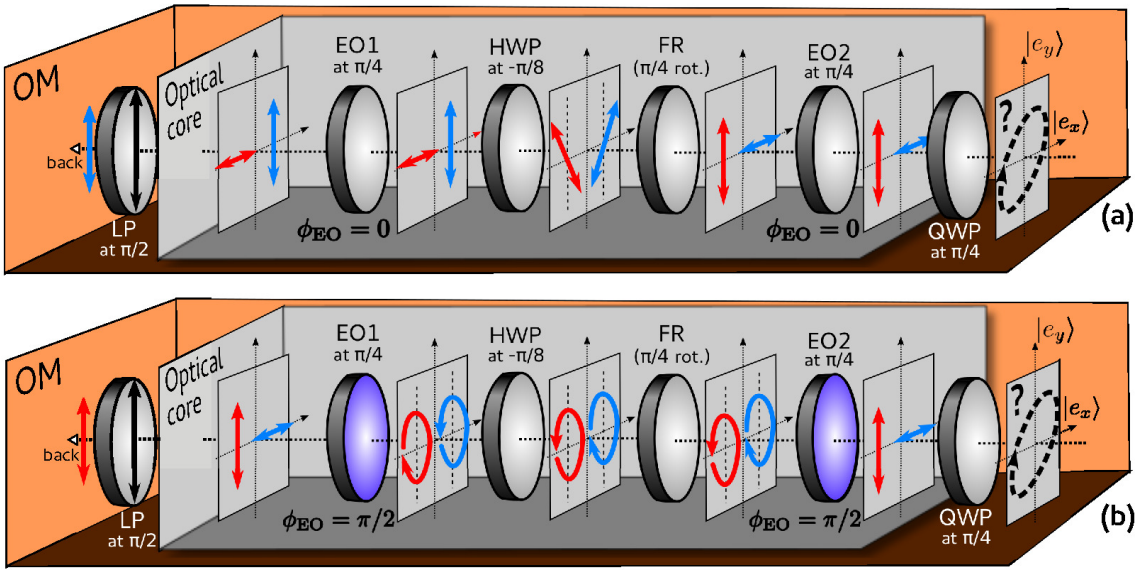

FIGURE 7.12: Orientation of the polarisation states in the OM for $\phi_{EO} = 0$ **(a)** and $\phi_{EO} = \pi/2$ **(b)**, for the backward propagation direction (right to left). The probing beam returns from the sample with an unknown polarisation state, which is composed of two linear orthogonal components, represented as red and blue in the diagram. These are sequentially selected, depending on the value of ϕ_{EO}. The two orthogonal components are represented in the diagram as being spatially separated for clarity. (adapted from Rivet *et al.* [2])

For any retardance ϕ_{EO} applied identically to both *EO*s, the Jones matrix describing the core of the optical module in the backward direction can be expressed on the basis $\{ |e_x\rangle , |e_y\rangle \}$ as

$$J_{core}^{back}(\phi_{EO}) = -j \begin{pmatrix} j \sin \phi_{EO} & \cos \phi_{EO} \\ \cos \phi_{EO} & j \sin \phi_{EO} \end{pmatrix} . \tag{7.21}$$

After traversing the optical core, the optical beam passes through the linear polariser, LP, oriented along $|e_y\rangle$, with the resulting field $|S_{in}(z)\rangle$ at the input of the probe fibre, as shown in Figure 7.10 (a). According to the retardance ϕ_{EO} of both *EO*s, this field becomes

$$|S_{in}(z)\rangle = P \cdot J_{core}^{back}(\phi_{EO}) \, |e_{back}\rangle , \tag{7.22}$$

where P is the Jones matrix of the linear polariser oriented along $|e_y\rangle$, described by

$$P = \begin{pmatrix} 0 & 0 \\ 0 & 1 \end{pmatrix} . \tag{7.23}$$

By further developing Equation (7.22), $|S_{in}(z)\rangle$ can be expressed as

$$|S_{in}(z)\rangle = -\left(-j\cos\varphi(z)\cos\phi_{EO} + e^{-2j\theta(z)}\sin\varphi(z)\sin\phi_{EO}\right)|e_y\rangle\,. \tag{7.24}$$

Due to the polarimetric response of the collecting fibre and the coupler described in the general matrix $J_{out}^{fibre}(\nu)$, the field $|S_{out}(z,\nu)\rangle$ in front of the detector is obtained as a transformation of $|S_{in}\rangle$:

$$\begin{aligned} |S_{out}(z,\nu)\rangle &= J_{out}^{fibre}(\nu)\,|S_{in}\rangle && \text{(7.25a)}\\ &= -\left(j\cos\varphi(z)\cos\phi_{EO}\right. \\ &\quad \left. + e^{-2j\theta(z)}\sin\varphi(z)\sin\phi_{EO}\right)|e_{out}(\nu)\rangle\,, && \text{(7.25b)} \end{aligned}$$

where $|e_{out}(\nu)\rangle = J_{out}^{fibre}(\nu)\,|e_y\rangle$. The complex amplitude $\hat{A}^{\phi_{EO}}(z)$, corresponding to the A-scan peak at the depth z of the scattering centre considered, can then be written from Equations (7.15) and (7.16) as

$$\begin{aligned} \hat{A}^{\phi_{EO}}(z) = -\alpha(z)\,&\left(j\cos\varphi(z)\cos\phi_{EO}\right. \\ &\left. + e^{2j\theta(z)}\sin\varphi(z)\sin\phi_{EO}\right)e^{j\varphi_{rand}}, \end{aligned} \tag{7.26}$$

where the random phase φ_{rand} is added to take into account the noise of the interferometer (caused by random changes in the OPD), and $\alpha(z)$ is defined by

$$\alpha(z) = r(z)e^{j\pi}\int \langle r_{out}(\nu)\,|\,e_{out}(\nu)\rangle\,d\nu. \tag{7.27}$$

To extract the polarimetric information encoded in the parameters φ and θ, irrespective of the polarimetric properties of the fibres in the interferometer, $\hat{A}(z)$ needs to be measured sequentially for two different values of ϕ_{EO}.

Similarly to the first design, given that the linear polariser is used as an analyser in the backward direction of propagation, the two polarisation states of the light returning from the sample and travelling through the fibres for the two values of ϕ_{EO} are identical. Therefore the coefficient $\alpha(z)$, which contains all the polarimetric disturbances of the fibres, can be eliminated in the exact same way as presented in the description of the first PS-OCT design in Section 7.1.1. Furthermore, the product $\langle r_{out}(\nu)\,|\,e_{out}(\nu)\rangle$ dictates the contrast of the interference signal, i.e. the SNR of the OCT signal. This can be optimised by adjusting the

fibre-based polarisation controller *PC* present in the reference arm, as pictured in Figure 7.10 (a). Since $\alpha(z)$ is eliminated in the procedure mentioned above, the adjustment of *PC* does not impact the polarimetric measurement in any way; it only influences the SNR of the OCT signal.

7.2.2 Sequential operation and the random phase variation in the interferometer

The analysis presented in this section is also applicable to Configuration A, since it also relies on an active optical element (a liquid crystal rotator) to be switched sequentially between two states. The relation of the switching speed with the time derivative of the random phase φ_{rand} in the interferometer determines not only the reliability of the retardance and optical axis orientation measurements, but also the strategy necessary to effectively measure the optical axis orientation, since this relies on a phase measurement of two sequentially-obtained signals.

Two case studies are presented, corresponding to two different switching rates of the two electro-optic polarisation modulators (EOs) in comparison with the variation of the random phase φ_{rand} in the system.

7.2.2.1 Fast set-up: Random phase φ_{rand} identical for the two sequential measurements

If the sequential measurements are carried out at a high switching rate of the EOs, the variation of φ_{rand} can be considered negligible from one measurement to the next. A function $\beta(z)$ can be defined to consider the two sequential measurements, one for $\phi_{EO} = \phi_0$ and the other for $\phi_{EO} = \phi_0 + \pi/2$, as follows:

$$\beta(z) = \frac{\sin\phi_0 \hat{A}^{\phi_0}(z) + \cos\phi_0 \hat{A}^{\phi_0+\pi/2}(z)}{\cos\phi_0 \hat{A}^{\phi_0}(z) - \sin\phi_0 \hat{A}^{\phi_0+\pi/2}(z)}. \tag{7.28}$$

By using the expressions for $\hat{A}^{\phi_{EO}}$ in Equation (7.26), $\beta(z)$ can be written according to the polarimetric properties of the sample:

$$\beta(z) = \tan\varphi(z) e^{-j(2\theta(z)+\pi/2)}. \tag{7.29}$$

The function $\beta(z)$ is therefore insensitive to the polarimetric properties of the fibres and couplers contained in $\alpha(z)$. Taking the equation above, the value of the one-pass retardance of the sample, $\varphi(z)$, is given by

$$\varphi(z) = \arctan|\beta(z)|, \tag{7.30}$$

with $\varphi \in [0, \pi/2]$ and the fast axis orientation $\theta(z)$ of the sample given by

$$\theta(z) = -\arg[\beta(z)]/2 - \pi/4 + m\pi, \tag{7.31}$$

where $\arg$ stands for the argument of the complex number in the bracket and m is an integer such that $\theta(z) \in [0, \pi]$.

As a result of the above demonstration, the measurement of two complex amplitudes for the two states of the EOs is enough to obtain the retardance and the orientation of the optical axis of the retarder. By calculating $\beta(z)$, the coefficient $\alpha(z)$ is eliminated, therefore the retardance $\varphi(z)$ and the fast axis orientation $\theta(z)$ can be determined independently from these properties.

7.2.2.2 Slow set-up: Random phase φ_{rand} varying between two sequential measurements

Considering now that the two sequential measurements are not carried sufficiently fast to ignore the random phase φ_{rand} variation in the interferometer, this means that different values of φ_{rand} must be taken into consideration for each of the two measurements. This could be the case if the active elements used in the design have a low switching rate, which is the case with the liquid crystal rotator *LCR* employed in configuration A (Section 7.1), or if the electro-optic modulators in configuration B are slow or are switched after the acquisition of each B-scan.

If only the net retardance of the sample is to be measured, one can measure the complex amplitude peak in the A-scan for $\phi_{EO} = 0$ and $\phi_{EO} = \pi/2$. In this case, $\varphi(z)$ can be extracted irrespective of the changes in the random phase, since the determination of the retardance relies solely on the amplitude:

$$\varphi(z) = \arctan\left|\frac{\hat{A}^{\pi/2}(z)}{\hat{A}^{0}(z)}\right|. \tag{7.32}$$

However, if one intends to measure the axis orientation of the sample as well, a possible solution consists in using the surface layer of the sample to produce a phase reference. Usually the surface layer of the medium is used in PS-OCT

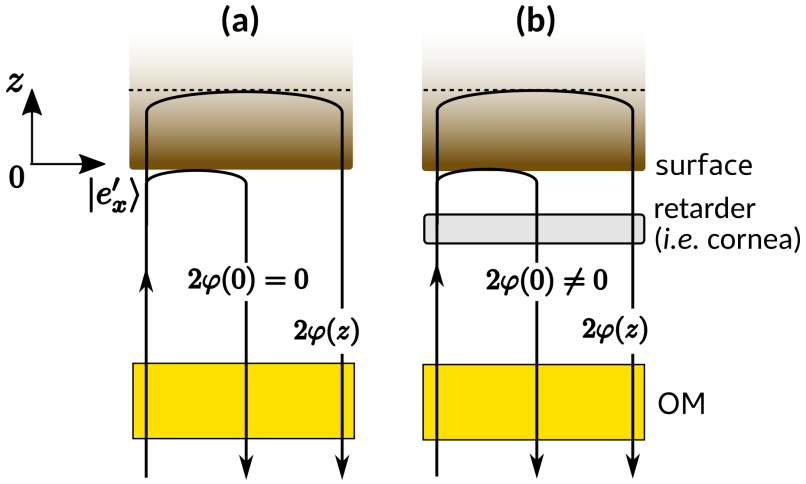

FIGURE 7.13: Representation of the two situations considered: **(a)** no retarder in front of the surface; **(b)** retarder in front of the surface, which as an example can be taken as corneal tissue. The sample is considered to not be a diattenuating one. (adapted from Rivet *et al.* [2])

	$\boldsymbol{\Delta\varphi_{\text{rand}} = 0}$	$\boldsymbol{\Delta\varphi_{\text{rand}} \neq 0}$
$\varphi(0) = 0$	$\phi_{EO} : \phi_0 \rightarrow \phi_0 + \pi/2.$	$\phi_{EO} : \pi/4 \rightarrow -\pi/4.$
$\varphi(0) = \pi/2$		$\phi_{EO} : \pi/4 \rightarrow -\pi/4.$
$\varphi(0) \neq 0,\ \varphi(0) \neq \pi/2$		$\phi_{EO} : 0 \rightarrow \pi/2.$

TABLE 7.2: Required retardance values ϕ_{EO} for the two electro-optic modulators, according to the retardance at the sample surface $\varphi(0)$ and to the variation of the random phase $\Delta\varphi_{rand}$ between the two states of the EOs.

measurements to reference the polarimetric properties of the fibre [23, 24], corresponding to a normalisation in relation to the surface. The generation of the circular polarisation state and the analysis of the returned polarisation state are performed in free space, in front of the sample, allowing independence of measurements from the fibre's polarimetric properties [1]. In order to eliminate the effect of the random phase, it is necessary to calculate the ratio

$$\hat{A}^{\phi_{EO}}_{norm}(z) = \frac{\hat{A}^{\phi_{EO}}(z)}{\hat{A}^{0}(z)}, \tag{7.33}$$

where $\hat{A}^0(z)$ is the complex amplitude for the peak within the A-scan corresponding to the surface, the value of which depends on the value chosen for the retardance of the electro-optic modulation, ϕ_{EO}.

This choice of values for ϕ_{EO} depends on whether a retarder element is placed or not in front of the sample surface, as shown in Figure 7.13. Table 7.2 presents the required values for ϕ_{EO} for each of the cases listed in the following Sub-Sections.

No retarder element in front of the sample surface, $\varphi(0) = 0$ When there is no retarder element in front of the surface, which could be the case if, for example, a skin sample is being imaged (as depicted in Figure 7.13 (a)), the net retardance imprinted by the surface is considered to be $\varphi(0) = 0$. The complex amplitude is therefore $\hat{A}^{\pi/2}(0) = 0$ and it cannot be used to normalise $\hat{A}^{\pi/2}(z)$.

In this case, the retardance values for the electro-optic modulators should be set to $\phi_{EO} = \pi/4$ and $-\pi/4$. By taking a modified version of Equation (7.28), one can define $\beta_1(z)$ as

$$\beta_1(z) = \frac{\hat{A}^{\pi/4}_{norm}(z) - \hat{A}^{-\pi/4}_{norm}(z)}{\hat{A}^{\pi/4}_{norm}(z) + \hat{A}^{-\pi/4}_{norm}(z)} = \tan\varphi(z) e^{-j(2\theta(z)+\pi/2)}, \tag{7.34}$$

where $\varphi(z)$ can be retrieved using

$$\varphi(z) = \arctan\left|\beta_1(z)\right|, \tag{7.35}$$

and where the axis orientation $\theta(z)$ of the sample is given by

$$\theta(z) = -\frac{1}{2}\arg\left\{\beta_1(z)\right\} - \frac{\pi}{4} + m\pi. \tag{7.36}$$

Retarder element in front of the sample surface, $\varphi(0) \neq 0$ If, however, a retarder element is present between the sample surface and the optical module itself (as pictured in Figure 7.13 (b)), one can no longer take the sample surface as having a retardance equal to zero. This is the case, for instance, when imaging the retina *in vivo* and *in situ*, since the anterior chamber of the eye will introduce additional birefringence in the measurement.

Two cases can be considered: $\varphi(0) = \pi/2$ and the case where $\varphi(0)$ is neither zero nor $\pi/2$. Considering the latter case, on the surface one would then obtain $\hat{A}^0(0) \neq 0$ and $\hat{A}^{\pi/2}(0) \neq 0$, hence these values can be used to normalise the complex amplitudes $\hat{A}^0(z)$ and $\hat{A}^{\pi/2}(z)$. Therefore, in the two states of the electro-optic polarisation modulators the values $\phi_{EO} = 0$ and $\phi_{EO} = \pi/2$ are taken, and $\varphi(z)$ can be obtained in the same manner as in Equation (7.32). The orientation of the optical axis $\theta(z)$ of the medium can be expressed as

$$\theta(z) - \theta(0) = -\frac{1}{2}\arg\left\{\frac{\hat{A}^{\pi/2}_{norm}(z)}{\hat{A}^{0}_{norm}(z)}\right\} + m\pi. \tag{7.37}$$

In this case, it is not possible to measure the absolute orientation of the optical axis, but only the orientation according to $\theta(0)$.

On the other hand, if $\varphi(0) = \pi/2$, the complex amplitude measured at the surface $\hat{A}^0(0)$ is null and cannot therefore be used to normalise $\hat{A}^0(z)$. One can employ the same strategy as in the case with no retarder in front of the sample surface (Section 7.2.2.2), and set the retardances of the two EOs ϕ_{EO} to $-\pi/4$ and $\pi/4$. It is possible to define a function $\beta_2(z)$ as

$$\beta_2(z) = \frac{\hat{A}^{\pi/4}_{norm}(z) + \hat{A}^{-\pi/4}_{norm}(z)}{\hat{A}^{\pi/4}_{norm}(z) - \hat{A}^{-\pi/4}_{norm}(z)} = \tan\varphi(z)e^{-j(2\theta(z)+\pi/2)}, \tag{7.38}$$

with $\varphi(z)$ able to be retrieved in the same way as before,

$$\varphi(z) = \arctan\left|\beta_2(z)\right|, \tag{7.39}$$

and the same holds for the axis orientation $\theta(z)$:

$$\theta(z) = -\frac{1}{2}\arg\left\{\beta_2(z)\right\} - \frac{\pi}{4} + m\pi. \tag{7.40}$$

7.2.3 Chromatic effects on the sequential optical module operation

In this section, a detailed analysis of the impact on the polarimetric measurements caused by the chromatic response of the optical elements within the second optical module design (configuration B) is presented. For configuration A such response has been experimentally found (when characterising the accuracy of the system using a Berek waveplate, as shown in Section 7.1.3.1), however no further modelling has been made due to insufficient information regarding the active optical element used (the liquid-crystal polarisation rotator).

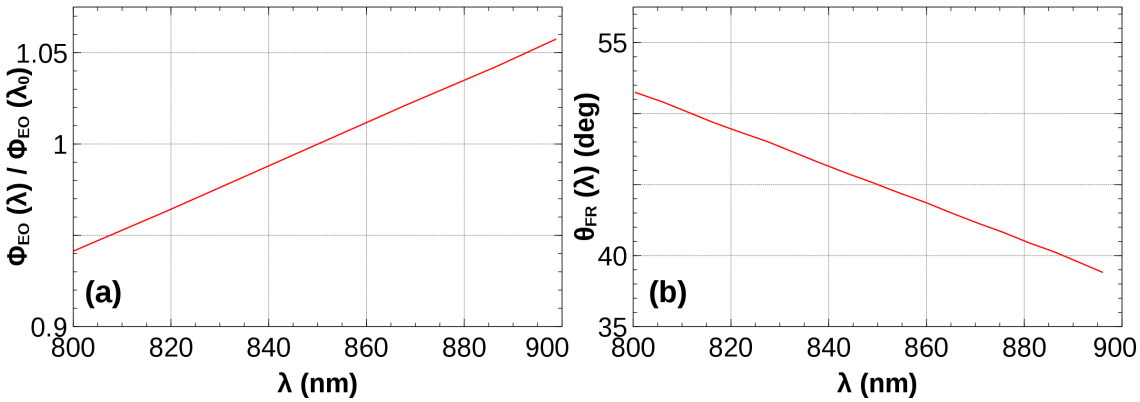

FIGURE 7.14: Chromatic response of **(a)** the electro-optic polarisation modulator and **(b)** the Faraday rotator employed in the numerical simulations. (adapted from Rivet *et al.* [2])

The optical module in configuration B is made of commonly available optical elements, including Faraday rotators, wave plates, linear polarisers and electro-optic polarisation modulators, which are present in many PS-OCT and other interferometric systems. While wave plates and linear polarisers with flat broadband responses are readily available, the chromaticity of Faraday rotators and electro-optic polarisation modulators must be taken into account. These necessarily introduce systematic errors (bias) on the polarimetric measurement of the sample being characterised.

Electro-optic polarisation modulators are usually built with two matched crystals arranged in series, oriented at 90 degrees in relation to each other, in order to suppress intrinsic birefringence and variations due to temperature changes. For the purpose of the simulations carried out in this Section, a Lithium Niobate ($LiNbO_3$) medium was employed, having a half-wave voltage V_π equal to $300\,\mathrm{V}$ at $\lambda_0 = 1\,\mu\mathrm{m}$ and $150\,\mathrm{V}$ at $\lambda_0 = 532\,\mathrm{nm}$, similar to the Newport model 4104 modulator employed in the system reported by Yamanari *et al.* [18]. Figure 7.14 (a) depicts the normalised retardance variation $\phi_{EO}(\lambda)/\phi_{EO}\,(\lambda_0)$ of the said electro-optic polarisation modulator versus wavelength, considering $\lambda_0 = 850\,\mathrm{nm}$.

For the Faraday rotator, a 45-degree Terbium Gallium Garnet rotator device has been considered. In order to model its chromatic response, the Verdet constant $V(\lambda)$ has been linearly interpolated using values from Barnes *et al.* [25], which give $V\,(\lambda = 900\,\mathrm{nm}) = 51\,\mathrm{rad/(T \cdot m)}$ and $V\,(\lambda = 800\,\mathrm{nm}) = 68.5\,\mathrm{rad/(T \cdot m)}$. With these parameters, it is possible to model the rotation angle θ_{FR} as a function of the operating wavelength λ, as depicted in Figure 7.14 (b) .

The sample considered in all these simulations is a linear retarder where its retardance $\varphi_{\mathrm{sample}}$ and optical axis orientation θ_{sample} are variable parameters. Furthermore, the optical source employed has its central wavelength $\lambda_0 = 850\,\mathrm{nm}$,

with two spectral bandwidths ($\Delta\lambda_1 = 50\,\mathrm{nm}$ and $\Delta\lambda_2 = 100\,\mathrm{nm}$) considered, depending on the case being studied.

Similarly to what has been done in Section 7.2.2, the analysis of the impact the chromatic behaviour of the optical elements have on the accuracy of the polarimetric measurements has been carried out assuming a fast and a slow configuration, ie. considering switching periods shorter or longer than the random phase variation $\Delta\varphi_{\mathrm{rand}}$, respectively. As presented in the said section, the fast case allows more flexibility in the choice of the values of ϕ_{EO}, since one does not need to take into consideration a reference surface on the sample in order to compensate for the random phase variation. Therefore, in the fast case the chromaticity analysis focused on different values of ϕ_{EO}, whereas for the slow case a specific set of ϕ_{EO} values has been chosen, with the analysis focusing on the impact of the different optical bandwidth values considered.

7.2.3.1 Fast set-up: Random phase φ_{rand} identical for the two sequential measurements

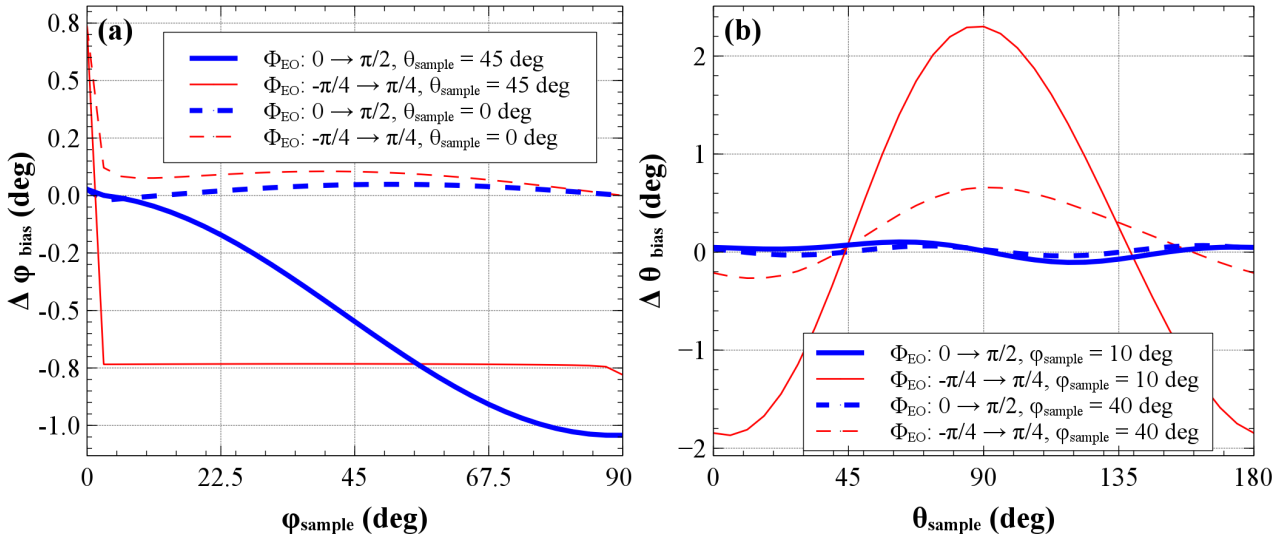

FIGURE 7.15: Measurement of the bias on **(a)** the retardance $\varphi_{\mathrm{sample}}$ and **(b)** the orientation angle θ_{sample} of a linear retarder. Thin (red) curves, retardance ϕ_EO switching from $-\pi/4$ to $\pi/4$. Thick (blue) curves, retardance ϕ_{EO} switching from 0 to $\pi/2$. Solid lines in **(a)**, fast optical axis of the sample oriented at 0 degrees. Dashed lines in **(a)**, fast optical axis of the sample oriented at 45 degrees. Solid lines in **(b)**, sample retardance equal to 10 degrees. Dashed lines in **(b)**, sample retardance equal to 40 degrees. (adapted from Rivet *et al.* [2])

The numerical simulations in this section assume that the switching rate of the optical module is sufficiently large to ensure that the random phase φ_{rand} is identical in the two states and that the collecting fibres do not change their

characteristics for the two sequential states. Consequently, the system operates as described in Section 7.2.2.1, with $\phi_{EO} = \phi_0$ being a free parameter, only constrained by the fact that the second sequential state must have $\phi_0 + \pi/2$ in order to achieve complete rotation of the returning polarisation state. In this particular simulation, the FWHM of the source spectrum is taken as $\Delta\lambda_2 = 100\,\mathrm{nm}$.

Two sets of values for ϕ_{EO} were chosen to model the chromatic behaviour of the optical module: $\phi_{EO} : 0 \rightarrow \pi/2$ and $\phi_{EO} : -\pi/4 \rightarrow \pi/4$. The biases on the measurement of the sample's retardance $\Delta\varphi_{\mathrm{sample}}$ and its optical axis orientation $\Delta\theta_{\mathrm{sample}}$ for either set are represented in Figure 7.15 (thick blue lines for $\phi_{EO} : 0 \rightarrow \pi/2$ and thin red lines for $\phi_{EO} : -\pi/4 \rightarrow \pi/4$).

Figure 7.15 (a) shows the bias on retardance for two different orientations of the retarders, at 0 degrees (dashed line), and at 45 degrees (solid line). Due to the chromatic response of the optical module, a coupling between $\varphi_{\mathrm{sample}}$ and θ_{sample} appears in the systematic errors.

The bias observed also differs according to the strategy ($\phi_{EO} : 0 \rightarrow \pi/2$ or $\phi_{EO} : -\pi/4 \rightarrow \pi/4$) used for the sequential measurement. For the case where $\phi_{EO} : -\pi/4 \rightarrow \pi/4$, the bias $\Delta\varphi_{\mathrm{sample}}$ is uniform except for weak sample retardances. By contrast, when the case $\phi_{EO} : 0 \rightarrow \pi/2$ is considered, the bias is low for a weak sample retardance but increases with it for $\theta_{\mathrm{sample}} = 45$ degrees, while no variation is observed for $\theta_{\mathrm{sample}} = 0$ degrees.

Figure 7.15 (b) represents the bias on axis orientation for two different sample retardances $\varphi_{\mathrm{sample}}$, at 10 degrees (solid line) and at 40 degrees (dashed line). Once more, due to the chromatic response of the optical module a coupling between $\varphi_{\mathrm{sample}}$ and θ_{sample} takes place, as shown by the systematic errors pictured. The bias $\Delta\theta_{bias}$ is less significant for the strategy $\phi_{EO} : 0 \rightarrow \pi/2$.

7.2.3.2 Slow set-up: Random phase φ_{rand} varying between two sequential measurements

In this Section it is assumed that the switching rate of the optical module is not large enough to ensure that the random phase does not vary between the two sequential steps; it is, however, large enough to guarantee that the properties of the collecting fibre and couplers do not vary during the aforementioned steps, as shown in the blue response curves of Figure 7.4.

Two sub-cases are distinguished in the following sub-sections: whether a retarder element is placed in front of the sample or not, as discussed earlier in Section 7.2.2.2.

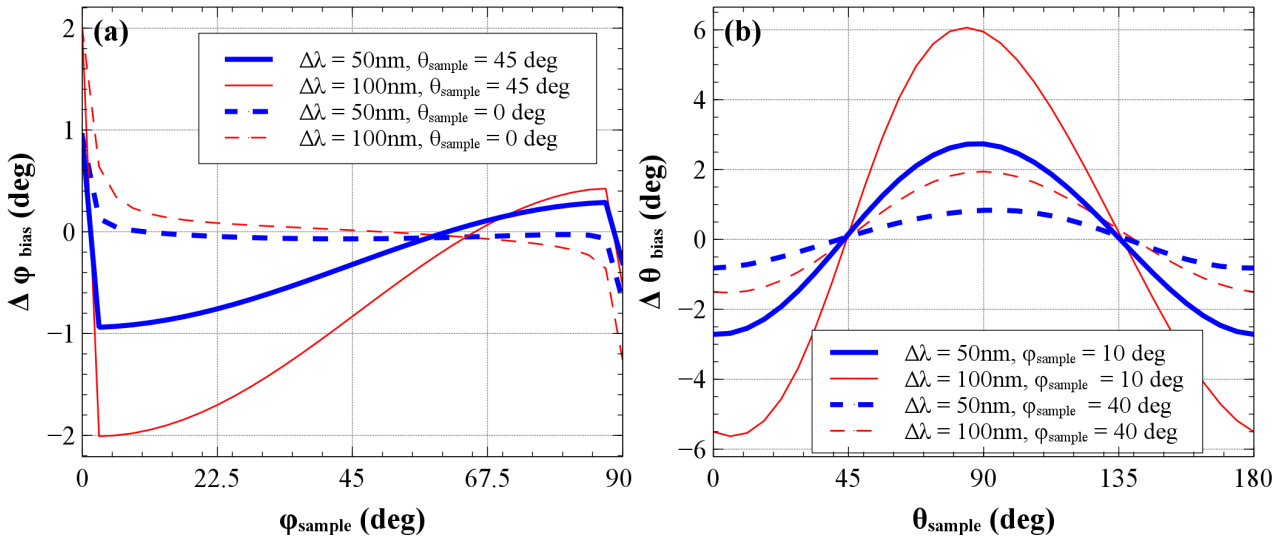

FIGURE 7.16: Measurement of the bias on **(a)** the retardance φ_{sample} and **(b)** the orientation angle θ_{sample} of a linear retarder. Thick (blue) curves: the FWHM of the optical source spectrum is equal to $\Delta\lambda_1 = 50\,\text{nm}$. Thin (red) curves: the FWHM of the optical source spectrum is equal to $\Delta\lambda_2 = 100\,\text{nm}$. Solid lines in **(a)**: sample oriented at 45 degrees. Dashed lines in **(a)**, sample oriented at 0 degrees. Solid lines in **(b)**: sample retardance equal to 10 degrees. Dashed lines in **(b)**, sample retardance equal to 40 degrees. (adapted from Rivet *et al.* [2])

No retarder element in front of the sample surface, $\varphi(0) = 0$ The biases on the measurements of both the sample retardance and its optical axis orientation for this case are represented in Figure 7.16. Two spectral bandwidths are considered for this case: $\Delta\lambda_1 = 50\,\text{nm}$ (thick blue curves) and $\Delta\lambda_2 = 100\,\text{nm}$ (thin red curves). In Figure 7.16 (a) the bias for the sample retardance φ_{sample} measurements is represented for two orientations of the sample's optical axis, $\theta_{\text{sample}} = 0$ degrees and $\theta_{\text{sample}} = 45$ degrees, while in Figure 7.16 (b) the bias for the sample's optical axis orientation θ_{sample} measurements is represented for two sample retardance values, $\varphi_{\text{sample}} = 10$ degrees and $\varphi_{\text{sample}} = 40$ degrees.

Again, due to the chromatic response of the components within the optical module, a coupling between the retardance and optical axis orientation measurements is present. In this case there is an additional amplification of this effect due to the normalisation required in order to remove the effects of the random phase variation, as described in Section 7.2.2.2. As expected from the response curves in Figure 7.14, the larger the bandwidth of the optical spectrum considered, the stronger the bias observed for both φ_{sample} and θ_{sample}.

As presented in Section 7.2.2.2, ϕ_{EO} must switch from $-\pi/4$ to $\pi/4$ in order to avoid the zero value at the normalisation factor $\hat{A}^{\pi/2}(0)$. By employing these values for ϕ_{EO}, the bias on the optical axis orientation is close to zero at 45 and

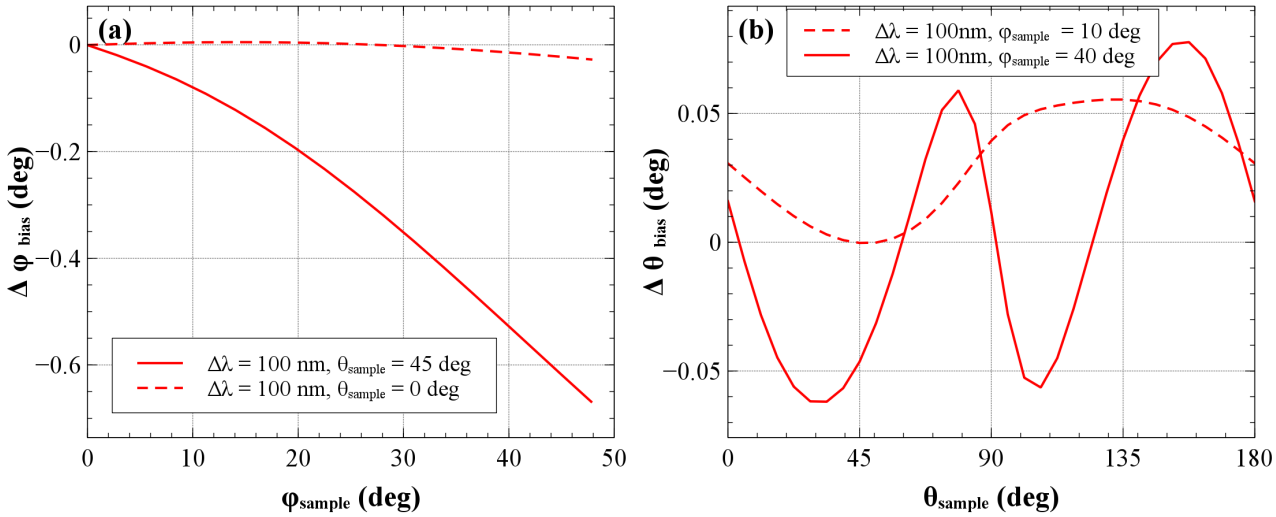

FIGURE 7.17: Measurement of the bias on **(a)** the retardance φ_{sample} and **(b)** the orientation angle θ_{sample} of a system made of a retarder (cornea) in front of a sample corresponding to the retinal nerve fibre layer (RNFL). Solid line in **(a)**, sample oriented at 45 degrees. Dashed line in **(a)**, sample oriented at 0 degrees. Solid line in **(b)**, sample retardance equal to 50 degrees. Dashed line in **(b)**, sample retardance equal to 10 degrees. (adapted from Rivet *et al.* [2])

135 degrees but increases for lower sample retardances and larger spectral bandwidths at 0, 90 and 180 degrees.

Retarder element in front of the sample surface, $\varphi(0) \neq 0$ To be consistent with other PS-OCT studies applied to retinal imaging [26, 27], the retarder element placed in front of the sample, assumed to have an equivalent effect to that of corneal tissue on polarisation-sensitive posterior segment imaging, is modelled with a one-pass retardance of 25 degrees and an optical axis orientation set arbitrarily at 0 degrees on the basis $\{ |e'_x\rangle , |e'_y\rangle \}$. The sample represents the retinal nerve fibre layer (RNFL) of the retina, and is modelled as having a one-pass retardance φ_{sample} between 10 and 50 degrees [28], with an optical axis orientation θ_{sample}.

Figure 7.17 (a) represents the bias $\Delta\varphi_{\text{sample}}$ on the measurement of the sample retardance for two different sample orientations, at 0 degrees (dashed line) and at 45 degrees (solid line). Figure 7.17 (b) shows the bias $\Delta\theta_{bias}$ affecting the measurements of the sample axis for two different sample retardances, 10 degrees (dashed line) and 50 degrees (solid line).

In this case, the retardance measured at the sample surface $\varphi(0)$ was assumed to be $\neq \pi/2$, hence the $\phi_{EO} : 0 \rightarrow \pi/2$ strategy was used. Due to that, the bias on the optical axis orientation measurements is weak (as is the case in Figure 7.15 (b)

when comparing the traces against those produced with the $\phi_{EO} : -\pi/4 \rightarrow \pi/4$ strategy) and inferior to those obtained in Figure 7.16 (b).

7.3 Configuration C: Snapshot (simultaneous) measurement

Unlike the two previous configurations presented, Configuration C does not rely on active optical elements to achieve single detector operation, whilst still meeting the other requirements stated at the beginning of this chapter. Instead, the two orthogonal polarisation states are encoded in the OPD by means of two different optical paths in the sample arm, a strategy reported in previous publications [14, 29].

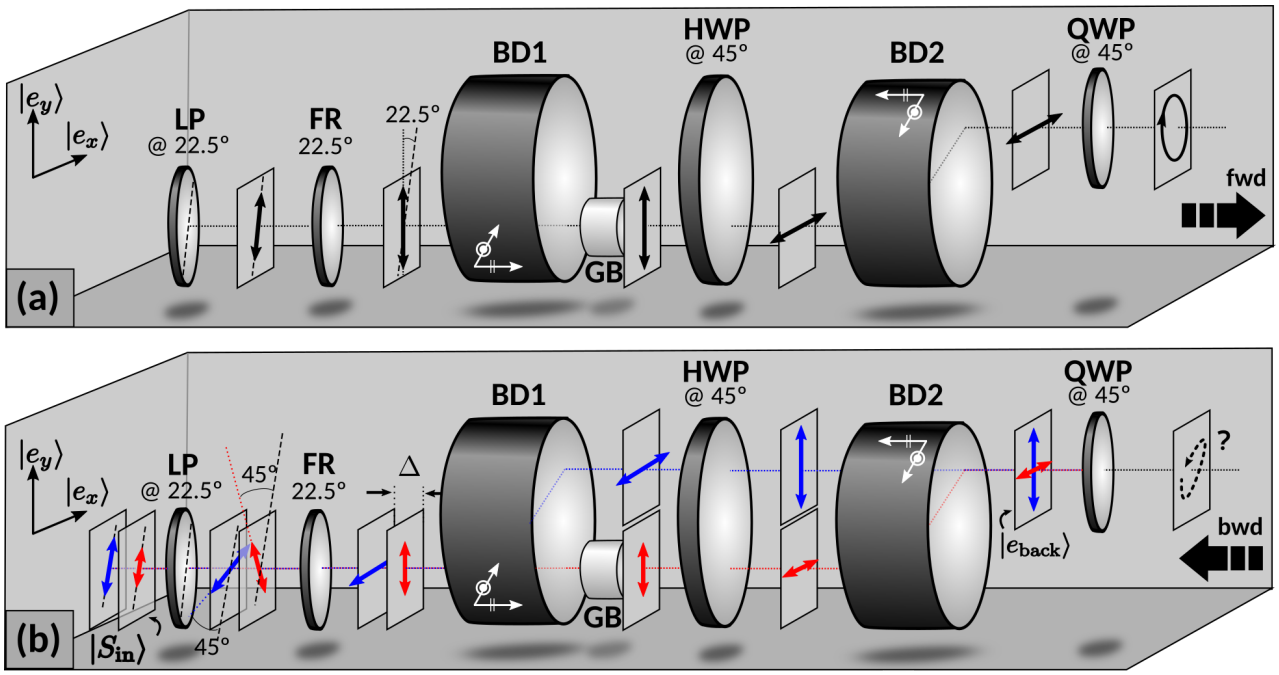

FIGURE 7.18: Passive, simultaneous sampling optical module design, and behaviour for the **(a)** forwards and **(b)** backward propagation directions. **LP**, linear polariser oriented at 22.5 degrees in relation to the horizontal ($\hat{x}$); **FR**, Faraday rotator performing a 22.5 degree rotation of the incident polarisation; **BD1-2**, beam displacers; **HWP**, half-wave plate oriented at 45 degrees; **QWP**, quarter-wave plate oriented at 45 degrees.

In Figure 7.18 a schematic representation of this configuration is presented, both for forward (a) and backward (b) propagation.

Similarly to Configuration B, this module design is also in-line (ensuring non-reciprocity in the same manner, by using a Faraday rotator), ensuring a constant (and circular) polarisation state in front of the sample. Light arriving from the

interferometer traverses a linear polariser LP oriented at 22.5 degrees (in relation to the y-axis), followed by a Faraday rotator FR which performs a 22.5 degree rotation on the incident polarisation state. The beam then crosses a pair of beam displacers (BD1 and BD2) which separate and reunite the two orthogonal polarisation components; since the polarisation state in the forward propagation direction has been aligned with one of the axis of the two BDs a single path is used (the one corresponding to an orientation along the y-axis). A half-wave plate HWP is used to rotate the incident polarisation by 90 degrees, and finally the linearly polarised beam (whose polarisation state is aligned with $\hat{x}$) crosses a quarter-wave plate QWP oriented at 45 degrees to ensure that the sample is illuminated with circularly polarised light.

Light returning from the sample crosses the QWP, achieving a similar result to that described in the two previous configurations. Since two orthogonal polarisation states are now present, two different paths are considered between the two beam displacers, and effectively this approach modulates the two orthogonal polarisation states in the modulation of the channelled spectra (the OPD). The delay Δ in path length is dependent on the thickness of the glass block GB; without this block the two optical paths are effectively identical in length, since the combination of the two beam displacers and the half-wave plate ensure that each orthogonal polarisation state has exactly the same propagation distance in glass (minus the thickness of GB).

Projection of the two polarisation states (now delayed in relation to each other) is achieved by the combination of the FR (which rotates them by 22.5 degrees) and the LP. As with the other two configurations, a single polarisation state is present on the light injected back into the fibre, therefore achieving insensitivity to any fibre-based disturbances that may occur afterwards.

Similarly to the two previous configurations, but especially concerning Configuration B, the additional elements introduced in the sample arm increase the dispersion mismatch between the two arms which decreases the axial resolution; the two beam displacers in particular add a significant amount of glass length which needs to be compensated either numerically, or by using the Master-Slave Interferometry technique [30–32] instead of the usual FFT-based one.

In addition to that, since the two orthogonal channels are multiplexed in the OPD one has to compensate the drop-off in second (deeper) channel due to the limited sampling resolution; in the case of SD-OCT this is a combined effect of the resolution of the diffraction grating and the line array, as presented in Section 3.2.2. Typically SS-OCT systems present smaller sensitivity drop-offs with

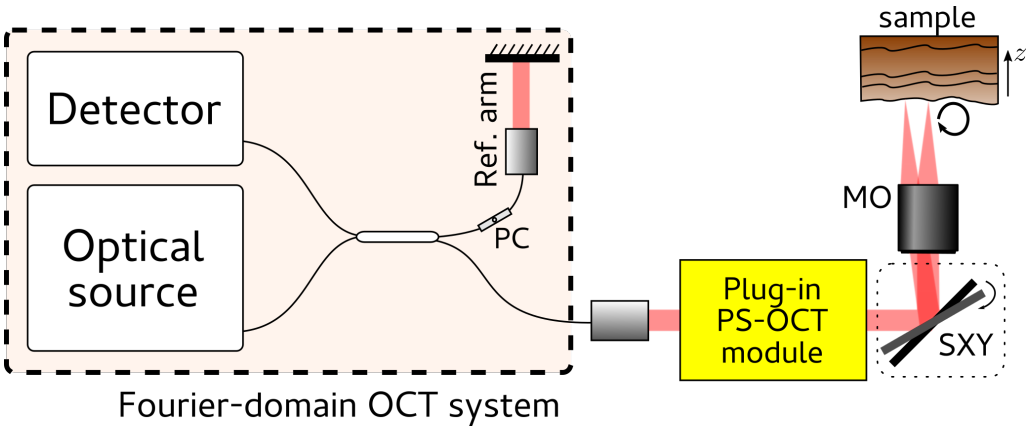

FIGURE 7.19: Schematic representation of a generic SM fibre-based SD-OCT system with a plug-in PS-OCT module ensuring circularly polarised illumination. This can be implemented in a Michelson or Mach-Zehnder configuration (a Michelson configuration is represented here), depending on the design of the PS-OCT module.

increasing OPD, achieving depth ranges of a few millimetres with commercial-grade sources. Thus, a SS-OCT coupled with this configuration would be an ideal combination since one would have access to a flatter drop-off curve and increased axial range. However, the phase stability of these sources is typically lower than that of SD-OCT systems; more research has to be carried out in order to assess the trade-off between these two methods.

7.4 Final remarks

In this chapter, three designs for PS-OCT configurations were presented. The original goal with Configuration A was to devise and implement a fibre-based PS-OCT system where the polarimetric disturbances caused by the fibres and couplers would not affect the polarimetric measurements of the sample, and to do so using a minimal amount of measurements (therefore using circularly polarised light) and a single detector (one spectrometer).

Configurations B and C are improvements over this original design, with both employing an in-line approach in the sample arm. This particularity allows for these configurations to be truly PS-OCT plug-in modules, capable of turning any existing OCT system into a polarisation-sensitive one, as shown in Figure 7.19.

A trade-off between implementation challenges and system performance has been found between all three configurations, which is summarised in Figure 7.20.

Both configurations A and B rely on active optical elements in order to temporally encode the two orthogonal polarisation states and in this way meet requirement (3). Depending on the switching rate of these optical elements it may not

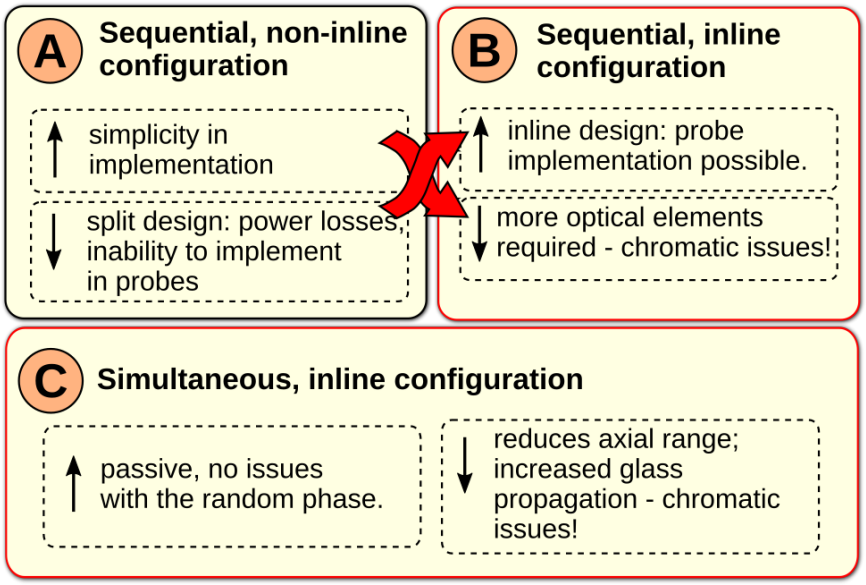

FIGURE 7.20: Summary of the three configurations presented in this chapter, along with their main strengths and weaknesses. The design of configurations B and C (highlighted) allow for their installation in any OCT system, thus making them effective plug-in modules for PS-OCT.

be possible, at first glance, to obtain a complete characterisation of the polarimetric properties of the sample (within the general PS-OCT limitations presented in Chapter 4). In Section 7.2.2 however it has been shown that by using the sample surface as a reference and adjusting the values of ϕ_{EO} accordingly it is possible to compensate for the effects of the random phase variation and thus retrieve a complete polarimetric characterisation of the sample. This can be extended to configuration A, although that has not been analysed in this study.

Configuration C bypasses the issue presented above altogether, whilst still employing a single-detector approach. This is achieved by encoding the two orthogonal polarisation states in the channelled spectrum modulation (ie., the OPD), thus allowing for simultaneous sampling of the two states. Due to this property, it is no longer necessary to resort to strategies such as the ones presented in Section 7.2.2 in order to retrieve the full polarimetric measurements from the sample. Moreover, by removing the necessity of having active optical elements which would typically require large operating voltages (such as certain variants of electro-optical polarisation modulators) electrical safety is improved, which is important if the PS-OCT module is to be implemented in a handheld or endoscopic probe which would be necessarily close to the patient. The cross-sectional surface of some of these active devices considered might also not be

uniform, which may restrict the lateral range should one attempt to install such a module in a full-field OCT system.

Any PS-OCT system is, by definition, subject to chromatic issues: polarisation elements such as waveplates, Faraday rotators, electro-optic polarisation modulators are designed for a specific wavelength or eventually for operation along a narrow range of wavelengths; and since high axial resolution in OCT systems is only achievable when employing wide optical bandwidths, these polarisation elements necessarily operate outside their design wavelength. This issue has been shown in some of the results in Section 7.1.3.1 (for Configuration A) and also extensively analysed in Section 7.2.3 (for Configuration B). However, one needs to stress out the fact that correcting for the chromatic issues is merely a calibration step; the biases do not vary with the environmental parameters or with the manipulation of the collecting fibres, hence they can be easily compensated.

Given that the chromatic behaviour observed in some polarisation elements seems to follow a linear relation (as shown in Figure 7.14), one may feel tempted to perform a hardware-based compensation by placing a polarisation element with an opposing chromatic response in series with the element in question. However, both Configurations B and C must follow the "in-line" design requirement; this means that the reciprocity must be broken (by employing a Faraday rotator), hence introducing an additional element with an opposing chromatic response would not cancel out the chromatic behaviour of the module.

References

[1] M. J. Marques, S. Rivet, A. Bradu, and A. Podoleanu, "Polarization-sensitive optical coherence tomography system tolerant to fiber disturbances using a line camera", *Opt. Lett.*, vol. 40, no. 16, pp. 3858–3861, 2015.

[2] S. Rivet, M. J. Marques, A. Bradu, and A. G. Podoleanu, "Optical module to extend any fourier-domain optical coherence tomography system into a polarisation-sensitive system", In press. 2016.

[3] M. J. Marques, S. Rivet, A. Bradu, and A. Podoleanu, "Spectral-domain, polarization-sensitive optical coherence tomography system insensitive to fiber disturbances", in *Optical Coherence Tomography and Coherence Domain Optical Methods in Biomedicine XX*, J. A. Izatt, J. G. Fujimoto, and V. V. Tuchin, Eds., vol. 9697, SPIE-Intl Soc Optical Eng, Mar. 2016. [Online]. Available: http://dx.doi.org/10.1117/12.2213479.

[4] C. E. Saxer, J. F. de Boer, B. H. Park, Y. Zhao, Z. Chen, and J. S. Nelson, "High-speed fiber–based polarization-sensitive optical coherence tomography of in vivo human skin", *Optics Letters*, vol. 25, no. 18, pp. 1355–1357, 2000. [Online]. Available: https://www.osapublishing.org/abstract.cfm?uri=ol-25-18-1355;%20http://www.ece.ucr.edu/~hylepark/publications/2/Saxer%20FiberPSOCT%20OL25(18)1355(2000).pdf.

[5] C. K. Hitzenberger and M. Pircher, "Muw approach of ps oct", in *Optical Coherence Tomography: Technology and Applications*, W. Drexler and J. G. Fujimoto, Eds., 2nd ed., Springer, 2015, ch. 34.

[6] J. E. Roth, J. A. Kozak, S. Yazdanfar, A. M. Rollins, and J. A. Izatt, "Simplified method for polarization-sensitive optical coherence tomography", *Optics Letters*, vol. 26, no. 14, pp. 1069–1071, 2001. [Online]. Available: http://www.osapublishing.org/fulltext.cfm?uri=ol-26-14-1069&id=64718;%20ftp://ftp.chara.gsu.edu/pub/users/shure/papers/downld2/article15.pdf.

[7] M. K. Al-Qaisi and T. Akkin, "Polarization-sensitive optical coherence tomography based on polarization-maintaining fibers and frequency multiplexing", *Optics express*, vol. 16, no. 17, pp. 13 032–13 041, 2008. [Online]. Available: http://www.osapublishing.org/oe/fulltext.cfm?uri=oe-16-17-13032&id=170503.

[8] N. Lippok, M. Villiger, C. Jun, and B. E. Bouma, "Single input state, single-mode fiber-based polarization-sensitive optical frequency domain imaging by eigenpolarization referencing.", *Optics Letters*, vol. 40, no. 9, pp. 2025–8, 2015.

[9] S. C. Rashleigh, "Acoustic sensing with a single coiled monomode fiber", *Optics letters*, vol. 5, no. 9, pp. 392–394, 1980. [Online]. Available: http://www.osapublishing.org/ol/fulltext.cfm?uri=ol-5-9-392.

[10] B. Cense, M. Mujat, T. C. Chen, B. H. Park, and J. F. de Boer, "Polarization-sensitive spectral-domain optical coherence tomography using a single line scan camera", *Optics Express*, vol. 15, no. 5, pp. 2421–2431, 2007. [Online]. Available: http://www.osapublishing.org/vjbo/fulltext.cfm?uri=oe-15-5-2421&id=130598.

[11] M. R. Hee, E. A. Swanson, J. G. Fujimoto, and D. Huang, "Polarization-sensitive low-coherence reflectometer for birefringence characterization and ranging", *JOSA B*, vol. 9, no. 6, pp. 903–908, 1992.

[12] M. Zurauskas and A. G. Podoleanu, "Multiplexing-based polarization sensitive en-face optical coherence tomography", *Journal of biomedical optics*, vol. 18, no. 10, pp. 106 010–106 010, 2013. [Online]. Available: http://reviews.spiedigitallibrary.org/article.aspx?articleid=1760313.

[13] E. Götzinger, B. Baumann, M. Pircher, and C. K. Hitzenberger, "Polarization maintaining fiber based ultra-high resolution spectral domain polarization sensitive optical coherence tomography", *Optics express*, vol. 17, no. 25, pp. 22 704–22 717, 2009. [Online]. Available: https://www.osapublishing.org/abstract.cfm?uri=oe-17-25-22704.

[14] Z. Wang, H.-C. Lee, O. O. Ahsen, B. Lee, W. Choi, B. Potsaid, J. Liu, V. Jayaraman, A. Cable, M. F. Kraus, *et al.*, "Depth-encoded all-fiber swept source polarization sensitive oct", *Biomedical optics express*, vol. 5, no. 9, pp. 2931–2949, 2014. [Online]. Available: http://www.osapublishing.org/boe/fulltext.cfm?uri=boe-5-9-2931&id=297388.

[15] S. Makita, "High-speed spectral-domain optical coherence tomography and *In Vivo* human eye imaging", PhD thesis, University of Tsukuba, 2007.

[16] S. Makita, T. Fabritius, and Y. Yasuno, "Full-range, high-speed, high-resolution 1-μm spectral-domain optical coherence tomography using bm-scan for volumetric imaging of the human posterior eye", *Optics express*, vol. 16, no. 12, pp. 8406–8420, 2008. [Online]. Available: https://www.osapublishing.org/abstract.cfm?uri=oe-16-12-8406.

[17] J. Zhang, S. Guo, W. Jung, J. Nelson, and Z. Chen, "Determination of birefringence and absolute optic axis orientation using polarization-sensitive optical coherence tomography with pm fibers", *Optics Express*, vol. 11, no. 24, p. 3262, Dec. 2003, ISSN: 1094-4087. DOI: 10.1364/oe.11.003262. [Online]. Available: http://dx.doi.org/10.1364/OE.11.003262.

[18] M. Yamanari, S. Makita, and Y. Yasuno, "Polarization-sensitive swept-source optical coherence tomography with continuous source polarization modulation", *Optics Express*, vol. 16, no. 8, p. 5892, Apr. 2008, ISSN: 1094-4087. DOI: 10.1364/oe.16.005892. [Online]. Available: http://dx.doi.org/10.1364/OE.16.005892.

[19] M. Berek, "Zur messung der doppelbrechung hauptsachlich mit hilfe des polarisationsmicroscops", *Zbl. Miner. Geol. Palaont.*, p. 388, 1913.

[20] M. Born and E. Wolf, *Principles of Optics: Electromagnetic Theory of Propagation, Interference and Diffraction of Light (7th Edition)*, 7th. Cambridge University Press, 1999, ISBN: 0521642221.

[21] *The berek polarization compensator model 5540*, Revision C, New Focus, Newport Corporation, 2012.

[22] S. Rivet, A. Bradu, and A. Podoleanu, "70 khz full 4x4 mueller polarimeter and simultaneous fiber calibration for endoscopic applications", *Optics Express*, vol. 23, no. 18, p. 23 768, Sep. 2015, ISSN: 1094-4087. DOI: 10.1364/oe.23.023768. [Online]. Available: http://dx.doi.org/10.1364/OE.23.023768.

[23] B. Braaf, K. A. Vermeer, M. de Groot, K. V. Vienola, and J. F. de Boer, "Fiber-based polarization-sensitive oct of the human retina with correction of system polarization distortions", *Biomedical optics express*, vol. 5, no. 8, pp. 2736–2758, 2014. [Online]. Available: https://www.osapublishing.org/abstract.cfm?uri=boe-5-8-2736.

[24] B. Baumann, W. Choi, B. Potsaid, D. Huang, J. S. Duker, and J. G. Fujimoto, "Swept source/fourier domain polarization sensitive optical coherence tomography with a passive polarization delay unit", *Optics express*, vol. 20, no. 9, pp. 10 229–10 241, 2012. [Online]. Available: https://www.osapublishing.org/abstract.cfm?uri=oe-20-9-10229.

[25] N. P. Barnes and L. B. Petway, "Variation of the verdet constant with temperature of terbium gallium garnet", *JOSA B*, vol. 9, no. 10, pp. 1912–1915, 1992. [Online]. Available: https://www.osapublishing.org/abstract.cfm?uri=josab-9-10-1912.

[26] B. Cense, T. C. Chen, B. H. Park, M. C. Pierce, and J. F. de Boer, "In vivo birefringence and thickness measurements of the human retinal nerve fiber layer using polarization-sensitive optical coherence tomography", *Journal of Biomedical Optics*, vol. 9, no. 1, p. 121, 2004, ISSN: 1083-3668. DOI: 10.1117/1.1627774. [Online]. Available: http://dx.doi.org/10.1117/1.1627774.

[27] R. W. Knighton and X.-R. Huang, "Linear birefringence of the central human cornea", *Investigative ophthalmology & visual science*, vol. 43, no. 1, pp. 82–86, 2002. [Online]. Available: http://arvojournals.org/article.aspx?articleID=2123365.

[28] M. Pircher, E. Götzinger, O. Findl, S. Michels, W. Geitzenauer, C. Leydolt, U. Schmidt-Erfurth, and C. K. Hitzenberger, "Human macula investigated in vivo with polarization-sensitive optical coherence tomography", *Investigative ophthalmology & visual science*, vol. 47, no. 12, pp. 5487–5494, 2006. [Online]. Available: http://iovs.arvojournals.org/article.aspx?articleid=2163676.

[29] W. Oh, S. Yun, B. Vakoc, M. Shishkov, A. Desjardins, B. Park, J. de Boer, G. Tearney, and B. Bouma, "High-speed polarization sensitive optical frequency domain imaging with frequency multiplexing", *Optics Express*, vol. 16, no. 2, p. 1096, Jan. 2008, ISSN: 1094-4087. DOI: 10.1364/oe.16.001096. [Online]. Available: http://dx.doi.org/10.1364/OE.16.001096.

[30] A. Bradu, K. Kapinchev, F. Barnes, and A. Podoleanu, "Master slave en-face oct/slo", *Biomed. Opt. Express*, vol. 6, no. 9, p. 3655, Aug. 2015, ISSN: 2156-7085. DOI: 10.1364/boe.6.003655. [Online]. Available: http://dx.doi.org/10.1364/BOE.6.003655.

[31] A. Bradu, M. Maria, and A. G. Podoleanu, "Demonstration of tolerance to dispersion of master/slave interferometry", *Optics Express*, vol. 23, no. 11, p. 14 148, May 2015, ISSN: 1094-4087. DOI: 10.1364/oe.23.014148. [Online]. Available: http://dx.doi.org/10.1364/OE.23.014148.

[32] S. Rivet, M. Maria, A. Bradu, T. Feuchter, L. Leick, and A. Podoleanu, "Complex master slave interferometry", *Optics Express*, vol. 24, no. 3, p. 2885, Feb. 2016, ISSN: 1094-4087. DOI: 10.1364/oe.24.002885. [Online]. Available: http://dx.doi.org/10.1364/OE.24.002885.

Chapter 8

Outlook and Future Work

IT IS CLEAR from the content presented in Chapters 3 and 4 that OCT is an imaging technique reaching maturity, with a number of commercial systems already on the market for more than a decade. The fundamental question posed in this thesis is what is left to do at this stage.

One can choose to address the current limitations present in the most commonly used detection schemes, SD- and SS-OCT, thus improving performance. This has been achieved through the development of novel optical sources, improved detectors and data processing algorithms.

Alternatively, one can extend the functionality of the OCT system by combining it with other imaging modalities, or by using the acquired signal for more than just providing structural information, as mentioned by the beginning of Chapter 1.

The work presented in this Thesis has mostly focussed on extending OCT functionality. Some of it has however appeared as a consequence of an attempt to address some of the issues in SD-OCT, namely that of the ambiguity in the sign of the optical path difference, also known as mirror (or conjugate) terms.

Fundamentally, two main subjects were researched: Talbot Bands in SD-OCT (described in Chapters 5 and 6), and fibre-based PS-OCT systems (described in Chapter 7). The content was organised as follows:

- In Chapter 5, the design of a spectrometer-based Talbot Bands OCT system with SLO technology is described and then characterised. The Talbot Bands behaviour allows control over the visibility profile of the SD-OCT system, addressing the issue of the mirror terms. Additional functionality has been added in the form of a second (confocal) channel which shares the same interface optics as the OCT system, thus creating a combined retinal OCT/SLO device with different degrees of simultaneity between the two channels, depending on the lateral size desired for the images acquired.

- In Chapter 6, a novel Talbot Bands configuration is presented and validated. The launching of the two beams from the object and reference arms employs

a single lens, and the splitter before the spectrometer is eliminated by employing two tilted diffraction gratings. As with the previously described system, by employing Talbot Bands, this configuration allows control over the visibility profile of the SD-OCT system with total mirror term elimination. A peculiar arrangement of the two diffraction gratings leads to the elimination of any interferometric contribution from the overlapped portions of the two beams, and so of mirror terms.

- In Chapter 7 three single mode fibre-based PS-OCT configurations are presented. All configurations presented are insensitive to any polarimetric disturbances introduced by the collecting fibre and coupler. They also use a minimal amount of measurements (illuminating the sample with circularly polarised light) and employ a single detector.

Talbot Bands in general, and their application to SD-OCT systems comprise an interesting effect which was appropriately studied in an academic setting. Moreover, the theory of Talbot Bands in a spectrometer combined with the sampling resolution of the pixel array fully describe the visibility profile of a SD-OCT system, as shown in Section 3.2.2.

However, implementing a Talbot Bands SD-OCT system comes with its own set of challenges. The alignment is slightly more complicated since bulk components are required to couple the two arms of the interferometer. Moreover, this requirement may give rise to polarisation and dispersion mismatches that reduce the available SNR.

Shifting the visibility profile with a Talbot Bands system while maintaining a large value for the sensitivity assumes that the drop-off curve caused by the sampling resolution of the line array is not significant. Given the constraints introduced by the current camera technologies on the pixel size, the only way of improving the sampling resolution is to increase the size of the projected spectrum, but this will mean that the optical power will be dispersed over a larger area, reducing the power per detector.

Swept-source technology has evolved significantly over the last few years, with commercial products already surpassing the performance achievable by SD-OCT systems. While the technology is not yet sufficiently mature at 800 nm, swept-sources operating at 1050 nm are a good compromise between axial/lateral resolution and long axial range. Operating at this wavelength also has an advantage in terms of larger tissue penetration, since radiation with a 1050 nm wavelength penetrates deeper into the tissue according to the graph of the therapeutic window, as shown in Figure 1.2.

Depending on the application considered for an OCT system, configurations such as those described in Chapters 5 and 6 can potentially be considered. The configuration in Chapter 5 allows for the installation of an additional confocal channel which provides a "bird's eye" view of the sample being imaged, and can secure a high degree of pixel-to-pixel correspondence between the OCT and the confocal channel, since both channels employ the same interface optics.

Some of the issues related to the dispersion/polarisation mismatch introduced by the bulk coupling optics (the beam-splitter) in the standard Talbot Bands configuration introduced in Chapter 5 were addressed by the configuration presented in Chapter 6. The geometrical and implementation constraints of the design presented limit the axial range attainable and the SNR (due to the use of diffraction gratings operating in reflection). Enhanced efficiency can be achieved using gratings operating in transmission; and the axial range can be improved by increasing the line density of the gratings, thus increasing the width of the cross-correlated profile.

Fibre-based PS-OCT operation is described for the three configurations presented in Chapter 7. Configuration A (Section 7.1) is a purposely-designed PS-OCT system, which requires a very specific interferometer configuration in order to meet the three requirements listed on page 144. On the other hand, Configurations B and C (Sections 7.2 and 7.3, respectively) can be implemented in a plug-in optical module which can turn any OCT system into a PS-OCT one.

Temporally encoding the two orthogonal polarisation states (i.e., sequential operation) may lead to an incomplete polarimetric characterisation due to the inability to accurately measure the phase, caused by the effect of the random phase of the interferometer; therefore, Section 7.2.2 presents a number of strategies to retrieve the complete polarimetric information from the sample, whilst still operating sequentially in time. Configuration C (Section 7.3) bypasses this problem altogether since, unlike Configuration B, it encodes the two orthogonal polarisation states in the channelled spectrum modulation (in the OPD), rendering simultaneous reading of the two orthogonal states possible (a snapshot measurement).

Configuration A has been experimentally validated with limited performance due to the components employed; however, it was sufficient to prove the concept and ensure that all three requirements on page 144 were met.

Configuration B has only been theoretically presented, with some numerical simulations carried out to model its performance; this is due to the fact that some of the components required were not available in order to carry out the experimental demonstration.

At the present stage, Configuration C is in the process of being implemented in a SS-OCT system operating at 800 nm. Since swept-source technology at this central wavelength is not very mature, this is again a proof of concept with limited performance, with a swept-source operating at a 200 Hz sweeping rate. This heavily restricts the scope of applications. A SS-OCT system has been chosen over a SD-OCT one due to the increased axial range allowed by the improved spectral sampling resolution. This increase in axial range is welcome since the usable range is split in half to accommodate both orthogonal polarisation components.

Future work might include implementing this configuration on a different central wavelength where swept-source technology is more mature, such as 1050-1060 nm.

Appendix A

Simulation code for Talbot Bands

The code here listed was written in Python and requires the `numpy`, `scipy` and `matplotlib` packages. It is an extension of the `MATLAB` code written by Michael Hughes during his PhD [1].

```
1  from numpy import *
2  from scipy import *
3  from matplotlib.pyplot import *
4
5  # simulation parameters
6
7  startinglambda = 817*10**-9
8  endinglambda = 837*10**-9
9
10 CCDLength = 0.01024      #CCD length in m
11 pixelWidth = 0.000010    #Pixel width in m
12 slitSepV = 0.000000833   #Slit separation in m
13 DGLength = 0.025         #In m, diffraction grating length
14 objProfileFWHM = 0.002   #in m, beam FHWM
15 refProfileFWHM = 0.002   #in m
16 objProfileCentre =  0.0125  #in m
17 refProfileCentre =  0.0125  #in m
18 # One of these two should be at the centre of DG (DGLength/2)
19
20 npxls = CCDLength / pixelWidth
21
22 N = 5000  # number of points for most operations - control the
      OPD range from here!     N=4000 & step 0.0000025 gives +-5 mm
       of OPD (10mm overall)
23 stepSize = 0.000005 # step between points on the simulation (m)
```

[1] M. Hughes, "Optical Coherence Tomography for Art Conservation and Archaeology: Methods and Applications", PhD thesis, University of Kent, 2010.

```
24 Ndash = 19999   # number of points for computing the wavetrain
     term
25 M = 6 # number of simulated profiles (applicable to one of the
     codes)
26
27 # control the position of the screen introduced in front of one
     of the beams
28 def screen(position, width, Npoints, DGLen):
29   mask = zeros(Npoints, dtype='float64')
30   for x in range(Npoints):
31     pos = x * DGLen / Npoints
32     if pos < position - width/2 or pos > position + width/2:
33       mask[x] = 1.
34     else:
35       mask[x] = 0.
36   return mask
37
38 def centralwavelength(startlmb=startinglambda, endlmb=
     endinglambda):
39   return 2 * pi /((lambdatowavenumber(startlmb) +
       lambdatowavenumber(endlmb)) / 2)
40
41 def lambdatowavenumber(lmbd):
42   return 2 * pi/ float(lmbd)
43
44 # bandwidth per pixel
45 def linearDisp(startlmb=startinglambda, endlmb=endinglambda,
     npixels=npxls):
46   return (lambdatowavenumber(startlmb) - lambdatowavenumber(
       endlmb)) / npixels
47
48 def flatTopProfile(beamFWHM, beamCentre):
49   DGPos = array([x * DGLength / N for x in range(N)], dtype='
       float64')
50   beamProfile = zeros(N, dtype='float64')
51   for x in range(N):
52     if DGPos[x] > beamCentre-(beamFWHM/ 2.) and DGPos[x] <
         beamCentre+(beamFWHM/2.):
53       beamProfile[x] = 1.
54   return DGPos, beamProfile
55
```

```
56 # generate Gaussian spot profiles
57 def gaussianSpotProfile(beamFWHM, beamCentre):
58   DGPos = array([x * DGLength / N for x in range(N)], dtype='
       float64')
59   beamProfile = zeros(N, dtype='float64')
60   for x in range(N):
61     beamProfile[x] = exp(-((DGPos[x] - beamCentre)**2) * 4 * log
         (2) / beamFWHM**2)
62   return DGPos, beamProfile
63
64 def myCentralWavelength(startlmb=startinglambda, endlmb=
     endinglambda):
65   return (endlmb-startlmb)/2. + startlmb
66
67 def sincProfile(startlmb=startinglambda, endlmb=endinglambda):
68   OPD = zeros(N, dtype='float64')
69   ourSinc = zeros(N, dtype='float64')
70   ld = linearDisp(startlmb,endlmb)
71   for z in range(N):
72     OPD[z] = (z -  N/2) * stepSize
73     Zmax = 0.25 * (npxls/(endlmb-startlmb)) *
         myCentralWavelength(startlmb, endlmb)**2
74     chi = (pi/2.) * (OPD[z] / Zmax)
75     ourSinc[z] = abs(sin(chi)/chi)**2
76   maxSinc = max(ourSinc) # normalise sinc term
77   sincFinal = zeros(N, dtype='float64')
78   sincFinal = ourSinc / maxSinc;
79   return OPD, sincFinal
80
81
82 def wavetrainTerm(objProfile,refProfile,OPD,startlmb=
     startinglambda,      endlmb=endinglambda, slitSep=slitSepV):
83   wavetrain = correlate(objProfile,refProfile)
84   Ndash = len(wavetrain)
85   OPDwavetrain = zeros(Ndash, dtype='float64')
86   centrelambda = centralwavelength(startlmb, endlmb)
87   for z in range(Ndash):
88     OPDwavetrain[z] = (z - N) / float(N) * DGLength *
         centrelambda / slitSep \#\# maybe some of the values here
          are hardcoded, and they shouldn't be!
89 wavetrainFinal = interp(OPD,OPDwavetrain,wavetrain)
```

```
90    return (1/max(wavetrainFinal))*wavetrainFinal, wavetrainFinal
91
92  def falloffProfile(wavetrain, sincTerm):
93    falloff = zeros(len(sincTerm), dtype='float64')
94    for z in range(len(sincTerm)):
95      falloff[z] = wavetrain[z] * sincTerm[z]
96    falloffLog = zeros(len(sincTerm), dtype='float64')
97    divider = max(falloff)
98    falloffLog = 10 * log10(falloff/divider)
99    return falloff, falloffLog
```

Plotting visibility profile of a single case, adjustable gap and beam width

```
1   if __name__ == "__main__":
2     DGL, objBeamProfile = flatTopProfile(0.004, 0.0125)
3     DGL2, refBeamProfile = flatTopProfile(0.004, 0.0125+0.000) #
        shift between beams can be adjusted here
4     figure(1)
5     plot(DGL, objBeamProfile) # plot the two beam profiles
6     plot(DGL2, refBeamProfile)
7     ourOPDrange, ourSincProfile = sincProfile(startinglambda,
        endinglambda)
8     wavetrain = correlate(objBeamProfile,refBeamProfile, 'same')
9     Ndash = len(wavetrain)
10    OPDwavetrain = zeros(Ndash, dtype='float64')
11    centrelambda = centralwavelength(startinglambda, endinglambda)
12    for z in range(Ndash):
13      OPDwavetrain[z] = (z - N/2) / float(N) * DGLength *
          centrelambda / slitSepV
14    wavetrainNorm = wavetrain/max(wavetrain)
15    wavetrainFinal = wavetrainNorm*ourSincProfile
16    wavetrainNorm.dump('wtrain.npy') # dump to binary file,
        readable by external plotting package
17    ourOPDrange.dump('OPD.npy')
18    ourSincProfile.dump('sinc.npy')
19    figure(2)
20    plot(OPDwavetrain, wavetrainNorm)
21    figure(3)
22    plot(OPDwavetrain, wavetrainFinal)
23    plot(OPDwavetrain, ourSincProfile)
24    show()
```

Plotting visibility profile for several cases, differing on the size of the gap between the two beams, iterating over M cases

```
if __name__ == "__main__":
  ourOPDrange, ourSincProfile = sincProfile(startinglambda,
     endinglambda)
  figure(1)
  plot(ourOPDrange*1000, ourSincProfile)
  show()
  for i in range(M):
    shiftingPos = (i-(M/2))*0.00254 + 0.0125
    DGL, objBeamProfile = gaussianSpotProfile(objProfileFWHM,
       objProfileCentre)
    DGL2, refBeamProfile = gaussianSpotProfile(refProfileFWHM,
       shiftingPos)
    figure(2)
    plot(DGL, objBeamProfile)
    plot(DGL2, refBeamProfile)
    normCurrentWTerm, currentWavetrainTerm = wavetrainTerm(
       objBeamProfile, refBeamProfile, ourOPDrange,
       startinglambda, endinglambda, slitSepV)
    currentFalloff, currentFallofflog = falloffProfile(
       currentWavetrainTerm, ourSincProfile)
    figure(3)
    plot(ourOPDrange*1000, currentFalloff, label="gap %f" % (
       shiftingPos-objProfileCentre))
    xlabel('OPD (mm)')
    ylabel('channeled spectrum visibility')
    filenameOutOPD = str(shiftingPos-objProfileCentre)+'OPD.txt'
    filenameOutFalloff = str(shiftingPos-objProfileCentre)+'
       falloff.txt'
    ourOPDrange.tofile(filenameOutOPD, '\n')
    currentFalloff.tofile(filenameOutFalloff, '\n')
  legend()
  show()
```

Plotting visibility profile for several cases, differing on the width of the two beams, iterating over the values in a user-supplied array

```
if __name__ == '__main__':
  beamSizes = array([0.0015, 0.0034, 0.008, 0.012])
  gap = 0.0001
```

```
  ourOPDrange, ourSincProfile = sincProfile(startinglambda,
     endinglambda)
  objBeamProfiles = zeros([len(beamSizes),N])
  refBeamProfiles = zeros([len(beamSizes),N])
  wavetrainterms = []
  fallOffs = []
  ourOPDrange.tofile('OPDs.txt','\n')
  for i in range(len(beamSizes)):
    DGL, objBeamProfiles[i] = gaussianSpotProfile(beamSizes[i],
       objProfileCentre)
    DGL2, refBeamProfiles[i] = gaussianSpotProfile(beamSizes[i],
        objProfileCentre+gap)
    figure(1)
    plot(DGL, objBeamProfiles[i], label="beam diameter %f" %
       beamSizes[i])
    wavetrainterms.append(wavetrainTerm(objBeamProfiles[i],
       refBeamProfiles[i], ourOPDrange, startinglambda,
       endinglambda, slitSepV)[0])
    fallOffs.append(falloffProfile(wavetrainterms[i],
       ourSincProfile)[0])
    print len(ourOPDrange)
    print len(fallOffs[i])
    figure(2)
    plot(ourOPDrange*1000, fallOffs[i], label="beam diameter %f"
        % beamSizes[i])
    currentFallOff = fallOffs[i].tofile(str(beamSizes[i]), '\n')
    xlabel('OPD (mm)')
    ylabel('channelled spectrum visibility (normalised values)')
  legend()
  show()
```

Plotting visibility profile with a screen introduced over one of the beams, partially truncating it

```
screenwidth = 0.0025 # width of the screen introduced over the
   reference beam
screenpos = 0.0085  # position of the said screen
O = 75
if __name__ == '__main__':
  screenposlist = []
  peakintensityList = []
  peaklocList = []
```

```
8   screenpos = 0.
9   figure(1)
10  for i in range(O):
11    if screenpos >= 0.012 and screenpos <= 0.013:
12      screenpos += 0.00005
13    else:
14      screenpos += 0.0005
15    cameraFallOff = sincProfile()[1]
16    DGL, objBeamProfile = gaussianSpotProfile(objProfileFWHM,
        objProfileCentre)
17    DGL2, refBeamProfile = gaussianSpotProfile(refProfileFWHM,
        objProfileCentre)
18    scrrefBeamProfile = refBeamProfile * screen(screenpos,
        screenwidth, N, DGLength)
19    # uncomment to show the plot of the two beam profiles before
        diffraction
20    # figure(1)
21    # plot(DGL*1000, refBeamProfile, 'b--')
22    # plot(DGL*1000, scrrefBeamProfile, 'r-')
23    # xlabel('diffraction grating axis (mm)')
24    # ylabel('beam profile (arb. units)')
25    ourOPDrange, ourSincProfile = sincProfile(startinglambda,
        endinglambda)
26    scrcurrentWavetrainTermNorm, scrcurrentWavetrainTerm =
        wavetrainTerm(objBeamProfile, scrrefBeamProfile,
        ourOPDrange, startinglambda, endinglambda, slitSepV)
27    profile = cameraFallOff*scrcurrentWavetrainTerm
28    ourOPDmm = ourOPDrange*1000
29    if screenpos < 0.0125:
30      plot(ourOPDmm, profile, 'b-', label='%.4f'%screenpos)
31    elif screenpos == 0.0125:
32      plot(ourOPDmm, profile, 'g', lw=1.5, label='%.4f'%
          screenpos)
33    elif screenpos > 0.0125:
34      plot(ourOPDmm, profile, 'r-', label='%.4f'%screenpos)
35    profile = nan_to_num(profile)
36    peakintensityListmax = amax(profile)
37    peaklocListmax = ourOPDmm[argmax(profile)]
38    print screenpos, peakintensityListmax, peaklocListmax
39    screenposlist.append(screenpos)
40    peakintensityList.append(peakintensityListmax)
```

```
41      peaklocList.append(peaklocListmax)
42    xlabel('optical path difference (mm)')
43    ylabel('channelled spectrum visibility, absolute values\n (
          screened profile normalised to no Talbot profile max)')
44    scrpos = array(screenposlist)
45    pkint = array(peakintensityList)
46    pkloc = array(peaklocList)
47    scrpos.tofile('screenposition.txt','\n')
48    pkint.tofile('peakintensities.txt','\n')
49    pkloc.tofile('peaklocations.txt','\n')
50    fig2 = figure(2)
51    ax2 = fig2.add_subplot(111)
52    ax2.plot(screenposlist, peakintensityList, 'b-')
53    ax2.set_xlabel('position of screen (m)')
54    ax2.set_ylabel('intensity maximum of sensitivity peak (arb.
          units)')
55    ax2b = ax2.twinx()
56    ax2b.plot(screenposlist, peaklocList, 'r-')
57    ax2b.set_xlabel('position of screen (m)')
58    ax2b.set_ylabel('intensity maximum location of sensitivity
          peak (mm)')
59    show()
```

Appendix B

Jones matrices used in the theoretical model

- Jones matrix of a polarisation rotator by an angle α in relation to either $|e_x\rangle$ or $|e'_x\rangle$, depending on the case described in the text:

$$J_{\mathrm{Rot}(\alpha)} = \begin{pmatrix} \cos\alpha & -\sin\alpha \\ \sin\alpha & \cos\alpha \end{pmatrix}. \tag{B.1}$$

- Jones matrix for a linear birefringent medium with retardance ϕ, oriented at an angle α in relation to either $|e_x\rangle$ or $|e'_x\rangle$, depending on the case described in the text:

$$J_{\mathrm{Bir}(\phi,\alpha)} = J_{\mathrm{Rot}(\alpha)} \cdot \begin{pmatrix} e^{j\phi/2} & 0 \\ 0 & e^{-j\phi/2} \end{pmatrix} \cdot J_{\mathrm{Rot}(-\alpha)}. \tag{B.2}$$

  The retardance introduced by a half-wave plate is $\phi = \pi$, and that by a quarter-wave plate is $\phi = \pi/2$. One can carry out the matrix multiplication present in the equation above to obtain Equation (4.5),

$$J_{\mathrm{Bir}(\phi,\alpha)} = \begin{pmatrix} \cos^2\alpha + \sin^2\alpha \cdot \exp(-j\phi) & \cos\alpha \cdot \sin\alpha \cdot (1 - \exp(-j\phi)) \\ \cos\alpha \cdot \sin\alpha \cdot (1 - \exp(-j\phi)) & \cos^2\alpha \cdot \exp(-j\phi) + \sin^2\alpha \end{pmatrix}. \tag{B.3}$$

- Jones matrix for a partial linear diattenuator with diattenuation D and oriented at an angle α in relation to either $|e_x\rangle$ or $|e'_x\rangle$, depending on the case described in the text:

$$J_{\mathrm{Diat}(D,\alpha)} = J_{\mathrm{Rot}(\alpha)} \cdot \begin{pmatrix} \left(\frac{1-D}{1+D}\right) & 0 \\ 0 & 1 \end{pmatrix} \cdot J_{\mathrm{Rot}(-\alpha)}. \tag{B.4}$$

- Jones matrix for a mirror:

$$J_{\text{Mirror}} = \begin{pmatrix} -1 & 0 \\ 0 & 1 \end{pmatrix}. \tag{B.5}$$

Appendix C

Peer-reviewed articles published during the course of the doctoral programme

1. Sylvain Rivet, **Manuel J. Marques**, Adrian Bradu, and Adrian Podoleanu. "Optical module to extend any Fourier-domain optical coherence tomography system into a polarisation-sensitive system", *Journal of Optics* 16.065607 (May 2016), DOI:10.1088/2040-8978/18/6/065607.

2. **Manuel J. Marques**, Sylvain Rivet, Adrian Bradu, and Adrian Podoleanu. "Polarization-sensitive optical coherence tomography system tolerant to fiber disturbances using a line camera", *Optics letters* 40.16 (August 2015), pp. 3858–3861, DOI: 10.1364/OL.40.003858.

3. **Manuel J. Marques**, Adrian Bradu, and Adrian Podoleanu. "Two-grating Talbot bands spectral-domain interferometer", *Optics letters* 40.17 (September 2015), pp. 4014–4017, DOI: 10.1364/OL.40.004014.

4. **Manuel J. Marques**, Adrian Bradu, and Adrian Gh. Podoleanu. "Towards simultaneous Talbot bands based optical coherence tomography and scanning laser ophthalmoscopy imaging", *Biomedical Optics Express* 5.5 (Apr. 2014), p 1428, ISSN: 2156-7085, DOI: 10.1364/BOE.5.001428.

IOP Publishing Journal of Optics
J. Opt. 18 (2016) 065607 (12pp) doi:10.1088/2040-8978/18/6/065607

Optical module to extend any Fourier-domain optical coherence tomography system into a polarisation-sensitive system

Sylvain Rivet[1,2], Manuel J Marques[1], Adrian Bradu[1] and Adrian Podoleanu[1]

[1] Applied Optics Group, School of Physical Sciences, University of Kent, Canterbury CT2 7NH, UK
[2] Université de Bretagne Occidentale, EA 938 Laboratoire de Spectrométrie et Optique Laser, 6 avenue Le Gorgeu, C.S. 93837, F-29238 Brest Cedex 3, France

E-mail: mjmm2@kent.ac.uk

Received 10 December 2015, revised 27 February 2016
Accepted for publication 30 March 2016
Published 6 May 2016

Abstract

This article presents a theoretical study on an optical module (OM) that can be inserted between an object under investigation and a Fourier-domain optical coherence tomography system, transforming the latter into a polarisation-sensitive optical coherence tomography optical coherence tomography (OCT) system. The module consists of two electro-optic modulators, a Faraday rotator, a linear polariser and a quarter-wave plate. A detailed description on how the module can be used to extract both the net retardance and the fast axis orientation of a linear birefringent sample is presented. This is achieved by taking two sequential measurements for different values of retardance produced by the electro-optic modulator. The module keeps measurements free from undesired polarimetric effects due to birefringence in the single-mode optical fibre and diattenuation in fibre-based couplers within OCT systems. Simulations have been carried out in order to evaluate the effects of chromatic behaviour of the components within the OM.

Keywords: polarisation-selective devices, optical coherence tomography, instrumentation, measurement, and metrology

(Some figures may appear in colour only in the online journal)

1. Introduction

Polarisation-sensitive optical coherence tomography (PS-OCT) methods emerged as early as 1992 [1], evolving from bulk-based to more compact fibre-based designs. PS-OCT systems operate either in time-domain [2–4] or in frequency-domain [5–7].

PS-OCT systems are useful in medical OCT applications due to the link between polarisation properties and the health state of tissue. In non-destructive testing, PS-OCT also provides birefringence information, useful in assessing the mechanical properties of the structures evaluated. Due to their versatility, easy alignment, compact size [8] and also to the need for single spatial mode selection, fibre-based systems are used in OCT practice. However, external factors (such as temperature and mechanical stress) affect the birefringence of single-mode fibres (SMFs) used in OCT systems, inducing disturbances [9] in the measured polarisation. This difficulty has been overtaken by (1) building specific OCT systems and (2) measuring (sequentially or instantaneously) the polarimetric properties of fibres so as to compensate for their effects. Yet the OCT systems dedicated to polarisation are sometimes complex and non versatile. Due to the use of optical fibres, the incident polarisation state is not a single-circular state, but this issue can be overcome by probing the sample with at least two orthogonal polarisation states [2, 7]. Alternatively, one can take into account the polarimetric properties of the fibres by performing careful calibration steps, in this way ensuring that the probing beam is in a single, circular polarisation state [10, 11].

Another solution is to perform in free space both the generation of the polarisation states and the analysis of their

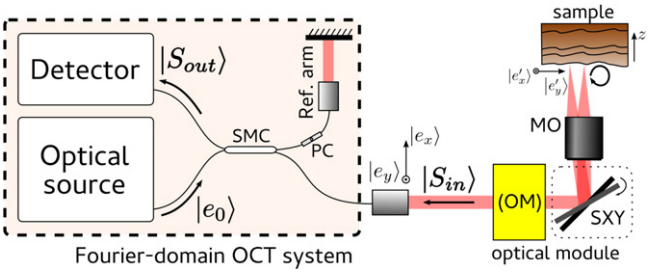

Figure 1. Fourier-domain PS-OCT system. The dashed rectangle corresponds to a fibre-based Fourier-domain OCT system. SXY, scanning head with two galvanometer scanners with axes oriented at 90° in relation to each other; MO, microscope objective; PC, fibre-based polarisation controller; SMC, single-mode fibre coupler. Only single-mode optical fibres are used. The field generated by the optical source is given by $|e_0\rangle$. The sample is probed with a circular polarisation state. $|S_{\text{in}}\rangle$ describes the field returning to the fibre-based part of the interferometer, and $|S_{\text{out}}\rangle$ describes the same field after propagation through the fibres and the single-mode fibre coupler.

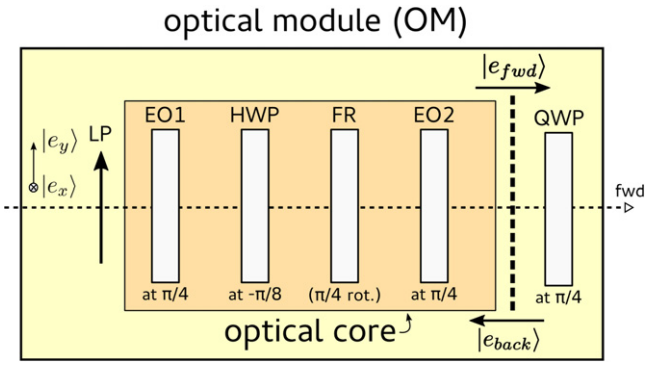

Figure 2. Optical module (OM) to convert any FD-OCT system into a PS-FD-OCT system. LP, LP oriented along $|e_y\rangle$ (side view of the diagram in figure 1). QWP, quarter-wave plate oriented at $\pi/4$ in relation to $|e_x\rangle$. Inside the OM, another optical block is defined as the optical core of the OM. The optical core consists of two electro-optic polarisation modulators (EO1 and EO2) oriented at $\pi/4$ according to $|e_x\rangle$, a half-wave plate (HWP) oriented at $-\pi/8$, and a Faraday rotator (FR) that induces a polarisation state rotation of $\pi/4$. The operation of the optical core is described in the main text. $|e_{\text{fwd}}\rangle$ describes the polarisation state of the light probing the sample before the quarter-wave plate (QWP) of the OM. $|e_{\text{back}}\rangle$ describes the polarisation state of light returning from the sample after passing through the QWP.

modifications caused by the sample. Such an approach has been adopted in Roth *et al* [12] and in Marques *et al* [13]. The solution presented in [12] requires at least three measurements to extract the polarimetric information. In our previously reported system [13], only two measurements were used because the input polarisation state was always circular. However, this required splitting the beam within the sample arm, bringing further losses.

To measure the sample's polarimetric properties, we propose a novel approach, without any calibration step involving the optical fibres. This approach is based on an in-line optical module (OM) placed before the sample being evaluated. By a suitable design of the module, this can be used to convert any conventional OCT system into a PS-OCT system. A theoretical model presenting the operation of such a module is developed in section 2. Two sequential measurements are used to provide polarisation characterisation of the birefringent sample that is independent from the polarimetric response of the SMF inside the interferometer. Simulations are carried out to evaluate how the fibre disturbances and the chromatic response of components within the OM affect the polarimetric measurements. Our simulations demonstrate that the effects due to fibre disturbances can be eliminated.

2. Theory

The OM (shown in figure 1 and detailed in figure 2, designed for free space operation) generates a circular polarisation state to probe the sample and to interrogate its polarimetric properties in two sequential steps. Probing the sample with circularly polarised light is a widely used technique to interrogate these properties [1, 3, 4, 14].

The OM is inserted after the sample arm fibre of a conventional Fourier-domain OCT (FD-OCT) system, which can be a spectrometer-based OCT (Sp-OCT) or a swept-source-based OCT (SS-OCT). For brevity, we refer only to the Sp-OCT method, but all the theory that follows is applicable to the SS-OCT method as well.

Scanning of the sample is performed by two galvo-scanning mirrors SXY placed after the OM. Since the angles of incidence of the beam on the two mirrors in the galvanometer scanning head are relatively large (45°), the Fresnel coefficients differ for perpendicular and parallel components in relation to the incidence plane of the wave directed to each galvanometer scanner. By having two galvanometer scanners at 90° in sequence, the Fresnel effect is cancelled, as the wave oscillating in the incident plane of the first mirror oscillates perpendicularly to the incident plane of the second mirror. Therefore, no effect on the polarisation state is considered via SXY. However if only one mirror was used, then its effect should be taken into account, which is not the case here.

Let us consider a single reflector in the sample arm of the interferometer, placed at z along the depth coordinate. The intensity $I(\nu)$ versus optical frequency ν measured at the spectrometer's camera is given by

$$I(\nu) = I_{\text{DC}}(\nu) + A(z, \nu)\mathrm{e}^{\mathrm{i}\frac{2\pi}{c}\nu 2z} + A^{*}(z, \nu)\mathrm{e}^{-\mathrm{i}\frac{2\pi}{c}\nu 2z}, \quad (1)$$

where $I_{\text{DC}}(\nu)$ is the DC component of the interferometric signal, $A(z, \nu)$ is the complex amplitude of the interference between the electric field returning from the sample proportional to $|S_{\text{out}}\rangle$ and the field $|r_{\text{out}}(\nu)\rangle$ from the reference arm. c is the speed of light and z is the depth of the object measured from optical path difference (OPD) = 0. The aforementioned field returning from the sample arm is given by $r(z)|S_{\text{out}}(z, \nu)\rangle$, where $r(z)$ is the complex amplitude reflection coefficient for a scattering centre located at depth z. In addition, the chromatic behaviour of fibres is taken into account by considering that the output fields are dependent on

ν. The complex amplitude $A(z, \nu)$ can be expressed as

$$A(z, \nu) = r(z)\langle r_{\text{out}}(\nu)|\ S_{\text{out}}(z, \nu)\rangle. \quad (2)$$

Throughout this theory section, the shape of the spectrum is considered to be flat along ν.

By Fourier transforming $I(\nu)$, an A-scan is obtained, i.e. a complex-valued peak corresponding to the single reflector located at depth z. Let $\hat{A}(z)$ be the complex value at the maximum of this peak. This is related to $A(z, \nu)$ as follows:

$$\hat{A}(z) = \int A(z, \nu)\mathrm{d}\nu, \quad (3)$$

and its absolute value $\hat{I}_{\text{interf}}$ can be written as

$$\hat{I}_{\text{interf}}(z) = |\hat{A}(z)| = \left| r(z) \int \langle r_{\text{out}}(\nu)|\ S_{\text{out}}(z, \nu)\rangle \mathrm{d}\nu \right|. \quad (4)$$

The field $|S_{\text{out}}(z, \nu)\rangle$ contains both the retardance of the sample under analysis, and the polarimetric properties of the fibres and couplers, which vary significantly with the environmental parameters. If the contributions from the sample and the fibres/couplers are decoupled, then the polarimetric response of the sample can be identified independently of that from the fibres.

2.1. Description of the OM

The OM comprises a total of six elements, starting with a linear polariser (LP) and ending with a quarter-wave plate (QWP), ensuring in this way a circular polarisation state in front of the sample (figure 2). Performing polarimetric measurements on the sample requires analysing the two orthogonal polarisation components. The LP however favours a single polarisation state. Therefore, to circumvent this limitation, an optical core comprising two electro-optic polarisation modulators (EOs), a half-wave plate (HWP) and a Faraday rotator (FR) is used according to the procedure described below. Depending on the propagation direction of the wave, forward and backward from the sample, the optical core is used to rotate the polarisation orientation by either 90° or 0° respectively. The different operation of the optical core does not affect the circular polarisation of the wave propagating towards the sample nor the polarisation state of the wave returned from the sample containing the polarisation properties of the sample.

Detailing the OM's behaviour further, linearly polarised light after the LP is oriented along $|e_y\rangle$ and propagates through an optical core comprising an electro-optic polarisation modulator (EO1) oriented at $\pi/4$, a HWP oriented at $-\pi/8$, a FR which rotates the incident polarisation by $\pi/4$, and a second electro-optic polarisation modulator (EO2) oriented at $\pi/4$. EO1 and EO2 are driven to exhibit the same retardance ϕ_{EO}. The orientation of their fast axes is defined in respect to $|e_x\rangle$ in the basis $\{|e_x\rangle, |e_y\rangle\}$.

In order to visualise the change of the polarisation states induced by the optical core in forward propagation, the retardance ϕ_{EO} is set to 0 or $\pi/2$, as shown in figure 3.

For the field going forward through the optical core (figure 3), there is no change in the polarisation state of light and this result can be generalised irrespective of the values of ϕ_{EO} introduced by EO1 and EO2. Indeed, the Jones matrix of the optical core in forward direction, $J_{\text{core}}^{\text{fwd}}$, is

$$J_{\text{core}}^{\text{fwd}}(\phi_{\text{EO}}) = -\mathrm{i}\begin{pmatrix} -1 & 0 \\ 0 & 1 \end{pmatrix}. \quad (5)$$

Therefore the field $|e_{\text{fwd}}\rangle = J_{\text{core}}^{\text{fwd}}\ |e_y\rangle = -\mathrm{i}\ |e_y\rangle$ after EO2, and is linearly polarised along $|e_y\rangle$. Then the electric field is converted into a circular polarisation state by the QWP oriented at 45°. The sample is modelled as a linear retarder with a net (or double-pass) retardance $2\varphi(z)$, and a fast axis orientation given by $\theta(z)$ in respect to the sample basis $\{|e_x'\rangle, |e_y'\rangle\}$, as defined in figure 1. This basis results from the transformation of the original $\{|e_x\rangle, |e_y\rangle\}$ basis by the reflections in the two galvo-scanners SXY.

Light back-reflected by the birefringent sample travels towards the QWP of the OM. The corresponding field $|e_{\text{back}}\rangle$ (figure 2) can be expressed on the vector basis $\{|e_x\rangle, |e_y\rangle\}$ as follows (see appendix B):

$$|e_{\text{back}}\rangle = \cos\varphi(z)|e_x\rangle - \sin\varphi(z)\mathrm{e}^{-2\mathrm{i}\theta(z)}\ |e_y\rangle. \quad (6)$$

The range for the one-pass retardance $\varphi(z)$ is considered from 0 to $\pi/2$, while the range for the fast axis orientation $\theta(z)$ is measured between 0 and π.

In the backward direction, the optical core modifies the polarisation state according to the retardance ϕ_{EO} imprinted by the two EOs. In particular, the core acts as a rotator of the polarisation state as shown in figure 4 for ϕ_{EO} set at 0 (a) or $\pi/2$ (b).

For any retardance ϕ_{EO} applied identically on both EOs, the Jones matrix describing the OM in backward direction can be written on the basis $\{|e_x\rangle, |e_y\rangle\}$ as

$$J_{\text{core}}^{\text{back}}(\phi_{\text{EO}}) = -\mathrm{i}\begin{pmatrix} \mathrm{i}\ \sin\ \phi_{\text{EO}} & \cos\phi_{\text{EO}} \\ \cos\phi_{\text{EO}} & \mathrm{i}\ \sin\ \phi_{\text{EO}} \end{pmatrix}. \quad (7)$$

After traversing the optical core, the beam passes through the LP, oriented along $|e_y\rangle$, with the resulting field $|S_{\text{in}}(z)\rangle$ at the input of the probe fibre, as shown in figure 1. According to the retardance ϕ_{EO} of both EOs, this field becomes

$$|S_{\text{in}}(z)\rangle = P \cdot J_{\text{core}}^{\text{back}}(\phi_{\text{EO}}) \cdot |e_{\text{back}}\rangle, \quad (8)$$

where P is the Jones matrix of the LP oriented along $|e_y\rangle$ described by

$$P = \begin{pmatrix} 0 & 0 \\ 0 & 1 \end{pmatrix}. \quad (9)$$

Then the field $|S_{\text{in}}(z)\rangle$ can be expressed according to

$$|S_{\text{in}}(z)\rangle = -\ (\mathrm{i}\cos\varphi(z)\cos\phi_{\text{EO}} + \mathrm{e}^{-2\mathrm{i}\theta(z)}\sin\varphi(z)\sin\phi_{\text{EO}})|e_y\rangle. \quad (10)$$

Due to the polarimetric response of the collecting fibre and of the coupler described in the general matrix $J_{\text{out}}^{\text{fibre}}(\nu)$, the field $|S_{\text{out}}(z, \nu)\rangle$ in front of the detector is obtained as a

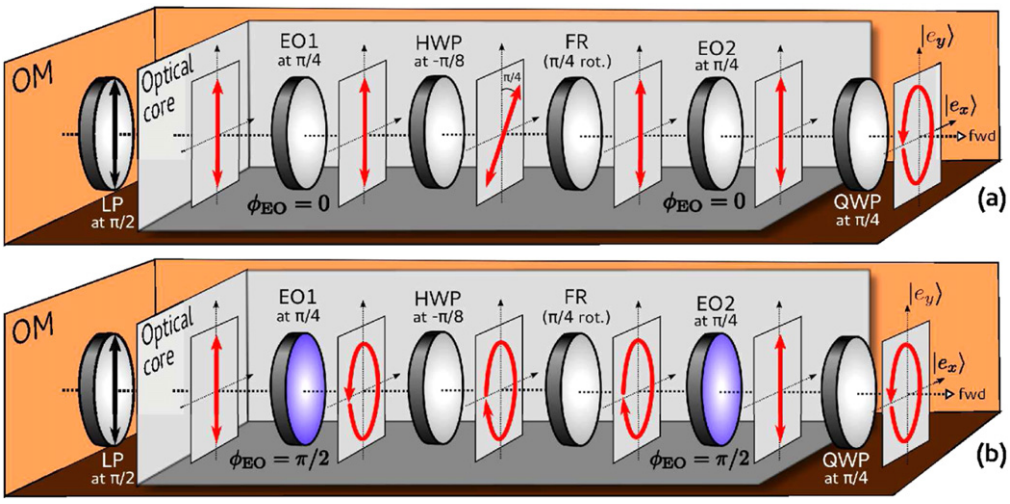

Figure 3. Orientation of the polarisation states within the OM (figure 2) for $\phi_{EO} = 0$ (a) and $\phi_{EO} = \pi/2$ (b) for forward propagation (left to right). Regardless of the value ϕ_{EO} of the EO's retardance, the output polarisation state is always circular.

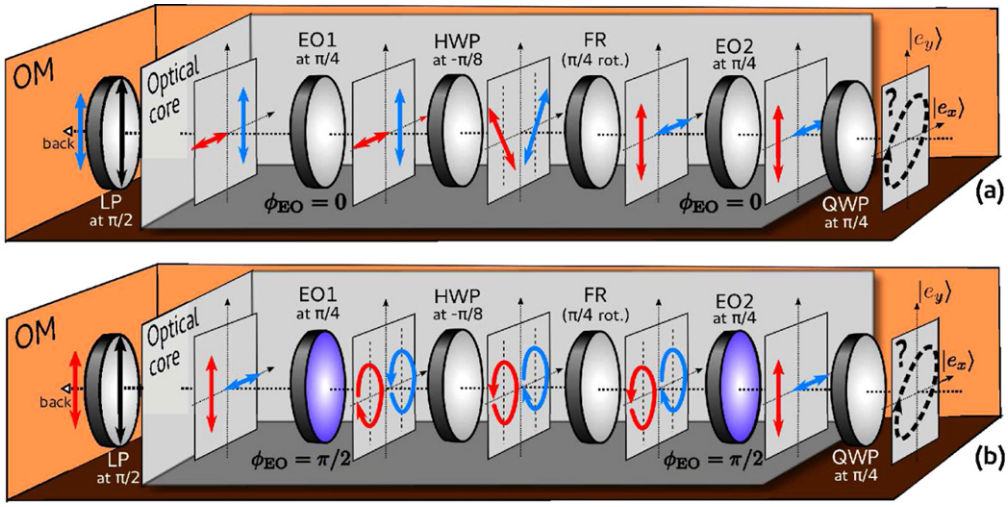

Figure 4. Orientation of polarisation states in the OM for $\phi_{EO} = 0$ (a) and $\phi_{EO} = \pi/2$ (b) for the backward propagation (right to left). The probing beam returns from the sample with an unknown polarisation state, which is composed of two linear orthogonal components, represented as red and blue in the diagram. These are sequentially selected, depending on the value of ϕ_{EO}. The two orthogonal components are represented in the diagram as being spatially separated for clarity.

transformation of $|S_{in}\rangle$, according to:

$$|S_{out}(z, \nu)\rangle = J_{out}^{fibre}(\nu)|S_{in}\rangle \tag{11}$$

$$= -(\mathrm{i}\ \cos\ \varphi(z)\cos\phi_{EO} + \mathrm{e}^{-2\mathrm{i}\theta(z)}\sin\varphi(z)\sin\phi_{EO})|e_{out}(\nu)\rangle, \tag{12}$$

where $|e_{out}(\nu)\rangle = J_{out}^{fibre}(\nu)|e_y\rangle$. Then the complex amplitude $\hat{A}^{\phi_{EO}}(z)$, for the A-scan peak corresponding to the depth z of the scattering centre, can be written from (2) and (3) as

$$\hat{A}^{\phi_{EO}}(z) = -\alpha(z)(\mathrm{i}\cos\varphi(z)\cos\phi_{EO} + \mathrm{e}^{-2\mathrm{i}\theta(z)}\sin\varphi(z)\sin\phi_{EO})\mathrm{e}^{\mathrm{i}\varphi_{rand}}, \tag{13}$$

where the random phase φ_{rand} is added to take into account the noise of the interferometer (caused by random changes in the OPD), and $\alpha(z)$ is defined by

$$\alpha(z) = r(z)\mathrm{e}^{\mathrm{i}\pi}\int\langle r_{out}(\nu)|\ e_{out}(\nu)\rangle\,\mathrm{d}\nu. \tag{14}$$

To extract the polarimetric information, φ and θ, irrespective of the polarimetric properties of the fibres in the interferometer, $\hat{A}(z)$ needs to be measured sequentially for two different values of ϕ_{EO}. Since the LP is used as an analyser in the backward direction, the two polarisation states of the light returning from the sample and travelling through the fibres for the two values of ϕ_{EO} are identical. It means that the coefficient $\alpha(z)$, which contains all the polarimetric disturbances of the fibres, is constant and can be eliminated by using a similar procedure to that described in our previous paper [13]. Furthermore, the product $\langle r_{out}(\nu)|\ e_{out}(\nu)\rangle$ dictates the contrast of the interference signal, i.e. the signal-to-noise

ratio of the OCT signal. This can be optimised by adjusting the fibre-based polarisation controller PC present in the reference arm as pictured in figure 1. Since $\alpha(z)$ is eliminated in the procedure mentioned above, the adjustment of PC does not impact in any way the polarimetric measurement.

We present two case studies for different switching rates of the EOs in comparison with the variation of the random phase φ_{rand} in the system.

2.2. Fast set-up: random phase φ_{rand} identical for the two sequential measurements

If the sequential measurements are carried out with a high switching rate of the EOs, the variation of φ_{rand} can be considered negligible from one measurement to the next. Let us define a function $\beta(z)$ to consider the two sequential measurements, one for $\phi_{\text{EO}} = \phi_0$ and the other for $\phi_{\text{EO}} = \phi_0 + \pi/2$, as follows

$$\beta(z) = \frac{\sin\phi_0 \hat{A}^{\phi_0}(z) + \cos\phi_0 \hat{A}^{\phi_0+\pi/2}(z)}{\cos\phi_0 \hat{A}^{\phi_0}(z) - \sin\phi_0 \hat{A}^{\phi_0+\pi/2}(z)}. \tag{15}$$

By using the expressions of $\hat{A}^{\phi_{\text{EO}}}$ in (13), $\beta(z)$ can be written according to the polarimetric properties of the sample as

$$\beta(z) = \tan\varphi(z) e^{-i(2\theta+\pi/2)}. \tag{16}$$

The function $\beta(z)$ is therefore insensitive to the polarimetric properties of the fibres and couplers contained in $\alpha(z)$. From (16), the value of the one-pass retardance of the sample, $\varphi(z)$, is given by

$$\varphi(z) = \arctan|\beta(z)|, \tag{17}$$

with $\varphi(z) \in [0, \pi/2]$ and the fast axis orientation $\theta(z)$ of the sample given by

$$\theta(z) = -\arg[\beta(z)]/2 - \pi/4 + m\pi, \tag{18}$$

where arg stands for the argument of the complex number in the bracket and m is an integer such that $\theta(z) \in [0, \pi]$.

As a result of the above demonstration, the measurement of two complex amplitudes for two ϕ_{EO} values (ϕ_0 and $\phi_0 + \pi/2$) is enough to obtain the retardance and the orientation of the optical axis of the retarder. By calculating $\beta(z)$, the coefficient $\alpha(z)$ incorporating the fibre polarimetric properties is eliminated, therefore the retardance $\varphi(z)$ and the fast axis orientation $\theta(z)$ are independent from these properties.

2.3. Slow set-up: random phase φ_{rand} not identical for the two sequential measurements

As the sequential measurements are not carried out sufficiently fast to ignore the random phase variation, a different random phase must be taken into consideration for each of the two sequential measurements. This could be the case if the EOs are switched after acquiring each 2D image (B-scan).

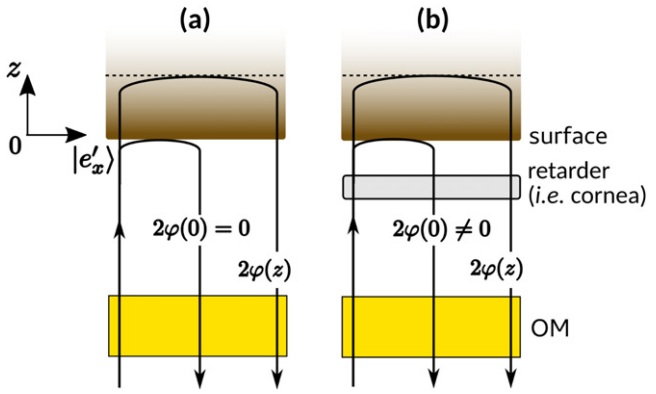

Figure 5. Representation of two situations: (a) no retarder in front of the surface, (b) retarder in front of the surface, corneal tissue for example. The sample is considered without diattenuation.

If we are only interested in the net retardance, we propose measuring the complex amplitude for $\phi_{\text{EO}} = 0$ and $\phi_{\text{EO}} = \pi/2$. Indeed, $\varphi(z)$ can be extracted irrespective of the random phase due to

$$\varphi(z) = \arctan\left|\frac{\hat{A}^{\pi/2}(z)}{\hat{A}^{0}(z)}\right|. \tag{19}$$

If we need to measure the axis orientation of the sample in addition to its retardance, then a possible solution consists in using the surface layer of the sample to produce a phase reference. Usually the surface layer of the medium is used in PS-OCT to reference the polarimetric properties of the fibre [5, 7] corresponding to a normalisation in relation to the surface. The coding and decoding is performed in free space, in front of the sample. This allows independence of measurements from the fibre's polarimetric properties [13]. To eliminate the random phase, we need to calculate the following ratio

$$\hat{A}^{\phi_{\text{EO}}}_{\text{norm}}(z) = \frac{\hat{A}^{\phi_{\text{EO}}}(z)}{\hat{A}^{\phi_{\text{EO}}}(0)}, \tag{20}$$

where $\hat{A}^{\phi_{\text{EO}}}(0)$ is the complex amplitude for the A-scan peak at the surface, the value of which depends on the electro-optic retardance ϕ_{EO}.

The choice of the values for ϕ_{EO} depends on whether a retarder element is placed in front of the surface or not (figure 5). The required values for ϕ_{EO} are listed in table 1 for each of the cases studied below.

2.3.1. No retarder element in front of the sample surface, $\varphi(0) = 0$. When there is no retarder element in front of the surface (e.g. skin), the net retardance imprinted by the surface is considered to be $\varphi(0) = 0$. The complex amplitude is therefore $\hat{A}^{\pi/2}(0) = 0$ and it cannot be used to normalise $\hat{A}^{\pi/2}(z)$. Hence, we propose measuring the complex amplitude for $\phi_{\text{EO}} = -\pi/4$ and $\phi_{\text{EO}} = \pi/4$, and studying

Table 1. Required retardance values ϕ_{EO} for the two EOs according to the retardance at the sample surface $\varphi(0)$ and the variation of the random phase $\Delta\varphi_{rand}$ between two switches of the EOs.

	$\Delta\varphi_{rand} = 0$	$\Delta\varphi_{rand} \neq 0$
$\varphi(0) = 0$		$\phi_{EO} : \pi/4 \rightarrow -\pi/4.$
$\varphi(0) = \pi/2$	$\phi_{EO} : \phi_0 \rightarrow \phi_0 + \pi/2.$	$\phi_{EO} : \pi/4 \rightarrow -\pi/4.$
$\varphi(0) \neq 0, \varphi(0) \neq \pi/2$		$\phi_{EO} : 0 \rightarrow \pi/2.$

the function $\beta_1(z)$ defined by

$$\beta_1(z) = \frac{\hat{A}_{norm}^{\pi/4}(z) - \hat{A}_{norm}^{-\pi/4}(z)}{\hat{A}_{norm}^{\pi/4}(z) + \hat{A}_{norm}^{-\pi/4}(z)} = \tan\varphi(z)e^{-i(2\theta(z)+\pi/2)}, \tag{21}$$

where $\varphi(z)$ can be retrieved using

$$\varphi(z) = \arctan|\beta_1(z)|, \tag{22}$$

and where the axis orientation $\theta(z)$ of the sample is given by

$$\theta(z) = -\arg[\beta_1(z)]/2 - \pi/4 + m\pi. \tag{23}$$

2.3.2. Retarder element in front of the sample surface, $\varphi(0) \neq 0$. An important application case is that of polarisation characterisation of the retina, where the measurement is affected by the birefringence of the anterior chamber structures in the eye. We refer to this case as that of a retarder element in front of the surface, where the retardance $\varphi(0) \neq 0$ for the surface.

If $\varphi(0) \neq \pi/2$, we have $\hat{A}^0(0) \neq 0$ and $\hat{A}^{\pi/2}(0) \neq 0$ for the surface, and they can be used to normalise the complex amplitudes $\hat{A}^0$ and $\hat{A}^{\pi/2}(z)$. In such cases we propose to measure the complex amplitude for $\phi_{EO} = 0$ and $\phi_{EO} = \pi/2$. According to (19), the one-pass retardance of the sample +retarder system $\varphi(z)$ can be calculated, while the optical axis $\theta(z)$ of the medium can be expressed as

$$\theta(z) - \theta(0) = -\arg\left[\frac{\hat{A}_{norm}^{\pi/2}(z)}{\hat{A}_{norm}^{0}(z)}\right]/2 + m\pi. \tag{24}$$

It is not possible in this case to measure the absolute orientation of the optical axis, but only the orientation according to $\theta(0)$.

If $\varphi(0) = \pi/2$, the complex amplitude $\hat{A}^0(0)$ is null and it is not possible to use it to normalise $\hat{A}^0(z)$. We therefore propose measuring the complex amplitude for $\phi_{EO} = -\pi/4$ and $\phi_{EO} = \pi/4$, and studying the function $\beta_2(z)$ defined by

$$\beta_2(z) = \frac{\hat{A}_{norm}^{\pi/4} + \hat{A}_{norm}^{-\pi/4}}{\hat{A}_{norm}^{\pi/4} - \hat{A}_{norm}^{-\pi/4}} = \tan\varphi(z)e^{-i(2\theta(z)+\pi/2)}, \tag{25}$$

where $\varphi(z)$ can be retrieved from

$$\varphi(z) = \arctan|\beta_2(z)|, \tag{26}$$

and the axis orientation $\theta(z)$ by

$$\theta(z) = -\arg[\beta_2(z)]/2 - \pi/4 + m\pi. \tag{27}$$

3. Simulations

The OCT system is modelled with a Gaussian broadband source at $\lambda_0 = 850$ nm for two situations: full width at half maximum (FWHM) $\Delta\lambda = 100$ nm and $\Delta\lambda = 50$ nm. The channelled spectrum is re-sampled to eliminate the chirp effect due to the dispersion of the OCT system, and the non-linearities in wavenumber present in the spectrometer. In each case, the channelled spectrum is sampled with 1000 points. The span of the spectrometer is equal to the FWHM of the source. The polarimetric response of the fibres is modelled by the product J^{Fibre} of different Jones matrices, accounting for the chromatic birefringence of the fibre and the possible diattenuation of the couplers, as follows

$$J^{Fibre} = J_{Rot(\alpha 1)} \cdot J_{Diat(D,\alpha 2)} \cdot J_{Bir(\phi(\nu),\alpha 3)} \cdot J_{Rot(\alpha 4)}, \tag{28}$$

where $J_{Rot(\alpha)}$ is the Jones matrix for a rotator that rotates the linear polarisation by an angle α, $J_{Diat(D,\alpha)}$ corresponds to a linear diattenuator with the diattenuation D and oriented at the angle α and $J_{Bir(\phi(\nu),\alpha)}$ corresponds to a linear retarder oriented at the angle α with retardance $\phi(\nu)$. In this simulation, the retardance $\phi(\nu)$ is expressed according to a mean retardance $\phi(\nu_0)$ and a parameter ΔT to take into account the polarisation mode dispersion (PMD) of fibres, as follows

$$\phi(\nu) = \phi(\nu_0) + 2\pi\Delta T(\nu - \nu_0), \tag{29}$$

with ν_0 being the central optical frequency of the source.

The field $|S_{out}(z, \nu)\rangle$ coming from the sample and travelling through fibres is expressed as follows

$$|S_{out}(z, \nu)\rangle = J_{out(\nu)}^{Fibre} \; |S_{in}(z, \nu)\rangle, \tag{30}$$

with

$$|S_{in}\rangle = J_{back(\nu,\phi_{EO})}^{OM} \cdot J_{sample(z)} \cdot J_{fwd(\nu,\phi_{EO})}^{OM} \cdot J_{in(\nu)}^{Fibre} \; |e_0\rangle, \tag{31}$$

where $|e_0\rangle$ is the input field from the source, $J_{sample(z)}$ is the Jones matrix of the sample after a round-trip in depth z, $J_{in(\nu)}^{Fibre}$ and $J_{out(\nu)}^{Fibre}$ respectively correspond to the polarisation changes of the light traveling from the source to the OM and from the OM to the detector, $J_{fwd(\nu,\phi_{EO})}^{OM}$ and $J_{back(\nu,\phi_{EO})}^{OM}$ correspond to the polarimetric response of the OM in forward and backward

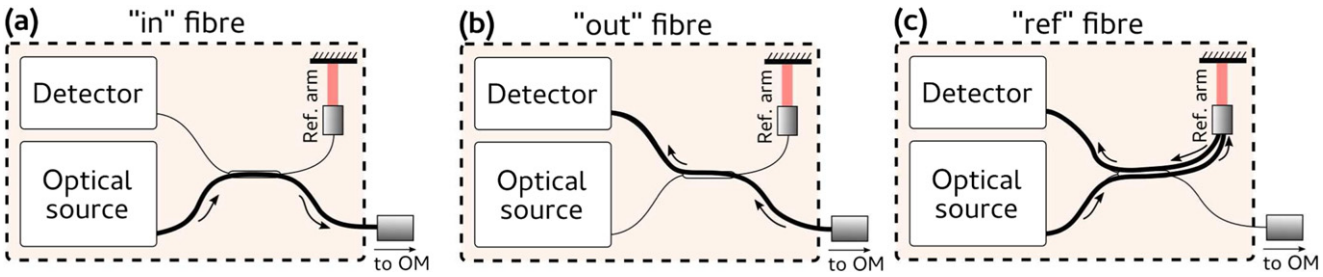

Figure 6. Schematic representation of the different fibre paths employed in the simulations.

Table 2. Coefficients for the fibres in the OCT system. PMD is considered to be equal to 0.1 ps/$\sqrt{\text{km}}$ for a single mode fibre, which corresponds to a delay of $\Delta T = 10$ fs for a 10 m fibre. Coefficients D, $\phi(\nu_0)$, α_1, α_2, α_3 and α_4 are arbitrarily chosen. D_{out}, $\phi(\nu_0)_{\text{out}}$ and ΔT_{out} are independently varied in the simulations to assess the effect of each one in the polarimetric measurements (refer to figure 7).

	Length (m)	D	$\phi(\nu_0)$ (rad)	ΔT (fs)	α_1 (rad)	α_2 (rad)	α_3 (rad)	α_4 (rad)
'In' fibre	10	0	$\pi/5$	10	$\pi/8$	1	$-\pi/8$	0
'Out' fibre	10	0, D_{out}	$\pi/8$, $\phi(\nu_0)_{\text{out}}$	10, ΔT_{out}	0	0.5	$\pi/12$	$\pi/2$
'Ref' fibre	20	0	$\pi/4$	14	$\pi/4$	0	$\pi/4$	$\pi/4$

directions defined by

$$J^{\text{OM}}_{\text{fwd}(\nu,\phi_{\text{EO}})} = J_{\text{Bir}(\pi/2,-\pi/4)} \cdot J^{\text{fwd}}_{\text{core}(\nu,\phi_{\text{EO}})} \cdot P, \tag{32}$$

and

$$J^{\text{OM}}_{\text{back}(\nu,\phi_{\text{EO}})} = P \cdot J^{\text{back}}_{\text{core}(\nu,\phi_{\text{EO}})} \cdot J_{\text{Bir}(\pi/2,\pi/4)}, \tag{33}$$

with P being the Jones matrix of the LP in the OM. The field $|r_{\text{out}}(\nu)\rangle$ coming from the reference arm is expressed with the Jones matrix of the reference fibre $J^{\text{Fibre}}_{\text{ref}}$, and a complex exponential term $e^{i\frac{2\pi\nu}{c}2z}$, considering the OPD between the two arms ($2z$) as follows

$$|r_{\text{out}}(\nu)\rangle = e^{i\frac{2\pi\nu}{c}2z} J^{\text{Fibre}}_{\text{ref}(\nu)} \; |e_0\rangle. \tag{34}$$

The simulation consists of two parts. Firstly, the Fourier transform of the intensity $S(\nu)(\langle S_{\text{out}}(z,\nu)|\, r_{\text{out}}(\nu)\rangle + \langle r_{\text{out}}(\nu)|\, S_{\text{out}}(z,\nu)\rangle)$, is calculated, where $S(\nu)$ is the power spectrum of the light source. Secondly, the complex amplitude associated with the depth z in the sample is measured at the maximum of the peak.

Let 'in' fibre and 'out' fibre denote the optical paths within the sample fibre, from the source to the OM and from the OM to the detector respectively, as presented in figures 6(a) and (b). 'Ref' fibre is represented in figure 6(c), which corresponds to the optical path from the source to the detector through the reference arm. Table 2 gives the parameters of the fibres used in the simulation. Here, PMD is considered as 0.1 ps/$\sqrt{\text{km}}$ for a SMF, which for a 10 m fibre corresponds to a delay of $\Delta T = 10$ fs, used in (29). The values of the coefficients in table 2 are arbitrarily chosen, and some parameters (D_{out}, ΔT_{out} and $\phi(\nu_0)_{\text{out}}$) in the 'out' fibre are independently varied in the next section to prove the insensitivity of the retardance and optical axis orientation measurements to the polarimetric response of fibres and couplers.

3.1. Effect of fibres on the polarimetric measurement of the sample

In the theoretical section we demonstrated that the polarimetric measurement of the sample is insensitive to fibre disturbances, since the generation and analysis of the polarisation states are done in free space, in front of the sample.

To verify this behaviour, a retarder sample oriented at 45° with a retardance of 10° is considered. The chromaticity of the elements in the OM is not considered at this stage. The random phase is assumed identical for the two sequential measurements (as presented in section 2.2). Finally, the FWHM of the source spectrum is equal to 100 nm centred at 850 nm.

The OM switches from $\phi_{\text{EO}} = 0$ to $\phi_{\text{EO}} = \pi/2$ and, according to (15), the retardance and the axis orientation are measured via (17) and (18). Figure 7 shows the bias of the retardance and the axis orientation by varying the properties of the 'out' fibre of the sample arm.

If we consider that the fibre characteristics are identical for the two sequential measurements, the biases on the retardance $\Delta\varphi_{\text{bias}}$ and on the axis orientation $\Delta\theta_{\text{bias}}$ are equal to zero regardless of the polarimetric properties of the 'out' fibre, i.e. its retardance $\phi(\nu_0)_{\text{out}}$ (thick blue line in figures 7(a) and (b)), its PMD ΔT_{out} (thick blue line in figures 7(c) and (d)), and its partial diattenuation D_{out} (thick blue line in figures 7(e) and (f)). It is commonly assumed in PS-OCT that fibres remain stable during sequential measurements [15, 16].

We can evaluate the behaviour of the biases on retardance and axis orientation if the 'out' fibre evolves between the two measurements. To do so, the parameters $\phi_{0,\text{out}}$, ΔT_{out} and D_{out} are increased by 1% during the switch of the electro-optics. The results are shown as thin red lines in figure 7. In addition to these weak biases (<1°), the chromaticity of the elements in the OM introduces other biases, as discussed in section 3.2.

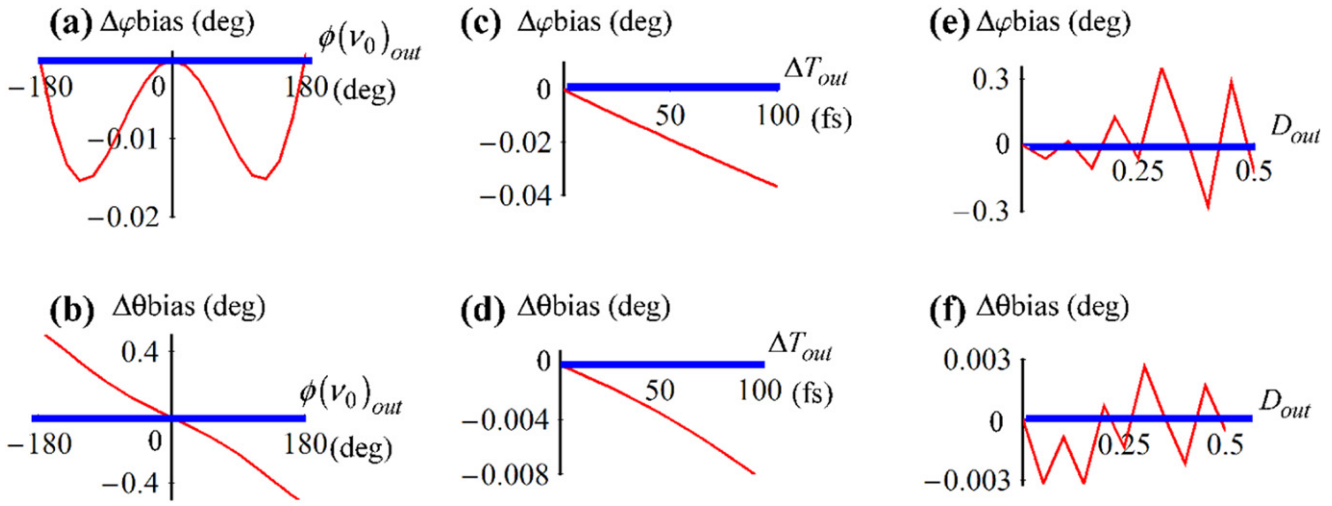

Figure 7. Measurement of the bias on the retardance φ_{sample} and on the orientation angle θ_{sample} of a sample, according to the retardance of the 'out' fibre (a) and (b), the PMD of the 'out' fibre (c) and (d), and the diattenuation of the 'out' fibre (e) and (f). Thick (blue) lines: the characteristics of the 'out' fibre are identical for the two sequential measurements. (a) and (b) thin (red) lines: the retardance of the 'out' fibre is $\phi(\nu_0)_{\text{out}}$ during the first measurement, $1.01 \times \phi(\nu_0)_{\text{out}}$ during the second measurement. (c) and (d) thin (red) lines: the PMD of the 'out' fibre is ΔT_{out} during the first measurement, $1.01 \times \Delta T_{\text{out}}$ for the second one. (e) and (f) thin (red) lines: the diattenuation of the 'out' fibre is D_{out} during the first measurement, $1.01 \times D_{\text{out}}$ during the second measurement.

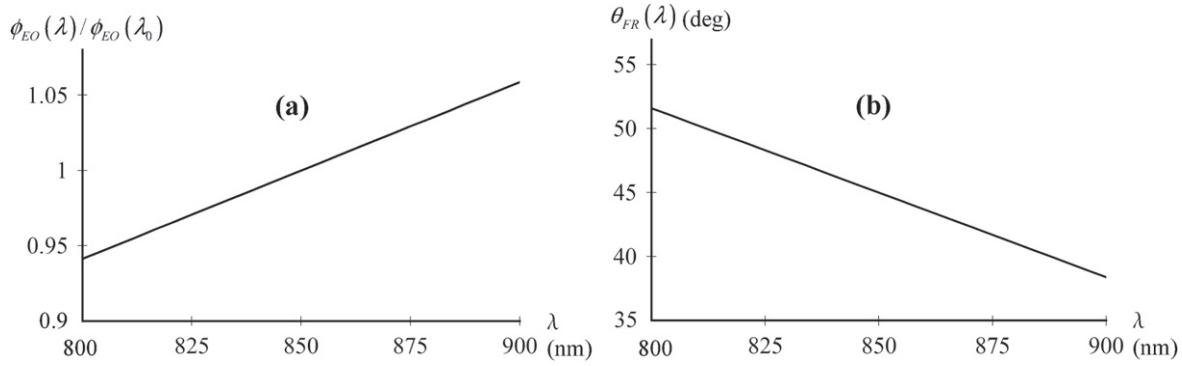

Figure 8. Chromatic response of the electro-optic polarisation modulator (a) and the Faraday rotator (b).

3.2. Effect of chromatic response of the OM on the polarimetric measurement of the sample

The OM is made of commonly available devices (FRs, wave plates, electro-optic polarisation modulators, LP), similar to those widely used in PS-OCT and in interferometric systems. While achromatic wave plates and LPs are readily available, the chromaticity of FRs and electro-optical polarisation modulators has to be taken into account. Consequently, systematic errors (bias) on the polarimetric measurement of the sample are induced.

Electro-optic polarisation modulators are usually built with two matched crystals arranged in series, oriented at 90° relative to each other, in order to suppress intrinsic birefringence and variations due to temperature changes. The simulation has considered a Lithium Niobate medium with a half-wave voltage V_π equal to 300 V at 1000 nm and 150 V at 532 nm (such as the Newport model 4104 which has been employed in the system reported in [17]). Figure 8(a) shows the normalised retardance variation $\phi_{\text{EO}}(\lambda)/\phi_{\text{EO}}(\lambda_0)$ of the electro-optic polarisation modulator versus wavelength used in the simulation, with $\lambda_0 = 850$ nm.

Figure 8(b) shows the rotation $\theta_{\text{FR}}(\lambda)$ of a 45° Terbium Gallium Garnet FR versus wavelength, which was used in the simulation. To model this, the Verdet constant $V(\lambda)$ of the rotator was linearly interpolated using values from [18], which give V as 51 rad Tm^{-1} for 900 nm and 68.5 rad Tm^{-1} for 800 nm.

3.2.1. Bias for the fast set-up case: random phase φ_{rand} identical for the two sequential measurements. In this section we consider that during the two sequential measurements the random phase is identical and fibres do not change their characteristics. The sample is a linear retarder where its retardance φ_{sample} and its axis orientation θ_{sample} are variable parameters. Let us also consider the FWHM of the

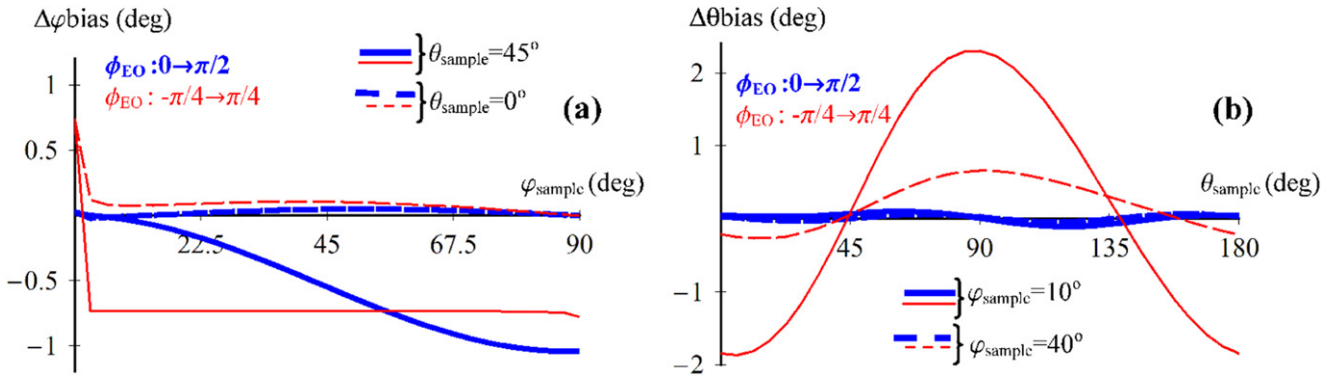

Figure 9. Measurement of the bias on the retardance φ_{sample} (a) and the orientation angle θ_{sample} (b) of a linear retarder. Thin (red) curves: retardance ϕ_{EO} switching from $-\pi/4$ to $\pi/4$. Thick (blue) curves: retardance ϕ_{EO} switching from 0 to $\pi/2$. Solid lines in (a): sample fast axis oriented at 45°. Dashed lines in (a): sample fast axis oriented at 0°. Solid lines in (b): sample retardance equal to 10°. Dashed lines in (b): sample retardance equal to 40°.

source spectrum to be $\Delta\lambda = 100$ nm, centred at $\lambda_0 = 850$ nm.

Biases on retardance and axis orientation are evaluated according to the values of φ_{sample}, θ_{sample} and the choice of retardance of the electro-optic polarisation modulators (table 1). In particular the study is carried out for two configurations to evaluate the impact of the parameter ϕ_0 on the biases: (1) sequential measurements, one for $\phi_{\text{EO}} = 0$ and the other one for $\phi_{\text{EO}} = \pi/2$ (thick blue curves in figure 9), (2) sequential measurements, one for $\phi_{\text{EO}} = -\pi/4$ and one for $\phi_{\text{EO}} = \pi/4$ (thin red curves in figure 9).

Figure 9(a) shows the bias on retardance for two different orientations of the retarders, at 0° (dashed line), and at 45° (solid line). Due to the chromatic response of the OM, a coupling between φ_{sample} and θ_{sample} appears in the systematic errors. The bias differs according to the strategy used for the sequential measurement. For the retardance ϕ_{EO} switching from $-\pi/4$ to $\pi/4$, the bias $\Delta\varphi_{\text{bias}}$ is uniform except for weak sample retardances. By contrast, for a switch with ϕ_{EO} from 0 to $\pi/2$, the bias is low for a weak retardance but increases with the retardance for θ_{sample} at 45° and no variation is observed for θ_{sample} at zero.

Figure 9(b) shows the bias on axis orientation for two different sample retardances, at 10° (solid line), and at 40° (dashed line). Once more, due to the chromatic response of the OM, a coupling between φ_{sample} and θ_{sample} takes place, as shown by the systematic errors. The bias $\Delta\theta_{\text{bias}}$ is less significant for the configuration ($\phi_{\text{EO}} = 0 \rightarrow \pi/2$).

3.2.2. Bias for slow set-up case: random phase φ_{rand} not identical for the two sequential measurements. In this section we consider that during the two sequential measurements the random phase is not identical and fibres do not change their characteristics. Two sub-cases are distinguished: a retarder element in front of the sample or none at all.

No retarder element in front of the sample: The sample is a linear retarder with the retardance φ_{sample} and the axis orientation θ_{sample}. Biases on retardance and axis orientation are evaluated according to the values of φ_{sample}, θ_{sample} and the choice of the FWHM of the source spectrum between 50 nm (thick blue curves in figure 10) and 100 nm (thin red curves in figure 10). Figure 10(a) shows the bias on retardance for two different sample orientations, one at 0° (dashed lines) and another at 45° (solid lines). The coupling between φ_{sample} and θ_{sample} is still present and amplified by the normalisation of the signal by the one defined at the surface. The larger the bandwidth, the larger the bias. Figure 10(b) shows the bias on axis orientation for two different sample retardances, of 10° (solid lines), and of 40° (dashed lines). Due to the need of employing the sample surface as a reference, it is necessary to switch ϕ_{EO} from $-\pi/4$ to $\pi/4$. With that, the bias on axis orientation is close to zero at 45° and 135° but increases for lower sample retardance and higher spectral width at 0°, 90° and 180°.

Retarder element in front of the sample: To be consistent with other retinal studies in the literature [19, 20], the retarder element corresponding to the cornea is chosen to have a one-pass retardance equal to 25° and its axis orientation is set arbitrarily at 0° on the basis $\{|e_x'\rangle, |e_y'\rangle\}$. The sample corresponding to the retinal nerve fibre layer (RNFL) has a one-pass retardance φ_{sample} between 10° and 50° and is oriented at the angle θ_{sample}. Biases on retardance and axis orientation are evaluated according to the values of φ_{sample} and θ_{sample} (figure 10). Figure 11(a) shows the bias on retardance $\Delta\varphi_{\text{bias}}$ for two different sample orientations, at 0° (dashed line) and at 45° (solid line). Figure 11(b) shows the bias on axis orientation $\Delta\theta_{\text{bias}}$ for two different samples, the first one having a retardance of 10° (dashed line), and the second one 50° (solid line). In this sub-case, since the retardance ϕ_{EO} is switched from 0 to $\pi/2$, the bias on axis orientation is weak (see figure 9(b)) and inferior to that obtained in figure 10(b).

4. Discussion and conclusions

The theoretical module presented requires some additional considerations regarding its practical implementation in an OCT system. The polarisation components within the OM increase the optical path length of the sample arm, which

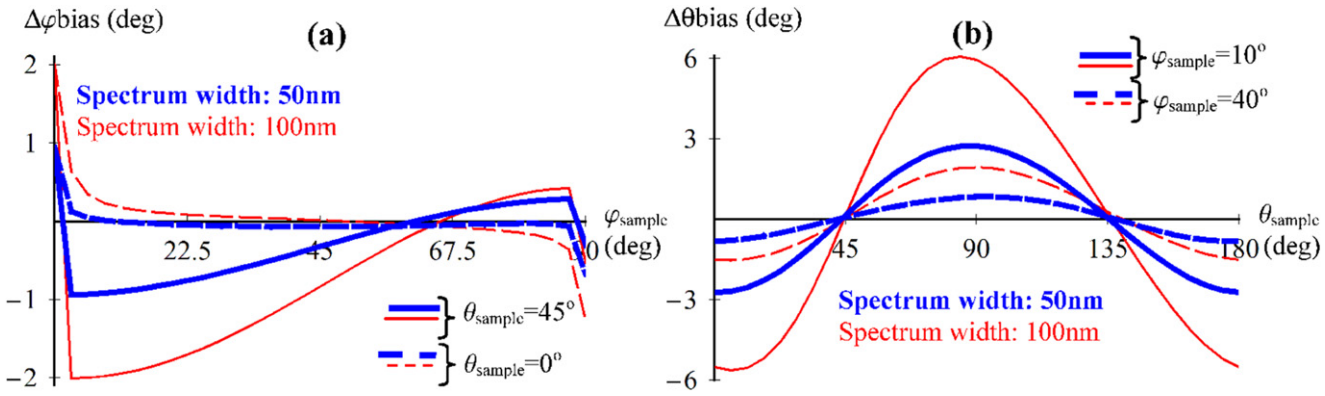

Figure 10. Measurement of the bias on the retardance φ_{sample} (a) and on the orientation angle θ_{sample} (b) of a linear retarder. Thin (red) curves: the FWHM of the source spectrum is equal to 100 nm. Thick (blue) curves: the FWHM of the source spectrum is equal to 50 nm. Solid lines in (a): sample oriented at 45°. Dashed lines in (a): sample oriented at 0°. Solid lines in (b): sample retardance equal to 10°. Dashed lines in (b): sample retardance equal to 40°.

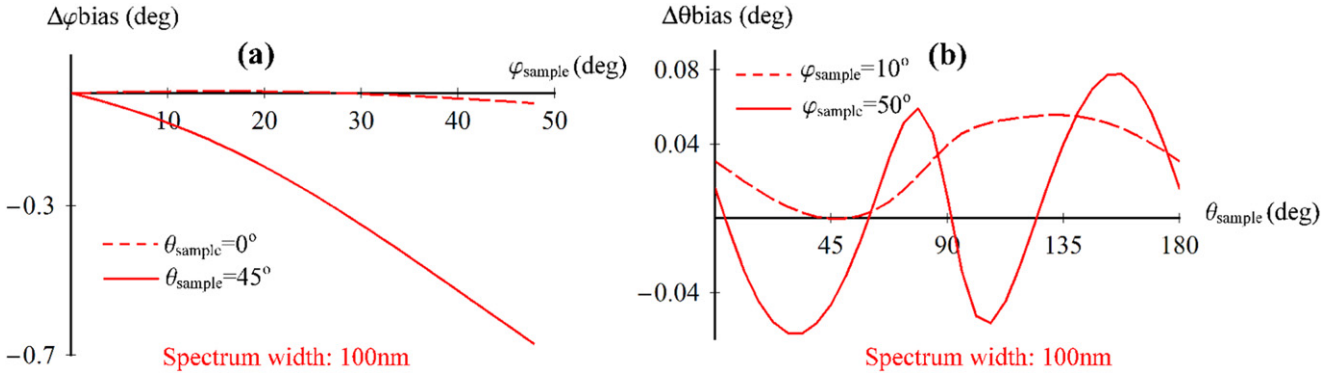

Figure 11. Measurement of the bias on the retardance φ_{sample} (a) and on the orientation angle θ_{sample} (b) of a system made of a retarder (cornea) in front of a sample corresponding to the retinal nerve fibre layer (RNFL). Solid line in (a): sample oriented at 45°. Dashed line in (a): sample oriented at 0°. Solid line in (b): sample retardance equal to 50°. Dashed line in (b): sample retardance equal to 10°.

demands a corresponding change in the optical path length of the reference arm. Moreover, inclusion of the OM in the system contributes to dispersion imbalance which needs to be compensated. Since perfect matching of dispersive properties of the different components in the reference arm would be difficult to achieve, we suggest the application of the Master–Slave interferometry method [21], that makes the system tolerant to the unmatched dispersion.

As mentioned before, the LP within the OM has two purposes: it ensures that the light entering the sample arm is polarised, and performs the selection of the polarisation state on the return path. Accomplishing these roles inevitably involves losses; nevertheless, these roles are present in any PS-OCT system, leading to similar losses. If the source is partially polarised, one can minimise the input loss by placing a polarisation controller in front of the optical source to match the polarisation state of the light entering the sample arm with the axis of the LP within the OM.

For practical implementation of the module there are two possibilities: (i) a free-space configuration which is not compact and can present some electric safety risk due to the high voltages required for the operation of the EO modulators and (ii) a fibre-based configuration which can be made more compact but will introduce additional implementation challenges. The new generation of ceramic EO modulators requiring lower driving currents [22] and compact FRs [23] allow for a fibre-based OM.

The theoretical model presented establishes a sequential procedure for employing a versatile OM that, when placed within the sample arm of the interferometer, can provide the net retardance and axis orientation of the sample. Due to the dual-pass nature of OCT systems, in a PS-OCT system it is not possible to measure any property other than linear retardance and linear diattenuation. Therefore, in this study, the only property being addressed is that of a linear retarder. The two sequential measurements require the acquisition of a channelled spectrum for each setting of the OM. The procedures and OM described ensure independence from potential internal disturbances created by the optical fibre, because the generation of the polarisation state (circular) and the analysis of the returned polarisation state are done in free space. The insensitivity of the system to fibre disturbances means that no calibration step is required in order to compensate for the polarimetric effects of the fibres. Distinction is made between short and long switching times of the EOs and equations are provided that establish the basis for the method presented, in

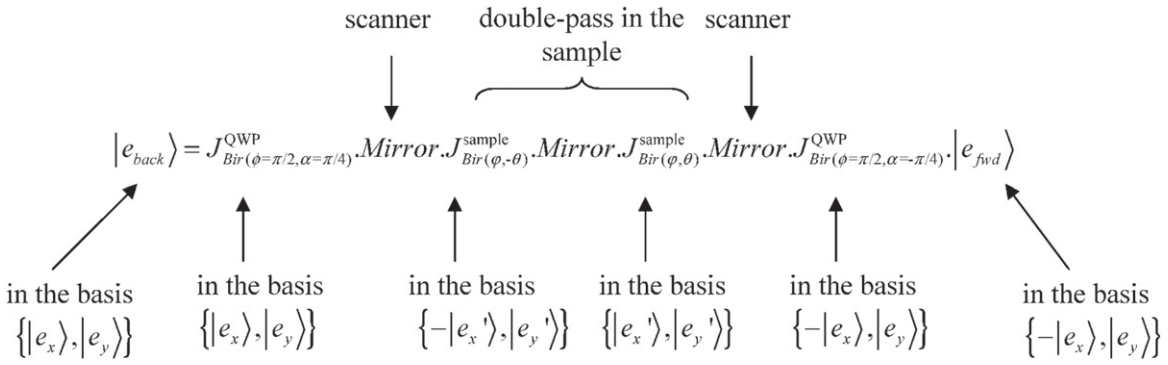

Figure B1. Calculation of the field $|e_{\text{back}}\rangle$ defined in the basis $\{|e_x\rangle, |e_y\rangle\}$.

respect to tolerance to phase disturbances when applied in a fast set-up and in a slow set-up. Simulations have been conducted to evaluate biases on retardance and axis orientation due to the chromatic response of the OM. These biases act as systematic errors related to the choice of the spectral width. In any polarimetric measurement employing wide bandwidth sources, there is always a compromise to be made in terms of performance (accuracy of the retardance and axis orientation measurements) and bandwidth (axial resolution of the OCT system). Also, the accuracy requirement is dependent on the sample in question.

The particular case of a retarder in front of the sample is covered, which is applicable in polarimetric measurements of the retina disturbed by the anterior chamber of the eye.

Although the theory presented referred to the interrogation of the optical spectrum at the interferometer output, the module suggested can equally be used in time-domain OCT systems.

Acknowledgments

S Rivet acknowledges the Marie-Curie Intra-European Fellowship for Career Development, No. 625509. A Bradu, M J Marques and A Podoleanu were partially supported by the European Research Council (ERC) under the European Union's Seventh Framework Programme, Advanced Grant agreement 'COGATIMABIO', 249889. A Podoleanu is also supported by the European Industrial Doctorate UBAPHO-DESA, FP7-PEOPLE-2013-ITN 607627, Royal Society Wolfson Research Merit Award and by the NIHR Biomedical Research Centre at Moorfields Eye Hospital NHS Foundation Trust and UCL Institute of Ophthalmology. M J Marques also acknowledges the University of Kent for his PhD support. The authors thank Sally Makin and Christopher Costa for proof-reading the manuscript.

Appendix A. Jones matrices used in the theoretical model

- Jones matrix of a polarisation rotator by an angle α in relation to either $|e_x\rangle$ or $|e_x'\rangle$, depending on the case described in the text:

$$J_{\text{Rot}(\alpha)} = \begin{pmatrix} \cos\alpha & -\sin\alpha \\ \sin\alpha & \cos\alpha \end{pmatrix}. \tag{A.1}$$

- Jones matrix for a linear birefringent medium with a retardance ϕ, at an angle α in relation to either $|e_x\rangle$ or $|e_x'\rangle$, depending on the case described in the text:

$$J_{\text{Bir}(\phi,\alpha)} = J_{\text{Rot}(\alpha)} \cdot \begin{pmatrix} e^{i\phi/2} & 0 \\ 0 & e^{-i\phi/2} \end{pmatrix} \cdot J_{\text{Rot}(-\alpha)}. \tag{A.2}$$

  The retardance introduced by a HWP is $\phi = \pi$, and by a QWP is $\phi = \pi/2$.
- Jones matrix for a partial linear diattenuator with diattenuation D and oriented at an angle α in relation to either $|e_x\rangle$ or $|e_x'\rangle$, depending on the case described in the text:

$$J_{\text{Diat}(D,\alpha)} = J_{\text{Rot}(\alpha)} \cdot \begin{pmatrix} \left(\frac{1-D}{1+D}\right) & 0 \\ 0 & 1 \end{pmatrix} \cdot J_{\text{Rot}(-\alpha)}. \tag{A.3}$$

Appendix B. Demonstration of equation (6)

In figure B1, the calculation of the field $|e_{\text{back}}\rangle$ is detailed. This calculation comprises the polarimetric changes affecting the field $|e_{\text{fwd}}\rangle$. All the calculations have been carried out considering the point of view of the optical source; this means that the basis for $|e_{\text{fwd}}\rangle$ is given by $\{-|e_x\rangle, |e_y\rangle\}$.

$J_{\text{Bir}(\phi,\alpha)}$ is defined in appendix A as the generic Jones matrix of a birefringent medium considered as a linear retarder with retardance ϕ, and oriented at an angle α in relation to either $|e_x\rangle$ or $|e_x'\rangle$, depending on the case described in the text. The Jones matrix for the mirror is given by

$$\text{Mirror} = \begin{pmatrix} -1 & 0 \\ 0 & 1 \end{pmatrix}. \tag{B.1}$$

References

[1] Hee M R, Huang D, Swanson E A and Fujimoto J G 1992 *J. Opt. Soc. Am.* B **9** 903

[2] Saxer C E, de Boer J F, Park B H, Zhao Y, Chen Z and Nelson J S 2000 *Opt. Lett.* **25** 1355–7

[3] Al-Qaisi M K and Akkin T 2008 *Opt. Express* **16** 13032–41

[4] Zurauskas M and Podoleanu A 2013 *J. Biomed. Opt.* **18** 106010

[5] Braaf B, Vermeer K A, de Groot M, Vienola K V and de Boer J F 2014 *Biomed. Opt. Express* **5** 2736

[6] Yasuno Y, Makita S, Endo T, Itoh M, Yatagai T, Takahashi M, Katada C and Mutoh M 2004 *Appl. Phys. Lett.* **85** 3023–5

[7] Baumann B, Choi W, Potsaid B, Huang D, Duker J S and Fujimoto J G 2012 *Opt. Express* **20** 10229–41

[8] Ding Z, Liang C P, Tang Q and Chen Y 2015 *Biomed. Opt. Express* **6** 1828

[9] Rashleigh S C 1980 *Opt. Lett.* **5** 392

[10] Lippok N, Villiger M, Jun C and Bouma B E 2015 *Opt. Lett.* **40** 2025–8

[11] Trasischker W, Zotter S, Torzicky T, Baumann B, Haindl R, Pircher M and Hitzenberger C K 2014 *Biomed. Opt. Express* **5** 2798

[12] Roth J E, Kozak J A, Yazdanfar S, Rollins A M and Izatt J A 2001 *Opt. Lett.* **26** 1069

[13] Marques M J, Rivet S, Bradu A and Podoleanu A 2015 *Opt. Lett.* **40** 3858–61

[14] Götzinger E, Baumann B, Pircher M and Hitzenberger C K 2009 *Opt. Express* **17** 22704–17

[15] Yamanari M, Makita S and Yasuno Y 2008 *Opt. Express* **16** 5892–906

[16] Zhang J, Guo S, Jung W, Nelson J and Chen Z 2003 *Opt. Express* **11** 3262–70

[17] Yamanari M, Makita S, Madjarova V D, Yatagai T and Yasuno Y 2006 *Opt. Express* **14** 6502–15

[18] Barnes N P and Petway L B 1992 *J. Opt. Soc. Am.* B **9** 1912–5

[19] Cense B, Chen T C, Park B H, Pierce M C and de Boer J F 2004 *J. Biomed. Opt.* **9** 121–5

[20] Knighton R W and Huang X R 2002 *Investigative Ophthalmology Vis. Sci.* **43** 82–6

[21] Bradu A, Maria M and Podoleanu A G 2015 *Opt. Express* **23** 14148–61

[22] Jiang H, Zou Y, Chen Q, Li K, Zhang R, Wang Y, Ming H and Zheng Z 2005 Transparent electro-optic ceramics and devices *Photonics Asia 2004* (International Society for Optics and Photonics) pp 380–94

[23] Shirasaki M, Kuwahara H and Obokata T 1981 *Appl. Opt.* **20** 2683–7

Optics Letters

Polarization-sensitive optical coherence tomography system tolerant to fiber disturbances using a line camera

Manuel J. Marques,[1,*] Sylvain Rivet,[1,2] Adrian Bradu,[1] and Adrian Podoleanu[1]

[1]Applied Optics Group, School of Physical Sciences, University of Kent, Canterbury CT2 7NH, UK
[2]Université de Brest, EA 938 Laboratoire de Spectrométrie et Optique Laser, SFR Scinbios, 6 avenue Le Gorgeu, C.S. 93837, 29238 Brest Cedex 3, France
*Corresponding author: mjmm2@kent.ac.uk

Received 20 May 2015; revised 23 July 2015; accepted 23 July 2015; posted 24 July 2015 (Doc. ID 241308); published 11 August 2015

This Letter presents a spectral-domain, polarization-sensitive optical coherence tomography (PS-OCT) system, where the light collection from the two arms of the interferometer is performed exclusively using single-mode fibers and couplers, and the two orthogonal polarization components are sequentially detected by a single line camera. Retardance measurements can be affected by polarimetric effects because of fiber birefringence and diattenuation in fiber couplers. This configuration bypasses such issues by performing polarization selection before the collection fiber through the combination of a polarization rotator and a linear polarizer. Retardance calibration is achieved with a Berek compensator. Similar net retardance maps of a birefringent phantom are obtained for two different settings of induced fiber birefringence, effectively demonstrating the tolerance of the configuration to fiber-based disturbances.

OCIS codes: (120.0120) Instrumentation, measurement, and metrology; (230.5440) Polarization-selective devices; (110.4500) Optical coherence tomography.

http://dx.doi.org/10.1364/OL.40.003858

Spectrometer-based optical coherence tomography (OCT) methods have been extensively used over the past decade as a way to image translucent structures [1]. Polarization-sensitive OCT methods emerged as early as 1992 [2], evolving from bulk-based to fiber-based designs, employing single or multiple detectors, and acquiring the resulting signal either in time domain [3–6] or in frequency domain [7–19]. Because of the selection of ballistic photons by the OCT system in a round-trip configuration, any sample being studied is regarded as a linear retarder and/or as a linear diattenuator [20]. The polarimetric measurements are nonetheless useful in the biomedical field, even if only partial information on polarization can be delivered; for example, measurement of linear retardance alone is useful in the characterization of the thickness of the retinal nerve fiber layer [6] or in the assessment of burned tissue in dermatology [5,19].

Fiber-based implementations are useful in the OCT practice because of their robustness and reliability. The configuration presented here belongs to this category. Additionally, a single-camera design is employed for cost-efficiency and simplicity of adjustment. However, external factors (such as temperature and mechanical stress) affect the birefringence of single-mode fibers (SMFs) used in OCT systems, inducing disturbances [21] in the measured polarization.

One way of bypassing the issue of the SMF birefringence is to perform the polarization selection before the collecting fiber. Roth *et al.* [3] devised such a time-domain, fiber-based system using a liquid-crystal modulator in the sample arm to vary the polarization state of the light, probing the medium according to three polarization states generated sequentially. Fiber-based polarization controllers are present, but only to maximize signal amplitude. This approach, however, means that the input polarization state of the light is not circular, which has an impact on the signal-to-noise ratio (SNR) of the images corresponding to the different polarization state settings. Moreover, three measurements have to be performed.

Al-Qaisi *et al.* [4] reported on a time-domain, single-detector, fiber-based system in which the sample is illuminated by circularly polarized light. However, polarization-maintaining (PM) fibers and couplers have to be used, and orthogonal polarization states must be modulated to multiplex polarimetric information in one single detector reading.

SMFs can be employed in a spectral-domain system as in Cense *et al.* [22], where a Wollaston prism separates the two orthogonal polarization states and projects them onto different parts of the same linear detector array. This approach requires fine tuning of the polarization state of the light using fiber-based polarization controllers. In addition, projecting the two polarization components onto different parts of the same detector reduces the available number of camera pixels per polarization component, and, therefore, the spectrometer resolution (which impacts the OCT axial range).

0146-9592/15/163858-04$15/0$15.00

The configuration presented in this Letter operates in a spectral-domain system and performs the polarization selection before the collecting fiber. In opposition to [3], the sample is illuminated with circularly polarized light. Since the selection is performed before the collecting fiber, SM fibers and couplers can be used without the need to fine-tune the polarization state as in [22]. The configuration presented here requires two sequential acquisition steps, as detailed below.

The experimental setup is described schematically in Fig. 1. Light from a superluminescent diode (SLD, Superlum, central wavelength 830 nm, bandwidth 20 nm, output power ~10 mW) is split between the two arms of a Mach–Zehnder interferometer at the directional splitter S1, 20% of which is directed to the reference arm and 80% to the sample arm. In the sample arm (shaded region in Fig. 1), a liquid-crystal polarization rotator (LCR, Meadowlark LPR-100-800) is employed to rotate the returned field from the sample between two states, corresponding to no rotation and to a 90 deg rotation. Switching between these two states is driven by a TTL signal generated by the computer's DAQ card, shown in Fig. 1 as TTL1.

The two arms of the interferometer are recoupled at S2, and the resulting signal is then directed toward a custom-built spectrometer, composing a 1200 l/mm transmissive Wasatch Photonics diffraction grating, a Basler sprint line camera (set to 400 μs line acquisition time) and a National Instruments PCIe-1429 Camera Link frame grabber (with a TTL2 triggering the start of each frame). An in-line polarization controller (PC, Newport F-POL-IL) in the reference arm is used to maximize the interferometric signal.

After acquisition, the channeled spectra are resampled [23], an inverse Fourier Transform (FT) is performed, and the A-scans are bundled together to form a B-scan. The two TTL signals in Fig. 1 are in phase; therefore, a 1024 pixel wide B-scan contains two identically sized B-scan images corresponding to the two rotation states of the liquid-crystal LCR, r_0, and r_{90}. The pair of images is refreshed at 2.5 Hz.

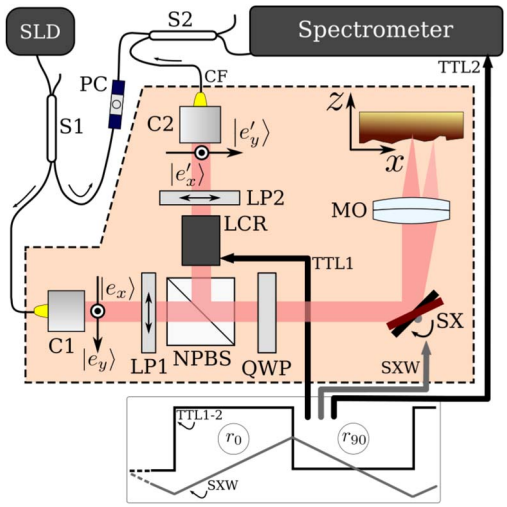

Fig. 1. Fiber-based PS-OCT system. C1-2, fiber collimators; PC, fiber-based polarization controller; LP1-2, dichroic linear polarizers; NPBS, nonpolarizing beam splitter; QWP, quarter-wave plate (oriented at 45 deg in respect to the polarization direction selected by LP1); SX, galvo-scanner; MO, microscope objective; CF, collecting fiber; LCR, liquid-crystal polarization rotator switching between states r_0 and r_{90}; SXW, line scanner triangular waveform, each period corresponding to the acquisition of two horizontally flipped images corresponding to the two states r_0 and r_{90}; TTL1-2, driving signals for the LCR switching and the spectrometer acquisition trigger, respectively.

The following theoretical model is based on a pure polarization rotator which can be implemented using the LCR as presented in this Letter, or an electro-optic modulator oriented at 45 deg in relation to the vector basis $\{|e'_x\rangle, |e'_y\rangle\}$ of Fig. 1. In the latter case, the state r_0 could correspond to an electro-optic retardance equal to 0 deg and the state r_{90} to a retardance equal to 180 deg (i.e., a half-wave plate). A realistic polarization rotator is nonideal and introduces errors in the measurement of the sample retardance; however, the system would still be insensitive to fiber disturbances as will be shown later.

After resampling, the intensity $I(\nu)$ versus the optical frequency ν at the spectrometer is given by

$$I(\nu) = I_{\mathrm{DC}}(\nu) + A_z e^{i\frac{2\pi}{c}\nu\cdot z} + A_z e^{-i\frac{2\pi}{c}\nu\cdot z}, \tag{1}$$

where A_z is the amplitude of the interference between the field returning from the sample measured at the collecting fiber CF output, and the field $|r_{\mathrm{out}}\rangle$ from the reference arm; c is the speed of light; and z is the depth of the medium measured from zero optical path difference (OPD = 0). The returning wave from the sample arm is $r(z)|S_{\mathrm{out}}(z)\rangle$, where $r(z)$ is the complex amplitude reflection coefficient for a scattering center located at depth z. By taking the FT of $I(\nu)$, we obtain the absolute value of A_z, given by

$$I_{\mathrm{interf}} = |A_z| \propto |\langle r_{\mathrm{out}}|S_{\mathrm{out}}(z)\rangle| \cdot |r(z)|, \tag{2}$$

where $\langle r_{\mathrm{out}}|S_{\mathrm{out}}(z)\rangle$ denotes the dot product between the complex conjugate of the field $|r_{\mathrm{out}}\rangle$ and the field $|S_{\mathrm{out}}(z)\rangle$, the latter containing both the retardance of the sample under analysis and the polarimetric response of the collecting fiber CF and coupler S2. Thus, decoupling these two contributions enables us to identify the polarimetric response of the sample independently from that of the fibers which vary greatly with environmental parameters.

In the sample arm, described within the shaded region in Fig. 1, linearly polarized light $|e_1\rangle = |e_y\rangle$ oriented parallel to the figure plane goes through the nonpolarizing beam splitter (NPBS). The polarization state is converted into circularly polarized light by means of a QWP oriented at 45 deg in relation to the axis of LP1. The beam is then laterally scanned with the galvo-scanner SX over the surface of the sample. Light returning from the sample goes through the QWP a second time. Before crossing the liquid-crystal rotator (LCR) [operating at 5 Hz], the field $|e_2\rangle$ contains the information of the retardance $\Phi(z)$ and the optical axis orientation $\theta(z)$ of the sample. This field can be expressed on a vector basis $\{|e'_x\rangle, |e'_y\rangle\}$ (see Fig. 1), defined as

$$|e_2\rangle = \cos\,\Phi(z)|e'_x\rangle + \sin\,\Phi(z)e^{2i\theta(z)}|e'_y\rangle. \tag{3}$$

The beam then passes through a linear polarizer LP2, oriented along $|e'_y\rangle$, with the resulting field $|S_{\mathrm{in}}(z)\rangle$ at the input of the collecting fiber. According to the rotation states, r_0 and r_{90} of the LCR, the field is written as follows:

$$|S_{\mathrm{in}}(z)\rangle = \begin{cases} \sin\,\Phi(z)e^{i[2\theta(z)+\varphi_{r0}]}|e'_y\rangle = |S_{\mathrm{in}}^{r0}(z)\rangle \\ \cos\,\Phi(z)e^{i\varphi_{r90}}|e'_y\rangle = |S_{\mathrm{in}}^{r90}(z)\rangle \end{cases}, \tag{4}$$

where φ_{r0} and φ_{r90} correspond to the additional phase introduced by the LCR in each of the states considered.

Because of the polarimetric response of the collecting fiber CF and coupler S2, $|S_{\text{in}}\rangle$ and $|e'_y\rangle$, respectively, are transformed into $|S_{\text{out}}\rangle$ and $|e_{\text{out}}\rangle$:

$$|S_{\text{out}}(z)\rangle = \begin{cases} \sin\Phi(z)e^{i[2\theta(z)+\varphi_{r0}]}|e_{\text{out}}\rangle = |S^{r0}_{\text{out}}(z)\rangle \\ \cos\Phi(z)e^{i\varphi_{r90}}|e_{\text{out}}\rangle = |S^{r90}_{\text{out}}(z)\rangle \end{cases}. \quad (5)$$

Following Eq. (2), the interferometric component can then be written as

$$I_{\text{interf}} = \begin{cases} |\sin\Phi(z)||\langle r_{\text{out}}|e_{\text{out}}\rangle r(z)| = I^{r0} \\ |\cos\Phi(z)||\langle r_{\text{out}}|e_{\text{out}}\rangle r(z)| = I^{r90}. \end{cases} \quad (6)$$

The absolute value of the retardance measurement in the medium, $|\Phi|$, is given by

$$|\Phi| = \arctan\left[\frac{I^{r0}}{I^{r90}}\right]. \quad (7)$$

In practice, the chromatic behavior of fibers must be taken into account by considering that $|r_{\text{out}}\rangle$ and $|S_{\text{out}}\rangle$ are dependent on ν. Eq. (6) thus becomes

$$I_{\text{interf}} = \begin{cases} |\sin\Phi(z)||\int\langle r_{\text{out}}(\nu)|e_{\text{out}}(\nu)\rangle r(z)\mathrm{d}\nu| = I^{r0} \\ |\cos\Phi(z)||\int\langle r_{\text{out}}(\nu)|e_{\text{out}}(\nu)\rangle r(z)\mathrm{d}\nu| = I^{r90}, \end{cases} \quad (8)$$

where $|\int\langle r_{\text{out}}(\nu)|e_{\text{out}}(\nu)\rangle\mathrm{d}\nu|$ yields the value of the FT corresponding to a single layer at depth z, as described in [24]. Using the two terms in Eq. (8), the ratio I^{r0}/I^{r90} becomes insensitive to the effects of either fibers or couplers (induced by their birefringence, diattenuation, and chromatic influence). The system exhibits tolerance to fiber disturbances, regardless of the rotator's imperfections.

To validate the system, a comparison of two sets of measured retardances $|\Phi|$ (represented as circles and crosses) with a calibrated reference was performed (Fig. 2). This was achieved with a Berek compensator (Newport model 5540), placed in the sample arm, between the QWP and the galvo-scanner SX (kept stationary). The Berek compensator provides a variable reference retardance through the variation of its indicator setting J. Between the two data sets, the Berek compensator was rotated by 45 deg. Some discrepancies are observed between the theoretical curve and the two experimental curves, which may be because of the fact that the LCR is not a pure

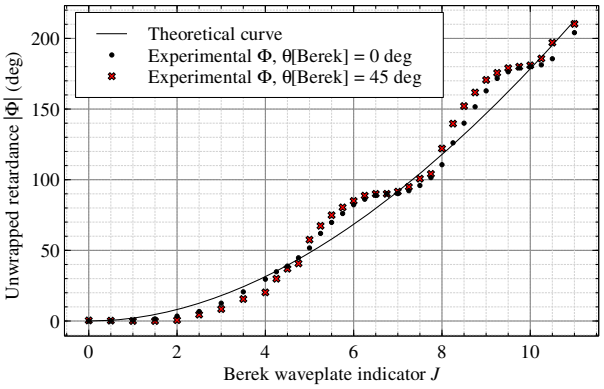

Fig. 2. Retardance measurements created by a Berek compensator in the sample arm versus the indicator, J, which is proportional to the retardance introduced by the compensator. Between the two experimental data sets (shown as black circles and red crosses), the Berek compensator was rotated by 45 deg around the propagating axis.

rotator at the central wavelength $\lambda_0 = 830$ nm of the SLD. This induces systematic errors for the retardance measurement which depend slightly on the axis orientation of the sample. PS-OCT imaging was then carried out on a plastic phantom which exhibited strong birefringence. In Fig. 3, the B(A)-scans corresponding to the two LCR rotation states (r_0 and r_{90}) are represented, as well as the corresponding calculated retardance maps $|\Phi|$.

To demonstrate the insensitivity of the system to the perturbations caused by the collecting fiber, two sets of images were generated (Cases 1 and 2). Between them, the polarization controller PC on the reference arm was adjusted to mimic such perturbations. Case 1 is represented in sub-Figs. 3(a)–3(c), with frame I_1^{r0} depicting the 2-D map for the state r_0, I_1^{r90} the 2-D map of r_{90}, and Φ_1 the net retardance map $|\Phi|$ resulting from the ratio I^{r0}/I^{r90} [Eq. (7)]. In the same way, sub-Figs. 3(d)–3(f) correspond to the same frames in Case 2. The lateral size in all images is 3.5 mm, and the usable range in depth is ~1.6 mm.

One issue that arises when calculating $|\Phi|$ with the method presented is that the regions of no signal (caused by either $r(z) \sim 0$ or $\langle r_{\text{out}}|e_{\text{out}}\rangle \sim 0$) in the analyzed images lead to erroneous values of $|\Phi|$ in the range of 0 to $\pi/2$. These are prevented by introducing a threshold before the calculations are carried out. The pixels whose values lie under the threshold are not taken into consideration and are set to zero in the final retardance map.

It is clear from comparing the two pairs of 2-D maps (I_1^{r0} versus I_2^{r0} and I_1^{r90} versus I_2^{r90}) that the maps corresponding to Case 2 have a different contrast from those of Case 1, as a result of the polarization disturbances which introduce a mismatch between the polarization states of the two arms of the

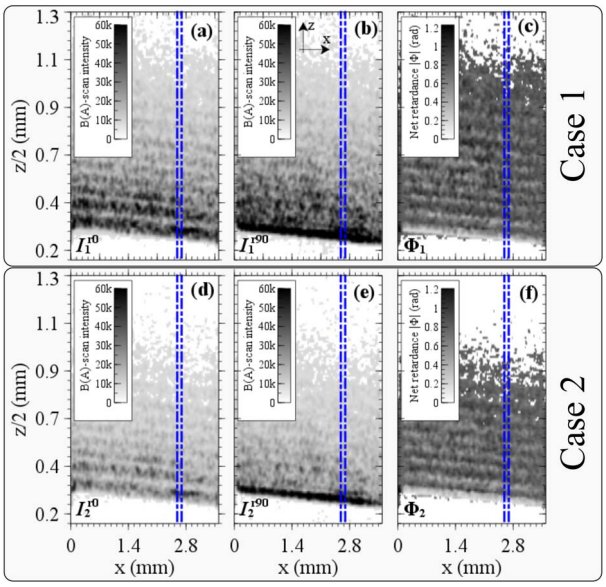

Fig. 3. B(A)-scans of a plastic phantom exhibiting birefringence. Between the top (Case 1) and bottom rows (Case 2), the PC settings in the reference arm were adjusted in terms of both pressure on the fiber and rotation to create different fiber-induced polarization states and simulate polarization disturbances. (a), (b), (d), and (e) correspond to the OCT B(A)-scans of the two rotation states; (c) and (f) depict the retardance maps for the two cases considered. The dashed region corresponds to the averaged A-scans represented in Fig. 4.

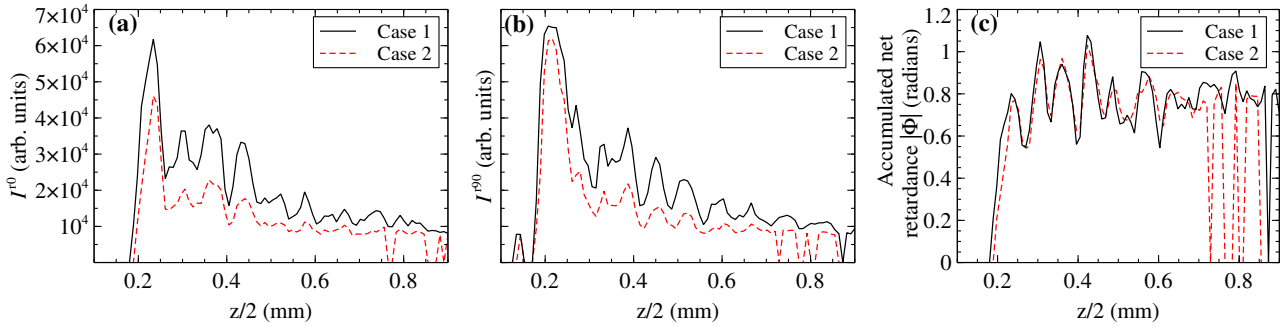

Fig. 4. A-scan comparison for the two cases considered taken within the dashed regions depicted in Fig. 3. (a), (b) A-scan for the two orthogonal polarization states (I_i^{r0}, continuous line; and I_i^{r90}, dashed line, for $i = 1, 2$). (c) Accumulated polarization retardance for the two cases. Some artifacts in the dashed traces (corresponding to I_i^{r90}) can be observed at larger depths, which are created because of the threshold level (set at 7000 arbitrary units in the B-scan pixels) being close to the noise level.

interferometer, lowering the interferometric modulation. Even so, the resulting retardance maps Φ_1 and Φ_2 [sub-Figs. 3(c) and 3(f)] show similar levels of birefringence, despite the perturbation introduced by the fiber. This is further verified in Fig. 4, where A-scans along $x \sim 2.6$ mm are represented for all six frames in Fig. 3, after some lateral averaging has been carried out within the area between the dashed lines. The white areas in the images refer to regions eliminated by the application of the same threshold to all images however, because of the variation of the SNR in I_i^{r0} and I_i^{r90} $(i = 1, 2)$ and the dot product $\langle r_{\text{out}}|e_{\text{out}}\rangle$, their extension in depth is different.

In conclusion, to measure solely the net retardance, a polarization-sensitive spectral-domain OCT system using a broadband source and a spectrometer has been demonstrated. The system is insensitive to the fiber-induced birefringence and does not require compensation methods. The sample is illuminated with circularly polarized light, which improves the efficiency of the retardance measurements in the case of a linear retarder. Because of its single-detector architecture, this system requires two measurements to be performed sequentially, while securing in this way the axial range allowed by the entire detector array during each measurement. For this proof of concept, a liquid-crystal device was employed as a polarization rotator, with some limitations in terms of acquisition speed and systematic errors in the retardance measurements. To improve the speed, an electro-optic modulator seems better suited. Such modulators can achieve response times shorter than liquid crystals; here a response time of less than 100 μs would suffice to cope with frame refresh periods of ms. Even more, a response time of less than 1 μs can allow switching between A-scans (considering a camera in the spectrometer operating at 100 kHz). In these examples, a switching time 10 times shorter than the acquisition time was considered. Such a strategy would also minimize motion artifacts between the two rotation states. Finally, the sample arm design can be improved in terms of optical power by changing the splitting ratio of the beam splitter from a 50/50 to a 90/10, ensuring that a large amount of reflected power from the sample is directed to the spectrometer.

Funding. European Research Council (ERC) (249889); Marie-Curie Intra-European Fellowship for Career Development (625509); NIHR Biomedical Research Center; UCL Institute of Ophthalmology; University of Kent.

REFERENCES

1. W. Drexler, M. Liu, A. Kumar, T. Kamali, A. Unterhuber, and R. A. Leitgeb, J. Biomed. Opt. **19**, 71412 (2014).
2. M. R. Hee, D. Huang, E. A. Swanson, and J. G. Fujimoto, J. Opt. Soc. Am. B **9**, 903 (1992).
3. J. E. Roth, J. A. Kozak, S. Yazdanfar, A. M. Rollins, and J. A. Izatt, Opt. Lett. **26**, 1069 (2001).
4. M. K. Al-Qaisi and T. Akkin, Opt. Express **16**, 13032 (2008).
5. M. Zurauskas and A. Podoleanu, J. Biomed. Opt. **18**, 106010 (2013).
6. R. G. Cucu, A. Gh. Podoleanu, R. B. Rosen, A. B. Boxer, and D. A. Jackson, Proc. SPIE **5140**, 113 (2003).
7. B. Park, M. C. Pierce, B. Cense, S.-H. Yun, M. Mujat, G. Tearney, B. Bouma, and J. de Boer, Opt. Express **13**, 3931 (2005).
8. M. Yamanari, S. Makita, V. D. Madjarova, T. Yatagai, and Y. Yasuno, Opt. Express **14**, 6502 (2006).
9. E. Götzinger, B. Baumann, M. Pircher, and C. K. Hitzenberger, Opt. Express **17**, 22704 (2009).
10. B. Braaf, K. A. Vermeer, M. de Groot, K. V. Vienola, and J. F. de Boer, Biomed. Opt. Express **5**, 2736 (2014).
11. Y. Yasuno, S. Makita, T. Endo, M. Itoh, T. Yatagai, M. Takahashi, C. Katada, and M. Mutoh, Appl. Phys. Lett. **85**, 3023 (2004).
12. B. Baumann, E. Götzinger, M. Pircher, and C. K. Hitzenberger, Opt. Express **15**, 1054 (2007).
13. Z. Wang, H.-C. Lee, O. O. Ahsen, B. Lee, W. Choi, B. Potsaid, J. Liu, V. Jayaraman, A. Cable, M. F. Kraus, K. Liang, J. Hornegger, and J. G. Fujimoto, Biomed. Opt. Express **5**, 2931 (2014).
14. M. Zhao and J. A. Izatt, Opt. Lett. **34**, 205 (2009).
15. C. Fan, Y. Wang, and R. K. Wang, Opt. Express **15**, 7950 (2007).
16. W. Trasischker, S. Zotter, T. Torzicky, B. Baumann, R. Haindl, M. Pircher, and C. K. Hitzenberger, Biomed. Opt. Express **5**, 2798 (2014).
17. N. Lippok, M. Villiger, C. Jun, and B. E. Bouma, Opt. Lett. **40**, 2025 (2015).
18. Z. Ding, C.-P. Liang, Q. Tang, and Y. Chen, Biomed. Opt. Express **6**, 1828 (2015).
19. K. H. Kim, M. C. Pierce, G. Maguluri, B. H. Park, S. J. Yoon, M. Lydon, R. Sheridan, and J. F. de Boer, J. Biomed. Opt. **17**, 066012 (2012).
20. B. Park and J. de Boer, in *Optical Coherence Tomography—Technology and Applications, Biological and Medical Physics*, J. G. Fujimoto and W. Drexler, eds. (Springer, 2008), pp. 653–695.
21. S. C. Rashleigh, Opt. Lett. **5**, 392 (1980).
22. B. Cense, M. Mujat, T. C. Chen, B. H. Park, and J. F. de Boer, Opt. Express **15**, 2421 (2007).
23. Y. Yasuno, V. D. Madjarova, S. Makita, M. Akiba, A. Morosawa, C. Chong, T. Sakai, K.-P. Chan, M. Itoh, and T. Yatagai, Opt. Express **13**, 10652 (2005).
24. J. F. de Boer, S. M. Srinivas, J. S. Nelson, T. E. Milner, and M. G. Ducros, in *Handbook of Optical Coherence Tomography*, B. E. Bouma and G. J. Tearney, eds. (Marcel Dekker, 2002), pp. 237–274.

Optics Letters

Two-grating Talbot bands spectral-domain interferometer

MANUEL J. MARQUES,* ADRIAN BRADU, AND ADRIAN PODOLEANU

Applied Optics Group, School of Physical Sciences, University of Kent, Canterbury CT2 7NH, UK
**Corresponding author: mjmm2@kent.ac.uk*

Received 6 May 2015; revised 29 July 2015; accepted 30 July 2015; posted 3 August 2015 (Doc. ID 244202); published 21 August 2015

A configuration for Talbot bands is presented in which two tilted gratings replace the splitter normally used for recombining the signals from the two interferometer arms. The two optical beams from the interferometer are launched by two fiber leads tightly brought together in the front focal plane of a collimating lens. As the tips of the two fibers are slightly off-axis, the emergent beams after the collimating lens are not parallel. In combination with the two tilted gratings, the nonparallel launching of the two beams leads to a total elimination of mirror terms even when the two beams overlap on either grating. The effects of several geometrical parameters on the visibility performance versus optical path difference between the two arm lengths of the interferometer are evaluated.

OCIS codes: (120.6200) Spectrometers and spectroscopic instrumentation; (120.3180) Interferometry; (050.0050) Diffraction and gratings; (060.1810) Buffers, couplers, routers, switches, and multiplexers; (120.0120) Instrumentation, measurement, and metrology.

http://dx.doi.org/10.1364/OL.40.004014

Talbot bands (TB) [1–4] represent a particular case of modulation of the channeled spectrum at the output of an interferometer illuminated by a broadband optical source. This modulation takes place for only one sign of the optical path difference (OPD) in the interferometer. In other words, a TB configuration can determine which optical path of the two interfering beams is longer or shorter than the other one. In optical-coherence-tomography (OCT) applications, the inability to make a distinction between the two signs of the OPD leads to superposition of cross-section images due to the positive and the negative OPD. This is known as the problem of mirror terms [2,5]. Several mirror term-removal methods have been described in the literature, such as sequential phase-shifting interferometry [6], phase shifting using a 3 × 3 splitter [7], resorting to phase modulation [8], or dispersion [9] to restore the full range and address the ambiguity of the OPD sign. These methods, however, require several images or steps in order to attenuate the mirror terms [10]. A TB configuration only requires a single spectral acquisition and no post-processing.

Previous studies of Talbot bands [2] have shown that the difference between conventional spectral-domain interferometry (SDI) configurations and TB configurations lies in the order that the two operations, interference and diffraction, are performed. In conventional SDI, the beams from the object and reference arms are first superposed, with the result being then sent to a spectrometer, i.e., interference is followed by diffraction on a grating or dispersion in a prism [11]. In these configurations, positive and negative OPD values of the same OPD modulus produce the same channeled spectrum modulation, i.e., such configuration cannot distinguish between positive and negative OPD values, as shown by the symmetric curve C_1 in Fig. 1. In a TB configuration, the two beams interfere on the line camera used in the spectrometer after the diffraction operation has been carried out. In all previous reports on TB configurations, the two beams from the interferometer are collimated and are sent parallel to each other to a single diffraction grating. Let us consider a gap, g, between the centers of the two beams, each of them determining a footprint with a beam diameter S on the grating. A TB configuration can be switched to a non-TB configuration by controlling the gap g. As long as g is at least equal to S, TB behavior is obtained, as depicted by the curve C_3 in Fig. 1. If however the beams are separated by less than S, the overlapping parts of the two beams exhibit interference first and diffraction after. These overlapping parts determine modulation of the channeled spectrum that is

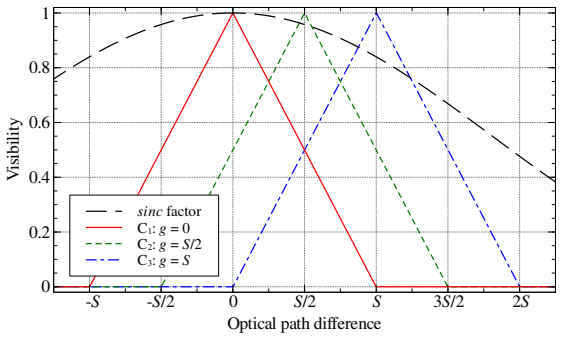

Fig. 1. Qualitative illustration of SDI intensity versus OPD in a setup consisting of an interferometer and a single grating. The curves C_2 – C_3 represent the correlation of power distribution within the two footprints of the incident beams on a single grating for different values of the spatial gap g between the beam centers [12]. The footprints are considered as top hats with widths $S = 4$ mm. The wider profile above (black dashed) is determined by the sinc factor [13].

independent on the OPD sign, i.e., mirror terms are reinstated, as shown by the curve C_2 in Fig. 1 for $g = S/2$. All the curves represented in Fig. 1 are simulation results from a spectrometer with a single diffraction grating where the beams projected onto it have a varying gap g between them.

Previous reports on Talbot bands [2,10] developed the explanation of the visibility curve versus OPD as determined by the product of C (shown in Fig. 1 for three values of gap g) with a sinc factor. The factor C, as detailed in [12] and further documented below, incorporates the properties of Talbot bands, while the sinc factor includes the spectrometer resolution determined by the optical bandwidth of light on each pixels of the line camera in the spectrometer [13].

A Mach–Zehnder (MZ) configuration may be employed for SDI if modulators are to be used in its arms [14]. In addition, in a TB-based system such as those reported in [10,12,15,16], a MZ configuration must be used in order to ensure a spatial separation between the footprints of the two beams on the diffraction grating or prism. In both cases, a splitter or a combination of splitters are employed to direct the output of the two arms of the interferometer toward the spectrometer.

We present here a configuration where such splitter is replaced by a pair of tilted diffraction gratings, illuminated by the two beams to be interfered at an angle. Such a configuration achieves two goals: (i) performs superposition of the two beams after their diffraction, in line with the TB procedure mentioned above and (ii) prevents the possibility to interfere for any part of the two beams that may fall on the same grating, securing no mirror terms even when some parts of the beams overlap. This means that a behavior as shown by the curve C_3 in Fig. 1 (visibility restricted to a single OPD sign) is always obtained, irrespective of the gap between the two beams.

As shown in Fig. 2, a MZ interferometer is implemented, employing two directional couplers: S1 splits the optical power between the two arms, object and reference, and S2, which diverts and collects light from the object via lens L3. In the reference arm, lenses L1 and L2 are used to route a collimating beam via two mirrors, M1 and M2 placed on a translation stage, TS, used to adjust the reference path length and thus vary the channeled spectrum-modulation frequency, enabling the study of the visibility profile of the spectrometer for different OPD values. Lens L2 focuses light into a single-mode fiber, SMFR, whose end is placed in a groove with the fiber end from the object arm, brought from S2 via SMFO. The two single-mode fibers (SMF) are closely laid together inside the groove, with their plastic buffers removed to minimize the distance between their tips. The two fiber ends are placed in the focal plane of lens L4. Each beam travels to a diffraction grating wherefrom the diffracted fan of rays is made convergent for each individual spectral component on a line camera CMOS, via a lens L5.

Due to the gap δ between the two SMF apertures, the two beams intersect at a distance f_4 from the lens L4, corresponding to the back focal plane of the lens L4. Because the directions of the two beams are divergent, if a single grating was used, rays of the same wavelength in the two beams would not superpose on the same pixel of the line camera. Therefore, a separate grating (DG1,2) is used for each beam. By tilting the two gratings in relation to each other, rays of the same wavelength are superposed on the line camera, implementing in this way the second operation, interference, after the first operation, diffraction. Therefore, each of the two diffraction gratings is mounted on an individual rotation stage. By rotating these stages, the diffracted rays of similar wavelength are made parallel in their way toward the spectrometer lens, L5. Let us consider the angle θ between the two collimated beams emerging from L4, as depicted in the diagram in Fig. 2. Following a trigonometric analysis, such angle can be approximated by $\tan\theta \approx \delta/(2f_4)$, and given that $f_4 \gg \delta$ we have $\theta \ll 1$. The correction required for the angle between the two gratings is less than 1 deg, therefore it cannot be visible in the sketch.

Further on from the back focal plane of L4, the beam directions will diverge, and the distance between their centers will scale with the distance L_{grat} between L4 and the pair of diffraction gratings DG1-2.

In order to employ the theory developed in [10,17], an equivalent gap g is inferred from the present configuration and extrapolated to the case of a conventional TB configuration using parallel beams incident on a single DG. It can be shown that at the grating level, the gap g between the two beams is approximately given by

$$g = \frac{1}{\cos\alpha}\frac{\delta}{2f_4}(L_{\text{grat}} - f_4), \tag{1}$$

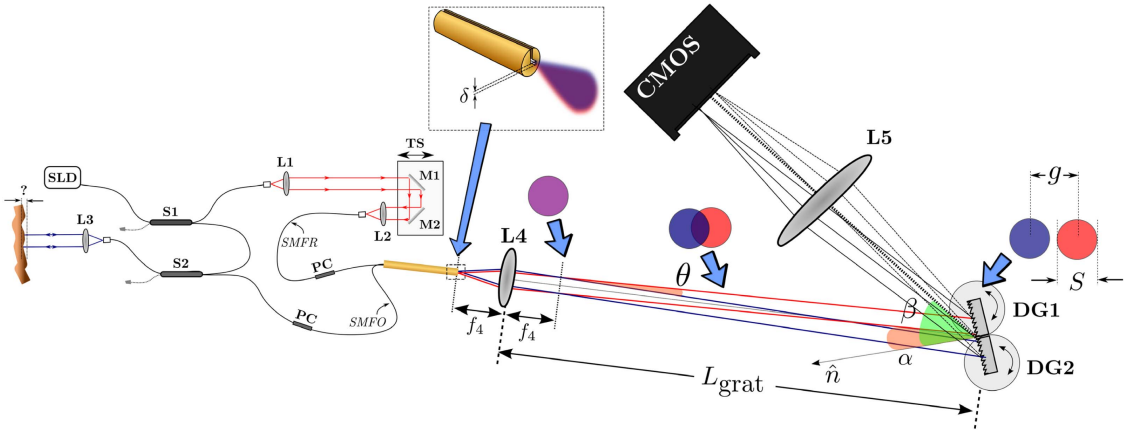

Fig. 2. Experimental setup. SLD, superluminiscent diode (Superlum SLD-381-HP1-DIL-SM-PD, $\lambda_0 = 831.1$ nm, $\Delta\lambda = 16$ nm, ~10 mW output power); S1-2, fiber-based directional couplers; L1-5, achromatic lenses; TS, translation stage; M1-2, flat silver mirrors; PC, fiber-based polarization controllers; DG1-2, ruled diffraction gratings operating in reflection (Thorlabs GR25-1210, 1200 l/mm at 1 μm); CMOS, line camera pixel array (Basler sprint spl-140 km, 140 klines/s). Inset, the two output fibers (SMFR and SMFO) aligned inside the groove.

where α is the angle between the axis of the lens L4 and the normal $\hat{n}$ to the grating surface.

Moreover, the number of grating lines illuminated by each beam determines the width of the C profile versus OPD, as described in [12,15]. This can be adjusted by varying the focal length f_4 of the lens L4.

From one grating groove to the next, the delay between the diffracted rays in the first order of diffraction amounts to λ_0 [2]. The equivalent number of grating grooves within the gap is given by $N = g/a$, where a is the grating groove periodicity. Therefore, according to the Talbot band theory [2], the profile of modulation contrast versus OPD, C, is shifted by $N\lambda_0$. The OPD value where C exhibits a maximum, $\mathrm{OPD}_{\max}$, is shifted from OPD = 0 by the same amount [10]:

$$\mathrm{OPD}_{\max} = \frac{g}{a}\lambda_0. \tag{2}$$

Given the wavelength used, $\lambda_0 = 831$ nm, and the grating groove periodicity of $a \sim 0.833$ μm, $\lambda_0/a = 0.831/0.833 \approx 1$, so $\mathrm{OPD}_{\max} \sim g$. Hence, by controlling the size of the gap g through manipulation of both L_{grat} and f_4, it is possible to achieve the same functionality as that previously reported [10,15,16], where a beam-splitter was used to direct the two spatially separated parallel beams onto the diffraction grating.

In order to characterize the visibility curves C of the system, several sets of measurements relating the channeled spectrum modulation to the OPD in the interferometer were carried out for different values of the gap g. These measurements were performed by recording the amplitude of the channeled spectrum modulation (obtained from the Fourier transform of the resampled spectrum) for several OPD values, which were varied in 20 μm increments using the TS. Different values of g were achieved by varying geometrical parameters of the spectrometer, namely the length L_{grat} between the collimating lens L4 and the pair of diffraction gratings DG1-2, and also the focal length f_4 of the lens L4. Such changes allow g to be adjusted in the range of 1 to several mm; however, an exact measure of it is difficult because the edges of the two diffraction gratings are contributing to the error in its determination. Estimation of the gap values are obtained by fitting curves obtained by theory to the experimental data [18]. The code we used, which was also employed to produce the curves C_1 – C_3 in Fig. 1, performed a cross-correlation of the beam profiles from the two arms of the interferometer, whose result was multiplied by the sinc factor adjusted to the spectrometer's sampling resolution. In practice, the beam profiles are not top hats, as considered for simplicity in Fig. 1, but Gaussian, therefore the simulation used Gaussian profiles.

According to Eq. (1), the larger the length L_{grat}, the larger the gap g between the two spots (measured in an equivalent Talbot band spectrometer using a single grating). In turn, the larger the gap g, the larger the intrinsic delay between the two diffracted waves, leading to a shift of the C profile along the OPD axis, as mentioned earlier. On the other hand, modifying f_4 changes both $\mathrm{OPD}_{\max}$ through g (given that $g \propto 1/f_4$) and the width of the C profile, given that the number of illuminated grating lines depends on the size of the footprint of the beam illuminating the grating, as described in [2,12].

In the first set of measurements, only the gap g was modified by opting for two L_{grat} values separated by approximately 40 cm, accomplished by moving the group comprising the pair of diffraction gratings DG1-2, the CMOS camera, and the lens L5 together along a direction given by the axis of L4. The results obtained are shown in Fig. 3. Considering the focal length of L4, $f_4 = 30$ mm and the projection angle $\alpha \sim 18$ degrees, the spot diameter of each beam on each grating is approximately $S \sim 2$ mm. Employing for simplicity, as in Fig. 1, a top hat power distribution within the footprint of each beam on the diffraction grating [2], the number of illuminated grating lines in each beam is $N = S/a = 2,400$. Cross-correlation of the two top hats, each of width $N\lambda_0$, leads to a triangular-shaped C profile (as shown in Fig. 1) covering a $2N\lambda_0$ base of ~4 mm. As expected, when considering more real Gaussian footprints, the effective C width is smaller than $2N\lambda_0$, as shown by the –10-dB width (3 mm) of the simulated profiles in solid line overlaid on the experimental data in Fig. 3.

The second graph in Fig. 3 corresponds to a larger distance L_{grat} which determines a gap g larger than the beam diameter S. This experiment shows that due to a larger gap g, the C profile moves to larger OPD values, as expected [10]. The shift on the visibility profile C toward larger OPD values presents the disadvantage of a decrease in visibility due to the spectrometer resolution (smaller values of the *sinc* factor as seen in Fig. 1).

The gap settings for the theoretical simulations were adjusted to fit the experimental curves, with a value of 3.3 mm for the $L_{\mathrm{grat}} = 112$ cm case and a value of 5.3 mm for the $L_{\mathrm{grat}} = 153$ cm case. Both experimental and theoretical data sets are normalized to the peak visibility of their respective data set. The $L_{\mathrm{grat}} = 153$ cm experimental data set has a peak value ~1 dB lower than the corresponding simulation data, which may be due to an imperfect alignment of the spectrometer after being reassembled following the change in L_{grat}.

A second set of experiments refer to the effect of the focal length f_4 of lens L4 on the visibility profile versus OPD. Figure 4 illustrates the visibility decay with OPD for two f_4 values, using $L_{\mathrm{grat}} = 153$ cm. The profile corresponding to $f_4 = 50$ mm displays a slight shift toward OPD = 0. Given that the gap is inversely proportional to f_4, a larger focal length yields a smaller gap g between the beams. However, increasing f_4 demands a proportionally larger L_{grat} value in order to achieve complete separation of the two beams. Furthermore, not achieving complete separation of the beams would lead to some parts of the two beams being diffracted by both gratings. These parts do not interfere, as commented above, reducing the overall interferometer performance.

The gap setting supplied to the simulations for $f_4 = 50$ mm is $g = 5.2$ mm. Due to implementation challenges, it proved

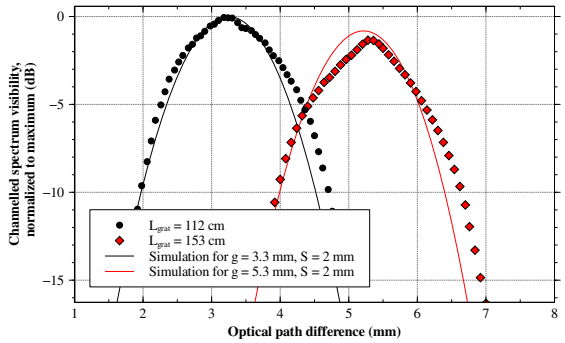

Fig. 3. Visibility profile versus OPD for the configuration in Fig. 1 with $f_4 = 30$ mm, for two values of L_{grat} (112 cm, black circles and 153 cm, red diamonds, corresponding to a g value of ~3.25 mm and ~5.25 mm, respectively).

difficult to ensure that the beam centers remained in the same relative positions during the spatial adjustments of the components. In addition, the effective areas of the diffraction gratings do not extend up to their support edges, and this contributes to the gap between the two beams. All these aspects make it difficult to accurately measure the gap g experimentally.

The beam diameter assumed $S = 3$ mm matches the experimental data, yielding a visibility profile width (FHWM) of around 2 mm. The peak location shifts toward smaller OPD values by ~0.4 mm, as shown in Fig. 4.

In conclusion, a novel Talbot band configuration is proposed, where the launching of the two beams from the object and reference arms uses a single lens, and where the splitter before the spectrometer is eliminated by using two tilted diffraction gratings. The two tilted gratings perform two functions: (i) allow superposition of the two diffracted beams on the line camera and (ii) due to their tilt, overlapped parts of the beams incident on each grating do not contribute to interference, leading to total elimination of the mirror terms. The adjustment of the relative tilt of the gratings is not more difficult than the alignment demanded by the beam-splitter conventionally used in front of the spectrometer in previous reports [10,15,16].

Elimination of the final splitter also brings advantages in terms of power efficiency, as all the optical power arriving at the diffraction gratings from both beams can be directed toward the detector array. In a conventional system with a splitter up to 50% of the incident, power is lost to the unused port of the splitter. Moreover, since both beams encounter optical elements with similar properties, this setup may present an extra advantage when handling large bandwidth signals as the splitting ratio of splitters depends on wavelength. Also, the eventual polarization disturbances introduced by the splitter are avoided.

From previous studies of Talbot band configurations [12,10], it is known that a smaller gap is desired to shift the visibility curve closer to OPD = 0 (Fig. 1, curve C_2). It is also known that if a larger axial range is desired, then C needs to be widened, which can be achieved by increasing f_4. However, this may lead to some overlap of the two beams before each grating, which is associated with the fact that the two beams are diverging from each other means that the optical power diffracted in the overlapped region will not contribute to the interference. This is not due to the TB configuration, but simply to the fact that rays of similar wavelength in the two beams are not diffracted along parallel directions due to the initial angle between the beams before diffraction. This particularity of the system effectively impedes mirror terms from arising at all, hence it is not possible to observe a behavior similar to that of curves C_1 and C_2 in Fig. 1. In addition, the SNR is also reduced since the optical power available for interference is lower than that if the full beam footprint was illuminating a single grating.

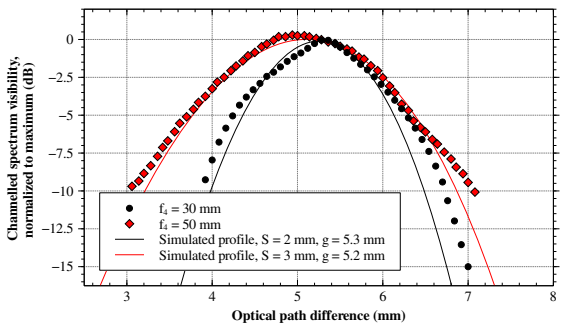

Fig. 4. Visibility profile versus OPD for the configuration with $L_{grat} = 153$ cm, for two values (black circles: $f_4 = 30$ nm, red diamonds: $f_4 = 50$ mm). Both experimental and theoretical data sets have been normalized to the peak value for the profile closer to OPD = 0.

A compromise has to be made in respect to the size of the gap between the two beams. It is known from previous reports on Talbot bands that the shift of the visibility profile versus OPD toward larger OPD values, typical for TB operation, leads to a lower visibility due to the factor C being moved to OPD values where the sinc factor is lower. Therefore, the gain in efficiency due to elimination of the final splitter somewhat compensates this reduction in visibility.

In order to ensure complete separation between the two beams just before the gratings, L_{grat} needs to be large (over 1 m). Assuming complete beam separation, from Eq. (1) and using the identity $\tan\theta \sim \frac{\delta}{2f_4} \sim \frac{g}{L_{grat}}$ we can write L_{grat} as

$$L_{grat} = f_4(1 + 2\delta^{-1}\cos\alpha). \quad (3)$$

To reduce L_{grat}, one can either reduce f_4 or increase δ. The former determines the size of the footprint on each grating, which then determines the number of grating lines illuminated and ultimately the width of the profile C and thus the axial range; the latter can be increased by separating the fibers in the launcher. There is a limit to this increase, since the larger the value of δ, the larger the aberrations via lens L4 due to the beams originating from off-axis-placed cores.

Funding. European Research Council (ERC) (249889); Moorfields Eye Hospital NHS Foundation Trust; UCL Institute of Ophthalmology; University of Kent.

REFERENCES

1. H. F. Talbot, Philos. Mag. **10**(62), 364 (1837).
2. A. G. Podoleanu, Opt. Express **15**, 9867 (2007).
3. Z. Benko, M. Hilbert, and Z. Bor, Am. J. Phys. **68**, 513 (2000).
4. A. L. King, Am. J. Phys. **39**, 1195 (1971).
5. B. Baumann, M. Pircher, E. Götzinger, and C. K. Hitzenberger, Opt. Express **15**, 13375 (2007).
6. E. Götzinger, M. Pircher, R. Leitgeb, and C. Hitzenberger, Opt. Express **13**, 583 (2005).
7. M. V. Sarunic, M. A. Choma, C. H. Yang, and J. A. Izatt, Opt. Express **13**, 957 (2005).
8. J. Zhang, J. S. Nelson, and Z. Chen, Opt. Lett. **30**, 147 (2005).
9. H. Bernd, B. Považay, A. Unterhuber, L. Wang, B. Hermann, S. Rey, G. Matz, and W. Drexler, Opt. Express **18**, 4898 (2010).
10. A. Bradu and A. G. Podoleanu, J. Biomed. Opt. **16**, 76010 (2011).
11. M. Wojtkowski, R. Leitgeb, A. Kowalczyk, T. Bajraszewski, and A. F. Fercher, J. Biomed. Opt. **7**, 457 (2002).
12. D. Woods and A. G. Podoleanu, Opt. Express **16**, 9654 (2008).
13. Z. Hu, Y. Pan, and A. M. Rollins, Appl. Opt. **46**, 8499 (2007).
14. M. E. Brezinski, *Optical Coherence Tomography: Principles and Applications* (Academic, 2006), p. 151.
15. P. Bouchal, A. Bradu, and A. G. Podoleanu, Opt. Express **20**, 5368 (2012).
16. M. J. Marques, A. Bradu, and A. G. Podoleanu, Biomed. Opt. Express **5**, 1428 (2014).
17. M. Hughes, D. Woods, and A. G. Podoleanu, Electron. Lett. **45**, 182 (2009).
18. M. Hughes, "Optical coherence tomography for art conservation and archaeology: methods and applications," Ph.D. thesis (University of Kent, 2010). Online: http://goo.gl/UCrdem

Biomedical Optics EXPRESS

Towards simultaneous Talbot bands based optical coherence tomography and scanning laser ophthalmoscopy imaging

Manuel J. Marques,* Adrian Bradu, and Adrian Gh. Podoleanu

Applied Optics Group, School of Physical Sciences, University of Kent Canterbury CT2 7NH, UK

*mjmm2@kent.ac.uk

Abstract: We report a Talbot bands-based optical coherence tomography (OCT) system capable of producing longitudinal B-scan OCT images and *en-face* scanning laser ophthalmoscopy (SLO) images of the human retina *in-vivo*. The OCT channel employs a broadband optical source and a spectrometer. A gap is created between the sample and reference beams while on their way towards the spectrometer's dispersive element to create Talbot bands. The spatial separation of the two beams facilitates collection by an SLO channel of optical power originating exclusively from the retina, deprived from any contribution from the reference beam. Three different modes of operation are presented, constrained by the minimum integration time of the camera used in the spectrometer and by the galvo-scanners' scanning rate: (i) a simultaneous acquisition mode over the two channels, useful for small size imaging, that conserves the pixel-to-pixel correspondence between them; (ii) a hybrid sequential mode, where the system switches itself between the two regimes and (iii) a sequential "on-demand" mode, where the system can be used in either OCT or SLO regimes for as long as required. The two sequential modes present varying degrees of trade-off between pixel-to-pixel correspondence and independent full control of parameters within each channel. Images of the optic nerve and fovea regions obtained in the simultaneous (i) and in the hybrid sequential mode (ii) are presented.

OCIS codes: (110.4500) Optical coherence tomography; (120.3890) Medical optics instrumentation; (110.0180) Microscopy; (110.4190) Multiple imaging; (170.4460) Ophthalmic optics and devices; (170.1790) Confocal microscopy.

References and links

1. T. Mitsui, "Dynamic Range of Optical Reflectometry with Spectral Interferometry," Jpn. J. Appl. Phys. **38**, 6133–6137 (1999).
2. M. Choma, M. Sarunic, C. Yang, and J. Izatt, "Sensitivity advantage of swept source and Fourier domain optical coherence tomography." Opt. Express **11**, 2183–2189 (2003).
3. M. Wojtkowski, R. Leitgeb, A. Kowalczyk, T. Bajraszewski, and A. F. Fercher, "In vivo human retinal imaging by Fourier domain optical coherence tomography." J. Biomed. Opt. **7**, 457–463 (2002).
4. J. F. de Boer, "Spectral/Fourier Domain Optical Coherence Tomography," in "Opt. Coherence Tomogr. - Technol. Appl.", , W. Drexler and J. Fujimoto, eds. (Springer, 2008), Biological and Medical Physics, Biomedical Engineering.
5. V. J. Srinivasan, D. C. Adler, Y. Chen, I. Gorczynska, R. Huber, J. S. Duker, J. S. Schuman, and J. G. Fujimoto, "Ultrahigh-speed optical coherence tomography for three-dimensional and en face imaging of the retina and optic nerve head." Invest. Ophthalmol. Vis. Sci. **49**, 5103–5110 (2008).

#207194 - $15.00 USD Received 26 Feb 2014; revised 31 Mar 2014; accepted 1 Apr 2014; published 4 Apr 2014

6. "3D OCT-2000 Spectral Domain OCT — Topcon Medical Systems, Inc." http://www.topconmedical.com/products/3doct2000.htm.
7. L. D. Harris, R. A. Robb, T. S. Yuen, and E. L. Ritman, "Display and visualization of three-dimensional reconstructed anatomic morphology: experience with the thorax, heart, and coronary vasculature of dogs." J. Comput. Assist. Tomogr. **3**, 439–446 (1979).
8. C. Dai, X. Liu, and S. Jiao, "Simultaneous optical coherence tomography and autofluorescence microscopy with a single light source," J. Biomed. Opt. **17**, 080502 (2012).
9. A. Gh. Podoleanu and D. A. Jackson, "Combined optical coherence tomograph and scanning laser ophthalmoscope," Electron. Lett. **34**, 1088–1090 (1998).
10. A. Gh. Podoleanu and R. B. Rosen, "Combinations of techniques in imaging the retina with high resolution," Prog. Retin. Eye Res. **27**, 464–499 (2008).
11. M. Pircher, E. Götzinger, and H. Sattmann, "In vivo investigation of human cone photoreceptors with SLO/OCT in combination with 3D motion correction on a cellular level," Opt. Express **18**, 13935–13944 (2010).
12. "OCT/SLO - Optos," http://www.optos.com/en-GB/Products/Ultra-widefield-imaging/OCT-imaging/OCTSLO/.
13. S. N. Markowitz and S. V. Reyes, "Microperimetry and clinical practice: an evidence-based review," Can. J. Ophthalmol. / J. Can. d'Ophtalmologie (2012).
14. K. V. Vienola, B. Braaf, C. K. Sheehy, Q. Yang, P. Tiruveedhula, D. W. Arathorn, J. F. de Boer, and A. Roorda, "Real-time eye motion compensation for OCT imaging with tracking SLO." Biomed. Opt. Express **3**, 2950–2963 (2012).
15. F. Larocca, D. Nankivil, S. Farsiu, and J. A. Izatt, "Handheld simultaneous scanning laser ophthalmoscopy and optical coherence tomography system." Biomed. Opt. Express **4**, 2307–2321 (2013).
16. D. X. Hammer, N. V. Iftimia, T. E. Ustun, J. C. Magill, and R. D. Ferguson, "Dual OCT/SLO Imager with Three-Dimensional Tracker," in "Ophthalmic Technol. XV," , vol. 5688, F. Manns, P. G. Soederberg, A. Ho, B. E. Stuck, and M. Belkin, eds. (Proceedings of SPIE Vol. 5688, 2005), vol. 5688, pp. 33–44.
17. A. Bradu, L. Ma, J. W. Bloor, and A. Gh. Podoleanu, "Dual optical coherence tomography/fluorescence microscopy for monitoring of Drosophila melanogaster larval heart," J. Biophotonics **2**, 380–388 (2009).
18. K. Komar, P. Stremplewski, M. Motoczynska, M. Szkulmowski, and M. Wojtkowski, "Multimodal instrument for high-sensitivity autofluorescence and spectral optical coherence tomography of the human eye fundus," Biomed. Opt. Express **4**, 2683 (2013).
19. Y. K. Tao, S. Farsiu, and J. a. Izatt, "Interlaced spectrally encoded confocal scanning laser ophthalmoscopy and spectral domain optical coherence tomography." Biomed. Opt. Express **1**, 431–440 (2010).
20. B. Potsaid, I. Gorczynska, V. J. Srinivasan, Y. Chen, J. Jiang, A. Cable, and J. G. Fujimoto, "Ultrahigh speed spectral/Fourier domain OCT ophthalmic imaging at 70,000 to 312,500 axial scans per second," Opt. Express **16**, 15149–15169 (2008).
21. S. Taplin, A. Gh. Podoleanu, D. Webb, and D. Jackson, "Displacement sensor using channelled spectrum dispersed on a linear CCD array," Electron. Lett. **29**, 896 (1993).
22. A. Gh. Podoleanu, "Unique interpretation of Talbot Bands and Fourier domain white light interferometry," Opt. Express **15**, 9867–9876 (2007).
23. P. Bouchal, A. Bradu, and A. Gh. Podoleanu, "Gabor fusion technique in a Talbot bands optical coherence tomography system," Opt. Express **20**, 5368–5383 (2012).
24. A. Gh. Podoleanu, D. Woods, "Power-efficient Fourier domain optical coherence tomography setup for selection in the optical path difference sign using Talbot bands," Opt. Lett. **32**, 2300–2302 (2007).
25. D. Woods and A. Gh. Podoleanu, "Controlling the shape of Talbot bands' visibility," Opt. Express **16**, 9654–9670 (2008).
26. A. Bradu and A. Gh. Podoleanu, "Attenuation of mirror image and enhancement of the signal-to-noise ratio in a Talbot bands optical coherence tomography system," J. Biomed. Opt. **16**, 076010 (2011).
27. M. Hughes, D. Woods, and A. Gh. Podoleanu, "Control of visibility profile in spectral low-coherence interferometry," Electron. Lett. **45**, 182–183 (2009).
28. Z. Hu, Y. Pan, and A. M. Rollins, "Analytical model of spectrometer-based two-beam spectral interferometry," Appl. Opt. **46**, 8499–8505 (2007).
29. S. Yun, G. Tearney, B. Bouma, B. Park, and J. de Boer, "High-speed spectral-domain optical coherence tomography at 1.3 mum wavelength." Opt. Express **11**, 3598–3604 (2003).
30. V.-F. Duma, K.-s. Lee, P. Meemon, and J. P. Rolland, "Experimental investigations of the scanning functions of galvanometer-based scanners with applications in OCT." Appl. Opt. **50**, 5735–5749 (2011).
31. M. Pircher, B. Baumann, E. Götzinger, and C. K. Hitzenberger, "Retinal cone mosaic imaged with transverse scanning optical coherence tomography." Opt. Lett. **31**, 1821–1823 (2006).
32. R. Leitgeb, C. K. Hitzenberger, A. F. Fercher, and Others, "Performance of Fourier domain xvs. time domain optical coherence tomography," Opt. Express **11**, 889–894 (2003).
33. A.N.S.Institute, "Safe use of lasers," Publ. by Laser Inst. Am. pp. ANSI Z 136.1–2000 (2007).
34. D. Merino, J. L. Duncan, P. Tiruveedhula, and A. Roorda, "Observation of cone and rod photoreceptors in normal subjects and patients using a new generation adaptive optics scanning laser ophthalmoscope." Biomed. Opt. Express **2**, 2189–2201 (2011).

#207194 - $15.00 USD Received 26 Feb 2014; revised 31 Mar 2014; accepted 1 Apr 2014; published 4 Apr 2014

35. W. Wieser, B. R. Biedermann, T. Klein, C. M. Eigenwillig, and R. Huber, "Multi-megahertz OCT: High quality 3D imaging at 20 million A-scans and 4.5 GVoxels per second." Opt. Express **18**, 14685–14704 (2010).
36. A. Gh. Podoleanu and D. A. Jackson, "Noise Analysis of a Combined Optical Coherence Tomograph and a Confocal Scanning Ophthalmoscope," Appl. Opt. **38**, 2116 (1999).
37. R. B. Rosen, M. Hathaway, J. A. Rogers, J. Pedro, P. Garcia, P. Laissue, G. M. Dobre, and A. Gh. Podoleanu, "Multidimensional en-face OCT imaging of the retina," Opt. Express **17**, 4112–4133 (2009).
38. L. Liu, N. Chen, and C. J. R. Sheppard, "Double-reflection polygon mirror for high-speed optical coherence microscopy," Opt. Lett. **32**, 3528 (2007).

1. Introduction

Due to a higher sensitivity and speed than their time domain (TD) counterpart [1,2], spectral domain (SD) methods dominate the OCT technology of eye imaging [3,4]. The SD-OCT methods produce fast A-scans, which are used to create real time cross-section (B-scan) images.

For several reasons (detailed below), an *en-face* image is also required when imaging the retina in the human eye. Besides the guidance of OCT examination, such an image can also be used to correct eye motions in the OCT data [5]. When the fundus image presents sufficient resolution, it may serve clinical assessment in conjunction with the B-scan OCT image. For instance, a commercial system from Topcon [6], uses an SLR digital camera to provide a full field image of the fundus. As another possibility, based on a summed voxel projection (SVP) [7], the strength of interference of all pixels along the depth within each A-scan needs to be summed up to produce a brightness value. Such a procedure is the most common method to produce a fundus-like image using SD-OCT technology, this image then being presented static to the user as shown in [8].

Another available option is to employ scanning laser ophthalmoscopy (SLO), and integrate such a system within a separate OCT set-up. This requires diverting some light from the returned beam from the retina, in a way similar to that previously practiced by the time domain technology of OCT combined with SLO [9–11]. Optos' OCT/SLO instrument [12] uses the same flying spot principle used in OCT imaging to sequentially generate an SLO image, effectively having both channels sharing the same optical scanning head [13]. A different principle was used in [14], where separate transversal scanners are used for a swept source OCT channel and for a SLO channel operating at different wavelengths via a dichroic splitter. The associated SLO channel provides imaging as well as it can be used as the tracker itself. A similar concept was implemented in a hand held probe, appropriate for imaging subjects with less stable fixation, such as children [15]. A SLO channel using a line camera and a galvo-scanner was added to a B-scan time domain OCT to create a sequential SLO/OCT system [16]. Sequential production of B-scans and confocal microscopy images has also been reported by means of fluorescence-based microscopy [17, 18]. By interlacing a spectrally-encoded confocal SLO frame and an OCT B-scan in alternate fashion [19], a fundus image is generated during the same time interval required to grab a B-scan.

All the methods and systems mentioned above allow the user to relate the features seen in the *en-face* image with the features in the OCT B-scan, with various degrees of pixel-to-pixel correspondence. These approaches show the interest for presenting an *en-face* image together with the SD-OCT investigation delivering B-scans.

In this paper, we refer to OCT using a broadband source and a spectrometer, from now on referred to as Sp-OCT technology [3, 20], inspired from the technology of spectral interferometry used for sensing [21]. An improved solution for the display of dual images [Sp-OCT B-scan]/[C-scan SLO] is presented, based on a Talbot bands (TB)-configuration [22]. In order to implement a conventional Sp-OCT configuration, a single splitter is needed to split light into a sample and reference path. However, this has the disadvantage of sending light back from the reference path towards the broadband source, which may lead to noise or even destroy the

#207194 - $15.00 USD Received 26 Feb 2014; revised 31 Mar 2014; accepted 1 Apr 2014; published 4 Apr 2014

optical source. Therefore, an isolator or a circulator may be needed to protect the source [20]. As another possibility, a two-splitter configuration may be used, where the reference path is recirculated, similar to that employed in [9]. In such a configuration, to add a SLO channel a 3rd splitter would be necessary to divert some of the sample light towards a SLO receiver. A better solution is presented in this paper, where the SLO channel picks up its signal from an otherwise wasted beam of light when the two interferometer arms are reunited by the second splitter. The configuration proposed has the advantage of a more efficient use of power originating from the eye, when compared with configurations having recirculation of the reference path, which would require a 3rd splitter to tap signal from the sample.

A second advantage of the solution presented is that of the improvement in the OCT channel sensitivity profile versus depth. A TB configuration allows a fine control of the position and span of the OCT channel's sensitivity profile over the optical path difference (OPD) axis [23].

In conventional implementations of Sp-OCT technology [3, 20], the spectrometer performs spectral analysis of the interference product delivered by the interferometer. In such set-ups, the order of the two operations, interference and diffraction (dispersion) [22] is interference first. The two beams returning from the interferometer's arms travel as a single beam along the same path between the interferometer and spectrometer. In a TB configuration, however, the sample and reference beams from the interferometer travel along distinct paths. A lateral offset is introduced between the two beams in their way towards the spectrometer, so that the projections of the two beams on the diffraction grating (or prism) are not fully overlapped. The non overlapping parts of the beam footprints are diffracted before they are interfered. This reversal of order of operation between interference and diffraction determines the characteristics of TBs [22]. One of such characteristics is a shift of the OCT visibility profile $V(\mathrm{OPD})$ away from a symmetric curve around $\mathrm{OPD}=0$ [24], the profile being determined by a factor $C_{TB}(\mathrm{OPD})$. This is due to the tilt of the wavefront after diffraction, which alters the overlap of the wavetrain lengths after diffraction, as explained in [22]. A rigorous description of the C_{TB} term is presented in [25] as the correlation of the spatial power distribution within the two beams. If the two footprints are not fully overlapped, as stated earlier, the C_{TB} profile will no longer be symmetric in relation to the $\mathrm{OPD}=0$ axis and therefore either the positive or the negative OPD branch will be more attenuated than the other one, as shown in [23, 26]. It was shown [27, 28] that the visibility profile $V(\mathrm{OPD})$ is described by:

$$V(\mathrm{OPD}) = C_{TB}(\mathrm{OPD}) \left(\frac{\sin \xi}{\xi} \right)^2, \tag{1}$$

where $\xi = \frac{\pi}{2} \cdot \frac{\mathrm{OPD}}{Z_{\max}}$ denotes the depth normalized to the maximum imaging range $Z_{\max}$, [28, 29], given by:

$$Z_{\max} = \frac{M\lambda_0^2}{4\Delta\lambda}. \tag{2}$$

In (2), $\Delta\lambda/M$ is the line camera pitch (M is the number of pixels used to photodetect the spectrum with bandwidth $\Delta\lambda$), and λ_0 is the central operating wavelength. The amount of sensitivity increase at a depth different from zero due to the shift of the C_{TB} profile depends on the relative width of the *sinc* profile $\left(\frac{\sin \xi}{\xi} \right)^2$, which in turn depends on the resolution of the spectrometer employed for the detection of the channeled spectrum. In most conventional Sp-OCT configurations, a fiber-based directional coupler is used to combine the two beams and produce their interference. In a Talbot bands configuration implementation, a bulk beamsplitter is employed to route the two beams towards the spectrometer, as the two beams need to

#207194 - $15.00 USD Received 26 Feb 2014; revised 31 Mar 2014; accepted 1 Apr 2014; published 4 Apr 2014

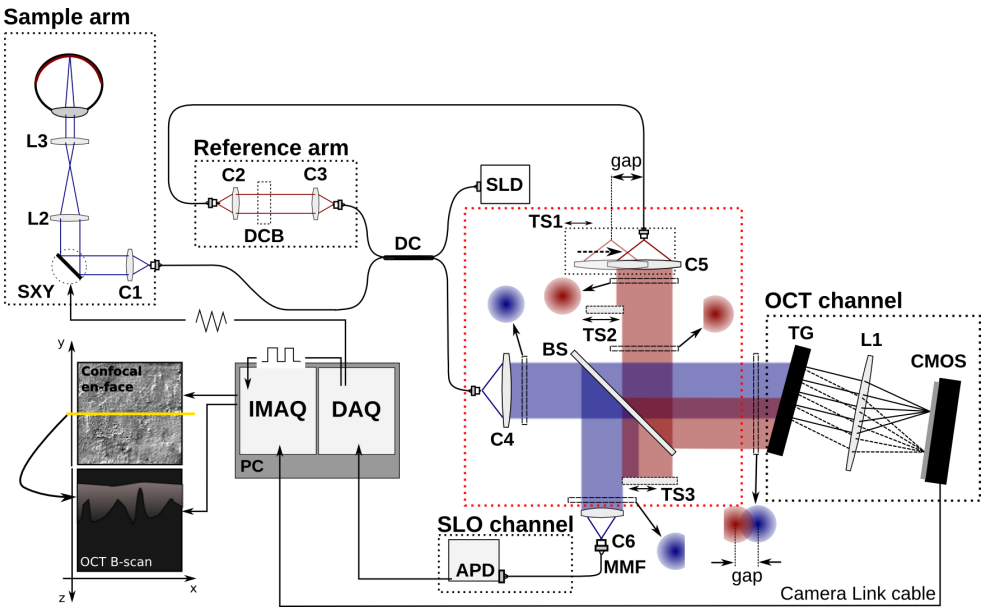

Fig. 1. Dual channel Sp-OCT/SLO set-up. C1-6: fiber collimators; SLD: super-luminescent diode; DC: fiber-based directional coupler; DCB: dispersion compensation block (adjustable, depending on the sample being imaged); TS1-3: translation stages; SXY: pair of orthogonal galvo-scanners; TG: transmission grating; L1-3: achromatic lenses; BS: bulk beam-splitter; MMF: multimode fiber; CMOS: line camera; APD: avalanche photo-diode; IMAQ: Camera Link-based image acquisition board; DAQ: multi-function data acquisition board. Region delimited by the red box: detail of the Talbot bands set-up. Cross-sections of the beams incident on the TG (OCT) and on the fiber collimator C6 (SLO) are shown for the sample beam in red and for the reference beam in blue. Note the gap present between the two beams as they are directed towards the OCT channel, which ensures a higher sensitivity at nonzero OPDs.

be spatially separated. It is this approach which then allows us to retrieve the confocal (sample) signal separately.

2. Experimental set-up

The dual channel Sp-OCT/SLO set-up is depicted in Fig. 1. Light from a super-luminescent diode *SLD* (Superlum SLD-381-HP1-DIL-SM-PD, Cork, Ireland - central wavelength $\lambda_0 =$ 830 nm, and spectral bandwidth $\Delta\lambda \approx 20$ nm) is directed towards the two interferometer arms (reference and sample) via a fiber-based 80/20 directional coupler *DC* (AC Photonics, Santa Clara, CA, US). Given the SLD's spectral bandwidth and central wavelength, an optical axial resolution in depth measured in air of approximately 15 μm results.

The 20% fraction of the initial power directed to the sample arm traverses a galvo-scanning head *SXY* (Crisel Instruments Galvoline G1432, Italy), comprising a line scanner *X* and a frame scanner *Y*, where the former deflects the beam horizontally and the latter vertically. The resulting beam scans the retina angularly, via lenses *L2* and *L3* of focal lengths $f[L2] = 7.5$ cm and $f[L3] = 3$ cm being employed to reduce the beam diameter at the pupil eye to ≈ 3 mm.

Light backscattered by the retina and light directed through the reference arm are re-united at the bulk beam-splitter *BS*, which features an 80/20 splitting ratio. 80% of the power returning

#207194 - $15.00 USD Received 26 Feb 2014; revised 31 Mar 2014; accepted 1 Apr 2014; published 4 Apr 2014

from the sample arm is directed towards the spectrometer in the OCT channel and the remaining 20% towards the SLO channel (forming the SLO *en-face* image). Similarly, the reference arm also sends 80% of its power through the beamsplitter. The gap between the two beams (adjustable by shifting the reference arm launcher *C5* using *TS1*) required by TB implementation secures sufficient spatial separation of the sample and reference beams to enable the multimode fiber *MMF* to select mainly the sample beam through the collimator *C6*. For better attenuation of the stray signal caused by the edge of the strong reference beam, a specially-devised spatial filter is implemented. This consists of a pair of opaque screens introduced before and after the beam-splitter along the path of the reference beam. These screens are attached to translation stages (*TS2/TS3*) so that their position can be adjusted with micrometric precision. The opaque screen attached to *TS2* trims the edge of the reference beam on the side of the sample beam directed towards *C6*. Due to diffraction registered at the edge of the beam caused by this screen, some light is directed towards *C6*, therefore a second screen attached to *TS3* is necessary. For better rejection of the reference signal, this is pushed towards the center of the collimator *C6*, and a small fraction from the edge of the sample beam is blocked, as shown exaggerated in the inset in Fig. 1. This introduces a small attenuation on the SLO channel, quantified by measuring the SLO signal with and without *TS3*, of 2.3 dB. By screening the reference arm beam with *TS2* by ~ 1 mm, a 3 dB attenuation of the reference power in the OCT channel is introduced. This figure was measured by evaluating the signal due to the reference beam with and without *TS2*. When using a mirror as a sample, the ratio between the sample signal power and leaked reference power in the multimode fiber leading to the SLO channel was of 35 dB. Without the two screens in place, this ratio reduces to 5 dB.

Due to the screen attached to *TS1*, the distribution of power in the transversal section of the reference beam results in a trimmed Gaussian curve. This affects the symmetry of the OCT sensitivity profile versus OPD, as documented in [24, 27]. However, the deviation of the profile from Gaussian has little influence on the final visibility profile due to the fact that the trimmed portion coincides with a wing of the sample beam (which carries less power) and not with the central part of the sample beam.

Spectral analysis of the OCT signal employs a diffraction grating (whose grooves are orthogonal to the plane of Fig. 1) working in transmission *TG* (Wasatch Photonics, Logan, UT, US), with 1200 lines/mm blazed at 830 nm, a CMOS line camera (Basler sprint spl-4096km, Ahrensburg, Germany) and an achromatic lens *L1* to focus the diffracted light onto the camera array. The diffracted beam covers ~ 1 cm over the array, which corresponds to 1024 out of the available 4096 pixels. This reduced number of pixels was employed to enable the camera to operate at high line rates (up to 100 kHz).

For each lateral scan, 1024 spectral points with 12-bit levels are buffered, followed by standard software-based processing (re-sampling in *k*-domain, zero padding and inverse FFT). After the FFT is performed on the input data, the number of pixels in depth in the B-scan OCT image is half of this number. For N_x pixels along the line (Ox), the image has a size $N_x \times 512$ pixel (width x depth).

The SLO channel is equipped with an avalanche photo-diode (*APD*, Hamamatsu C5460-01, Japan), with a cut-off frequency $f_c = 100$ kHz. Its output is then digitized by an analogue-to-digital converter within a *DAQ* (National Instruments PCI-6110, Austin, TX, US). The reflected fraction of the sample arm power (at the beamsplitter *BS*) is directed to the *APD* via collimator *C6* and multi-mode fiber, *MMF*.

The SLO channel delivers an *en-face* (constant depth scan or C-scan) comprised of multiple T-scans (lateral reflectivity profiles). Each of these T-scans is acquired during the active half-periods of the line scanner (x axis). The OCT channel delivers a B-scan (cross section) OCT image, which in turn is comprised of several A-scans (axial reflectivity profiles) taken during

#207194 - $15.00 USD Received 26 Feb 2014; revised 31 Mar 2014; accepted 1 Apr 2014; published 4 Apr 2014

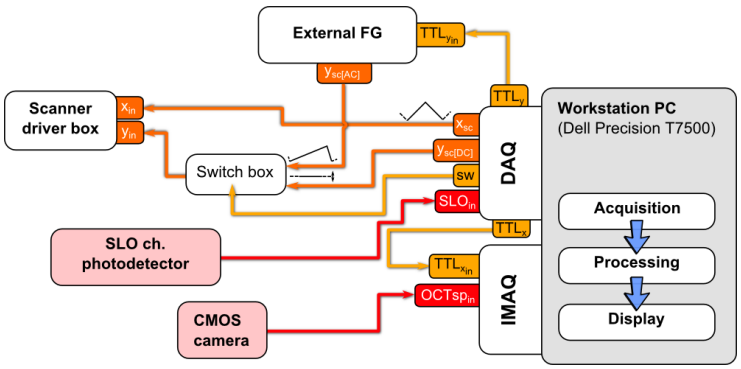

Fig. 2. Schematic diagram of the control system of the OCT/SLO set-up to achieve the three modes of operation. The multi-function data acquisition card (DAQ) and the External Function Generator deliver signals to the X-scanner and the Y-scanner via the Scanner driver box. The Switch box is used in the sequential modes only. The detected spectra from the CMOS camera are sent through a Camera Link bus to the image acquisition (IMAQ) card while the analog SLO signal is sent to the DAQ card.

the same active half-period of the line scanner.

The control system of the OCT/SLO set-up is depicted schematically in Fig. 2. The workstation PC is equipped with two distinct cards. The DAQ drives the two transversal scanners and acquires the SLO signal to produce the SLO image. The IMAQ card (National Instruments PCIe-1429, Austin, TX, US) interfaces the CMOS line camera in the spectrometer with the PC, thus acquiring the spectra which will yield the OCT image.

The line scanner *X* is driven by a triangular or saw-tooth waveform, x_{sc}, generated by the control software. The frame scanner *Y* is driven by a saw-tooth signal (90% duty cycle), produced by an external function generator (Hewlett-Packard 8116A, Palo Alto, CA, US) and triggered by a computer via one of the DAQ's digital ports (TTL_y). The external function generator is employed to synchronize the LabVIEW frame acquisition loop with the saw-tooth waveform generation.

When a single *Oxz* frame is needed (B-scan), the *y* scanner is held stationary and a DC offset is applied to it, controlled by the DAQ output $y_{sc}[\mathrm{DC}]$. This allows the user to map the position of the cursor placed over the *en-face* image to the corresponding B-scan being acquired, depending on the operating mode chosen, as it will be presented over the next section. Switching between the two signals, saw-tooth for the SLO regime and DC in the OCT regime is performed via a Switch box, whose output is selected via the TTL_{sw} signal. This signal is generated in *software* and channelled via the DAQ's digital port (sw) towards the switch box.

Furthermore, the DAQ also drives the buffering of the spectra which will be used, after their FFTs, to form the B-scan, where the succession of A-scan acquisitions is controlled via the TTL signal (TTL_x).

3. Timing and acquisition speed constraints

The operation of the OCT/SLO instrument depends on a set of constraints introduced by the hardware available at present, whose parameters can be manipulated to trade-off resolution by speed and vice-versa.

With regards to the OCT channel detection, the CMOS camera allows various acquisition settings [20]. The absolute maximum line rate attainable by the CMOS camera used is 312 kHz, however such figure is only possible when several of the signal-enhancing features of the

#207194 - $15.00 USD Received 26 Feb 2014; revised 31 Mar 2014; accepted 1 Apr 2014; published 4 Apr 2014

camera are turned off, such as vertical binning – which enables the two 4096×10 μm CMOS lines to effectively behave as a single 4096×20 μm line – and also when reading a smaller subset of the whole 4096 pixel array [20]. With such line rates, the signal-to-noise ratio (SNR) will diminish, hence the choice of the line rate will necessarily introduce a trade-off between speed and sensitivity. Throughout all the experimental work carried out, the line rate was chosen to be in the range of 50-100 kHz, which enabled several of the aforementioned features of the CMOS camera. This determines an acquisition time per spectra of $\delta t_{OCT} \sim 10 - 20$ μs.

The inertia of the galvo-scanners *SXY* constrains the speed of lateral scanning as well. Therefore, the line scanner's triangular waveform is limited to 500 Hz to prevent heating and reliability issues [30].

Lastly, there is the issue of the lateral resolution. Let us say that the Airy disc diameter of the beam focused on the retina is D_0. Then the lateral image size is $\Delta X = D_0 N_x$. D_0 can be approximated by $1.22 \cdot \frac{f\lambda_0}{D}$, where f is the focal length of the eye, D is the scanning beam diameter and λ_0 is the central operating wavelength. For an eye length of $f \approx 25$ mm, using $\lambda_0 = 840$ nm and $D = 3$ mm, $D_0 \approx 8.5$ μm. Considering the aberrations of the eye, D_0 can be approximated as ≈ 10 μm. Given the line scanner's frequency of 500 Hz, this means that a half-period will take 1 ms. Assuming a CMOS camera line rate of 100 kHz, this means that only $N_x = N_S = 100$ adjacent A-scans can be retrieved during one half-period, which effectively limits the lateral range to $N_S D_0 = 1$ mm. Any scanner amplitude setting which would project a raster scan with a larger span than that will under-sample the object in terms of the optical resolution. In such a case, there will be more than a single Airy disc diameter within each electronic pixel, i.e. within each A-scan.

The SLO channel also introduces a limit in the lateral size, albeit larger than that imposed by the OCT channel: the APD used has a bandwidth $f_{3\text{dB}}$ of 100 kHz, which determines a rise time $t_{rise} = 3.5$ μs for the impulses at the APD output. For the same line scanner speed (500 Hz) as above, this allows $N_y[\text{SLO}] = 280$, i.e. an increase in the SLO lateral size. This may be of interested if higher resolution SLO images are desired, even without pixel-to-pixel correspondence.

Taking all these constraints into account we have devised three modes of operation, with varying degree of pixel-to-pixel correspondence and allowable acquisition times.

3.1. Simultaneous, small lateral size

In this mode, the system acquires an OCT B-scan frame during each SLO frame acquisition (Fig. 3(i)). The B-scan OCT image has pixel-to-pixel correspondence with a selected line placed over the SLO image by a cursor (whose y coordinate is used to select the instant when the B-scan is buffered amongst all the SLO T-scans), and the frames in the two channels refresh simultaneously. Pixel-to-pixel correspondence (Fig. 3(iii)) means that the two channels have the same lateral size, that is $N_x[\text{SLO}] = N_x[\text{OCT}] = N_S$. Moreover, since a square aspect ratio was chosen, $N_x = N_y$, taking into account that $N_x = 100$ for $\delta t_{OCT} = 10$ μs it means that the two frames (SLO: 100×100 pixels; OCT: 100×512 pixels) can be refreshed in $T_y = \frac{1}{2} \cdot T_x N_S =$ 100 ms, i.e. at 10 Hz (the effective frame rate is closer to 8 Hz due to the signal processing time). The $\frac{1}{2}$ factor in the expression for T_y stems from the fact that both ramps of the triangular scanning waveform are employed in the imaging process, which means that during the complete period of the x-scanning waveform ($T_x = 2$ ms) two OCT/SLO frames are acquired.

This choice of image size enables simultaneous imaging with pixel-to-pixel correspondence in the two channels at high refresh rates. Due to the imposed short lateral size, this mode of operation is suitable for small size imaging of the eye, imaging photoreceptor cells, as presented

#207194 - $15.00 USD Received 26 Feb 2014; revised 31 Mar 2014; accepted 1 Apr 2014; published 4 Apr 2014

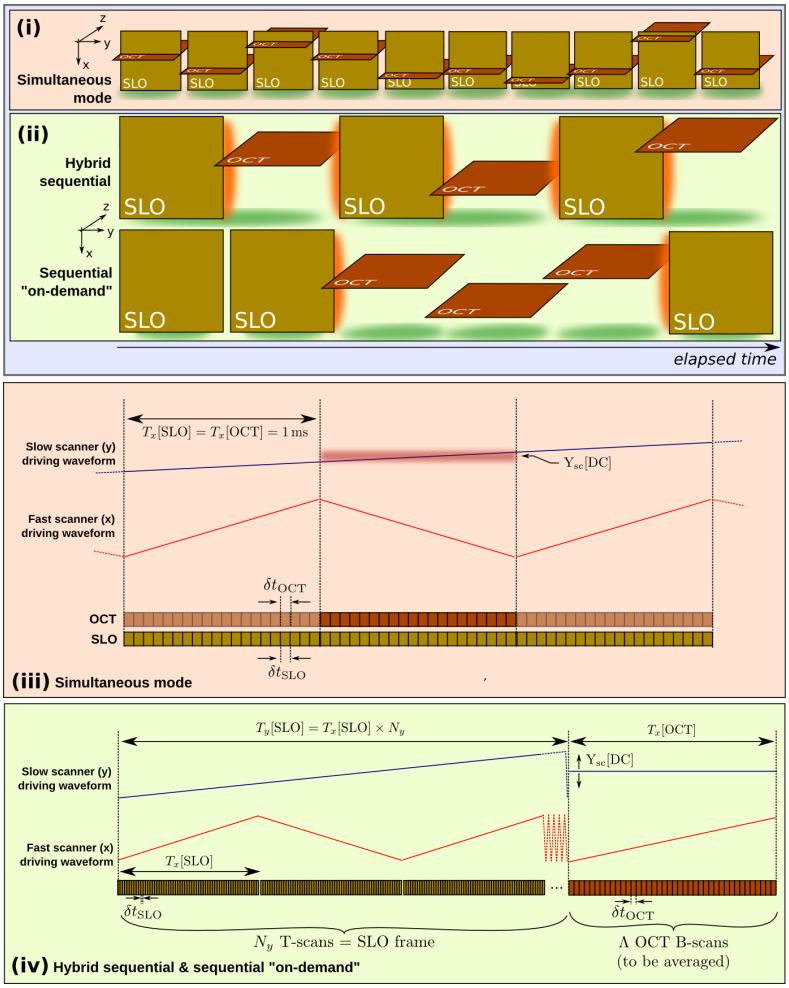

Fig. 3. Schematic description of the various modes of operation implemented. (i) and (ii) Sequence of frames in the three modes of operation, where the green shadows show the frame refresh period, and the orange glow shows the instants when the system switches between the two regimes, if applicable. (i) Simultaneous mode of acquisition: the two frames, OCT and SLO are acquired and refreshed at the same time: illustration of different vertical positions in the SLO image where the OCT B-scan is selected from by varying $Y_{sc}[\mathrm{DC}]$: a single OCT B-scan is captured, even though more can be buffered if necessary; (ii) Hybrid sequential and sequential "on-demand": the system is toggled between the two regimes (SLO and OCT), and signal is acquired in each regime on separate time intervals; the toggle is automatic in the hybrid sequential mode or performed manually in the sequential "on-demand" mode. In the hybrid mode the two images are refreshed at the same time, even though they are not acquired simultaneously. (iii) and (iv): Scanner waveforms (x and y) and illustration of integration time on pixels within the spectral acquisition events, δt_{OCT}, (orange rectangles) each leading to an A-scan and integration time on pixels within a T-scan, δt_{SLO} (brown rectangles) in all three modes. (iii) Simultaneous mode of acquisition; (iv) Hybrid sequential and sequential "on-demand" modes of acquisition.

#207194 - $15.00 USD Received 26 Feb 2014; revised 31 Mar 2014; accepted 1 Apr 2014; published 4 Apr 2014

in [31], with or without adaptive optics. Furthermore, if lateral resolution is not a major concern, the image size can be increased and such a mode can also be used as an assistive technique for retinal tracking, where only the major features are required (e.g. fovea, optic nerve) in order to supply information to the tracking algorithm, or to suppress motion artifacts already present in the images. The increased frame rate (up to ≈ 8 Hz) makes this mode of operation tolerant to movement.

However, if a larger lateral size ($N_x > N_S$) is desired, or if the SNR needs to be increased, this mode is no longer suitable. Achieving the same lateral size in both channels is only made possible by accepting signals of different time duration. This leads to two additional possible modes of operation, where the system operates in a single regime at any given time (Fig. 3(ii)).

3.2. Sequential "on-demand"

In this mode of operation (Fig. 3(ii)), the system continuously refreshes the SLO frames until the user switches the system to the OCT B-scan regime, at which moment the last SLO frame is frozen for guidance of the OCT imaging. During the SLO regime (lasting $T_y[\mathrm{SLO}]$), the frame scanner is driven by a ramp which is part of a saw-tooth waveform, generated by *FG*, with a 90% duty cycle to minimize the return dead time (Fig. 3(iv)).

When the system is switched to the OCT regime, the frame scanner is stopped at a vertical position selected by $Y_{sc}[\mathrm{DC}]$, determining the *y*-coordinate of each B-scan being displayed. Furthermore, the speed of the line scanner is slowed down to allow for a larger N_x and for an increased δt_{OCT}. Considering the maximum number of pixels $N_x = 280$ allowed by the APD bandwidth, the line scanner speed in the OCT regime is reduced to $f_x' = \frac{N_S}{N_x} \cdot f_x = \frac{100}{280} \cdot 500 =$ 180 Hz. For longer spectrometer exposure times, even lower frequency f_x' values are needed.

This mode of operation presents the obvious drawback of less tolerance to eye movements, as the SLO image is no longer refreshed. However, this mode of operation allows for more freedom in setting the lateral image size and the OCT channel parameters, since the timing of each frame is not tied to the time constraints of the SLO channel. In essence, the system operates in the two regimes at independent frame rates, which may make it flexible to perform an array of clinical scenarios, where image quality and size in both channels are more important than the exact correspondence between the two images.

In terms of pixel-to-pixel correspondence, some variations result from a regime to the next due to the change of image size when switching from 500 Hz to 180 Hz ramps applied to the line scanner. This can be compensated by a corresponding decrease in the voltage V_x applied to the line scanner in the OCT regime in comparison to the value applied in the SLO regime, correction that can be accurately worked out using the position sensing signal delivered by the scanning driver board.

3.3. Hybrid sequential

In this mode the pixel-to-pixel correspondence between the OCT and the SLO frames is improved by automatically switching repetitively between the two modes, as shown in Fig. 3(ii).

For better SNR in the OCT channel, the CMOS camera's integration time was increased to $\delta t_{OCT} = 20\ \mu$s. Furthermore, an averaging feature of OCT frames is also incorporated, which will determine an adjustable time for the system in the OCT regime, $T_x[\mathrm{OCT}]$ depending on the number of OCT images Λ to be averaged (Fig. 3(iv)). The time in the OCT regime increases linearly from $T_x[\mathrm{OCT}]$ (for a single OCT acquisition) to $\Lambda \cdot T_x[\mathrm{OCT}]$ when Λ frames are acquired to be averaged, thus yielding a better SNR. The averaging process in the OCT regime may not affect the toggle time if $\Lambda \cdot T_x[\mathrm{OCT}]$ is kept lower than $T_x[\mathrm{SLO}]/10$. For $N_y = 100$, $T_y[\mathrm{SLO}] = 200$ ms, which means that $1 < \Lambda < 10$. For $N_y = 280$, $T_y = 560$ ms, so $1 < \Lambda < 28$.

#207194 - $15.00 USD Received 26 Feb 2014; revised 31 Mar 2014; accepted 1 Apr 2014; published 4 Apr 2014

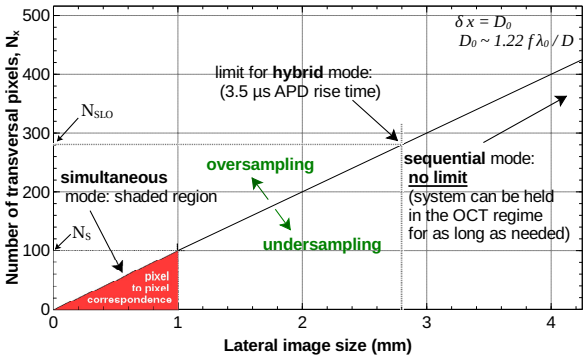

Fig. 4. Relation between the number of pixels, N_x, determining the lateral image size and the mode of operation applicable. The red shaded region corresponds to the settings which allow pixel-to-pixel correspondence between the OCT and SLO images, which is limited at $N_x = N_S$. Lateral image size is calculated using $N_x \cdot D_0$, with $D_0 \approx 10\ \mu$m.

For larger SLO images, Λ could be even larger without affecting the toggle time.

3.4. Lateral size constraints

Depending on the mode of operation chosen, the maximum lateral image size attainable without loss of resolution varies according to the graph in Fig. 4. The line across the plot corresponds to the special case where the lateral pixel size matches the Airy disc diameter D_0. Above the line, the electronic pixel size is smaller than the Airy disc diameter, i.e. the system over-samples both OCT and SLO signals. Below the line, the Airy disc diameter D_0 is larger than the electronic pixel size, i.e. the system under-samples the signals. Note that the line scanner period is maintained at 1 ms for all SLO operations, but it might be modified during the OCT regime, depending on the mode of operation chosen.

True pixel-to-pixel correspondence (red shaded region) is only attainable when operating in the simultaneous mode, which limits the lateral image size to less than 1 mm.

A degree of pixel-to-pixel correspondence is still achievable for $N_S < N_x < N_{\mathrm{SLO}}$, i.e. for $100 < N_x < 280$, if correction of lateral image size is made to compensate for the swing variation of the *x*-scanner with the frequency of the applied signal.

Over $N_x = 280$, the APD starts behaving as a low-pass filter due to its finite rise time, hence the line rate has to be reduced in order to maintain the lateral resolution whilst allowing for a larger lateral size. This will necessarily have an impact on the frame refresh rate, making the system more prone to motion-induced artifacts.

4. Demonstration of the working principle

Figure 5 (i) shows the sensitivity profile versus OPD. The launcher *TS1* was laterally moved by ~ 0.25 mm to create the gap necessary for TB implementation, which determines a shift of the peak of sensitivity from OPD $= 0$ to -1.8 mm as shown by the red circles and green triangles. The TB sensitivity profile conserves its width from the non-Talbot band case, but the maximum sensitivity reduces by about 2 dB. However, at larger depths, the gain exceeds 6 dB. The green curve shows the TB sensitivity versus OPD with the screen on *TS2* in place. As demonstrated in [25], the sensitivity profile is given by the correlation of the power distribution within the footprints of the two beams incident on the diffraction grating. Due to diffraction on the screen edge, the power distribution of the reference beam is changed to a wider footprint

#207194 - $15.00 USD Received 26 Feb 2014; revised 31 Mar 2014; accepted 1 Apr 2014; published 4 Apr 2014

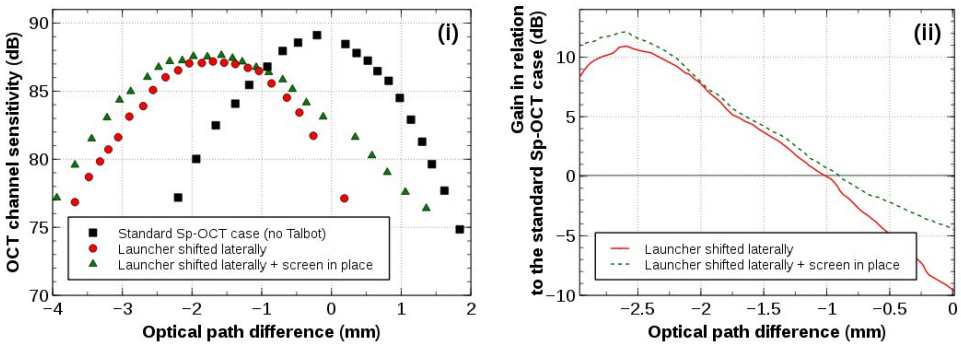

Fig. 5. (i) OCT channel sensitivity. Black squares: conventional Sp-OCT, beams coincide spatially; Red circles: launcher moved laterally by ~ 0.25 mm to produce Talbot bands; Green triangles: launcher moved laterally by ~ 0.25 mm to produce Talbot bands and screen (*TS2*) placed on the edge of the laterally-shifted reference arm beam); (ii) Relative sensitivity for the Talbot bands configurations in respect to the conventional Sp-OCT for: launcher shifted laterally (red solid line), launcher shifted laterally and screen in place (green dashed line).

with secondary lobes. This was documented in [27], where a screen was also used to modify the distribution of power in the reference beam across the grating. Therefore, a slight improvement of the sensitivity results.

The sensitivity was measured following the procedure described in [32] for the non-TB case (black curve, Fig. 5) and OPD set at -1 mm. For the two integration time values used in this study, $\delta t_{OCT} = 10$ and 20 μs, sensitivities of 82 dB and 87 dB were obtained, respectively.

Following the system characterization, several *in-vivo* retinal images were acquired from the eye of one of the authors (AP), covering different features in the eye: the foveal region and the optic nerve region. Ethical approval was obtained from the Faculty of Sciences' Ethics Committee. Power to the eye was less than 750 μW, in accordance with standards [33].

4.1. Dual SLO/OCT retinal images

Figure 6 presents images obtained with the system running under the simultaneous mode refreshing at 3 Hz. The line scanner is driven with a triangular signal of period 2 ms and the camera integration time is 10 μs. Two possibilities are presented, small size imaging with a lateral pixel size less or equal to the optical transversal resolution, constrained by the limited number of lateral pixels achievable as explained above, and large size imaging, where the system still operates with the same number of pixels and so the images are under-sampled.

In each box in Fig. 6, SLO frames are shown at the top with a resolution of 100 × 280 pixels (width × height). OCT frames are shown at the bottom row with a resolution of 100 × 150 pixels (width × depth, cropped from 512 axial pixels to emphasize the region under analysis).

In Fig. 6(i) to 6(iii) the SLO images are about 500×500 μm^2, therefore the pixel mesh is denser than the actual optical resolution of the system. In (i) the edge of the optic nerve head is shown.

In Fig. 6(ii), the volunteer looked halfway between the fovea and the optic nerve. The small size imaging allows distinguishing individual photo-receptors when the eccentricity of the location on the retinal image exceeds 5º. For such eccentricity, the cone spacing is larger than ≈ 10 μm [34]. In (iii) photo-receptor cells are still visible, along with the choroid layer (yellow arrow).

#207194 - $15.00 USD Received 26 Feb 2014; revised 31 Mar 2014; accepted 1 Apr 2014; published 4 Apr 2014

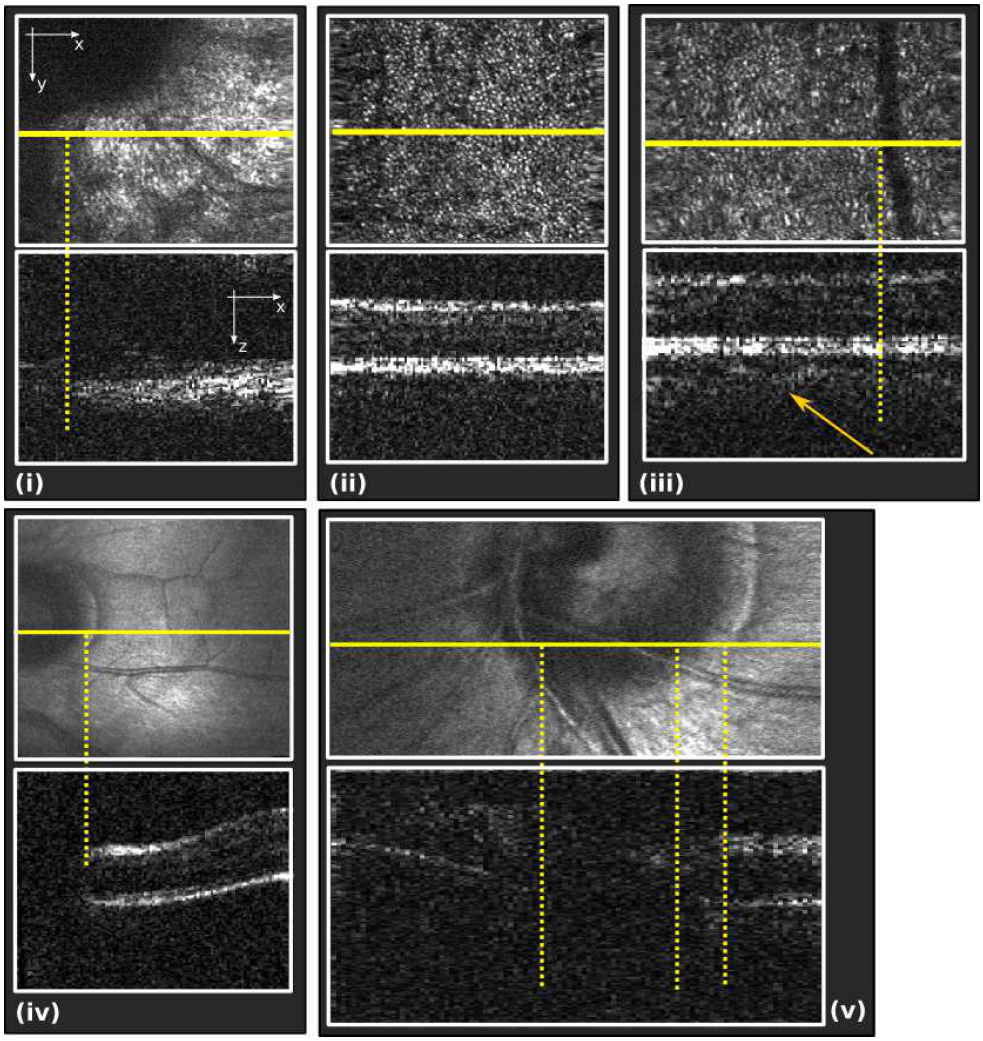

Fig. 6. Retinal images obtained while running the system in the simultaneous mode of operation at a frame rate of ≈ 3 Hz. SLO frames (top image in each frame) are 100×280 pixels and OCT frames (bottom image in each frame) are 100×512 pixels (here cropped to 100×150 pixels to emphasize the region under analysis). (i) edge of the optic nerve head, lateral size $\approx 500 \times 500\ \mu\text{m}^2$; (ii) region between the optic nerve and the fovea, in an area featuring larger photo-receptors ($\approx 10\ \mu$m), lateral size $\approx 500 \times 500\ \mu\text{m}^2$; (iii) pair of SLO and OCT images (lateral size $\approx 500 \times 500\ \mu\text{m}^2$) featuring a blood vessel; the choriod (yellow arrow) is visible below the nerve fiber layer; (iv) optically under-sampled OCT image of the area between the foveal region and the optic nerve, lateral image size $\approx 2 \times 2.5\ \text{mm}^2$; (v) optically under-sampled OCT image of the optic nerve, the region in focus is the shallower retinal layer, lateral size $\approx 1.5 \times 0.8\ \text{mm}^2$. The OCT B-scans correspond to the location of the horizontal lines overlaid on the SLO C-scans.

#207194 - $15.00 USD Received 26 Feb 2014; revised 31 Mar 2014; accepted 1 Apr 2014; published 4 Apr 2014

Larger values for the lateral image size were also considered. In Fig. 6(iv), the line scanner was driven with ≈ 600 mVpp determining about 2 mm lateral size. This size is larger than that obtained by multiplying the assumed Airy disc diameter of ≈ 10 μm with the number of transversal pixels $N_x = 100$, so the image is obviously under-sampled in the lateral direction, as commented above in connection to Fig. 4.

Figure 6 (v) contains an optically under-sampled OCT image as well, since the lateral size is over 1 mm. The focal region was on the shallower retinal tissue, hence the corresponding OCT profile only maps the *x*-coordinates where the optic nerve is situated.

Features are sufficiently well seen in both columns, however due to the high speed of the camera, the OCT images are noisy. Even so, contours and main layers are easily identified at this frame rate.

Figure 7 features the results obtained with the OCT/SLO set-up operating in hybrid sequential mode. During the OCT regime, the lateral scanning duration of the line scanner is 20 ms and the camera integration time was increased to 20 μs, which enabled us to use more pixels in the lateral dimension of the OCT B-scans. Images of the foveal region and of the optic nerve are presented. The lateral image sizes considered ranged from 2.6 to 5 mm. Again, two image size values are employed: a medium lateral size of 2.6 mm, where the lateral pixel size in the SLO image is of the same order as the optical transversal resolution and a larger lateral size of 5 mm, where the SLO images are under-sampled. For both sizes, the same number of lateral electronic pixels $N_x \approx 500$ is used in both OCT and SLO regimes.

Figures 7(i) and 7 (ii) differ mostly on the location of the focal point (in depth) - the former features a better defined retinal surface, whereas the latter emphasizes the *lamina cribrosa*, deep within the optic nerve. Given their lateral size (2.6×5.2 mm^2) these images are sufficiently sampled, furthermore the OCT images are better defined than in the previous case since the exposure time is twice as large which improves the SNR.

In Fig. 7(iv) several OCT B-scan slices taken at different y positions are shown with their corresponding SLO image. These feature the optic nerve with a large lateral size of $\sim 5 \times 6$ mm^2.

A good match was found between the features visible in the SLO image and those seen in the corresponding OCT B-scans. The correspondence is also clear in (iii) and (v), the former with a significant intercept of a sub-retinal blood vessel and the latter with a good correspondence of features from the foveal region.

5. Discussion

A particular set of three parameters was employed here which allowed simultaneous operation with pixel-to-pixel correspondence: (i) a state of the art line camera performing spectral scanning in 10 μs; (ii) lateral scans at 1 ms, the fastest achievable period with a galvo-scanner having a sufficiently large mirror to perform low loss scanning and (iii) a finite bandwidth in the SLO channel, using a 100 kHz APD amplifier. Therefore, the choice of three regimes described here is specific for the current level of Sp-OCT technology combined with that of fast galvo-scanners only and it is not applicable to the swept source-OCT method of spectral domain OCT, where A-scan rates of over 1 MHz are possible [35].

Choosing between the three modes of operation described above, simultaneous, sequential "on-demand" and hybrid sequential, a decision has to be made in terms of the trade-off between the range of configurable parameters and the need of pixel-to-pixel correspondence. Here by parameters we understand the voltage/frequency of the signals driving the lateral scanners and the CMOS camera's integration time.

The simultaneous mode of operation is suitable for small size imaging only, such as in adaptive optics. If matching the optical resolution with the electronic sampling resolution is not of

#207194 - $15.00 USD Received 26 Feb 2014; revised 31 Mar 2014; accepted 1 Apr 2014; published 4 Apr 2014

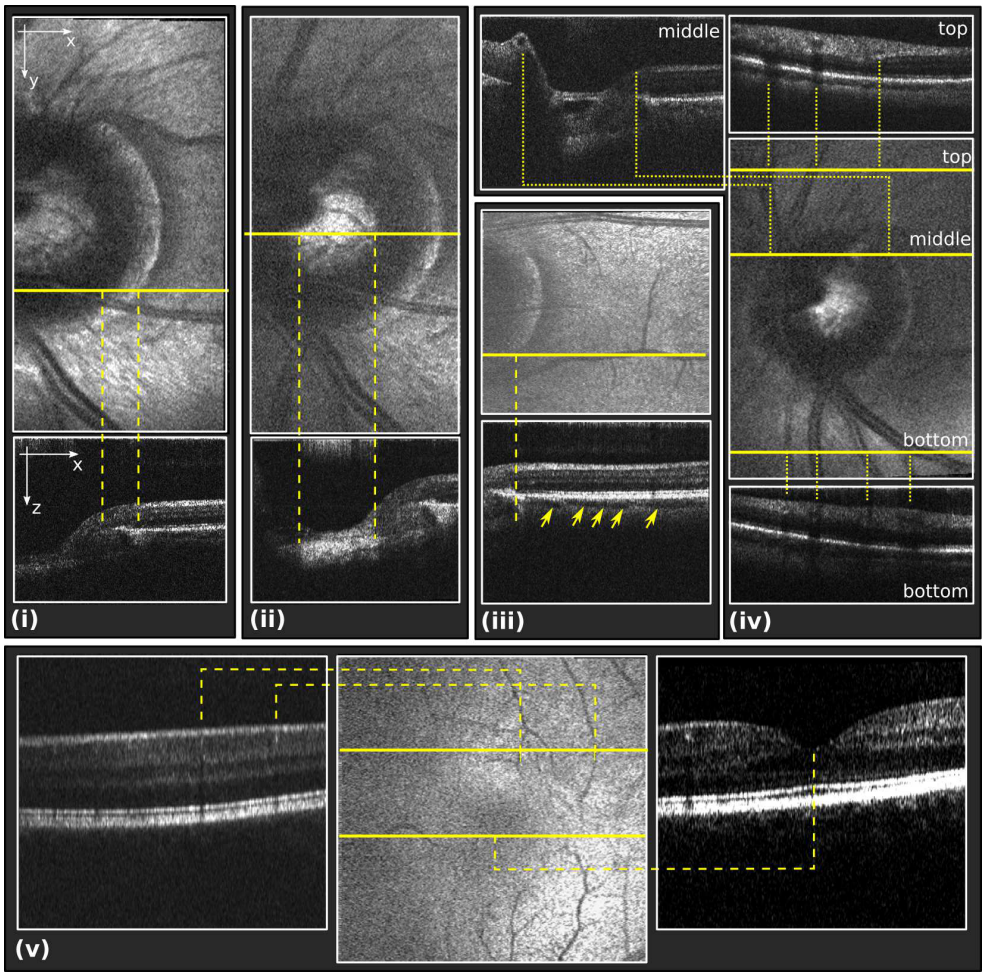

Fig. 7. Images obtained with the OCT/SLO set-up operating in hybrid sequential mode (SLO top, OCT bottom). The images in (i), (ii) and (iii) have sufficient sampling whilst the images in (iv) and (v) are under-sampled. (i) and (ii): area between the optic nerve and the shallower retinal tissue (lateral size 2.6×5.2 mm^2); (i): focus on shallow layers; (ii): focus at the *lamina cribrosa*'s depth; (iii): area located in the vicinity of the optic nerve, the OCT B-scan cut intercepts a blood vessel along its course (yellow arrows), lateral size 2.6×5.2 mm^2; (iv): detail of the optic nerve region (5×6 mm^2 lateral size) emphasizing several positions of the cursor with varying features selecting the associated OCT B-scans; (v): fovea region, lateral size 5×5 mm^2. The OCT B-scans are obtained from an average of $\Lambda = 4$ OCT frames. The positions of the OCT cuts along the Y-axis correspond to the location of the horizontal lines overlaid on the SLO C-scans.

#207194 - $15.00 USD Received 26 Feb 2014; revised 31 Mar 2014; accepted 1 Apr 2014; published 4 Apr 2014

concern, then the image can be subsampled by increasing the amplitude of voltages applied to the two galvo-scanners. This may be the case when using the SLO channel to perform retinal tracking, when major features in the SLO are sufficient, as suggested in [14].

The sequential "on-demand" mode of operation is suitable for investigation situations where total freedom is needed in terms of image size and quality of image in each channel, irrespective of the quality of signal in the other channel, and when instabilities of the eye position are not of concern.

Lastly, the hybrid mode of operation represents a trade-off between the simultaneous regime and the sequential on demand, where sufficient large size images can be achieved with some degree of pixel-to-pixel correspondence between the images in two channels, moderately affected by the eye movement. This is the regime of operation of the Optos system [12] currently used in clinical investigations.

Different systems exist on the market and in several research labs. Our study suggests that, for instance, if a system is normally being used in the sequential mode of operation, then there is no point in maintaining such mode when the image size is not a determinant factor. Such a system can also, with some modifications as described here, be made to operate in the simultaneous mode, where the frame rate is determined by the speed of the spectrometer and by the speed of the line galvo-scanner in each case.

The notions of pixel-to-pixel correspondence and simultaneity in the simultaneous mode of operation are slightly different from the same notions applied to [Time-domain OCT]/SLO developed in the past [10, 11, 36], where pixel-to-pixel correspondence between the *en-face* OCT image and the SLO image referred to all pixels in the transversal section of the images. Here, pixel-to-pixel correspondence refers to the lateral cut only, sampled by the B-scan along one of the T-scan lines in the SLO image. It should also be noted that the correction procedure of OCT B-scan image in [37] based on the SLO image collected simultaneously is applicable to the simultaneous mode of operation described here. This is not illustrated here, but with the vertical scanner stopped, lateral movements of the eye can be traced from the breakages of vertical lines in the SLO image, during the acquisition of sets of B-scan OCT images.

As another parallelism of simultaneous technologies, in both TD-OCT/SLO and in the Sp-OCT/SLO presented here, it is the OCT channel that slows down the SLO acquisition. In general, the SLO channel can be made to work faster than the OCT channel. Large size *en-face* OCT images determine a slower frame rate of the simultaneous acquisition, of $2-4$ Hz. For reduced image size however, simultaneity was maintained with sufficient signal to noise ratio by using resonant scanners [11]. In Sp-OCT, even though faster frame rates are achievable for the B-scan OCT image in comparison with the ones obtained with *en-face* TD-OCT, they are not as fast as to allow simultaneity with a large number of pixels in the transversal section; hence the regime with only 100 pixels described here. Replacing the line galvo-scanner with a resonant scanner allows increasing the acquisition speed of the SLO channel, however this will impose a too high speed for the camera. For instance, by swapping the galvo-scanner used here with a resonant scanner at 8 kHz would have meant a $16\times$ faster SLO channel. However, for the same $N_x = 100$ pixels, this would have demanded a camera 16 times faster i.e. operating at a 1.6 MHz line rate. The maximum rate the authors are aware of is ~ 300 kHz [20].

6. Conclusions

In this paper we discussed the possibility of combining a spectrometer based Talbot bands OCT configuration with SLO technology, compatible with limitations imposed by the current technology in terms of speed of linear cameras. While there are transversal scanners which can work faster than the galvo-scanners used in this paper, such as resonant ones, utilization of faster transversal scanners is not compatible with a simultaneous mode of operation OCT/SLO

#207194 - $15.00 USD Received 26 Feb 2014; revised 31 Mar 2014; accepted 1 Apr 2014; published 4 Apr 2014

as described here due to the limited line rates of CCD or CMOS cameras. Utilization of a galvo-scannner instead of a polygon mirror [38] or of a resonant scanner allows the three different modes of operation to be implemented, where the line scanner is slowed down in the OCT regime in comparison with the SLO regime to allow for an increased number of A-scans. That is not possible with a resonant scanner, which operates at a fixed rate.

Alternatively, the bandwidth of the SLO channel can in principle be increased, allowing more optical pixels to be scanned within the same 1 ms ramp. While a 10 times increase in the bandwidth of the SLO channel is possible, this would have ruled out operation in the simultaneous mode, as an increase by a factor of 10 of the camera rate (to maintain pixel-to-pixel correspondence) is not feasible. If a faster SLO regime is desired, then the only alternative is to employ one of the two sequential regimes presented.

A Talbot bands configuration was employed in this report which allowed the derivation of optical signal for the SLO channel with little loss introduced to the OCT channel, however the three modes of operation presented can equally be implemented on any other spectrometer based OCT channel combined with an SLO channel. A TB configuration in the OCT channel redistributes sensitivity from small OPD values to larger OPD values, i.e. a TB configuration presents the potential of enhancing the signal from larger depths. In this paper, the sensitivity was skewed towards larger OPD values, however the peak sensitivity is less than in a non TB configuration, due to the *sinc* factor in Eq. (1). The overall sensitivity reduced by ≈ 10 dB at depths below 0.5 mm. This, however, does not present a disadvantage in comparison with conventional Sp-OCT technology. Normally, an imaging depth-range centered on the axial position corresponding to OPD $= 0$ and for a signal roll-off of up to 10 dB is avoided in practice of eye imaging, as a buffer range to cover fluctuations of the axial eye position. Mirror terms might occur when due to the axial eye motion, the retinal image is moved to the other side of the zero-delay (OPD $= 0$) depth [20]. In other words, the conventional technology presents maximum sensitivity within an axial range which cannot be used in practice; more exactly, the sensitivity maximum is placed at an axial position in front of the retina. In opposition, a TB configuration can make use of a more suitable sensitivity curve profile versus OPD, with its maximum placed within the retina. The larger the gap between the sample and reference beams in their way towards the diffraction grating, the larger the shift of the axial position of the maximum sensitivity from OPD $= 0$.

Some loss of sensitivity is also incurred in practice by transferring from a conventional Sp-OCT configuration to a TB configuration due to the need of securing similar polarization and dispersion in the two beams travelling towards the grating. This problem does not exist in conventional Sp-OCT, as the two beams travel along the same path after they interfered. Therefore, more work is required in optimizing the TB configurations to achieve similar efficiencies as conventional Sp-OCT configurations. Even so, overall, at larger depths, a TB configuration can offer better sensitivity, as proven in [26].

Acknowledgements

M. J. Marques acknowledges the support of the University of Kent through his University Scholarship. A. Bradu and A. Gh. Podoleanu acknowledge the support of the European Research Council (ERC) (http://erc.europa.eu) COGATIMABIO 249889. A. Podoleanu is also supported by the NIHR Biomedical Research Centre at Moorfields Eye Hospital NHS Foundation Trust and UCL Institute of Ophthalmology.